Novel small-molecule hole transport materials: towards ideal packing and doping

Thesis submitted in fulfilment of the requirements for the degree of Doctor of Philosophy

Benjamin Vella

School of Chemistry

College of Science and Engineering

University of Glasgow

June 2024

Abstract

Hole transport materials (HTMs) are crucial components in various types of electronic devices, particularly in energy conversion systems where they facilitate the rapid movement of charge from the active layer to the electrode. In light of the pressing need to shift away from unsustainable, non-renewable energy production through fossil fuels, developing low-cost energy-converting technology is of utmost importance for a more sustainable future.

Despite significant progress in the field of HTMs, characterised by a plethora of organic and inorganic materials being introduced monthly, the 'ideal' HTM remains elusive. This would represent a material that is cost-effective to produce, high-performing, reliable, and stable. The challenge stems from the intricate nature of the interactions between HTM structures and their behaviour in a film. All different elements of molecular structure contribute to the bulk charge transport properties, making it difficult to isolate individual influences from the observed net effect. Additionally, the need for chemical doping of HTM systems to increase carrier concentrations introduces further complexity, as the choice of additives and resulting doping reaction products profoundly impact the film characteristics. **Spiro-OMeTAD**, a widely used organic HTM in solar cell technologies, exemplifies these challenges, requiring chemical additives for adequate conductivity and suffering from poor film formation due to weak intermolecular interactions. It also suffers from costly synthesis and purification that hinder its widespread commercialisation.

Consequently, there is a pressing need for research to explore molecular structures designed to allow robust interactions between adjacent molecules in films, in order to overcome the shortfalls of **Spiro-OMeTAD**. In doing so, the links between molecular structure and bulk properties must be investigated. This thesis presents a series of HTMs synthesised through condensation chemistry, aiming to address some of the shortcomings of current HTM technologies and pave the way for more efficient and affordable solutions in electronic devices. These HTMs are used as a test bed to investigate the packing behaviour of linear organic HTMs, as well as their interactions with some common chemical additives that have non-trivial consequences on the final conductivity of the HTM film. The aim is to uncover structure-function relationships that will guide the smarter design of future HTMs. The three main chapters of this thesis consistently highlight a key observation: while chemical modifications to the HTM structure provide great control over its optical and electrochemical properties, they often lead to unexpected side effects in their oxidation and charge transport behaviour that necessitate further investigation. Comprehensive studies must therefore be conducted on any newly developed HTMs to uncover and mitigate these effects.

Table of Contents

Acknowledgements

I would like to begin by thanking my supervisors Prof. Graeme Cooke and Dr. Pablo Docampo, for welcoming me into their research groups and for their continuous support throughout my studies. Thanks also to Prof. Peter Skabara who acted most recently as my secondary supervisor, and before that, as my supervisor for my Masters project, which was what originally brought me to Glasgow five long years ago. Special thanks to Drs. Alex Harkiss, David Philips, Michele Cariello and Liam McCarron, who helped me find my feet during my first days (or months) in the lab, during COVID times where this took far longer than normal. Their patience with me as I fumbled many a first reaction is to be commended.

The same goes for all members of the Cooke and Docampo groups, who fostered a lovely work environment throughout these four years: Dr. Dylan Wilkinson, Lewis, Frances (now Dr. Frances Tracey!), Abdul-Wasir, Abarna, Cyrus, Gregor, Dr. Namrata Pant, Fraser, Marcin, and Ivan, who made daily lab work so much more enjoyable. In particular, I thank Dylan, Fraser and Marcin, as well as Dr. Paula Laborda Lalaguna from the Kadodwala group for their time spent helping me finalise results from this thesis for corrections or publication. I also thank our associates in the School of Chemistry who contributed time and expertise towards several measurements presented within; Dr. Claire Wilson for X-ray diffraction measurements, Dr. Giovanni Rossi and Eirinn-Rose McWilliams for mass spectrometry, Andy Monaghan for thermogravimetric analysis and differential scanning calorimetry measurements, and Dr. Stephen Sproules for electron paramagnetic resonance measurements. Thanks also to Dr. Adam Brookfield at the EPSRC for additional EPR analysis and expert help, and to Miriam Fsadni at Newcastle University for computational analysis and expertise. I would also like to thank my former project students Temaira O'kane and Madeleine McRoberts for their time spent in the Docampo group, serving as much of a learning experience for me as it was for them.

Outside the lab, I thank all of the amazing people I have met here that have turned Glasgow into a second home: Lewis, Marcin, Frances, Jess, Tess, Tom and Ellie, The Michaels (Cairns and Lammy), Eleanor, Tia, Francesca, Belinda, and Nicky. Cairns, your unending patience living with me for four years should win you some awards. Special heartfelt thanks goes to my lovely Łucja for her undying patience and love throughout the toughest times of this journey. I appreciate all that you do for me every moment of every day.

A few words hereunder for friends and family back home:

Grazzi l-ewwel u qabel kollox lill-familja tiegħi ghall-għajnuna u l-kuraġġ kollu li għamluli tul mhux biss dal-proġett, iżda ħajti kollha. Mingħajr l-imħabba u l-wens tagħhom, dan il-kapulavur qatt ma kien jilħaq il-qofol tiegħu. Ħajr kbir lil ommi u missieri, lil oħti, liz-zijiet u lin-Nina tagħna, kif ukoll lin-nanniet Ġużi, Antida, Karmnu u Mary. Huwa ta' pjaċir u unur kbir

għalija li nista ngħaddilkom kopja ta' dan il-ktejjeb, li ssawwar minn bosta teoremi, tħassib, ċifri u tqattigħ ta' xagħar. Filwaqt li l-aħħar passata żebgħa ngħatat hawn ġo l-Iskozja, is-sisien ta' dan ix-xogħol inbnew ħafna żmien ilu max-xagħra ta' Ġnien Ingraw. Tajjeb mela li l-manuskritt jerġa' jsib ruħu fil-post li dejjem ħa nqisu dari.

Lil sħabi kollha li żammew kuntatt tul dal-perjodu ta' distanzi kbar: Luke, Francesco, Steve, Giulia, Karl, Tina, is-Sant, Sean, Liam, u Samuel, ħajr lilkom, u ejja niltaqgħu daqt ħa nieħdu erbgħa birra. Żammejtuni f'sikti tul il-ġenn ta' din ir-riċerka. Lis-sur Justin, li kien hawn miegħi jaħdem fuq id-dottorat tiegħu ukoll, grazzi mmens tal-kumpanija u l-ħbiberija tiegħek.

Fl-aħħar, nixtieq inrodd ħajr lil żewġ għalliema li kelli meta kont għadni fil-bidu tal-istudji tiegħi: is-Sra. Julia Alexander Cilia u Dott. Jean-Pierre Tabone Adami, għalliema tal-kimika dak iż-żmien fi ħdan il-kulleġġ Stella Maris u s-*sixth form* ta' San Alwiġi. Kien permezz tagħkom, li seddaqtu din l-imħabba tiegħi lejn dan is-suġġett waqt l-istudju għall-*O levels* u l-*A levels*, li fl-aħħar wasalt biex nikteb dan it-teżi. Għintuni naqbad l-ewwel irkaptu tal-ġmiel minsuġ fl-iskala atomika, kemm bit-tagħlim eċċellenti kif ukoll bl-attitudni tant simpatika tagħkom. Nibqa dejjem niftakar id-diskursati fuq il-*Marillion* mad-Dott. Tabone Adami. Il-kontribut tagħkom it-tnejn kien bla qies mingħajr ma tafu, u b'hekk ma nistax ma nsemmikomx.

Thank you all. Grazzi lil kulħadd.

Author’s declaration

This thesis comprises original work undertaken by Benjamin Vella unless otherwise stated in the relevant sections of the text. Research contained within this thesis was conducted at the School of Chemistry within the University of Glasgow, with Prof. Graeme Cooke and Dr. Pablo Docampo as joint primary supervisors, and Prof. Peter Skabara as secondary supervisor, from October 2020 to April 2024.

Signed:

Date: 08/12/2024

List of Figures

List of Tables

List of Abbreviations

CBM	Conduction Band Minimum
CPCM	Conductor-like Polarisable Continuum Model
c-Si	Crystalline Silicon
CV	Cyclic Voltammetry
DA	Donor-Acceptor
DFT	Density Functional Theory
DOSY	Diffusion Ordered Spectroscopy
DSC	Differential Scanning Calorimetry
DSSC	Dye-Sensitised Solar Cells
EDOT	Ethylenedioxythiophene
E_g	Energy Gap
$E_{g,opt}$	Optical Energy Gap
ESI	Electrospray Ionisation
ETL	Electron Transport Layer
ETM	Electron Transport Material
FF	Fill Factor
FTIR	Fourier Transform Infrared Spectroscopy
HOMO	Highest Occupied Molecular Orbital
HTL	Hole Transport Layer
HTM	Hole Transport Material
ICT	Intramolecular Charge Transfer
IP	Ionisation Potential
ITO	Indium Tin Oxide
J_{sc}	Short Circuit Current
kMC	Kinetic Monte Carlo
LUMO	Lowest Unoccupied Molecular Orbital
NOESY	Nuclear Overhauser Effect Spectroscopy
OLED	Organic Light-Emitting Diode
OS	Organic Semiconductor
PCE	Power Conversion Efficiency
PSC	Perovskite Solar Cell
PV	Photovoltaic
SCXRD	Single-Crystal X-Ray Diffraction

SOMO	Singly-Occupied Molecular Orbital
SS-NMR	Solid-State Nuclear Magnetic Resonance
SWV	Square-Wave Voltammetry
TAD	Triarylamine Derivative
T_c	Cold Crystallisation Temperature
T_d	Decomposition Temperature
T_g	Glass Transition Temperature
TGA	Thermogravimetric Analysis
T_m	Melting temperature
TPA	Triphenylamine
UV	Ultraviolet
VBM	Valence Band Maximum
V_{oc}	Open Circuit Voltage
VT-NMR	Variable-Temperature Nuclear Magnetic Resonance

1 Introduction

As the climate crisis rages on, the need for more widely available renewable energy sources is more important than ever. The impact of non-renewable energy sources on our environment has become one of the most pressing issues we face today, in no small part due to the polluting emissions from the burning of fossil fuels and the inherently finite nature of these energy sources.[1,2] These concerns were addressed in the 2015 United Nations Climate Change Conference, leading to the signing of the Paris agreement in which various countries agreed to reduce CO_2 emissions, aiming to keep the global temperature rise to 'well below 2 degrees Celsius above pre-industrial levels'.[3] Unfortunately, little international action has been taken to put this limit into practice. One further international climate conference, COP26, took place in 2021 in order to accelerate action towards the goals originally established in Paris six years prior, with the resulting negotiations involving many world leaders concluding that while the 1.5 °C limit is still in sight, much more action is needed across the board to stick to it.[4]

A key step in addressing this crisis is the transition towards more renewable energy production, thus phasing out fossil fuels as the main global energy source. To this end, sunlight is widespread across most of the Earth's surface. Harvesting this light from such an abundant source of energy has potential to be one of the most effective means towards sustainable economic growth.[5] Solar photovoltaic technology has therefore become an area of significant research interest as new technologies are developed to more efficiently capture the Sun's energy. Key to the operation of any photovoltaic device are the interesting electronic properties of a class of materials known as semiconductors.

Semiconductors have become essential materials in a wide range of components for modern electronics. They are integral to the design of transistors, photodetectors, lasers, light-emitting diodes and solar cells to name a few. These components are found in countless readily available technologies, such as computers, smartphones, televisions, and energy generators such as solar panels.[6] The design and characterisation of new semiconductors to suit emerging technological demands is thus a continuing area of research, and spans a very wide range of organic, inorganic, and hybrid materials. This chapter gives a brief introduction to the physical characteristics that make up a semiconductor, highlighting the key differences in charge transport mechanisms between inorganic and organic semiconductors. The great potential of organic semiconducting materials is illustrated, as well as the present challenges they currently face in energy applications.

1.1 Electronic structure and charge transport

Semiconducting materials are commonly applied in electronic devices as charge transport layers, which shuttle positive or negative charges (holes or electrons) between different device components and electrodes to complete a circuit. A wide range of both organic and inorganic materials have been employed for both hole and electron transport, and each type presents a unique set of advantages and disadvantages that must be carefully considered. This thesis focuses on organic HTMs as key components within electronic devices, but the same concepts can be applied when considering electrons in electron transport materials (ETMs).

A semiconducting material is broadly defined as one which has a conductivity between that of a conductor and an insulator. In more scientific terms, this conductivity arises from two factors: the number of free charges within the material and their corresponding mobilities.[7] Electron or hole mobility (μ_e / μ_h) describes the ease by which charges can move through the medium under an electric field, and this is an important parameter to consider when characterising new HTMs.[8] The conductivity (σ_e / σ_h) is then defined as the product of carrier mobility and carrier concentration, for both electrons and holes. For materials used as holes transporters, it is far more convenient to define the movement of a small number of positive vacancies compared to a much larger number of moving electrons.[9] The hole conductivity σ_h is thus defined by Equation 1-1, where n_h is the concentration of holes within the conducting medium.[8]

$$\sigma_h = \mu_h \cdot n_h \tag{1-1}$$

Conduction in semiconducting materials is only possible through the movement of charges in excited states. The process by which an electron or hole moves through a semiconducting medium, and the nature of these excited states, is fundamentally different for organic and inorganic semiconductors. The following subsections will compare and contrast the two domains, detailing the charge transport mechanisms in both inorganic and organic materials. The great potential of organic semiconductors (**OS**s) for hole transport is emphasised, in order to set the stage for the work presented in this thesis.

1.1.1 Inorganic semiconductors and band structure

Inorganic semiconductors have a covalently bonded structure, where the atomic orbitals from individual atoms split into pairs of bonding and antibonding orbitals. The bonding orbitals are occupied by electrons and have slightly lower energy than the individual atomic orbitals, while the unoccupied antibonding orbitals have slightly higher energy.

In a solid containing many atoms (such as a crystal), the large number of similar energy levels occupied by these molecular orbitals effectively form two continua of occupied and unoccupied bands, separated by a forbidden energy gap, $\mathbf{E_g}$.[9] The highest occupied band contains the valence electrons and is accordingly called the valence band. The lowest unoccupied band is known as the conduction band. The difference in energy between the lowest unoccupied band and the highest occupied band, is called the band gap.[10] A key feature of inorganic semiconductors is band transport, which arises from the delocalisation of the electronic wavefunctions over the whole lattice. This gives inorganic semiconductors high mobilities, as electrons can move effortlessly within their energy bands, throughout the solid.

The band gap dictates whether the material is classified as a metal, semiconductor, or insulator. In a metal, there is no energy gap between occupied and unoccupied bands, thus electrons may easily move through the solid to conduct electricity or heat (Figure 1-1a).[9] Insulators have a band gap greater than ~3 eV, which prohibits thermal excitation of electrons from filled to empty states where they would be free to move under an electric field, leading to minimal conductivity (Figure 1-1c).[11] Semiconductors inhabit a middle ground, where the energy gap is lower than ~3 eV. Inorganic semiconductors are typically characterised by narrow bandgaps (e.g. 1.11 eV for silicon, 1.43 eV for GaAs).[10] A filled valence band is inert, offering no empty states through which electrons can move, thus prohibiting the flow of charge. At any temperature above absolute zero, an electron in a semiconductor may be thermally excited from the valence band into the conduction band through the absorption of a photon of sufficient energy. The electron in the conduction band, as well as the hole left behind in the valence band are both free to move under an electric field, and current may flow (Figure 1-1b).

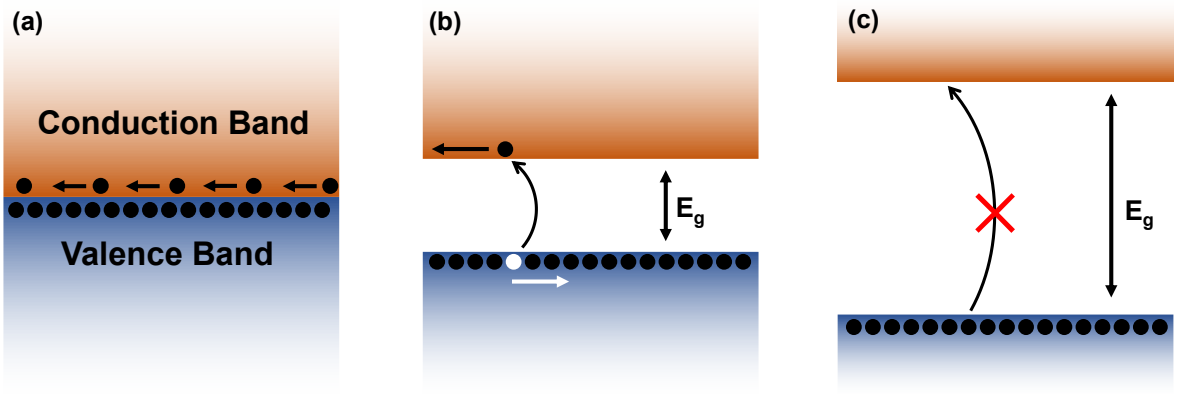

Figure 1-1: Schematic illustrating the distribution of energy states in (a) a metal; (b) a semiconductor; and (c) an insulator.

As the width of the energy gap affects the number of thermally excited electrons in the conduction band, this affects the intrinsic conductivity of a semiconductor at room temperature thus making $\mathbf{E_g}$ an important parameter to consider for potential device applications. In the dark or in the cold, very few electrons gain enough energy to cross the band gap into an unoccupied state. This lack of free carriers thus leads to low intrinsic conductivities for semiconductors. It follows that this intrinsic conductivity scales inversely with the width of the band gap and is the key difference between semiconductors and insulators.

1.1.2 Organic semiconductors and discrete structure

The electronic structure of an OS differs significantly from that of inorganic semiconductors, due to the different nature of bonding throughout the solid. Amorphous molecular solids are held together by non-covalent interactions such as van der Waals forces, dipole-dipole interactions, hydrogen bonding, and π-π interactions. This contrasts with the comparatively stronger covalent bonds that are found in an inorganic semiconductor lattice.[6,10] The space between adjacent, randomly oriented molecules due to the lack of a tightly σ-bonded network leads to very limited orbital overlap and the band approximation in Section 1.1.1 no longer holds. Furthermore, the local fluctuations in polarisation energies around each randomly oriented molecule leads to a perturbation in energy levels across all localised states, leading to a Gaussian distribution of states centred around each energy level.[12]

The key difference between organic and inorganic semiconductors is the extent to which the electronic wavefunctions extend across the bulk material. Within inorganic semiconductors, the intimate bonding between individual atoms in a crystal lattice leads to wavefunctions that extend throughout the whole material. Mobile charges can therefore move through the bulk with little hindrance. In OSs, the wavefunctions only extend across a few molecules. The electronic structure is thus better represented as being comprised of discrete energy levels. Here, the occupied and unoccupied states are defined by the frontier bonding and antibonding orbitals, in this case π and π* orbitals. These contain the highest occupied molecular orbital (**HOMO**) and lowest unoccupied molecular orbital (**LUMO**) respectively. Rather than band transport, charges must hop from molecule to molecule through frontier orbitals at slightly different energy, in a thermally activated tunnelling mechanism (Figure 1-2).[13]

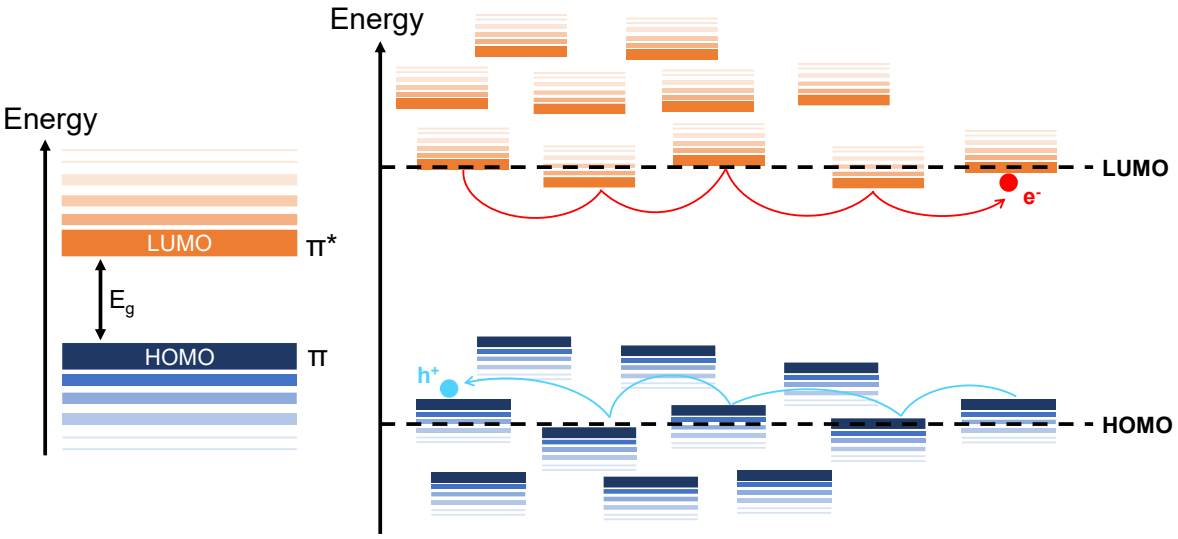

Figure 1-2: The electronic structure of a single organic semiconductor molecule depicting the frontier orbitals (left), and the hopping mechanism of charge transport showing the movement of charges through various HOMO and LUMO levels in a solid (right).

Most OSs in their pristine state have fully occupied π-orbitals and empty π* orbitals. The $\mathbf{E_g}$ in this case is the HOMO-LUMO gap, which is analogous to the bandgap for inorganics. Accordingly, an electron may be excited from the filled HOMO into the vacant LUMO upon absorption of a photon of sufficient energy. This allows for a crude estimation of the optical HOMO-LUMO gap, $\mathbf{E_{g,opt}}$, from routine UV-Visible spectroscopy measurements, where it represents the energy required to generate an electrostatically bound electron-hole pair or 'exciton'. While there are key differences between $\mathbf{E_{g,opt}}$ and the fundamental energy gap (namely, the binding energy of the exciton),[14] there are countless studies in the literature that routinely use the estimated $\mathbf{E_{g,opt}}$ as a rough HOMO-LUMO gap as part of a suite of characterisation techniques for new HTMs.[14–17] This gives some preliminary information to the optical properties of the material, informing potential device applications where factors such as optical transparency and the energy of photons required to generate excitons need to be known.

1.2 Organic semiconductors for energy applications

OSs represent a new chapter in semiconductor technology, offering unique advantages over inorganic alternatives, and many versatile applications. Unlike their inorganic counterparts, which include elemental materials (silicon, germanium) or compound ones (cadmium sulfide, gallium arsenide), OSs are characterised by molecular or polymeric structure, with carbon and hydrogen forming the backbone of the material. This opens up the world of organic chemistry as a tool for modifying various properties of the semiconducting material.

From a research perspective, organic materials are far easier to produce, purify, and process through routine synthetic chemistry techniques in standard laboratories. This contrasts with silicon, which must be mined from the earth as quartzite, requiring extensive processing and purification in order to yield sufficiently pure silicon for electronics.[18] The versatility of organic materials shines through their adaptability to a wide range of device applications through facile molecular modification. Structural modifications of organic molecules allow the easy tuning of various properties, including the HOMO-LUMO gap (thus optical absorption and fluorescence), as well as the oxidation behaviour. Moreover, their solubility in organic solvents facilitates easy deposition onto substrates, making them viable candidates for solution processing and large-scale printing.

Despite these benefits, OSs still do not offer equally attractive charge transport properties to inorganic semiconductors. Crystalline silicon (c-Si) possesses exceptionally high hole mobility (~1000 $cm^2V^{-1}s^{-1}$)[9], a property crucial for various applications such as solar power technologies. This is a direct result of the tightly-bound lattice. OSs typically exhibit significantly lower mobilities, with the best examples still lagging behind silicon by several orders of magnitude (~10^{-3} $cm^2V^{-1}s^{-1}$).[19] This limitation represents the main bottleneck hampering the commercial viability of OSs. For instance, OLED technology is the main technology that embraces OSs, but very thin emissive films are required to compensate for inadequate charge transport through the active layer. This also limits the applicability of solution spin coating, in favour of more costly thermal evaporation which can yield much thinner films.[20] Nowadays, the majority of successful technologies are a mix of organic and inorganic components, as is the case with perovskite solar cells (PSCs).[5,21]

While inorganic semiconductors may seem to overcome the charge transport limitations of their organic counterparts, they still pose significant challenges to which organic materials prove superior. The synthesis of new organic materials from an abundant reservoir of carbon and hydrogen provide a leading edge over the inorganic domain, where materials often face scarcity issues during sourcing. Prime examples include tellurium and ruthenium, which are rare earth metals commonly used in many thin-film solar technologies such as dye-sensitised solar cells (DSSCs).[22]

Crystalline silicon is another notable example, as it must have extremely high purity for use in electronics, and the extensive purification process represents another expensive step in the c-Si production chain.[23,24] The use of inorganic materials for flexible applications is also severely limited by their rigidity and heavy weight.[10] From the point of view of photovoltaics (PV), first-generation c-Si solar panels remain the dominant product on the market despite their high cost of production. At the end-of-life stage, these modules are discarded in landfills, aggravating the pre-existing problem of electronics waste.

Worse yet, PV components may be incinerated, releasing toxic gases into the atmosphere. The difficulty in recycling silicon and other inorganic semiconductors requires the use of fresh materials for the production of new devices.[25] This linear economy is clearly not sustainable in an age of dwindling resources and an increasing concern towards atmospheric pollution. The future of PV therefore necessitates embracing a technology that is easier to source, recycle and reuse. OSs are a promising candidate in this regard, offering better long-term prospects for incorporation into circular economies.[26]

In order for OSs to compete with established PV technology, their charge transport limitations described above must be addressed. In the context of HTMs, the biggest limitation towards the widespread application of organic HTMs is the low conductivity of the materials. This arises from two factors, low hole mobility and low concentration of free holes (Equation 1-1). Low free hole concentration arises from relatively wide HOMO-LUMO gaps, wider than typical bandgaps for inorganic materials.[10] This reduces the likelihood of thermal excitation of electrons into the LUMO, leading to a very low concentration of mobile charges at room temperature. Indeed, intrinsic OSs typically show insulating behaviour in their pure form. The low mobility is a consequence of the lack of strong covalent bonding between molecules in an organic HTM. The intermolecular distances in organic materials are significantly longer than interatomic distances in a silicon crystal. Charge hopping is fundamentally slower than band transport, leading to the reduced mobilities. Mobility is affected by a number of other features of the organic HTM, such as crystallinity/amorphous nature, packing, impurities, and temperature.[27]

Significant research has thus been devoted to the design of organic hole transporting systems with increased conductivity, such that they may rival their inorganic alternatives. From Equation 1-1, conductivity can be improved by increasing either the concentration or the mobility of the free holes. The former is readily achieved through chemical doping, while the latter can be achieved through tailored design of HTMs with high intrinsic mobility. These techniques are further detailed below in Section 1.3.

1.3 Overcoming the charge transport limits of organic HTMs

In order for many OSs to be used effectively in a variety of device applications, additional charges must be created through the use of chemical additives. This process is commonly termed ‘doping’, in analogy to the process typically used in inorganic semiconductors where impurities are introduced to the lattice to introduce additional free positive or negative charges to increase conductivity.[28]

Doping of OSs involves a similar process, but is achieved through a partial oxidation ('p-doping') or reduction ('n-doping') of the material. As this thesis focuses on hole transporting small-molecules, the following discussion will deal exclusively with doping as the oxidation of a small portion of the bulk. Oxidation removes an electron from the HOMO, creating radical cations wherein the highest occupied orbital has single occupancy (**SOMO**) and is slightly deeper in energy than the surrounding HOMO energies. As a result, there is a thermodynamic driving force for an electron to hop from a pristine molecule HOMO to a neighbouring SOMO, in what is effectively a redox reaction.[29] The hole is thus transferred onto another molecule, and the process repeats in order to transport the hole across the bulk. The oxidised species functions as the 'dopant', which possesses a positively charged vacancy that can travel through the matrix (Figure 1-3).

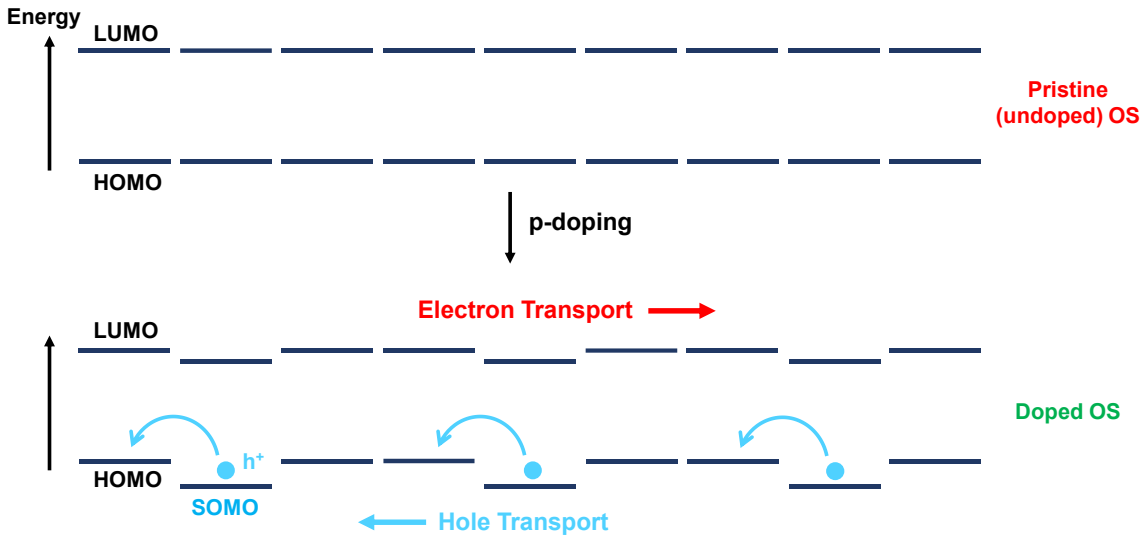

Figure 1-3: Schematic of the effect of chemical doping on the energetics of an organic semiconductor film.

In the context of devices such as PSCs, efficient charge extraction from the perovskite absorber and transport to the electrodes is paramount. The record holding devices normally utilise a doped hole-transport layer, often including the state-of-the-art HTM 2,2',7,7'-tetrakis[N,N-di(4- methoxyphenyl)amino]-9,9'-spirobifluorene (**Spiro-OMeTAD**). **Spiro-OMeTAD** is a small-molecule HTM that was originally developed for use in DSSCs, and remains one of the most popular HTMs in a variety of different devices such as light-emitting diodes (LEDs), OLEDs, and PSCs.

In the case of PSCs, **Spiro-OMeTAD** has very favourable energy alignment with the valence band of many popular perovskite compositions. Perovskite materials typically have valence band energies around -5.4 – -5.7 eV.[30,31] The HOMO level of a HTM must be slightly shallower in energy in order to allow for the easy crossing of holes from the perovskite into the HTM for transport.[32] **Spiro-OMeTAD** is typically found to have a HOMO level of -5.1 eV, thus providing a small offset that is amenable to hole injection from the perovskite.[33]

However, in its pristine (undoped) state, **Spiro-OMeTAD** has very low conductivity of around 3×10^{-8} S cm^{-1}, which would induce a very high series resistance in a device.[34,35] Chemical doping can increase this conductivity by up to four orders of magnitude, and has been achieved through a variety of additives. The most commonly used oxidants for doping HTMs in PSCs are bis(trifluoromethylsulfonyl)imide (**TFSI**) salts such as lithium bis(trifluoromethylsulfonyl)imide (**LiTFSI**) and the cobalt (III) complex tris(2-(1H-pyrazol-1-yl)-4-tert-butylpyridine)cobalt (III) tri[bis(trifluoromethane)sulfonimide] (**FK209**). Their molecular structures are shown in Figure 1-4.

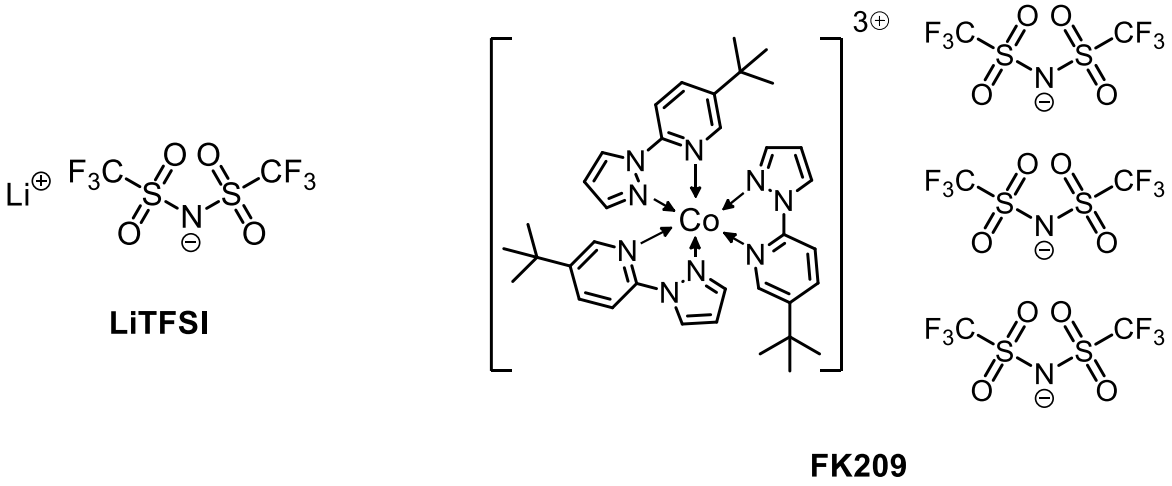

Figure 1-4: Molecular structures of two commonly employed chemical oxidants for HTMs: **LiTFSI** (left) and **FK209** (right).

The oxidation of **Spiro-OMeTAD** with **LiTFSI** is now well understood to involve an indirect mechanism, with **LiTFSI** promoting the formation of the charge transfer complex between **Spiro-OMeTAD** and oxygen.[35] In air, a small amount of weakly bound **Spiro-OMeTAD$^{+\cdot}$O$_2^-$** is formed from the charge transfer reaction between **Spiro-OMeTAD** and atmospheric oxygen. This is a result of the low ionisation potential (**IP**) of **Spiro-OMeTAD** and the high electron affinity of molecular oxygen, which allows for oxygen to extract an electron from the HOMO of **Spiro-OMeTAD**.[35] The HOMO in **Spiro-OMeTAD** is mainly situated on the triphenylamine (TPA) arms, so the resulting radical cation is likely to be centred around the TPA nitrogen atom, delocalised over the three phenyl rings.[36] The resulting concentration of oxidised **Spiro-OMeTAD** in air is negligible, but the addition of **LiTFSI** causes the displacement of O_2^- with $TFSI^-$, forming **Spiro-OMeTAD$^{+\cdot}$TFSI$^-$** and shifting the equilibrium towards more oxidised **Spiro-OMeTAD** (**Spiro$^+$**) as detailed in Scheme 1-1. Lithium is consumed in the reaction, forming a series of lithium salts (LiO_2 and Li_2O_2) as byproducts.[35,37]

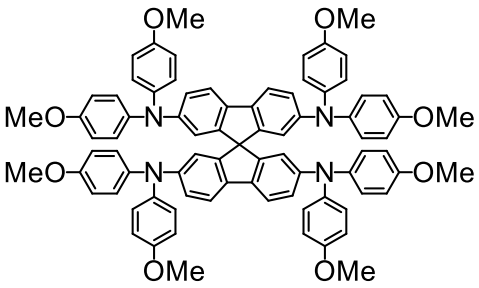

Spiro-OMeTAD
('Spiro')

$$\text{Spiro} + O_2 \rightleftharpoons \text{Spiro}^{\bullet+}O_2^{\bullet-}$$

$$\text{Spiro}^{\bullet+}O_2^{\bullet-} + \text{LiTFSI} \longrightarrow \text{Spiro}^{\bullet+}\text{TFSI}^- + \text{Li}_x\text{O}_y$$

Scheme 1-1: Molecular structure of **Spiro-OMeTAD** (left) and the **LiTFSI** doping mechanism (right).

The $TFSI^-$ anion stabilises the **Spiro-OMeTAD** radical cation, and is itself inert due to its highly delocalised negative charge.[38,39] This delocalisation also means that the hole in the **Spiro-OMeTAD$^{+\cdot}$** radical is weakly bound to $TFSI^-$, and can move through the matrix under an electric field as described in Figure 1-3 above, thus resulting in enhanced conductivity. Since a reaction with atmospheric oxygen is part of the mechanism, doping with **LiTFSI** is somewhat ambiguous, since an arbitrary 'curing' step in an oxygen-rich environment is required for the generation of the **Spiro-OMeTAD$^{+\cdot}$O$_2^-$** species to start the doping reaction. This makes quantifying the amount of generated **spiro$^+$** difficult, which can complicate analysis and reproducibility.

Other additives that directly oxidise the HTM offer more control in the degree of oxidation. With **FK209**, the doping mechanism is similar in that **Spiro-OMeTAD$^{+\cdot}$** is formed, and is stabilised by a $TFSI^-$ counterion. In this case, the **FK209** directly oxidises **Spiro-OMeTAD** through the concomitant reduction of the cobalt (III) centre to cobalt (II). The mechanism does not require oxygen, as the driving force for oxidation is provided entirely by the reduction of Co (III) to Co (II).[40] **FK209**, as well as the fully organic 2,3,5,6-tetrafluoro-7,7,8,8-tetracyanoquinodimethane (**F4-TCNQ**) are two commonly used examples of direct chemical oxidants that are routinely employed in chemical doping.[40–44] **F4-TCNQ** can also oxidise **Spiro-OMeTAD** through a redox reaction, itself becoming the counterion that remains bound to the oxidised species in a charge-transfer complex. It is an example of a fully molecular oxidant, that does not introduce ionic impurities into the bulk HTM and thus provides a more hydrophobic alternative to traditional lithium or cobalt-based dopants.[44] The reaction schemes detailing the **FK209** and **F4-TCNQ** oxidations of **Spiro-OMeTAD** are illustrated in Schemes 1-2 and 1-3.

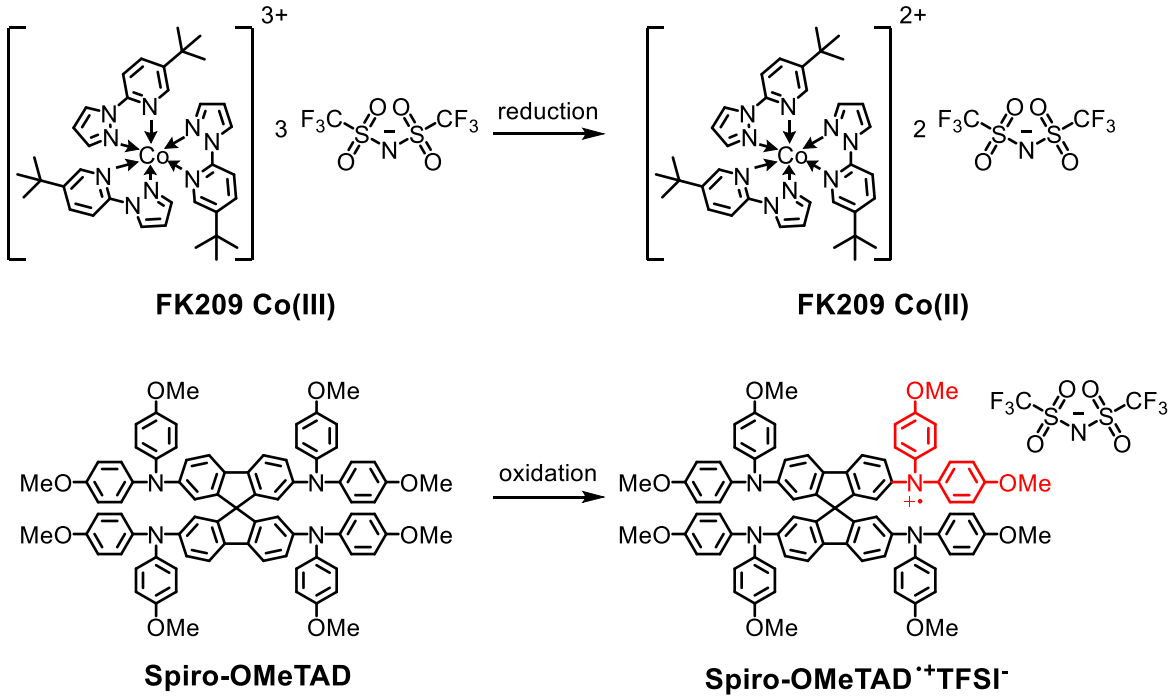

Scheme 1-2: Direct **FK209** oxidation mechanism showing the redox half-reactions involved in the oxidation of **Spiro-OMeTAD**.

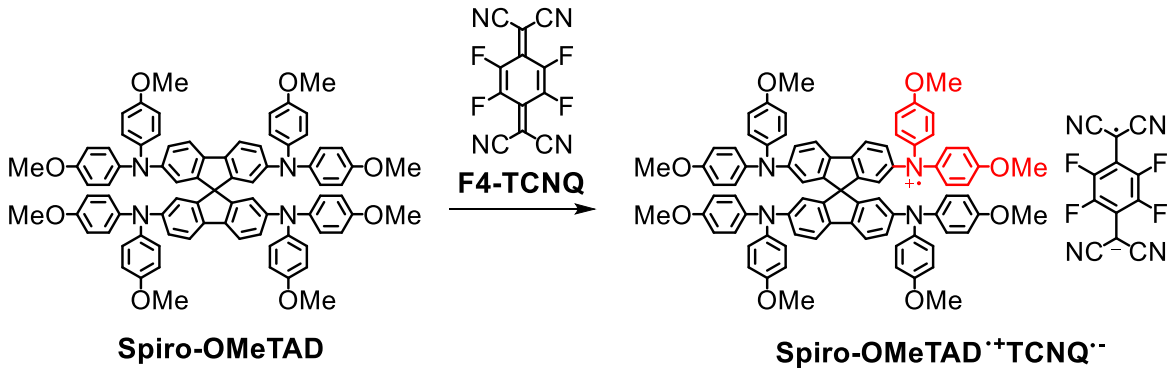

Scheme 1-3: Direct **F4-TCNQ** oxidation of **Spiro-OMeTAD**, to form the charge-transfer complex.

While chemical doping imparts greatly increased conductivity through generation of additional free holes to compensate for low mobility, significant research effort is also focused on developing HTMs with intrinsically high mobility, that would not require doping.[45–47] Dopant-free HTMs incorporate smart designs that allow closer interactions between adjacent molecules to overcome the mobility problem. Fully conjugated backbones, for instance, allow for a rigid core that facilitates π-π stacking. This allows for easier intermolecular charge hopping between HOMO levels in a stack, increasing mobility.[46]

Triarylamine-based derivatives (**TADs**) have also shown great promise, sometimes possessing intrinsic hole mobilities higher than those found for doped **Spiro-OMeTAD**, which can still limit the fill factor (**FF**) of devices that incorporate it.[48] However, while numerous dopant-free HTMs have been developed to date, none have managed to dethrone **Spiro-OMeTAD** + **LiTFSI** + **FK209** as the state-of-the-art HTM preparation. Therefore, the search for new, low-cost, and greener HTM systems that can address the mobility limitation of **Spiro-OMeTAD** continues.

1.4 Beyond **Spiro-OMeTAD**: New generation HTMs

While chemical doping effectively addresses the conductivity and mobility issues faced by **Spiro-OMeTAD**, there are still drawbacks hindering its widespread commercial viability. The lithium salts produced as byproducts from **LiTFSI** doping, as well as residual **LiTFSI** itself are hygroscopic, and promote the ingress of water into devices which shortens their lifetime. Many photovoltaic devices such as PSCs are particularly sensitive to this, as perovskite materials are known to be prone to moisture-induced degradation, often requiring sealing in inert atmospheres for long-term studies.[49] Morphological issues, such as pinholes in **LiTFSI**-doped films, further exacerbate water ingress by creating channels through which water can penetrate into the device and cause degradation.[50] As Li^+ is not covalently bonded to the hole transporting molecule, these ions can also migrate under an electric field to cause degradation in other layers of the device.[51,52] Finally, and perhaps most significantly, the synthesis of **Spiro-OMeTAD** involves a multi-step process with extensive and wasteful purification procedures and transition metal-catalysed cross-coupling steps, resulting in a very high cost of production.[53,54]

Significant research has actively explored alternative HTM designs to address these challenges in PSCs and other devices. This spans both molecular and polymeric structures, with conducting polymers like poly(bis(4-phenyl)(2,4,6-trimethylphenyl)amine) (**PTAA**) and poly(3-hexylthiophene-2,5-diyl) (**P3HT**) as exemplars of the polymeric approach. Conjugated polymers such as **PTAA** have already been implemented as HTMs in PSCs reaching efficiencies as high as 23%.[55] These polymeric HTMs share the solution processability and amorphous nature of their small-molecule counterparts, while also exhibiting higher temperature resistance and resistance to mechanical stress. On the other hand, there are several issues unique to polymeric structures that hamper their widespread application. Polymer synthesis suffers from low batch-to-batch reproducibility, due to variations in polydispersity which drastically affects film morphology and the electronic properties of the resulting polymer.

The ill-defined molecular weights are dependent many subtle variations in the synthetic procedure, which complicates characterisation, as different labs synthesising the same polymer are likely to produce different results depending on their varying preparation techniques. The need for chemical doping also persists in many polymeric HTMs, thus leading to the same long-term stability issues faced by the small-molecule HTMs.[56,57]

Of the many alternatives developed, a very promising new generation of HTMs incorporating the ethylenedioxythiophene (**EDOT**) core has shown particular promise. The first **EDOT** based HTM (**H101,** Figure 1-5) came about in 2014 and was produced by means of a one-pot synthesis involving palladium catalysis and a Suzuki coupling. **H101** was incorporated into PSCs to give efficiencies as high as 13.8%, comparable to that of **Spiro-OMeTAD** at the time.[53] The synthesis of **H101** is markedly simpler than that of **Spiro-OMeTAD**, but still required transition-metal catalysis to proceed successfully. Therefore, further developments introduced an imine analogue (**EDOT-OMeTPA**) which introduced condensation chemistry as a low-cost route to synthesising HTMs. **EDOT-OMeTPA** was prepared using simple Schiff base condensation chemistry to form the imine bond between the **EDOT** core and the triphenylamine (TPA) units. This analogue was again comparable to **Spiro-OMeTAD** in PSC applications, but benefitted from a far simpler and cleaner synthesis, with the final condensation reaction yielding the product in good yield with water as the only side product. The resulting HTM was also fully conjugated and this was expected to improve charge transport through the more robust delocalised π-system. The product HTM was found to have a HOMO level even closer to the perovskite VBM than that of **H101** as a result of the additional electron-withdrawing capability of the imine bond, thus improving the V_{OC} of the resulting devices.[58]

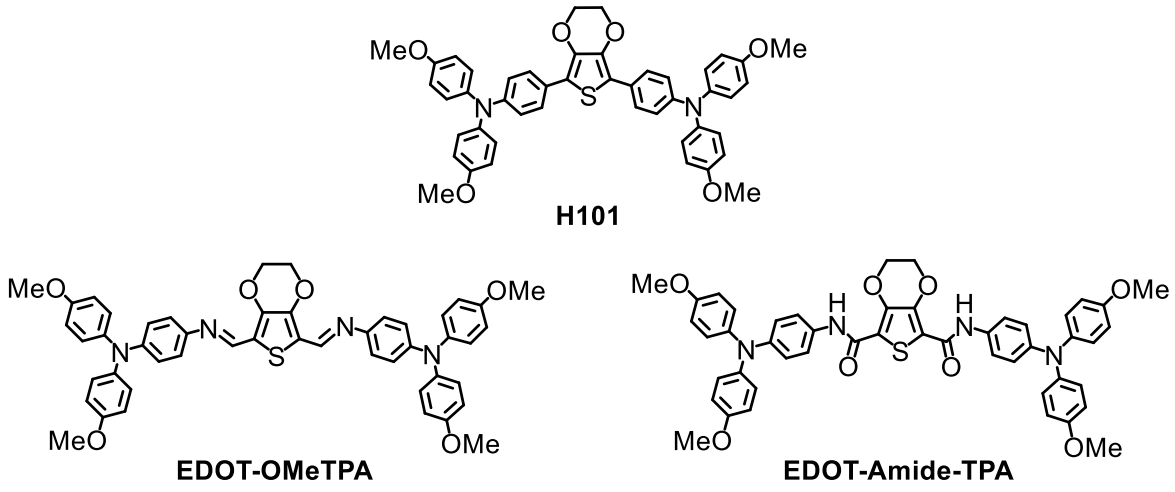

Figure 1-5: Three ethylenedioxythiophene (**EDOT**) HTM structures, showing the evolution of the linker groups from a simple C-C bond (**H101**) to conjugated imine (**EDOT-OMeTPA**) to amide group (**EDOT-Amide-TPA**).

EDOT-Amide-TPA is a non-conjugated analogue of **EDOT-OMeTPA** which can also be prepared through condensation chemistry. This molecule lacks the fully conjugated backbone of **EDOT-OMeTPA**, as the imine bond has been replaced by amide groups. The amide groups introduce the possibility of hydrogen bonding interactions.[54] Intermolecular hydrogen bonding can compensate for the lack of conjugation through the backbone by promoting closer packing between HTM molecules. A reduced average intermolecular distance should allow for easier hole hopping which leads to increased mobility. Indeed, similar mobility values have been reported for pristine **EDOT-Amide-TPA** compared to its conjugated analogues **H101** and **EDOT-OMeTPA**.[16,54] This shows that a fully conjugated backbone is not essential for good charge transport, the most important factor is the ease of hopping between one HOMO to another on an adjacent molecule.

The three molecules in Figure 1-5 above are examples of linear HTMs, which consist of a core connected to one or two 'arms' either through a C-C bond such as in **H101** or through some other linker group. They benefit from straightforward synthesis and the possibility of strong π-π stacking interactions which are allowed by the close packing of linear structures. Donor-acceptor (DA) structures are one type of linear HTM structure, where the HTM is comprised of an electron-deficient core (the 'Acceptor', A) bonded on one (DA) or both sides (DAD) by electron-rich moieties (the Donor(s), D). These materials often present simpler syntheses than materials such as **Spiro-OMeTAD**, and possess easily tunable energy levels which can be achieved by chemical modification of either the donor or the acceptor groups. The presence of separate electron-rich and electron-deficient parts of the molecule also introduces a dipole through the molecule which has myriad benefits on the film formation.[13] D-A-type HTMs also benefit from intramolecular charge transfer (**ICT**), which allow further control of the energy levels (and thus, the absorption properties) of the HTM through modification of the electron-deficient or electron-rich moieties.[26,56] The HOMO of the HTM is controllable through modification of the donor, and the LUMO is controllable through the acceptor.[1]

Triphenylamines (**TPA**) are commonly used as donor groups due to their good thermal stability, with suitably high glass transition temperature ($\mathbf{T_g}$) that allows the molecules to withstand the operational temperatures of PSCs. TPAs also have low IPs (6.80 eV),[1] favourable for charge injection and hole hopping. Generally, oxidation of TPA-based HTMs occurs through the removal of an electron from the central nitrogen, forming a radical cation which is stabilised by extensive delocalisation across the aromatic rings as shown in Scheme 1-4.[36]

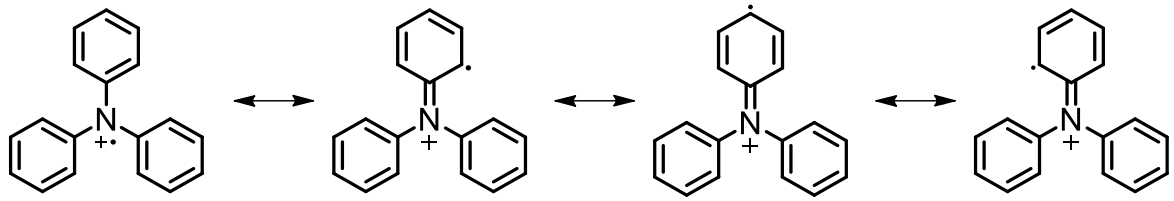

Scheme 1-4: Resonance structures showing the delocalisation of the unpaired electron on TPA moieties.

1.5 Structure-function relationships for smarter HTM design

The intermolecular interactions between HTMs at the molecular level govern the macroscopic properties of the solid film. It follows that a good understanding of these intermolecular interactions is pivotal when seeking to design HTMs with optimised film forming properties to address the current limitations of **Spiro-OMeTAD**. The poor film-forming qualities associated with **Spiro-OMeTAD** stem from its inherently globular molecular structure. This arises from the orthogonal geometry induced by the tetrahedral carbon around the spiro core, leading to significant intermolecular charge hopping distances. **Spiro-OMeTAD** molecules are unable to stack efficiently, and are not brought closer together through hydrogen bonding or dipole-dipole interactions, thus hindering charge transport. **Spiro-OMeTAD** can only form weak van der Waals forces. Consequently, during the spin coating process, molecules poorly adhere to each other resulting in poor film quality and significant porosity. These factors collectively contribute to the low long-term stability observed in **Spiro-OMeTAD**-based devices. Tailoring the intermolecular interactions to encourage denser molecular packing is a good approach towards optimal film formation and charge transport. Adopting a linear geometry such as those found in the **EDOT**-based molecules (Figure 1-5) allows for π-π stacking interactions between neighbouring HTM molecules. In the context of film formation, this has several distinct advantages to both film formation and hole mobility as is the case with hydrogen bonding, discussed earlier.

The **EDOT**-based small molecules also contain a strong dipole through the molecular core, which further supports close molecular packing through dipole-dipole interactions. Strong dipoles can even induce a level of self-assembly and long-range order.[61] In the **EDOT** core, the cyclic ether attached to the thiophene ring represents the most electropositive region of the molecule.[54] With its strong dipole and planar core, smooth and pinhole-free film formation has been observed with **EDOT-Amide-TPA** compared to far poorer films formed by **Spiro-OMeTAD**.[54]

Despite the wide range of synthetic tools available to create a vast array of HTM structures, designing new HTMs is still a very nuanced process. Even minor alterations to a molecule can result in substantial (and often unpredictable) changes on the bulk properties. The impact of each chemical modification must therefore be carefully considered. For example, strong dipoles across an HTM molecule may have the unintended consequence of high dipole disorder in the resulting film. This has been shown to contribute to significant energetic noise within the film, which hinders the percolation of charge through the material and lowers the hole mobility.[13] Therefore, while the presence of strong dipoles is beneficial for film formation, another layer of complexity is introduced into the system.

1.6 The current state of HTM research

In the development HTMs for PSCs, several features are essential for achieving optimal performance. The ideal HTM must be cost-effective to produce, and exhibit good air and moisture stability in order to withstand continued operation in commercial units. The alignment of energy levels between the HTM and other components within the device is crucial for efficient charge transfer and overall photovoltaic performance. Additionally, high hole mobility is necessary to ensure effective charge transport within the layer itself. Solubility in common organic solvents is important to simplify processing through printing techniques. Beyond these basic requirements, the HTM should remain amorphous in its solid state, with a high glass transition temperature ($\mathbf{T_g}$) to withstand elevated operating temperatures. The transition to a crystalline state is undesirable as crystalline HTMs often lead to grain boundaries and incomplete contacts at the interfaces of the device, causing J-V hysteresis and ultimately reducing overall device efficiency.[32]

When evaluating the suitability of OSs for optoelectronic applications, a variety of routine laboratory characterisation techniques are employed to study these materials at the molecular level. UV-Visible absorption and fluorescence spectroscopy, along with cyclic voltammetry (**CV**), are commonly used to determine the electronic energy levels of the materials. A UV-Visible absorption spectrum reveals which photon energies are sufficient to excite an electron to a higher energy state. From the absorption onset, the HOMO-LUMO energy gap may be estimated as the minimum energy required for excitation. This analysis can be performed in solution or on thin films. It is important to note that the absorption properties of a material in solution may differ from those in the film state, due to the solvent's influence on the stability of both the neutral and excited states. On the other hand, if the absorption profiles of film and solution measurements overlap, it can indicate amorphous character in the film, which effectively resembles the random molecular orientation in solutions.[54]

CV is another technique that reveals the IPs of species in solution, i.e. the energy required to remove an electron from a molecule to create a cation. This measurement offers a rough estimation of the HOMO energy, a crucial parameter for structuring the energetic interfaces within a full device. Spectroscopic and electrochemical techniques, therefore, become essential in estimating the energetics of any new material. Data from these experiments are often complemented by quantum chemical calculations, through density functional theory (**DFT**). DFT provides calculations of optimised molecular structures, energy levels, and spectroscopic properties. DFT, applied using atomic orbital basis sets like B3LYP, is popular due to its balance of accuracy and computational cost, offering significant insight with relatively low effort. Researchers can utilise these computational methods in parallel with experimental work to maximise efficiency.[62–65]

Further materials characterisation involves thermochemical analysis, which provides critical information regarding phase transitions of the solid material. Given the importance of thermal stability in maintaining the amorphous phase, thermogravimetric analysis (**TGA**) is used to determine the thermal decomposition temperature of a species. Differential scanning calorimetry (**DSC**), on the other hand, can detect phase changes such as glass transitions or crystallisation, which are undesirable for maintaining device stability under normal operating conditions.[66,67]

Newly synthesised organic materials are typically characterised using a suite of techniques, including mass spectrometry, nuclear magnetic resonance (**NMR**) spectroscopy, and infrared (**IR**) spectroscopy. These techniques are essential for assessing the purity of the synthesised material, but they also provide additional insights at the molecular level. For instance, ^{1}H-NMR spectroscopy analyses the electronic environments surrounding the protons within an organic molecule, revealing details about hydrogen bonding and other non-covalent interactions present in solution. Intermolecular hydrogen bonding or π-π stacking interactions have a concentration-dependent effect on the chemical shift of the protons involved. IR spectroscopy can then complement this information in the solid state, where it can compare these interactions between crystalline and amorphous forms. This comparison is particularly useful for understanding the nature of ordering, or lack thereof, within thin films. Powder and single crystal X-ray diffraction (**XRD**) techniques also offer information about structural order within powders, crystals, and films, wherein long-range order gives defined reflections on a diffractogram, while amorphous materials show no defined reflections. A perfect crystal represents the most ordered form of a material, typically achieved through slow crystallisation. In contrast, solution-processed films tend to be highly disordered, as there is less time for proper molecular ordering during film formation. XRD can then be used to elucidate the ordering, or lack thereof, in a thin film.[68–70]

As charge transport is the crux of HTM function, several techniques are employed to measure the conductivity and mobility of new devices. Lateral current-voltage (JV) measurements are among the simplest methods to determine the film conductivity of organic materials. This technique involves measuring the current response across a thin channel filled with HTM deposited through spin coating. From the resulting JV curves, the conductivity can be estimated. providing valuable information about the electrical performance of the material in real-world devices. The hole mobility is another important parameter to compare and contrast different HTM candidates. It is a complex characteristic that depends on the film morphology and purity, as well as extrinsic factors such as the identity and quality of the interfaces around the hole transporter.[71] It can be measured by a number of techniques involving the current-voltage characteristics of thin films between injecting electrodes. The space charge-limited current (**SCLC**) technique is a very common tool used to determine hole mobility. The organic material is sandwiched between hole-selective contacts, and the current-voltage characteristics are measured. At lower voltages, charge transport is seen to be ohmic, with a linear dependence of current to the applied voltage. At higher voltages the ohmic relationship is disrupted and a quadratic dependence of current on the applied voltage is observed. This is the space charge-limited regime, and the gradient from this region can be extrapolated to find the intrinsic hole mobility of the material.[71–73]

Further characterisation of newly developed HTMs frequently involves testing the developed materials within small-scale solar cells. In this regard, PSCs are a relatively new type of photovoltaic technology that has garnered much research attention in the last 10 years. Perovskites are characterised by a crystal structure with a unit cell formula ABX_3, typically composed of an organic cation, a divalent metal, and an anion. Their solution processability allows PSCs to be fabricated through a range of facile methods such as spin coating, dip coating, and ink-jet printing. The flexibility in processing methods makes perovskites among the most adaptable choices in photovoltaic (PV) technology, making this accessible to researchers across the globe. Perovskite design increasingly incorporates mixed cations and halides. Pure perovskite compounds commonly used in PV applications, like $MAPbX_3$, $FAPbX_3$, and $CsPbX_3$ (where X = Br or I), often encounter issues with thermal and structural instability.[74] By blending different cations and halides, it is possible to combine the beneficial attributes of each component while mitigating their individual limitations. For instance, combining cesium (Cs), methylammonium (MA), and formamidinium (FA) in a triple-cation configuration enables the production of high-quality perovskite films, which can achieve stabilised power conversion efficiencies (PCEs) exceeding 26% as the current record when used with **Spiro-OMeTAD** as the hole transporting layer.

These triple-cation perovskite films are also more resistant to environmental variables, such as temperature fluctuations, solvent vapours, and heating protocols, leading to greater thermal stability.[75]

Despite its inherent challenges, **Spiro-OMeTAD** remains the preferred choice among HTMs. However, to advance OSs toward widespread commercial adoption, it is crucial to address the limitations associated with these materials. Two of the most significant obstacles include the high cost of synthesis and insufficient charge transport capabilities. These issues highlight the ongoing need for the development of new HTMs that can overcome these drawbacks, pushing the field towards large-scale commercialisation and contributing towards a more sustainable future.

One promising alternative to **Spiro-OMeTAD** is **EDOT-Amide-TPA**, which has demonstrated competitive performance in side-by-side comparisons. Notably, **EDOT-Amide-TPA** offers the advantage of lower synthetic costs, making it a more economically viable option. Moreover, this material provides a promising foundation for the synthesis of a broader family of HTMs through condensation chemistry, offering a pathway toward the development of next-generation HTMs which is explored in this thesis.

1.7 In this work

This thesis addresses some of the present challenges faced by molecular OSs used as HTMs. By focusing on simple, linear designs produced through condensation chemistry, families of chemically related structures were easily prepared, demonstrating the utility of amide and imine condensations towards low-cost HTMs. The effects of structural variations were then explored to test a variety of hypotheses. The final conductivity of a thin HTM film is found to be dependent on the interplay between many factors, such as doping level, the ordering of dipoles within the film, and the stability of the oxidised HTM.

The main findings of this work reveal that there is a delicate interplay between molecular structure and the charge transport properties within the film. Pinpointing exactly what makes a good HTM remains difficult, because the process of changing the material's properties through chemical modification results in unintended effects to the final conductivity, requiring a thorough revision of the underlying hypotheses. However, through these amide and imine materials, some of the effects that contribute towards the final conductivity could be disentangled. Reducing dipole disorder within HTM films enhances the conductivity by minimising energetic noise. Chapter 2 demonstrates this by introducing three amide-based HTMs with varying intermolecular interactions. By inducing zero-dipole pairs between molecules, conductivity is enhanced as a result of reduced energetic noise. Chemical doping for HTMs requires specific recipes tailored to each HTM.

Chapter 3 challenges common assumptions regarding chemical doping using the amide HTMs, highlighting the need for specificity in doping different HTMs. Chapter 4 expands on this concept, examining two isomeric, imine-based HTMs. Significant differences in conductivity were observed upon direct oxidation with **FK209** between the two isomers at the same additive loading, underscoring the complexity of doping processes, the presence and detrimental effect of side reactions, and the necessity for careful screening of additives for new HTM systems.

2 An investigation into intermolecular hydrogen bonding and dipole disorder in amide HTMs

The contents of this chapter have now been published as an article titled “Overcoming the mobility penalty introduced by dipole disorder in small-molecule HTM films” in the Journal of Materials Chemistry A, DOI: https://doi.org/10.1039/D4TA00956H

2.1 Introduction

In most OSs, hole conduction occurs through a thermally assisted hopping mechanism between various HOMO energy levels within the layer.[13] The average hopping distance is therefore directly related to the conductivity, and is determined by myriad factors such as sterics and the geometry of the HTM packing. Many different intermolecular interactions such as hydrogen bonding, π-π stacking, and dipole-dipole interactions can also affect the packing and morphology of an amorphous HTL, especially when multiple competing interactions are present. Probing the effects of all possible interactions on the film morphology is challenging, as the sum of all interactions makes it difficult to disentangle the individual effects. Through various measurements such as single-crystal X-ray crystallography (**SCXRD**) in the solid state, solution nuclear magnetic resonance (**NMR**) spectroscopy, Fourier Transform Infrared (**FTIR**) spectroscopy and theoretical calculations on simulated HTM films, useful information into the possible interactions occurring in small, ordered domains within the amorphous film can be inferred. A good understanding of the combined intermolecular forces governing the packing distance in the hole transport layer (**HTL**) is essential for tailoring the design of future HTMs. This will also help forthcoming research in the field to move away from trial-and-error approaches, greatly reducing waste and speeding up HTM design.

It has been previously shown by Young, *et al*. that strong dipole moments through the HTM can significantly reduce conductivity due to increased energetic disorder. Strong dipole moments frequently arise in molecules with polar moieties, and lead to a reduction in the hole mobility wherein this becomes smaller and more dependent on the strength of the electric field applied to the semiconductor.[76] Later, Pope, *et al*. showed using kinetic Monte Carlo (**kMC**) simulations, that a disordered energy landscape within the film gives rise to trap states and inefficient pathways for charge to percolate through the material.[13] A high degree of global dipole ordering is required to counteract this effect, which is unlikely to be achieved in a solution-processed film.[12] It is therefore essential to consider not just the effect of the dipoles in isolation, but the combined effects of all possible noncovalent interactions on the correlated disorder within a film.

A good-quality HTM film is essential to minimise series resistance in solar cells and reach optimum PCE.[32] This point remains one of the main drawbacks of using **Spiro-OMeTAD** for solar cell applications i.e. inadequate film formation stemming from a lack of strong intermolecular interactions in the film. To this end, the Docampo group have recently synthesised HTMs with an amide-based backbone through the use of simple condensation chemistry, the first of which being **EDOT-Amide-TPA**. This molecule shows remarkable film-forming ability, yielding pinhole-free thin films and record PCEs comparable to those achieved by **Spiro-OMeTAD** in PSC architectures.[54] These properties arise from the planarised core afforded by strong intramolecular hydrogen bonding through the amide groups, as well as the central dipole through the **EDOT** core. This is in strong contrast with **Spiro-OMeTAD**, which can form limited intermolecular interactions due to its globular structure, leading to significant pinhole formation within the film.

In this work, we aim to gain a fuller view on the myriad intermolecular interactions coexisting within HTM films, and compare three related amides, these being **EDOT-Amide-TPA** (**1**), **DEDOT-Amide-TPA** (**2**), and **TPABT** (**3**), shown in Figure 2-1.

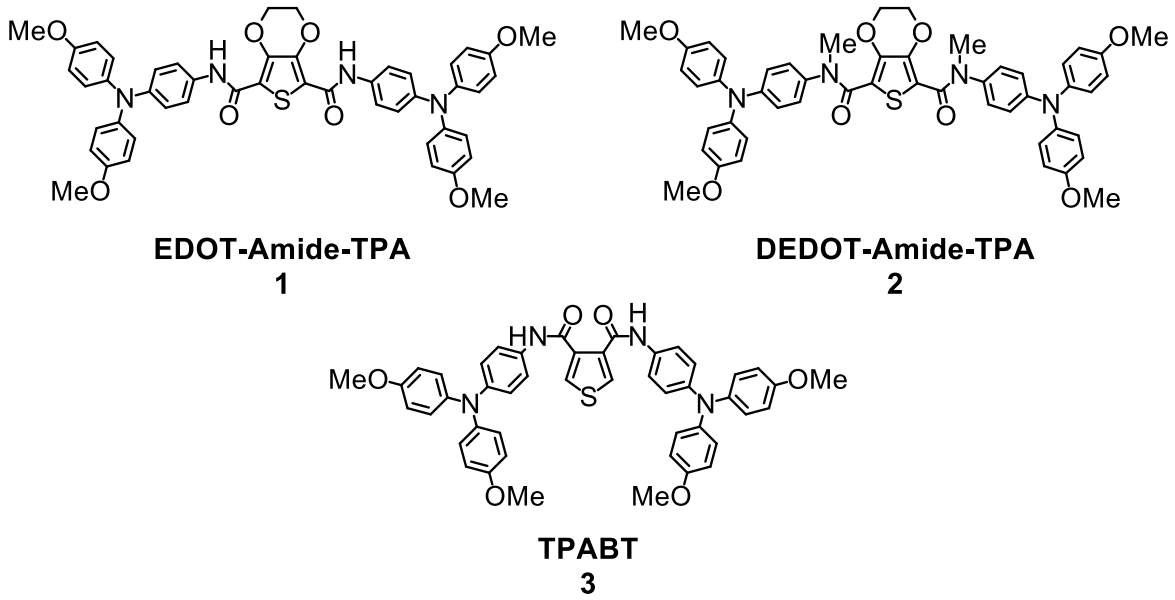

Figure 2-1: Molecular structures of the three amide-based HTMs discussed in this chapter.

All compounds possess strong dipoles through the core of the molecule, differing only in hydrogen bonding capability. Through single-crystal X-ray data, it is shown that modifying the hydrogen bonding properties of the molecules can promote the formation of intermolecularly hydrogen bonded pairs with antiparallel-oriented dipoles in the crystal (HTM **3**). An order of magnitude increase is then observed in the film conductivity of compound **3** compared to compound **1** in which the amide bonds cannot form these molecular pairs.

While observations of intermolecular interactions in crystalline states are not directly transferable to more disordered films, they provide valuable insight into the morphological behaviour of the films. These claims are substantiated through theoretical calculations involving DFT modelling and kMc simulations. DFT is a powerful computational technique that offers an excellent compromise between computational time and accuracy. It is routinely used in many fields of chemistry to investigate the electronic structure of chemical systems. This can reveal useful information such as visualisations of the HOMO and LUMO, their corresponding energies (thus leading to a calculated estimation of the HOMO-LUMO gap) and the electron density distribution across a molecule.[62,77,78] DFT operates by assuming that each electron in a system does not interact with the other electrons, thus negating the Coulombic repulsion forces between electrons. The energy of an electronic system is defined in terms of the number of electrons and their probability density at any point in space. Exchange and correlation functionals are then applied to represent the effects of Coulomb interactions.

The chosen functionals, which vary depending on the system of interest, have great ramifications on the quality of the computed results. Two functionals are utilised in this thesis: PBE0 and B3LYP. The PBE0 functional was chosen for the purposes of optimising structures for Monte Carlo simulations, as it provides the appropriate balance between accuracy and computational cost. On the other hand, the B3LYP functional is the most successful functional in terms of its overall performance, and remains the preferred functional for routine determination of molecular energy levels and electron density.[79] B3LYP is thus used later on in this thesis for more routine molecular geometry optimisations. In this chapter, DFT and kMC simulations are used to show how the formation of small amounts of these molecular pairs within an otherwise amorphous film could directly explain the observed increase in conductivity. A kMC simulation uses a general algorithm for repeated random sampling, used to model large systems involving many discrete particles moving randomly from state to state.[79] Subsequent configurations of the system are generated in a random fashion. In modelling HTM films, the film can be represented as an array of molecules containing a set number of holes. The Monte Carlo algorithm can then simulate the random movement of holes under an electric field, with varying contribution from local effects introduced by the molecular dipoles.[13] The simulation results presented in this chapter reveal that the presence of strong dipoles within the film leads to reduced mobility, unless molecules orient in such a way where the dipoles are aligned antiparallel to one another, thus cancelling out the dipoles.

Further NMR and FTIR evidence for the presence of hydrogen bonding in solution and the solid state is also presented. Through these spectroscopic measurements, very similar hydrogen bonding interactions between molecules are observed in solution as well as the solid.

FTIR measurements also reveal that the solid state hydrogen bonding does not significantly differ between the crystal and the thin films. One can therefore reasonably conclude that hydrogen bond-assisted pairing is the most likely candidate for the observed trends in conductivity. This establishes useful guidelines for the design of future low-cost HTMs, particularly those featuring strong dipoles in their core. The energetic disorder arising from misaligned dipoles in the film can be effectively neutralised by the careful tailoring of H-bonds to support the antiparallel arrangement of the dipoles thus reducing dipole disorder. This is reflected in the charge transport results, where HTM **3** reaches the highest measured film conductivity across the doping range, and also shows the highest pristine hole mobility across the amide series. Solar cells fabricated with the amide HTMs show distinct differences in photovoltaic characteristics, with cells employing compound **2** as the hole-transport layer exhibiting the lowest PCE. This is a result of high series resistance across the devices which is likely due to the insufficient charge transport seen through films of HTM **2**. HTM **3** again shows a leading edge in PCE over HTM **1** as a result of improved J_{SC}, further supporting the hypothesis that increased dipole ordering leads to improved charge transport. The solar cell results demonstrate the applicability of dipole ordering as a means towards improved solar energy conversion.

2.2 Results and Discussion

2.2.1 Synthesis

To explore the effect of intermolecular interactions of molecular HTMs and their effect on the resulting charge transport properties, the molecular packing within the films must be carefully controlled. Here, hydrogen bonding is an easily modifiable property in these amides, and has a strong effect on the resulting stacking.[54,80] In this work, three molecules are compared: HTM **1** which incorporates strong intramolecular hydrogen bonding, HTM **3** which possesses strong intermolecular bonding capability as well as some intramolecular hydrogen bonding, and HTM **2** where hydrogen bonding is not possible.

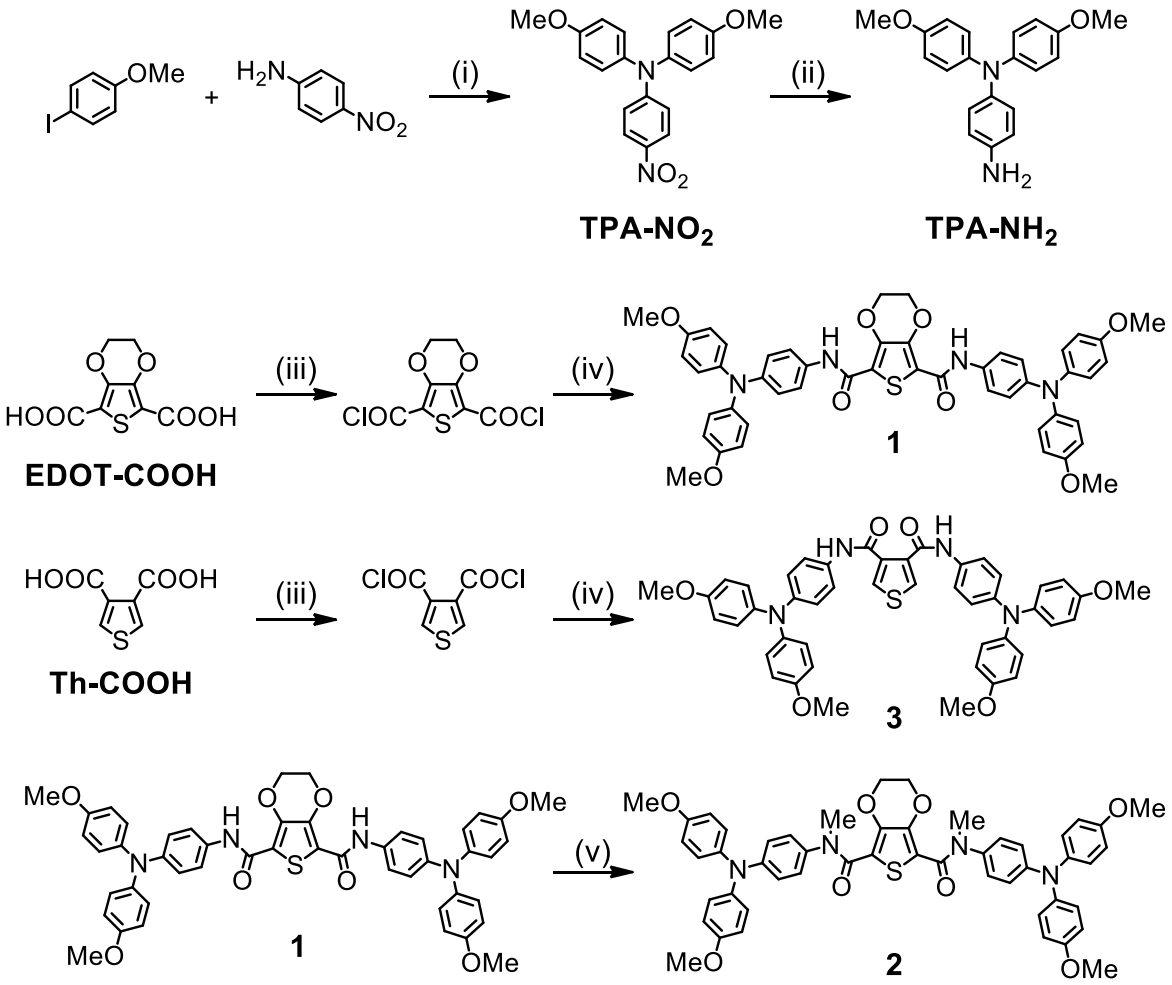

Scheme 2-1: Condensation chemistry-based syntheses of the three HTMs used in this study. (i): K_2CO_3, copper powder, 18-crown-6, DMF, reflux (150 °C, 16 hours), yield 67%; (ii): 10% palladium on carbon, hydrazine hydrate, dry THF, reflux (66 °C, 16 hours); (iii): thionyl chloride, THF, reflux (66 °C, 2 hours); (iv): 4-amino-4',4''-dimethoxytriphenylamine, triethylamine, THF, 25 °C, 16 hours, yield 70%; (v): sodium hydride, dry THF, iodomethane, 40 °C, 16 hours, yield 48%. Detailed syntheses in the Methodology, Section 5.1.2.

The three amide materials were prepared through very simple condensation chemistry. Compound **2** is the N,N-dimethylated analogue of compound **1**, which allows a like-to-like comparison involving only a chemical change that thwarts the ability of compound **2** to form hydrogen bonds. Compound **3** is an analogue of **1** with a thiophene ring as the central core instead of **EDOT**. By employing readily available, carboxylic acid-functionalised cores, the triphenylamine donor units were attached to the acceptor cores following conversion of the acid groups to the acid chloride derivatives, as detailed in Scheme 2-1. The dimethylated analogue **2** was prepared from compound **1** *via* a one-pot methyl substitution reaction at the amide nitrogens. These synthetic strategies allowed facile synthesis of compounds **1** and **3**, with compound **1** requiring very simple purification *via* recrystallisation from DMSO and washing with methanol. Compounds **2** and **3** were purified using column chromatography followed by recrystallisation from ethanol. All synthesised HTMs **1** - **3** were placed in a vacuum oven at 50 °C for at least 4 hours prior to further analysis, in order to remove any volatile solvents from the samples.

The commercial viability of any newly developed material hinges upon the cost of production, which involves expenses from synthesis and purification. In this regard, the utility of condensation chemistry is demonstrated through the facile synthesis of HTMs **1** – **3**. All HTMs were synthesised in a maximum of 4 sequential synthetic steps, using minimal transition metal catalyst in the reduction of **TPA-NO_2** only. In order to contrast these syntheses with that reported for **Spiro-OMeTAD**, a cost analysis was carried out for the synthesis of HTMs **1** – **3**. Synthetic cost was estimated based on the experimental amounts given in the Experimental, Section 5.1.2. Procedures published by Osedach, *et al*. and Petrus, *et al*. were used to estimate the materials cost based off of online prices obtained from Merck as the primary supplier.[54,81,82] Prices were converted from GBP to USD to allow comparison with the literature value for the cost of **Spiro-OMeTAD**, using an exchange rate of £1 = $1.28 as of 29/05/2024. Therefore the total costs are subject to change depending on availability and demand, as well as fluctuations in currency value. Full analysis tables are given in the Appendix, Section 9.3. HTM **1** proves to be the cheapest material to produce owing to its facile purification which does not require column chromatography. This leads to a low material cost of $5.74/g for HTM **1**. HTMs **2** and **3**, which required column chromatography using halogenated solvents for purification, have increased production costs at $16.76/g and $15.48/g respectively. This is in contrast to the synthetic process required to obtain **Spiro-OMeTAD**, wherein multiple purification steps and transition metal catalysts, followed by sublimation to yield sufficiently pure material for optoelectronics applications result in a synthetic cost around $91/g.[16,58]

The purity of the synthesised materials was assessed through ^{1}H and ^{13}C NMR spectroscopy as well as mass spectrometry. It is essential to ensure analytical purity of the substances of interest, since the presence of impurities within a sample of HTM is likely to impact its charge transporting and film forming properties. The ^{1}H NMR spectra of the intermediates **TPA-NO_2** and **TPA-NH_2** are given in the Appendix, Section 9.1 (Figures 9-1 and 9-2). Only a minor component of residual solvent was observed after purification, with no other side products observed. To characterise the final compounds, ^{1}H and ^{13}C NMR spectroscopy was performed on the samples after purification. The spectra are shown in Figures 9-3 – 9-5. The spectra show that the final compounds **1** – **3** have been appropriately purified by chromatography and recrystallisation, with only minor traces of solvent left behind in the samples. Samples were stored in a nitrogen-filled glove box when not in use to prevent the adsorption of additional water during storage, thus preventing oxygen or moisture-induced degradation. Mass spectra were also recorded for HTMs **1** – **3**, courtesy of Dr. Giovanni Enrico Rossi at the School of Chemistry. These are given in the Appendix, Section 9.2 (Figures 9-15 – 9-17). The molecular ion peaks seen in the mass spectra confirm the identities of the final products.

2.2.2 HTM Characterisation

Knowledge about the electronic energy levels of prospective HTMs is crucial for their successful implementation into devices. For instance, to achieve maximum charge transfer efficiency in a perovskite solar cell, the HOMO energy level of the HTM must be aligned slightly shallower than the valence band of the perovskite, normally in the range of -5.4 – -5.7 eV.[30,57] For example, triple-perovskite compositions such as cesium-formamidinium-methylammonium (**CsFAMA**) have a valence band maximum of around -5.7 eV.[30] A prospective HTM at a junction with such a perovskite should thus have suitable energy level alignment to allow for easy hole transfer from the perovskite into the HTL.

The optical and electrochemical properties of the amide molecules were investigated through light absorption measurements and CV, in order to estimate their electronic energy levels. For all spectroscopic and electrochemical measurements, solutions were prepared in dichloromethane using the purified powders obtained from the chemical synthesis described above. The UV-Visible absorption characteristics are depicted in Figure 2-2a, and the main results are summarised in Table 2-1. Tauc plots (Figure 2-2b) were used to find the absorption onset from the absorption spectra, from which the optical bandgaps ($\mathbf{E_g}$) were estimated.

All materials show very large Stokes shifts between their absorption and emission maxima, showing that they undergo large geometrical deformations upon light excitation.[53] Interestingly, **Spiro-OMeTAD** has a reported Stokes shift as low as 42 nm.[16]

The electrochemical behaviour of newly developed HTMs is equally important in determining their charge transport properties within the context of a solar cell. Figure 2-3a shows the cyclic voltammograms of the three amides, all of which show a reversible one-electron oxidation implying good electrochemical stability. The IPs of our materials were then estimated from the electrochemical data, using square-wave voltammograms (Figure 2-3b) to better extract the oxidation peaks. The halfway potentials and IPs extracted from the electrochemistry experiments are given in Table 2-2.

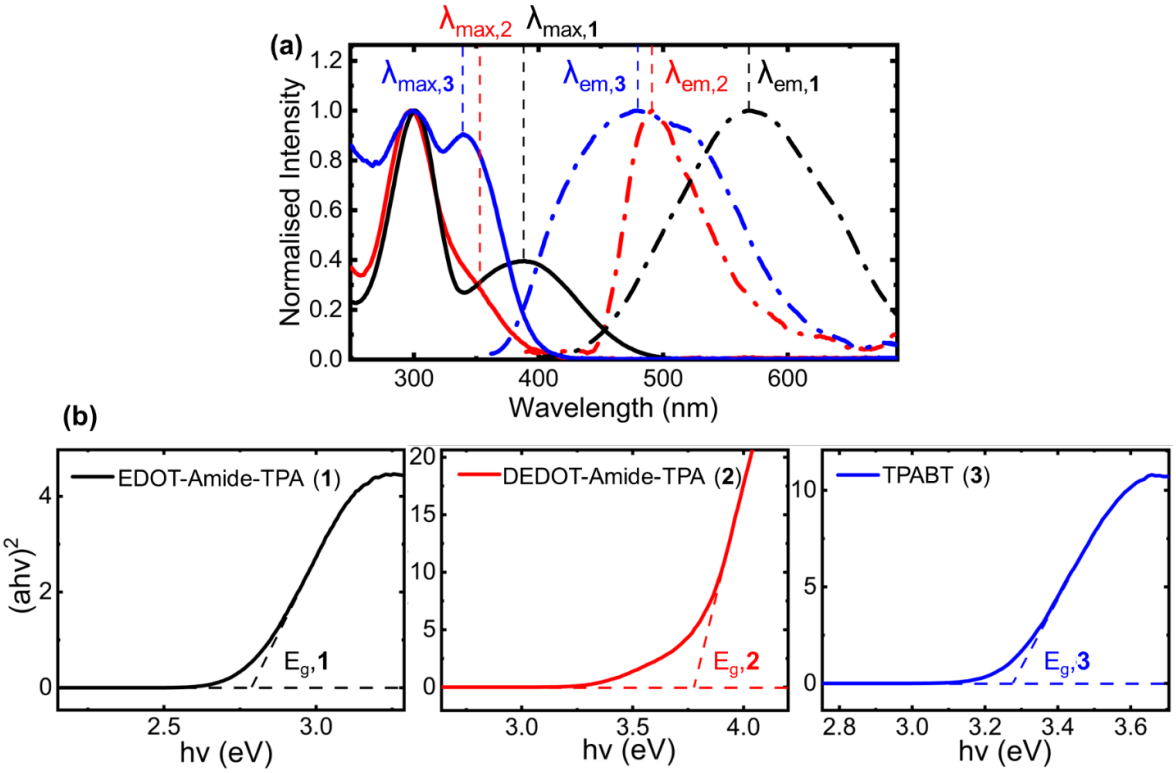

Figure 2-2: (a) Stacked UV-Visible absorption (solid lines) and fluorescence spectra (dotted lines) of the amide materials, with maximum absorbance and emission wavelengths labelled. All spectra were measured in DCM solution at concentrations of 10^{-5} M. Fluorescence spectra were acquired after excitation at the labelled λ_{max} of the corresponding absorption spectrum. (b) Tauc plots constructed from the absorption spectra of the amide materials.

Table 2-1: Optical properties measured from UV-Visible absorption and fluorescence spectroscopy.

HTM	λ_{max} (nm)	λ_{em} (nm)	Stokes shift (nm)	Stokes shift (cm^{-1})	E_g (eV)
1	387	572	185	8357	2.78
2	352	492	140	8084	3.77
3	340	480	140	8578	3.27

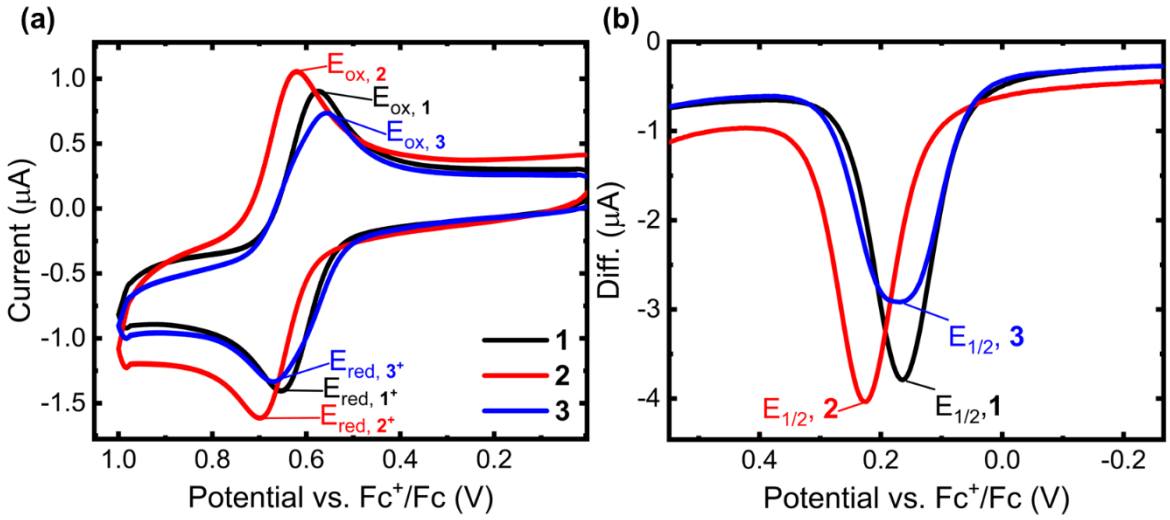

Figure 2-3: (a) Cyclic voltammograms, (b) square-wave voltammograms of the amide materials, referenced to the Fc/Fc^+ redox couple. Voltammograms were measured in DCM solution at a concentration of 10^{-4} M. Voltammograms recorded using a platinum disc working electrode, platinum wire counter electrode, and silver wire pseudo-reference electrode, 0.1 M $TBAPF_6$ electrolyte. Fc^+/Fc was used as external reference. Scan rate = 0.1 V s^{-1}.

Table 2-2: Estimated IPs for our amide materials, from CV measurements.

HTM	$E_{1/2}$ (V) vs. Fc^+/Fc	IP (eV)	IP + E_g (eV)
1	0.164	- 4.97	- 2.16
2	0.224	- 5.04	- 1.26
3	0.168	- 4.96	- 1.69

While IPs estimated from solution CV data should not be used as a direct measure of the HOMO energies in the solid state,[14] they point towards the energy band alignment with many common perovskite compositions employed in solar cells, such as **$MAPbI_3$** and various triple-cation perovskite compositions.[57,84] The results above show that all three amide HTMs have IPs aligned slightly shallower than many common perovskite valence energy bands, facilitating easy hole injection into the HTL. As the first reduction potentials were not experimentally accessible, a rough estimation of the LUMO was obtained by adding the optical bandgap to the IP (**IP+E_g**, Table 2-2). The very shallow values obtained indicate effective electron blocking capability, preventing their injection from the perovskite and thereby minimising charge recombination within the HTL.[85]

The thermal properties of an HTM must also be investigated, as it must be able to withstand the operating temperatures of the chosen application without degrading. This is especially true in the context of solar cells, where the HTM will be exposed to many heating/cooling cycles, with maximum operational temperatures reaching as high as 80°C.[54]

The glass transition temperature ($\mathbf{T_g}$) is an important parameter to consider, as the HTM must remain amorphous throughout the operational lifetime without transitioning into the crystalline state. In this regard, crystallinity within the HTL is generally undesirable, as it leads to poor charge injection due to incomplete contacts at the HTM interfaces.[86,87] For the purposes of this study in particular, the melting points determined from DSC can also shed light on the different intermolecular interaction capability of the three amide materials, which govern the phase transition behaviour of all organic molecules.

All TGA and DSC analyses in this thesis were carried out by Andy Monaghan at the School of Chemistry, using the purified powders obtained directly from chemical synthesis. Figure 2-4 shows the thermochemical analysis results. All three amide compounds show remarkable thermal stability, as is typical for many aromatic amides.[54] The lowest thermal decomposition temperature ($\mathbf{T_d}$) was recorded for HTM **3** at 310°C, followed by HTM **1** at 349°C, and HTM **2** having the highest T_d at 370°C. From the DSC results, there is a clearly observable trend in melting temperatures ($\mathbf{T_m}$) arising from differing intermolecular hydrogen bonding capability. HTM **2** has the lowest $\mathbf{T_m}$ at 199°C, followed by compound **3** at 228°C, then compound **1** with the highest $\mathbf{T_m}$ of 294°C. This correlates with a complete lack of hydrogen bonding in compound **2**, leading to weak intermolecular forces holding the solid together which can be easily broken with elevated temperatures. Glass transitions ($\mathbf{T_g}$) are also observed above 90°C for all amides, revealing their polymorphic character. For HTM **1**, an additional crystallisation ($\mathbf{T_c}$) is observed at 155°C which is in good agreement with previous literature.[54] As all thermal transitions exceed the operational temperatures of photovoltaic devices, these amides are expected to remain stable against thermally-induced morphological changes throughout the life cycle of the device.

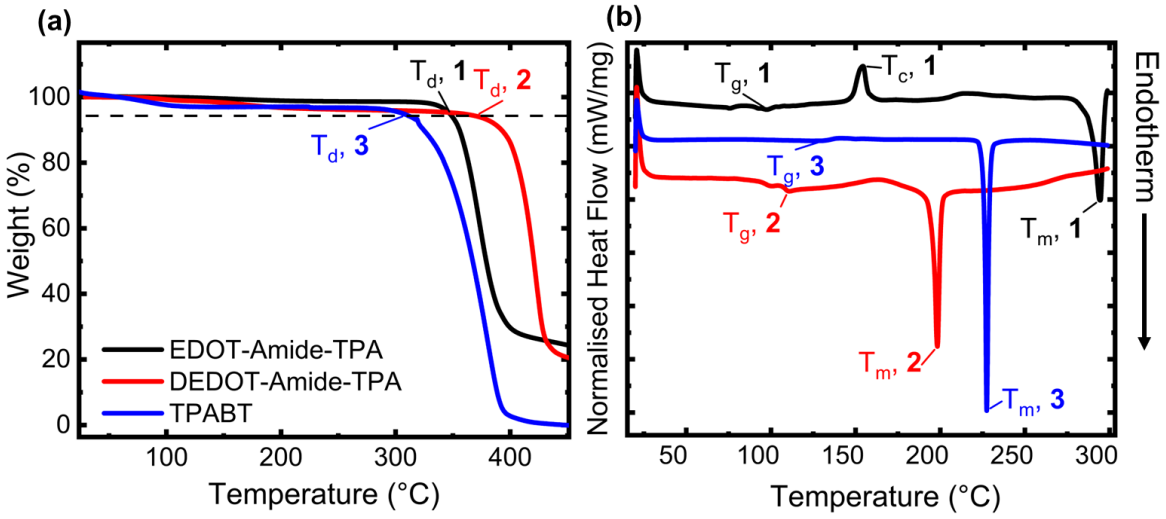

Figure 2-4: (a) Stacked TGA of the amide HTM powders. Dotted line shows 95% weight. (b) DSC showing the first heating cycle of the three amide HTM powders. Heating rate = 10 °C min^{-1}. Normalised heat flow values have been removed from the axis, as graphs were offset vertically to improve clarity.

2.2.3 Solution-state insights into intermolecular interactions

As the intermolecular interactions between different HTM molecules are pivotal to bulk charge transport, it is important to gain insight into the nature and strength of these interactions. A variety of spectroscopic techniques may be used for this purpose, and NMR spectroscopy is a powerful solution technique routinely used to probe for hydrogen bonding and π-π stacking interactions in a variety of fields of research.[88,89] The amide molecules **1** and **3** possess amide groups which contain both hydrogen bond donor (N-H) and acceptor (C=O) moieties. Therefore, intermolecular and intramolecular hydrogen bonds are expected to be present in these molecules in solution. As protons are directly involved in the hydrogen bond and experience changes to their chemical shift as a result, ^{1}H-NMR spectroscopy is the most suitable technique to probe for hydrogen bonds.

The intermolecular interactions in solution were investigated through a series of ^{1}H-NMR experiments. Spectra were acquired at a range of temperatures and concentrations in $CDCl_3$, at 25 °C. $CDCl_3$ is an ideal solvent for this purpose, as its low polarity ensures that it forms no competing hydrogen bonds with our amides, and has thus been widely used in such studies.[69,90,91]

The amide and aromatic proton resonances of HTM **1** shift upfield (8.4 ppm, 7.4 – 6.7 ppm respectively) as the concentration is increased (Figure 2-5a). Such shifting pattern with increasing concentration is widely reported to be a result of increased π-π stacking, which exposes protons to secondary magnetic fields from ring currents that shield the signal.[92,93] HTM **1** is therefore able to undergo stacking interactions, suggesting that the core of the molecule is planar to allow for close proximity of neighbouring molecules. This planar geometry is likely to be induced by strong intramolecular hydrogen bonds between the amide N-H groups and the oxygen atoms on the **EDOT** moiety, which are concentration-independent and do not affect the chemical shifts across the series.[70,94]

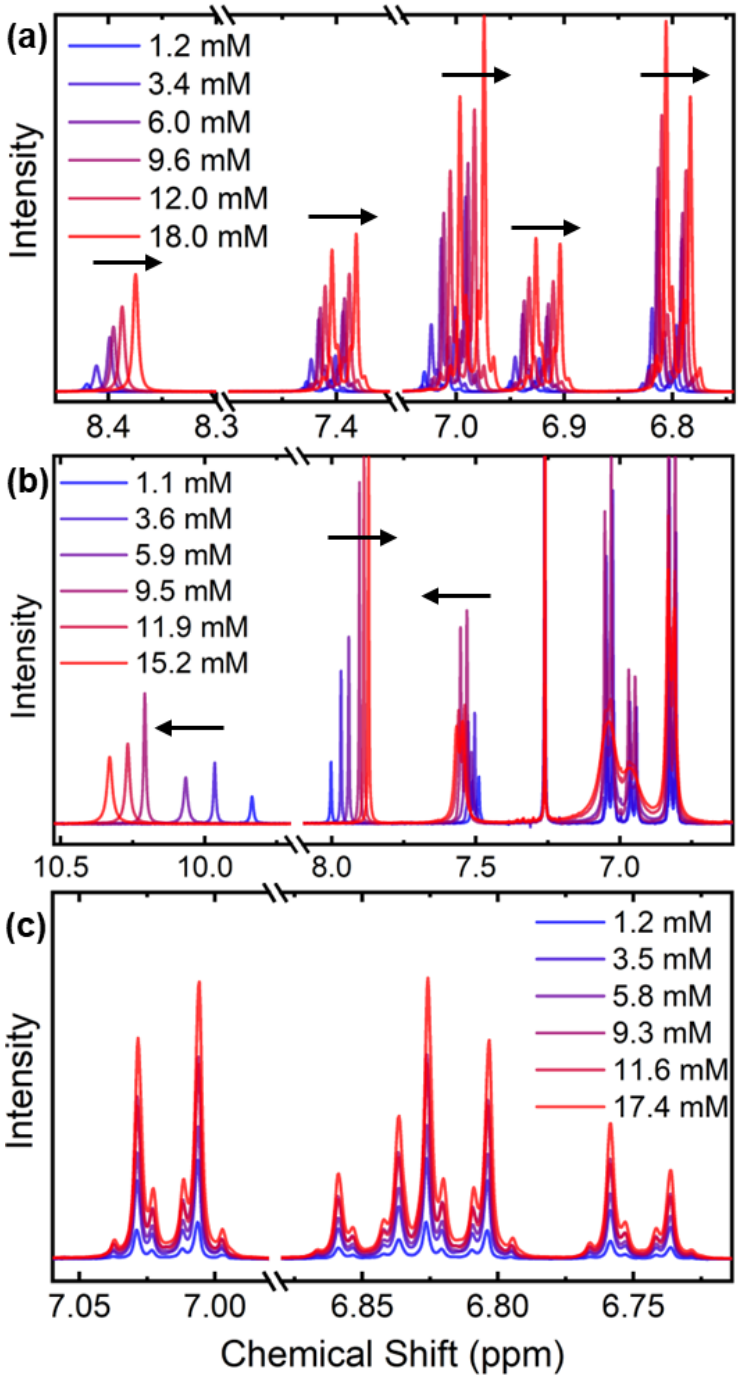

Figure 2-5: Partial ^{1}H-NMR spectra, recorded in $CDCl_3$ at 25 °C, of (a) HTM **1** and (b) HTM **3** at different concentrations, showing shifts in their amide and aromatic proton resonances, and (c) HTM **2**, showing no shifts across the concentration range.

The existence of strong intramolecular hydrogen bonds can be proven through disruption by the addition of DMSO-d6 (Figure 2-6a,b), or by increasing the temperature in a variable temperature NMR (**VT-NMR**) experiment (Figure 2-6c,d). Increasing the temperature is widely known to break many non-covalent interactions, and similarly, DMSO is known to be a strong hydrogen bond acceptor and competes with other hydrogen bonds in solution.[69,77,94] Increasing the fraction of DMSO-d6 in the $CDCl_3$ solution of compound **1** leads to a progressive downfield shift of the amide proton resonance (Figure 2-6a).

This indicates the disruption of the intramolecular hydrogen bonds in favour of stronger ones formed between DMSO and the amide protons. The VT-NMR experiment further supports this assignment, as increasing temperature is seen to disrupt both the intramolecular hydrogen bonding (upfield shift in the amide protons) and the π-π stacking (downfield shift in the aromatic protons) (Figure 2-6c).

In compound **3**, a more complex system of concentration-dependent interactions is observed, likely involving hydrogen bonding and aromatic stacking interactions simultaneously (Figure 2-5b). The amide bonds in compound **3** are situated close enough that they can engage in one intramolecular hydrogen bond, leaving one hydrogen bond donor and one acceptor free for interactions with other molecules. We observe a downfield shift in the amide proton resonance (9.8 ppm) with increasing concentration as a result of increasing saturation of free hydrogen bonding sites.

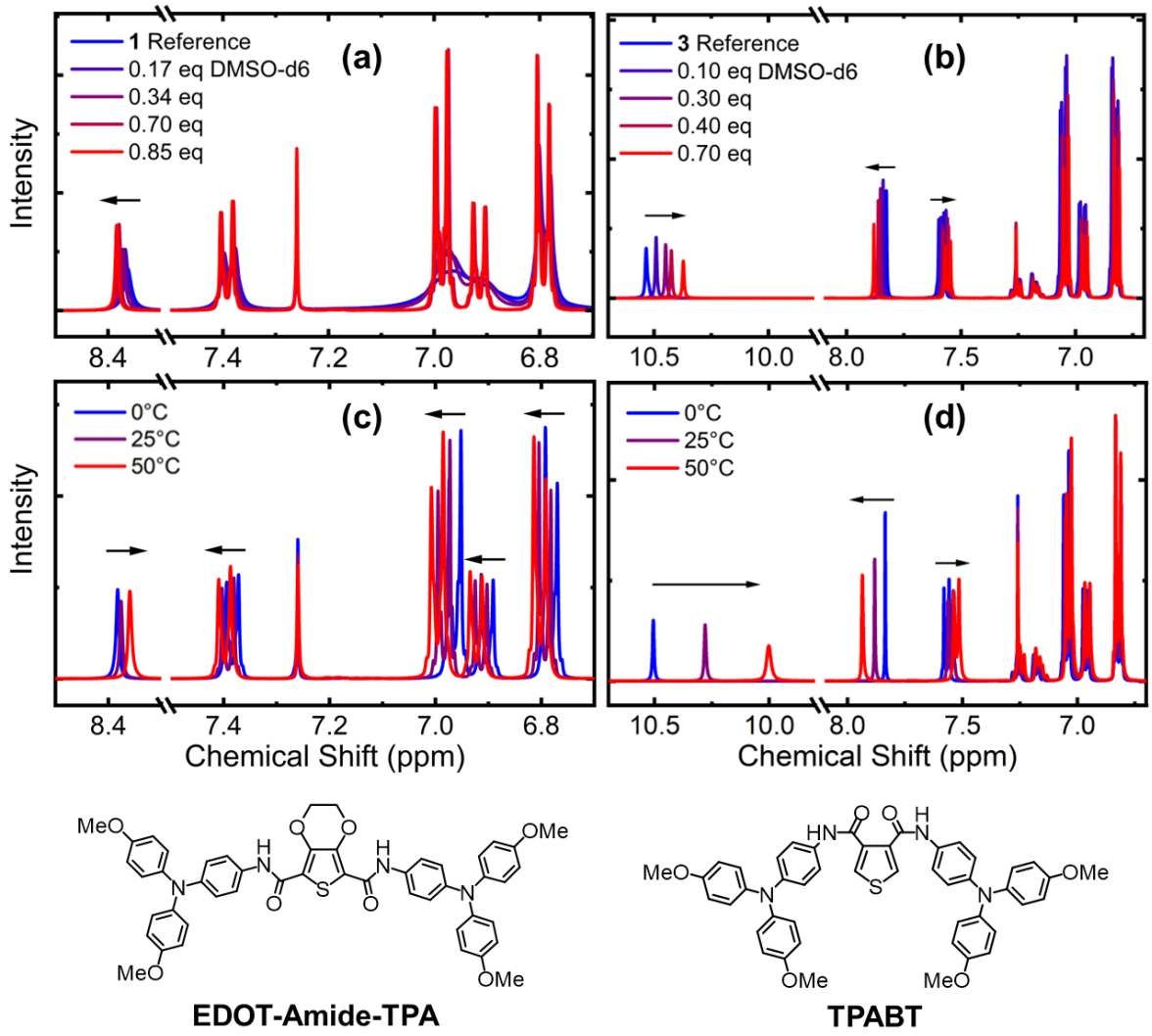

Figure 2-6: Partial ^{1}H-NMR spectra, recorded in $CDCl_3$ at 25 °C showing the aromatic and amide proton regions, (a, c) of compound **1** with increasing fraction of DMSO-d6 or increasing temperature respectively, (b, d) of compound **3** with increasing fraction of DMSO-d6 or increasing temperature respectively.

The thiophene proton signal at 8.0 ppm shifts upfield, indicating a π-π stacking interaction involving the core thiophene rings which may be brought together in solution by favourable intermolecular hydrogen bonding interactions at higher concentrations.

All of these complex concentration-dependent shifting patterns in HTM **3** could be directly replicated by increasing the temperature in VT-NMR, or increasing the fraction of DMSO-d6 in solution, which had the same effect as reducing the concentration (Figure 2-6b,d). This further illustrates the complexity of the intermolecular interactions happening in solution, showing that the interactions occur in tandem, and are disrupted simultaneously. Nevertheless, the capability of HTM **3** to form intermolecular and intramolecular hydrogen bonds in solution has been illustrated. These can contribute beneficial film-forming properties to the material.

HTM **2** was developed specifically to block hydrogen bonding by means of the methyl groups installed on the amide linkers. Figure 2-5c shows no concentration-dependent shifting in the aromatic region, indicating an absence of any concentration-dependent effects. Notably, this also reveals that the steric bulk of the methyl groups combined with the lack of intramolecular hydrogen bonds (therefore a more twisted core) prevent π-π stacking through the core at higher concentrations, contrasting with our observations on HTM **1**. Through these NMR studies, the nature of intermolecular interactions have been observed in solution. When employed in functional devices, these materials are generally used in the solid-state. It is therefore critical to ensure that these interactions are still present in thin films of the amide HTMs.

2.2.4 Solid-state packing of amide-based HTMs

The presence of hydrogen bonds in solution does not necessarily translate into the solid state. The solution NMR experiments in Section 2.2.3 above give conclusive evidence regarding the propensity of HTMs **1** and **3** to form hydrogen bonds in solution, but the solid state landscape must then be investigated to determine whether they are also present within a thin film.

In order to verify the presence of intermolecular hydrogen bonding in the solid state, FTIR spectroscopy was performed on purified samples of the three amide materials. Recording the powder spectra allows investigation of the intermolecular interactions between different HTM molecules, without the influence of solvent that is present in solution measurements such as ^{1}H NMR. Here, the $\nu_{C=O}$ and ν_{N-H} stretching modes are routinely used in many different scientific fields to detect hydrogen bonding interactions.[95,96] The FTIR spectra for HTMs **1** and **3** are in good agreement with published literature.[54,80] Figure 2-7 shows the relevant regions in the FTIR spectra of the amides.

Those amides possessing N-H bonds (HTMs **1** and **3**) have N-H stretching bands at wavenumbers below 3400 cm^{-1}, characteristic of hydrogen bonded amides[67,96]. For compound **1**, sharp C=O and N-H stretches are observed at 1662 cm^{-1} and 3372 cm^{-1} respectively. N-H stretching vibrations in this region have been reported for an amide N-H intramolecularly hydrogen bonded to an **EDOT** oxygen atom,[97] further supporting a planar core for HTM **1**. HTM **3** presents two broadened N-H stretches at 3239 cm^{-1} and 3180 cm^{-1}, and two broad C=O stretches at 1647 cm^{-1} and 1628 cm^{-1}. N-H stretches below 3400 cm^{-1} are characteristic of hydrogen bonding.[67,96] The presence of two resolved carbonyl and N-H stretching modes in HTM **3** suggests that there are two different hydrogen bonding environments: a strong intramolecular hydrogen bond between amide the amide bonds, and a weaker intermolecular hydrogen bond between the free N-H and carbonyl groups of different molecules.[98]

This complements the shift patterns observed in the solution NMR experiments on HTM **3** (Figure 2-5b), where increasing concentration favours more hydrogen bonding between different molecules. These intermolecular hydrogen bonds clearly persist in the solid state, giving rise to two distinct signals in the FTIR spectrum. HTMs **1** and **3** are thus shown to possess amide bonds capable of hydrogen bonding in both solution and solid states.

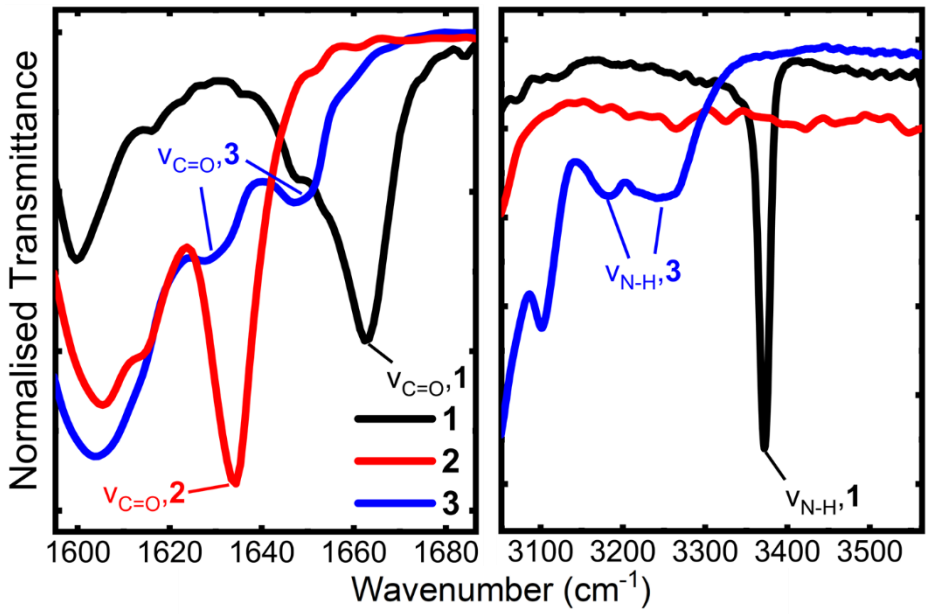

Figure 2-7: Partial powder FTIR spectra of neat HTMs **1** - **3**, showing the carbonyl stretch region (left) and the N-H stretching region (right).

The solid materials may be amorphous or may possess some crystalline character. Powder X-ray diffraction (**PXRD**) or single crystal X-ray diffraction (**SCXRD**) are powerful techniques in materials science, wherein they reveal the presence of ordering within materials in the solid state. In characterising different solid-state phases of the same material, it is important

to determine the differences in structural ordering between the different forms. Here, PXRD is used to probe the synthesised powders and thin films. SCXRD is then used to unambiguously show the conformation of molecules in the crystalline state, which acts as the ideal scenario to show the effect of intermolecular interactions on the packing. The presence of hydrogen bonding interactions can also be determined from the resolved crystal structures to support the spectroscopic analysis shown above. The resolved crystal structures are also used as a benchmark for DFT modelling and FTIR measurements, where the hydrogen bonding environment in the crystal vs. thin films can be compared.

The powder X-ray diffractograms recorded from as-synthesised samples of HTMs **1** – **3** are shown in Figure 2-8. The presence of defined Bragg peaks for HTMs **1** and **3** reveals the crystallinity of these materials that was achieved through the final recrystallisation step in the synthesis. The diffractogram for HTM **1** closely matches literature reports.[54] For HTM **2**, the absence of any defined reflections shows the amorphous nature of the powder even after a recrystallisation procedure, indicating that the molecule precipitates in a disordered fashion.

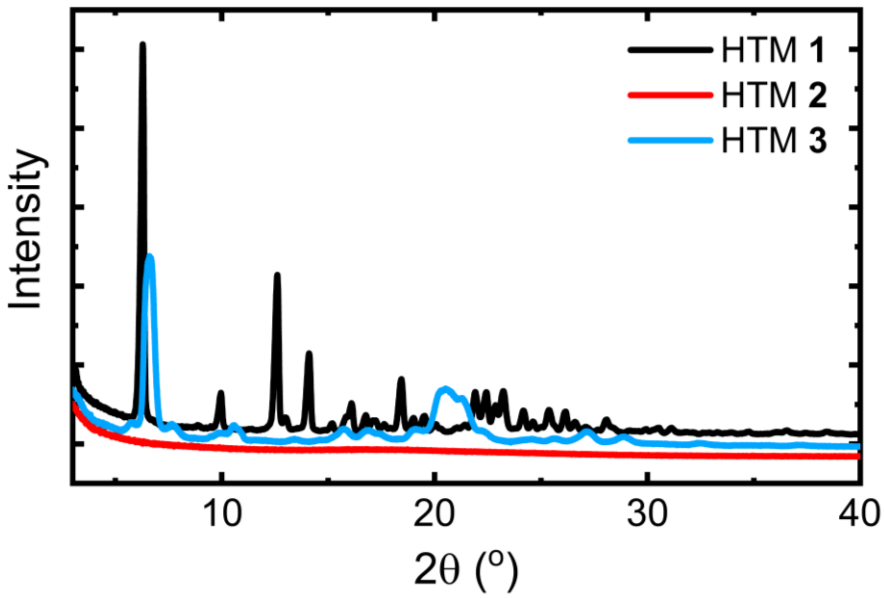

Figure 2-8: PXRD recorded for HTMs **1** - **3**, as neat powders obtained after recrystallisation.

This preliminary analysis reveals the propensity of HTMs **1** and **3** towards forming ordered structures. However, as spin coating forces a much quicker precipitation of the material, it is likely that order might be lost in the resulting films. It is thus important to compare these powder diffractograms to similar data measured from thin films. Figure 2-9 shows the XRD patterns measured from thin films of HTMs **1 – 3** on glass substrates coated with fluorine-doped tin oxide (**FTO**), wherein no reflections arising from the HTMs are seen. The diffractograms are identical to those measured for a blank FTO slide, revealing the highly disordered nature of the films.

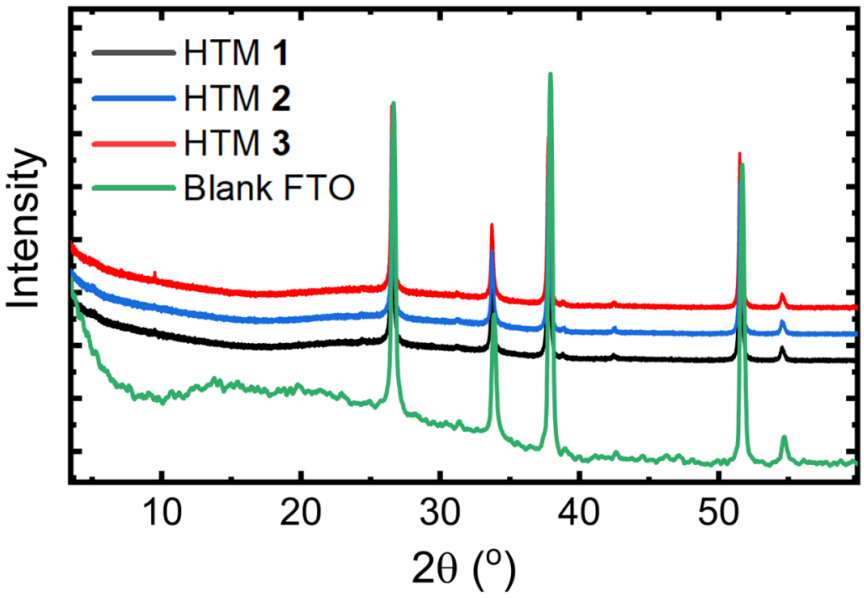

Figure 2-9: Film X-ray diffractograms recorded for spin coated thin films of HTMs **1** – **3** deposited onto FTO. Only FTO reflections are visible, indicating no significant reflections arising from the films themselves.

Spin coating of organic semiconducting materials often results in the creation of disordered films with highly amorphous character, as seen above. For materials such as **Spiro-OMeTAD** that can form no intermolecular interactions, spin coating notoriously produces highly porous films, requiring much more concentrated solutions to yield thicker films which ensures good interfacial contact.[43,99] It is therefore worth investigating the effect of the intermolecular interactions between the amide HTMs on their packing properties.

SCXRD provides valuable information regarding the presence and significance of hydrogen bonding or dipole-dipole interactions within ordered crystals, which represent the 'ideal' or lowest energy arrangement of molecules in a solid. To grow single crystals, 2 mg of HTMs **2** and **3** were dissolved in 3 mL of chlorobenzene in a capped vial, which was allowed to evaporate slowly through small holes in the lid. Crystals of HTM **1** were significantly more challenging to grow, but suitable crystals were grown through a similar slow evaporation process from 3 mL of a 1:1 dichloromethane:ethanol mixture. The vastly different crystallisation properties of **1** compared to **2** and **3** are ascribed to the low solubility of compound **1** in most solvents, which hindered slow nucleation of large crystals, in favour of more rapid precipitation. Single-crystal structures of HTMs **2** and **3** were resolved by Dr. Claire Wilson at the School of Chemistry, while the structure for compound **1** was resolved by the UK National Crystallography Service.

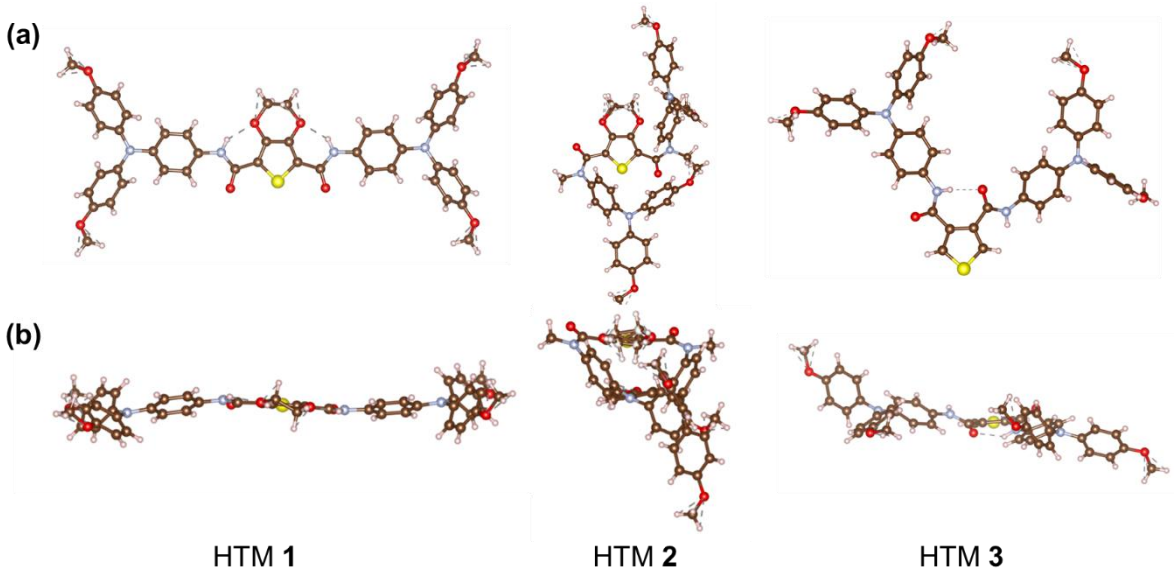

Figure 2-10: Top and side-on views of HTMs **1** – **3**, obtained from the resolved X-ray crystal structure data. A more twisted structure for HTM **2** is observed compared to the DFT-optimised structure.

The molecular structures from resolved X-ray data (Figure 2-10) show the distinct spatial orientation adopted by HTM **2**, which is far more twisted than HTMs **1** and **3**. These have a planarised core by virtue of the intramolecular hydrogen bonding between the amide hydrogens and the dioxane oxygen lone pairs (HTM **1**) or the amide carbonyl oxygen lone pairs (HTM **3**). HTMs **1** and **3** are thus expected to pack closer together in thin films, bringing the HOMOs in closer proximity thus allowing more efficient charge hopping. Such inclination towards close packing was previously observed in solution through NMR studies (Figures 2-5, 2-6).

In an amorphous film, such as one produced through spin coating, the molecular packing is much more disordered compared to a crystal. However, the absence of long-range order does not necessarily negate the existence of small, ordered aggregates, which could significantly influence hole transport properties. In this context, X-ray crystal structures, while not representative of the amorphous film, provide the best-case scenarios for ordered domains, and gives an idea of the expected configuration patterns in these small aggregates. It is worth noting that HTM **3** crystallised as a solvate, incorporating chlorobenzene molecules into the crystal structure, which is likely to have some effect on the packing density of the resulting crystal. As chlorobenzene is also the major component of the spin coating solution of all three materials, any effects that the chlorobenzene molecules have on the crystallisation of HTM **3** would also be expected in the amorphous film case.

To quantify any improvement of packing and how this might affect charge transport, the distance between the nitrogen atoms on the TPA side groups was compared across different molecules in the crystal structures. This is worthy of investigation as charges hopping through an HTM film do so through the HOMOs, which are mainly located on these TPA groups.[54] From the resolved crystal structures, a clear reduction in the nearest measured TPA N-N distance is observed from 5.166 Å in HTM **2** to 5.040 Å in HTM **3**. HTM **1** has a nearest distance between that of **2** and **3** at 5.108 Å. Interestingly, in the crystal structure for HTM **3,** the formation of distinct molecular pairs is observed, formed through intermolecular hydrogen bonds across the amide groups (Figure 2-11). These can be thought of as isolated, tightly packed pairs where the dipoles are oriented antiparallel to each other thus leading to zero net dipole. Since the crystal of compound **3** formed as a solvate with chlorobenzene, these crystallisation conditions may have either promoted the formation of these molecular pairs, or alternatively the presence of these pairs may have allowed the crystal to trap solvent molecules. In any case the crystal structure indicates the propensity of HTM **3** molecules to form these molecular pairs *via* H-bonding interactions through the amide bonds.

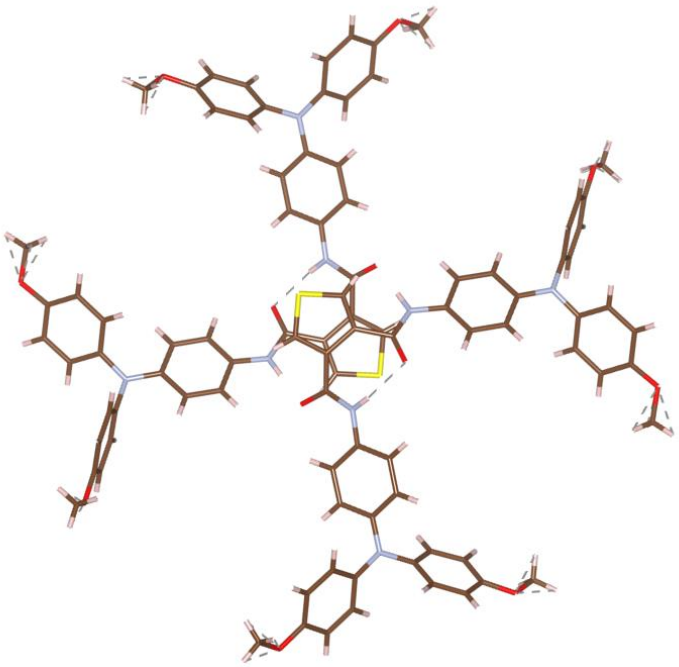

Figure 2-11: An isolated molecular pair of HTM **3** extracted from the crystal structure, formed by intermolecular hydrogen bonding through the amide bonds.

In the case of HTM **1**, molecules form repeating units of closely packed antiparallel strands. This results in neighbouring molecules that are oriented both antiparallel to one another on the one hand (with dipole moments that cancel out), and neighbours that are oriented in the same direction on the other (where the dipole moment is enhanced). The calculated binding energies (Table 2-4) of antiparallel pairs in HTMs **1** and **3** show that these are more stable than molecules oriented either orthogonally (**3**) or parallel (**1**) to one another.

Therefore, while the dipole of monomers remains high, stable antiparallel pairs quench the dipoles on these sites so that the overall level of correlated energetic disorder in the film is reduced. For HTM **2**, parallel and antiparallel pairs have similar stabilities, so that the correlated energetic disorder remains high. Without any hydrogen bonding capability, HTM **2** is likely to adopt a more disordered and less dense packing arrangement in the film which is expected to significantly hinder conductivity.[12] All likely packing scenarios are illustrated in a simplified graphical representation in Figure 2-12.

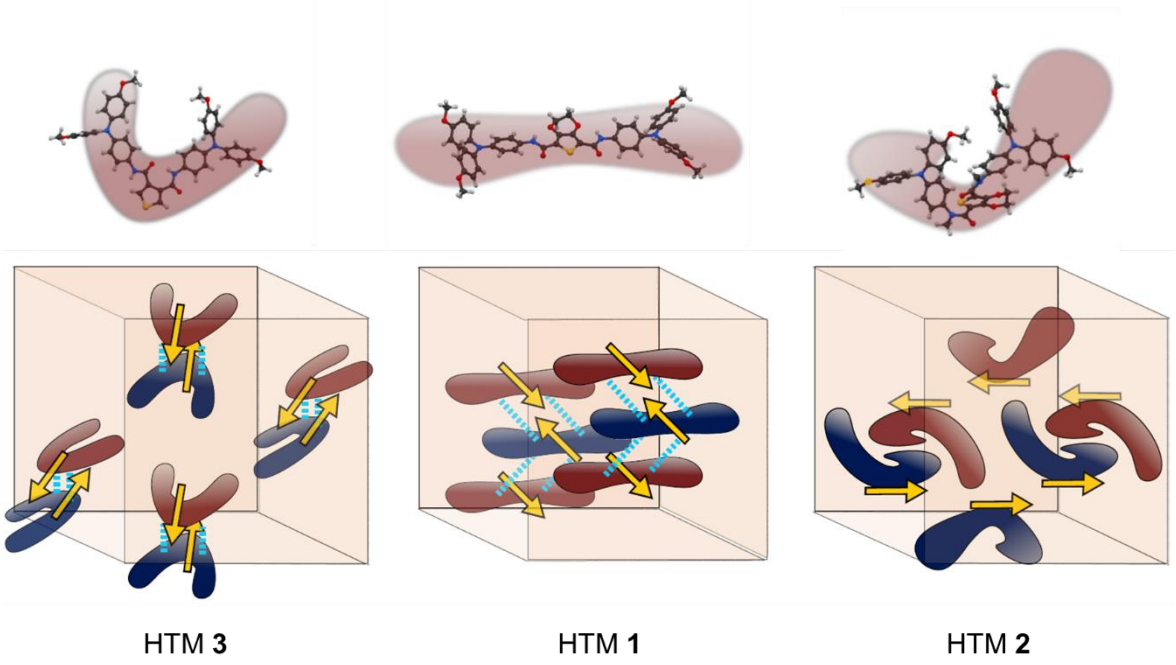

Figure 2-12: Graphical representation of the molecular packing seen in the crystal structure of HTMs **1** – **3**.

The intermolecular interactions observed in a resolved crystal X-ray structure are not necessarily present within an amorphous film, and additional studies must be performed to ensure that they persist in a more disordered system. In order to determine the presence of intermolecular interactions in thin films, solid-state FTIR measurements were performed, comparing the single crystal FTIR spectra to those of powders recovered from spin coated films. Here, single crystals represent the most ordered system of a particular species when it is allowed to pack slowly into an extended network. Conversely, spin coating is a rapid and effective method for depositing thin films onto substrates, and as seen in the PXRD data in Figure 2-9, the resulting films are amorphous.

Thin films were thus spin coated onto glass substrates from chlorobenzene solution (HTM **2**) or mixtures of chloroform/chlorobenzene (HTMs **1** and **3**). The films were then removed with a razor and the resulting powder was collected for FTIR. Crystals were also grown for this measurement using the same methodologies as used for SCXRD, and were allowed to dry to remove residual mother solvent.

By employing FTIR spectroscopy to examine N-H and C=O stretches in the film vs. the crystal, it is observed that the bonding environment in both cases is remarkably similar, revealing a near-perfect overlap of peaks in both the C=O and N-H stretching regions (Figure 2-13). Notably, there is no significant broadening observed in the film IR spectrum, indicating that even in a thin film, the presence of non-hydrogen bonded amide linkers is minimal. The identical vibrational frequencies seen in all cases indicates that the hydrogen bonding systems in our thin films do not deviate significantly from the crystal, and any interactions observed in the crystal have sufficient time to form in the more rapid spin coating process. HTMs **1** and **3** can thus form extensive hydrogen bonds when spin coated, with the crystal structure giving a good indication of preferred packing orientations between molecules.

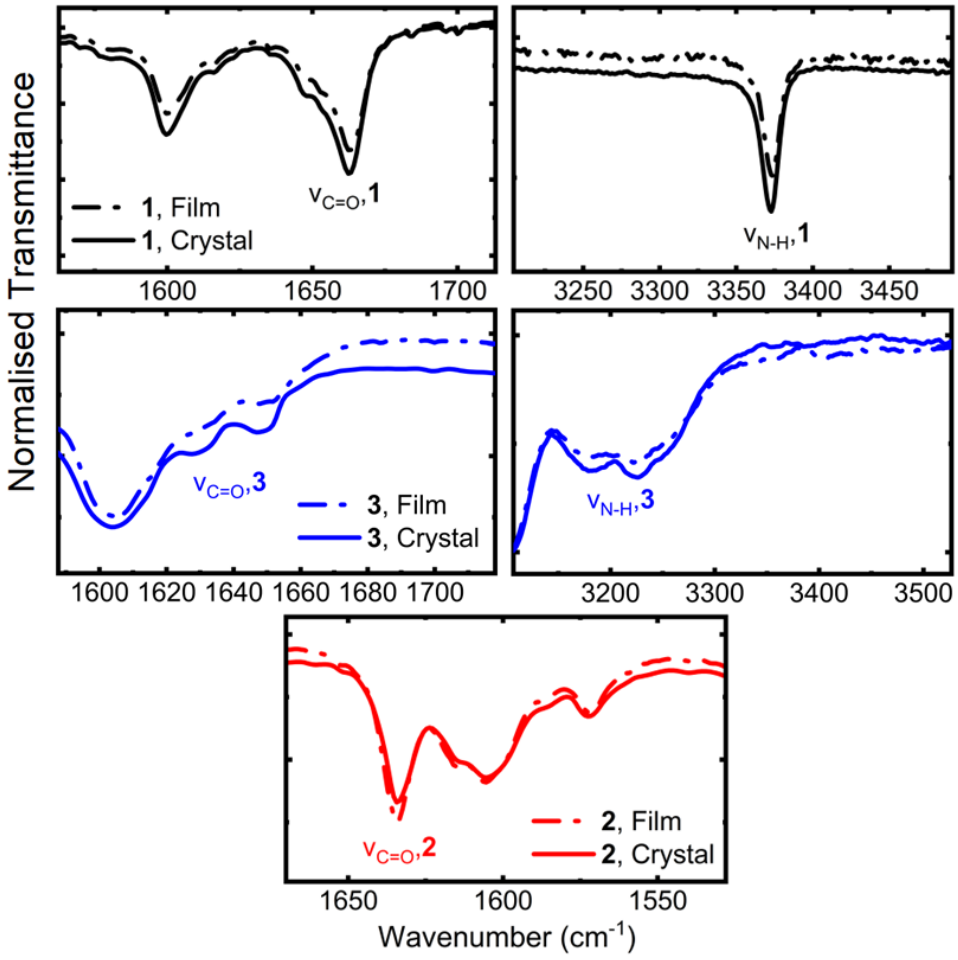

Figure 2-13: Comparative solid-state FTIR spectra of the three amides, measured from either powder samples scraped from spin coated films (dotted lines) or from single crystals of the HTMs (solid lines).

2.2.5 Computational analysis of molecular dipoles and crystal molecular pairs

The computational analysis in this chapter was performed in collaboration with Miriam Fsadni at Newcastle University.

Dipole disorder in spin coated films has been shown to affect the energetic landscape of a film leading to negative effects on the resulting conductivity.[13] Besides the hydrogen bonding capabilities demonstrated by the amide materials above, all molecules used in this study also have a strong dipole within the core. A large dipole disorder may therefore arise in a spin coated film, which can adversely affect the charge transport properties. Zero dipole moment is expected to have the most ordered energy landscape and thus the most favourable conditions for efficient charge hopping. In amorphous materials, the interaction of randomly oriented, permanent dipole moments of the ground state molecules gives rise to correlated energetic disorder which scales with the magnitude of the dipole moment. High dipole moments have been shown to quench charge mobility in both simulation and device-based experiments, as charges percolate through the system via energetically preferred routes[13]. In this regard, computational methods are useful tools that allow modelling of the effect of the dipoles themselves, as well as the effect of the dipole ordering on the resulting mobility.

Single molecule properties of HTMs **1 – 3** were thus investigated using DFT at the PBE0/def2-sv(p) level in order to gain insight into their charge transport behaviour, and the results are summarised in Table 2-3. All three amides were found to have high ground-state dipole moments (p_{DCM}), with HTM **2** having the lowest at 8 Debye.

Table 2-3: DFT results performed at the DFT(PBE0)/def2-sv(p) level of theory as implemented within the Orca (v. 5.1) quantum chemistry package[100], with predicted orbital energies and dipole moments for the three amide-based HTMs, compared to **Spiro-OMeTAD**. [a]PBE0/def2-sv(p) with C-PCM(CH_2Cl_2) implemented; [b]PBE0/def2-sv(p); [c]based on $HOMO_{DFT,DCM}$ with correction factor (-0.206 eV) applied.[101] 'Gap' refers to the calculated HOMO-LUMO gap, and 'Spiro' refers to **Spiro-OMeTAD**. [d]IP values are from CV data recorded in DCM, given in Figure 2-3, except: [e]Literature value.[102]

HTM	p_{DCM} (D)[a]	$HOMO_{vac}$ (eV)[b]	$HOMO_{DCM}$ (eV)[a]	$HOMO_{calc}$ (eV)[c]	$LUMO_{vac}$ (eV)[b]	$LUMO_{DCM}$ (eV)[a]	IP (eV)[d]	Gap_{DCM} (eV)
1	13.0	-4.87	-5.09	-5.29	-1.82	-2.01	-4.97	3.08
2	8.0	-4.92	-5.23	-5.43	-1.30	-1.44	-5.04	3.79
3	10.6	-4.87	-5.03	-5.23	-1.16	-1.34	-4.96	3.69
Spiro	3.3	-4.60	-4.91	-5.12	-0.75	-1.09	-4.90[e]	3.82

In their research, Pope, *et al*. speculated that high dipoles in the neutral HTM molecules may drive self-assembly in a film and reduce energetic disorder. However, they found that very high levels of order, unlikely to be achieved in solution-processed films, are required to counteract the deleterious effects of the dipole moment on hole mobility.[13] The formation of highly ordered, low-dipole domains within an otherwise amorphous film could be possible through hydrogen bonding, and may assist in the formation of molecule pairs with antiferromagnetically oriented dipoles, resulting in a dramatic drop in the overall level of energetic disorder and improved charge transport behaviour. Since hole transport can be thought of as repeated charge transfer reactions between cationic radicals and adjacent neutral molecules, it is worth noting that the dipole moments of excited state molecules are often considerably different to that of the corresponding neutral molecules. This is due to the increase in the difference in charge density across the dipole.[103,104] Both ground state and excited state dipoles contribute to the overall dipole remaining within a film. However, as the hole density in OS films is so low, the contributions from excited state molecules are often neglected in similar computational analyses on disordered systems, as modelling the ground state dipoles is sufficient to accurately describe the systems.[105,106]

The spatial orientation and geometry of the amide molecules is a key factor that determines their packing efficiency. Optimised geometries from DFT calculations (Figure 2-14) provide some insight into possible intermolecular interactions within device films, with the availability of hydrogen bonding groups and relative planarity of these molecules likely affecting their preferred packing behaviour. The predicted conformations of compounds **1** and **3** are very similar to the resolved crystal structures (Figure 2-10), while the predicted structure of HTM **2** is less twisted than in the crystal. In HTM **3**, the adjacent amide proton and oxygen are oriented towards each other across the ring with a calculated interatomic distance of 1.731 Å, consistent with strong intramolecular hydrogen bonding. Such a conformation would leave the remaining amide hydrogen atom and carbonyl oxygen atom free to participate in intermolecular hydrogen bonding while the V-shape exposes the core, facilitating interactions with multiple neighbouring molecules. HTM **1** was found to have a planar core structure, with its amide protons directed towards the dioxane oxygens, at a calculated distance of 2.014 Å. This conformation would facilitate close packing of molecules along one plane, in good agreement with our spectroscopic results. Dimethylated HTM **2** exhibits greatly reduced planarity, as expected due to the lack of intramolecular hydrogen bonding and steric hindrance from the bulky amide methyl groups. The preferred orientation of the molecule, when compared to the parent **1**, suggests that this molecule might also exhibit a lower packing density within the film, which may result in larger hopping distances between HOMO levels.

The DFT results also illustrates the predicted distributions of the HOMO and LUMO, where the HOMO is mostly located on the triphenylamine arms and the LUMO is centred on the **EDOT** or thiophene core.

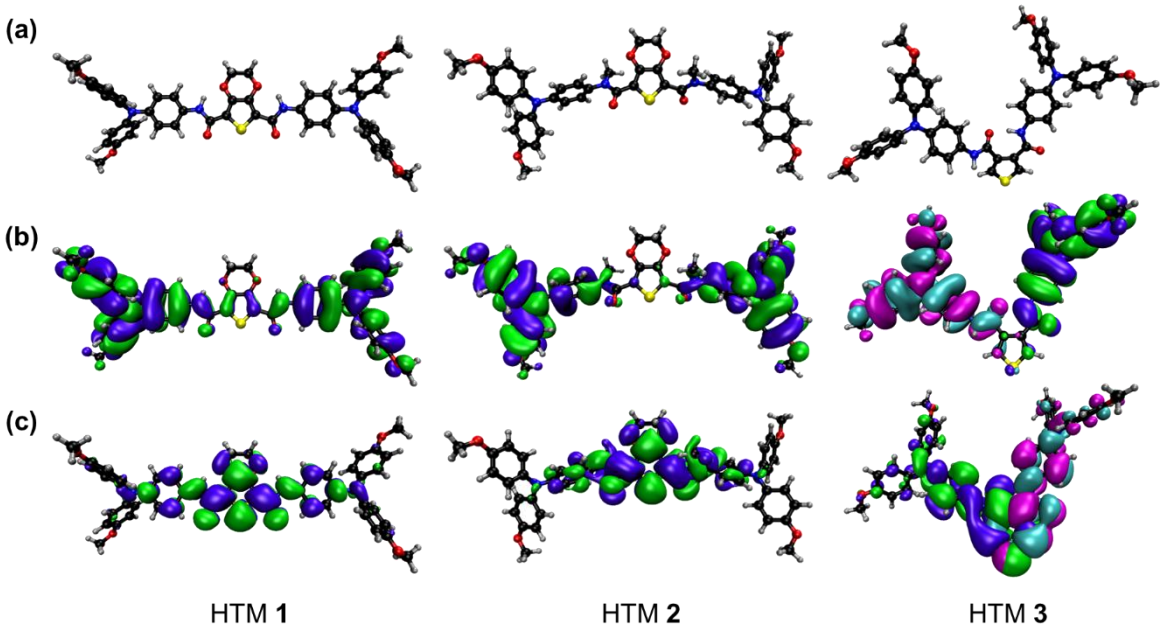

Figure 2-14: (a) Theoretical (PBE0/def2-sv(p)) optimised structures in DCM, overlayed with visualisations of (b) HOMO and (c) LUMO of our three amide HTMs. For **3**, the destabilised HOMO-1 (-5.16 eV) and stabilised LUMO+1 (-1.18 eV) orbitals are also shown in cyan and magenta due to hydrogen bonding across the thiophene core.

The crystal structures of **1** and **3**, show distinct hydrogen-bonded pairs, and the ^{1}H-NMR and FTIR experiments suggest these may already form in concentrated solutions as well as in the powders (Figures 2-5, 2-7). Molecular pairs forming in solution would remain intact during spin-coating if their binding energy is sufficiently high. Therefore, the binding energies of the molecular pairs extracted from the crystal structure data may further support the presence of these pairs in amorphous thin films. If the pairs are closely bound, these could act as a single hopping site with an overall dipole moment that is either reduced or enhanced, depending on the relative orientations of the individual molecules.

Since a high overall dipole moment in a thin film has been shown to quench mobility, the existence of stable reduced-dipole pairs is expected to contribute to enhanced charge transport. Figure 2-13 shows the different molecule pairs extracted from the amide crystal structures, with the arrows indicating the relative orientation of monomer **EDOT** and thiophene cores. Table 2-4 gives the ground-state Debye dipole moments, binding energies and intermolecular distances of the molecule pairs shown in Figure 2-15, as well as the relative orientation of the molecules involved.

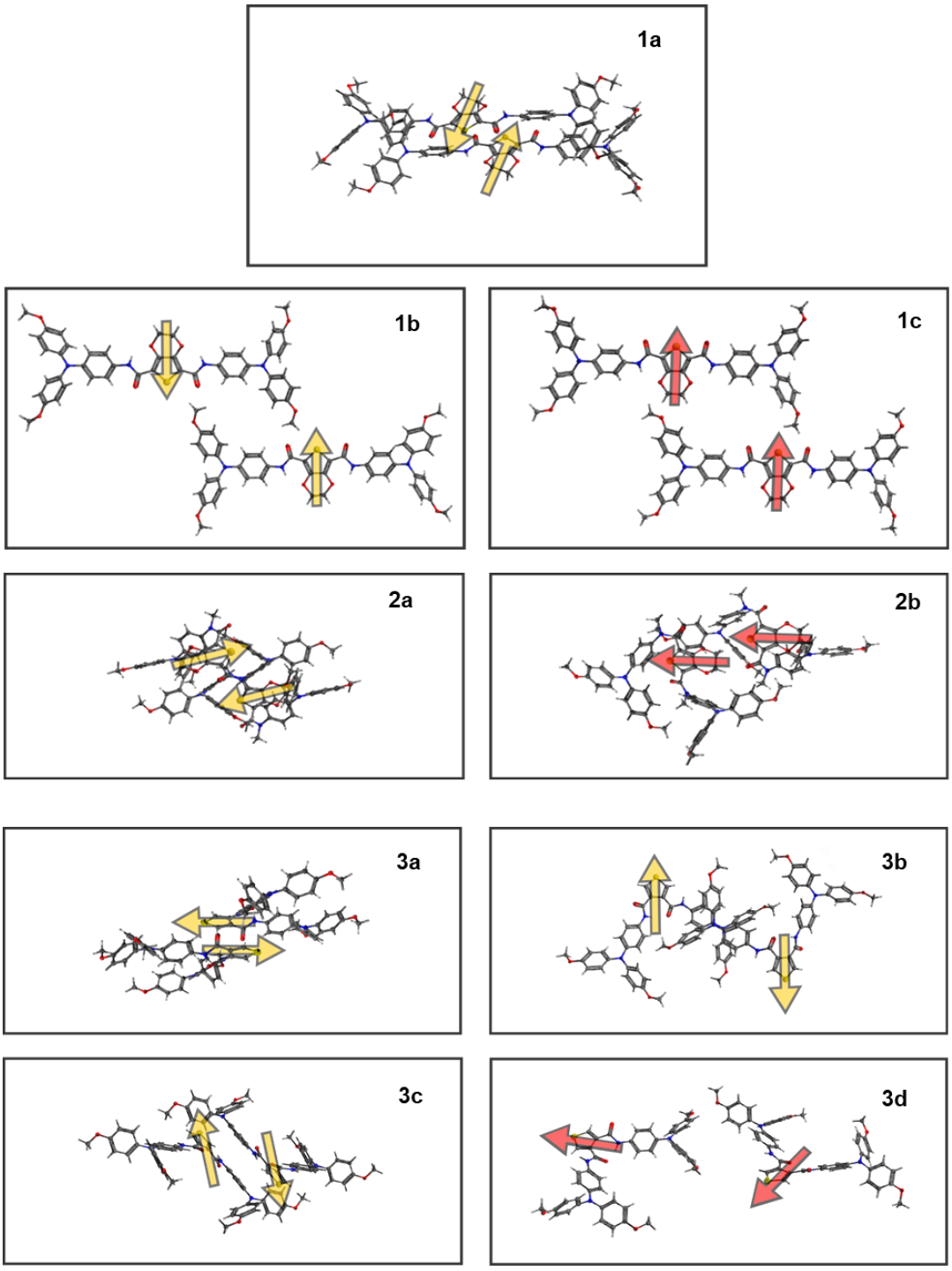

Figure 2-15: Close-lying molecule pairs extracted from the crystal structures of HTMs **1** (1a-c), **2** (2a,b) and **3** (3a-d), with arrows showing the relative orientation of their respective cores. Antiparallel molecule orientation is shown using yellow arrows, while parallel and orthogonal orientations are shown using red arrows.

Table 2-4: Properties of amide pairs extracted from the single crystal X-ray structures, shown in Figure 2-15, with their theoretical dipole moments and binding energies, from DFT (PBE0/def2-sv(p)) calculations in vacuum. *Molecular pair exhibits hydrogen bonding at the amide linkers.

Pair	Orientation	Dipole (D)	Binding Energy (eV)	Intermolecular Distance (Å):		
				Cores	Shortest	TPA N—N
1a	**antiparallel***	**0.0**	**0.86**	**4.0**	**2.7**	**5.0**
1b	antiparallel	0.0	0.31	15.5	2.7	10.9
1c	parallel	21.0	0.29	13.9	2.4	14.8
2a	**antiparallel**	**0.0**	**0.78**	**8.0**	**2.5**	**5.2**
2b	parallel	7.1	0.58	3.7	2.3	9.9
3a	**antiparallel***	**0.0**	**0.84**	**3.6**	**2.1**	**12.1**
3b	antiparallel	0.0	0.36	15.0	2.9	5.0
3c	antiparallel	0.0	0.29	9.7	2.7	9.0
3d	orthogonal	8.6	0.07	19.3	2.9	9.0

0 Debye antiparallel pairs with short core-to-core distance are found to have the highest binding energies, between 0.8 and 0.9 eV. If these pairs form in solution, they are likely to remain intact in the film and would contribute to a lower energetic disorder. In compound **3**, antiparallel arrangements (Figure 2-13, **3a**) of molecules are by far the most stable and parallel pairs are not found. The binding energies of antiparallel pairs (**1a**) is also highest in HTM **1**. However, when the molecules are oriented parallel (**1c**), the overall dipole is greatly enhanced to 21 D. In HTM **2**, the difference in binding energies between quenched dipole antiparallel pairs (**2a**) and enhanced dipole parallel 7 D pairs (**2b**) is only 0.2 eV, so that once formed, both are likely to be stable in the film. It is worth noting that hydrogen bonded antiparallel pairs **3a** and **1a** have short core-to-core distances (~4 Å), enabling them to operate as a single hopping site with a quenched dipole moment. While other configurations of HTMs **1** and **3** exhibit longer core to core distances, they still form short contacts between TPA side units on which the HOMO is located. In HTM **2**, dipole enhanced parallel pairs **2b** have the shortest core-to-core distance, while dipole quenched antiparallel pairs **2a** have short TPA N-N distances.

From these calculations, the proportion of quenched-dipole pairs compared to dipole enhanced pairs is greatest in HTMs **1** and **3**. In a film, HTM **1** would still have an overall more complex potential energy landscape than **3**, since the molecules have a higher dipole moment and are still expected to reduce conductivity. In HTM **2**, the difference in the stability of favourably and unfavourably oriented molecular pairs is small, so that the correlated energetic disorder in the film remains high.

2.2.6 kMC simulations of hole hopping

Having directly observed the effects of intermolecular interactions in solution and in the solid state, it is important to be able to correlate these observations with the charge transport behaviours of a thin film. Simulations were performed using an in-house kMC code.[13] Further simulation details are provided in Section 2.4.4.

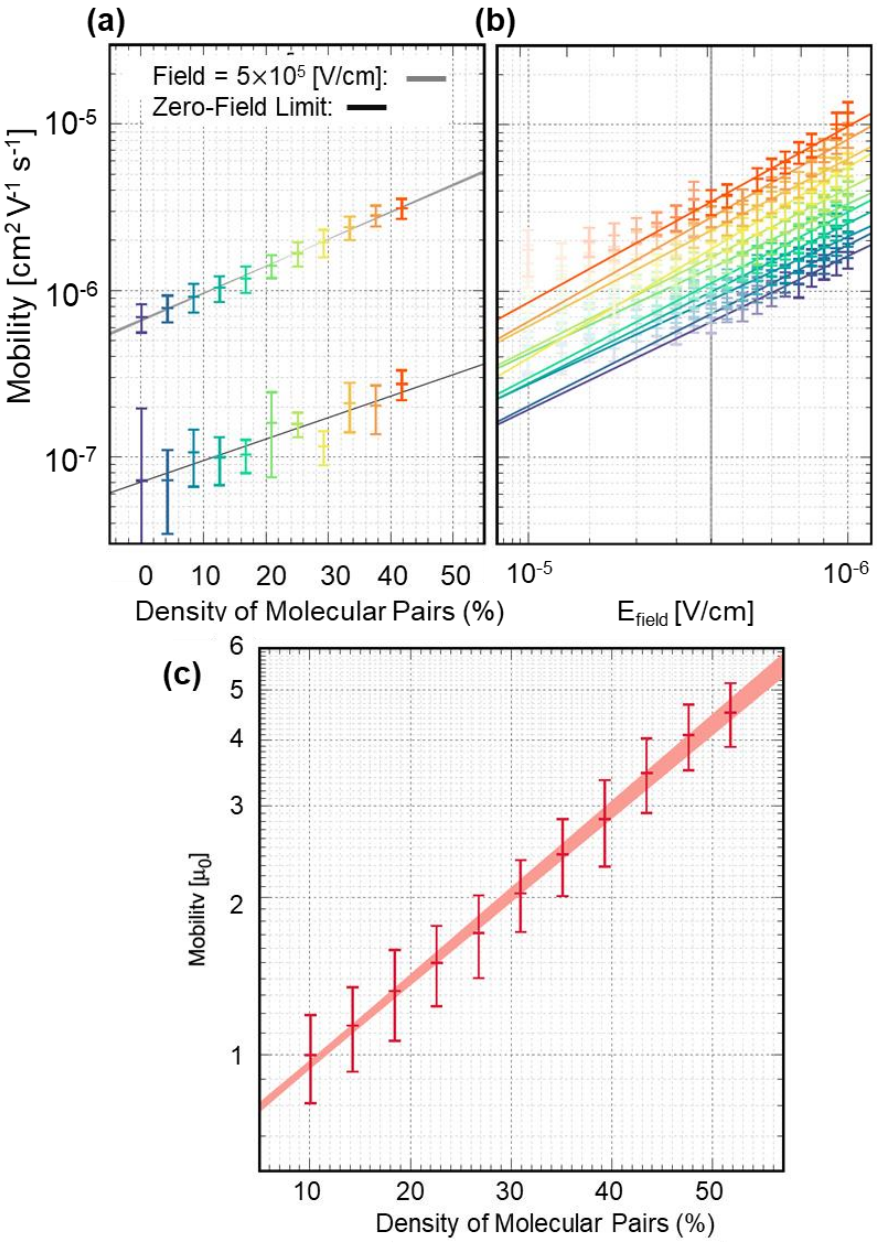

Figure 2-16: (a) legend showing the calculated mobility against a range of pair densities, at a field strength of 5×10^5 V cm^{-1} (top plot) and at zero field (bottom plot), (b) Calculated mobility against field strength with increasing pair density according to the colour scheme shown in (a). (c) normalised mobilities against pair density.

Figure 2-16b shows the dependence of the hole mobility, $\boldsymbol{\mu_h}$, on the applied electric field, E_{Field}, for a range of systems with pair densities ranging from zero to 42%, fitted to a Poole-Frenkel-type equation ($\mu_h \propto e^{\beta\sqrt{E_{Field}}}$).

Poole-Frenkel behaviour is observed for electric fields between 4×10^5 and 9.5×10^5 V cm^{-1}, which was used to extrapolate to the zero-field mobility. Figure 2-16a shows that the mobility increases logarithmically with the pair density from $7 \pm 1 \times10^{-7}$ cm^2 V^{-1} s^{-1} to $2 \pm 0.5 \times10^{-6}$ cm^2 V^{-1} s^{-1}, with an increase in pair population from 0% to 42%. Increasing the pair population to just 30% results in an almost three-fold increase in mobility, as shown in the normalised mobility plot in Figure 2-16c.

While a 30% pair population seems large for an amorphous material, it could be achieved if there is a large enough energetic driving force for stable molecular pairs to form, which is found to be the case for all three amides (Table 2-4). While the material remains disordered and dipoles remain high, the molecular pairs with quenched dipoles serve to reduce the correlated noise width. Both gradients in Figure 2-16a for the zero field and high field case are similar, suggesting that the effect of the pair population on the mobility does not change with the applied electric field but instead results in a global increase in the mobility. While other parameters such as hopping distance and electronic coupling also influence the mobility, the effect of the dipole is included in the exponential term of the hopping rate equation and its influence is likely to be dominant. Therefore, the ability of HTMs **1** and **3** to form energetically favoured 0 Debye hydrogen bonded pairs is consistent with these high dipole materials being able to have high mobilities and may cause a large difference in measured conductivity when compared with HTM **2**. It is also worth noting that simulations were run for fully disordered systems and, therefore, introducing some degree of dipole ordering would further increase the mobility of these systems.[12]

2.2.7 Charge transport measurements

In order for these materials to function as effective HTMs, they need to have appreciable hole conductivity and mobility in order to quickly shuttle holes from the hole-injecting medium to the electrode. Conductivity in small-molecule HTMs is directly affected by the morphology of the film, with the molecular packing having a big effect on the percolation of charge through the material. Having demonstrated the robust intermolecular interaction capabilities of our molecules in both solution and solid state, the effects of these interactions on the thin-film conductivities was investigated.

Like many OSs, our amide materials require the action of chemical doping to gain appreciable conductivity for solar cell applications. To maintain consistency in the oxidation of all HTMs, the additive **FK209** was used as oxidant, which undergoes a well-established redox reaction directly with the HTMs.[42] This has the added benefit of not requiring exposure to oxygen to achieve the requisite oxidation, as is the case with other conventional oxidants such as **LiTFSI**.

Samples doped with **LiTFSI** are often stored in dessicators for an arbitrary period of time which complicates reproducibility.[35] By employing **FK209**, oxidation is ensured to be a direct result of the doping, eliminating the ambiguity that arises in **LiTFSI**-treated systems where a 'curing' process in a dry oxygen environment is needed for effective doping.

As Figure 2-17 shows, **FK209** readily oxidises all amide HTMs, yielding well-defined growth of oxidised species peaks in their UV-Visible absorption spectra. The addition of **FK209** to solutions of HTMs **1** – **3** caused an immediate colour change from pale yellow solutions to deep blue and green solutions. **Spiro-OMeTAD** solutions treated with **FK209** turned from a pale green to deep red. These observations correlate well with the observed absorbances in the resulting spin coated film UV-visible spectra below. New absorbances at 600 – 800 nm for the amide HTMs explain the observed blue colour of the oxidised solutions. Meanwhile, a growing absorption band at relatively shorter wavelength for oxidised **Spiro-OMeTAD** (~540 nm) confers the observed red colour to the solution.

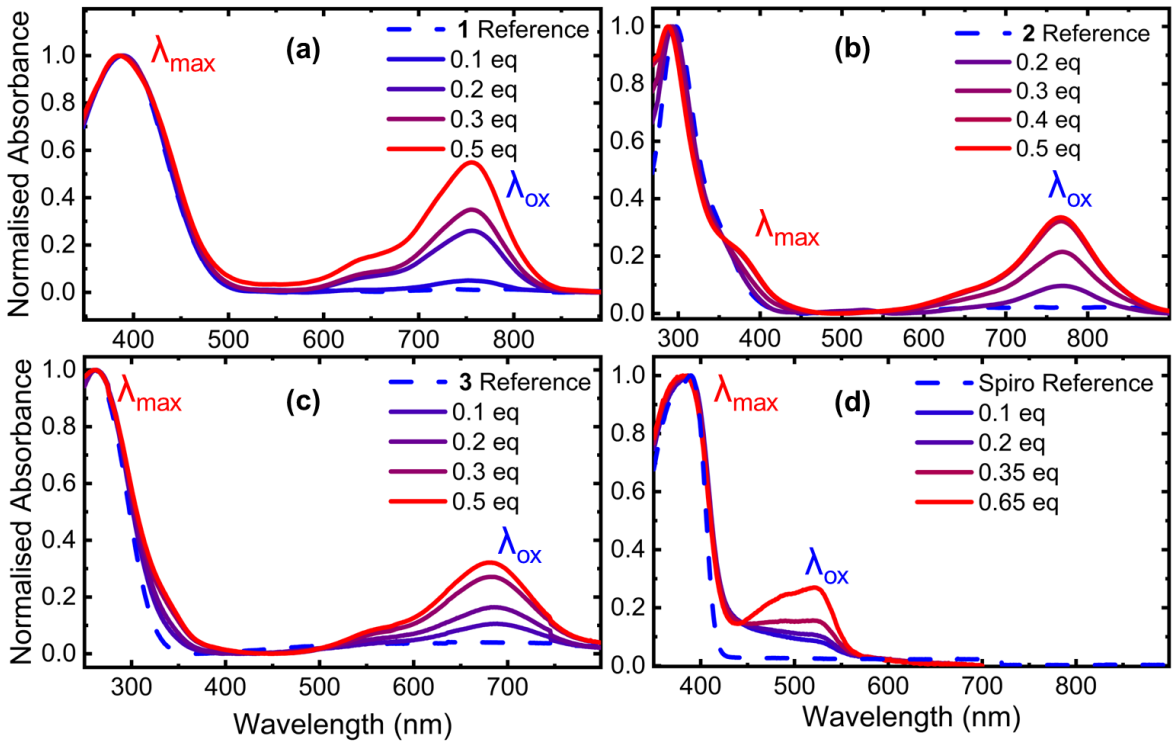

Figure 2-17: Normalised film UV-Visible absorption spectra of (a) HTM **1**, (b) HTM **2**, (c) HTM **3**, and (d) **Spiro-OMeTAD** at varying degrees of **FK209**-mediated oxidation. All spectra were normalised by setting the λ_{max} peak absorbance to 1.

When working with doped HTM systems, the standard practice in the field has normally involved monitoring the degree of oxidation using some measure of the equivalents of added oxidant.[53,107,108] When comparing doping between different HTMs, this method completely negates the chemical reactivities of different HTMs to the additive used, as well as the reactivity of a single HTM to different chemical additives, instead effectively assuming a 1:1 reaction between the HTM and the oxidant.

This introduces errors when comparing different systems, due to ill-defined concentration of oxidised species, which is the important parameter to consider. In order to standardise the conductivity experiments, a new method to accurately quantify the degree of oxidation from the film UV spectra of oxidised solutions is introduced. The ratio of absorbances intensity of oxidised HTM peaks to unoxidised peaks in the film UV spectra can be used as a measure of oxidation if the molar extinction coefficients of both the neutral and the oxidised species is known. The extinction coefficients of all neutral species were thus estimated from UV-Visible absorption spectra collected during their characterisation. To determine the extinction coefficients of oxidised species, a titrimetric method published by Nguyen, *et al*.[48] was used to generate a precisely known amount of oxidised species using silver bis(trifluoromethanesulfonyl)imide (**AgTFSI**). This oxidant has been previously used for its excellent chemical reactivity, as the reduction of Ag(I) to $Ag_{(s)}$ and subsequent precipitation of metallic silver out of solution drives the reaction to completion[109].

Furthermore, it generates the same oxidised complex as **FK209** would, i.e. **HTM$^+$TFSI$^-$**, thus producing the same spectral properties that can be used to calculate the molar extinction coefficient of the oxidised species. **AgTFSI** successfully oxidises solutions of all amide HTMs, as well as **Spiro-OMeTAD**, giving rise to features in the UV-Visible absorption spectrum identical to those observed through **FK209** oxidation (Figure 2-18). Identical colour changes were observed in the solutions, accompanied by the precipitation of a metallic residue.

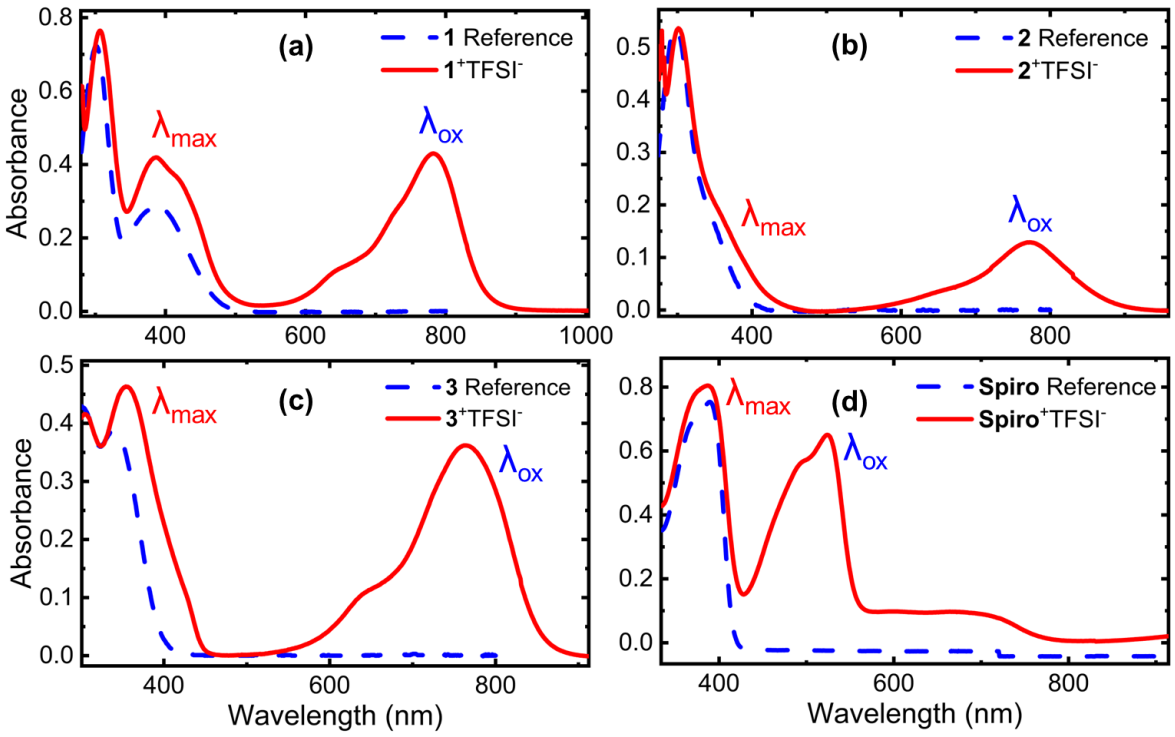

Figure 2-18: Film UV-Visible absorption spectra of pristine and oxidised HTMs (a) HTM **1**, (b) HTM **2**, (c) HTM **3**, and (d) **Spiro-OMeTAD**, showing the new peak arising from the TFSI- salt after reaction with one equivalent of **AgTFSI**.

This residue is identified to be metallic silver, formed as the reduced product from the redox reaction between the HTMs and **AgTFSI**. The estimated molar extinction coefficients are summarised in Table 2-5.

Table 2-5: Calculated molar extinction coefficients of all neutral and oxidised HTMs, obtained from solution UV-Visible absorption spectra recorded in dichloromethane. Concentration and cuvette path length are specified, and the molar extinction coefficients were then calculated using the Beer-Lambert law, A = εbc.

Species	A_{max}	Concentration (mM)	b (cm)	ε (cm^{-1} M^{-1})
1	0.285	0.0100	1	**28500**
2	0.18	0.0100	1	**18000**
3	0.389	0.0100	1	**38900**
Spiro	0.755	0.0095	1	**79759**
EDOT$^+$TFSI$^-$	0.43	0.0169	1	**25444**
DEDOT$^+$TFSI$^-$	0.129	0.0114	1	**11316**
TPABT$^+$TFSI$^-$	0.363	0.0127	1	**28583**
Spiro$^+$TFSI$^-$	0.651	0.0184	1	**35380**

Thin films of amide HTMs treated with **FK209** were deposited onto patterned indium tin oxide (**ITO**) substrates for conductivity measurements by solution spin coating. Conductivity results are shown in Figure 2-19. Significant influence of the dipole ordering and HOMO packing distance is seen in the conductivities, as HTM **3** shows the highest conductivity, about an order of magnitude greater than that of HTM **1** across most of the oxidation range. The results agree well with the calculated degree of dipole ordering seen through our crystal structures and the predicted hopping behaviour from simulation experiments reported above, i.e. **3** > **1** >> **2**. HTM **3** showed the formation of stable, zero dipole pairs in the crystal structure, which are likely to also form during spin coating as previously demonstrated through FTIR (Figure 2-13). Consequently, this amide gives the highest conductivity at 50% oxidation. HTM **2** showed the lowest conductivity as there is no impetus for ordered dipoles due a lack of hydrogen bonding interactions, as well as a looser packing expected from its highly twisted structure. The experimental results also show that the calculated single molecule dipole moments alone fail to predict the trend in conductivity, as the conductivity of HTM **2** was orders of magnitude lower than that of HTMs **1** and **3**.

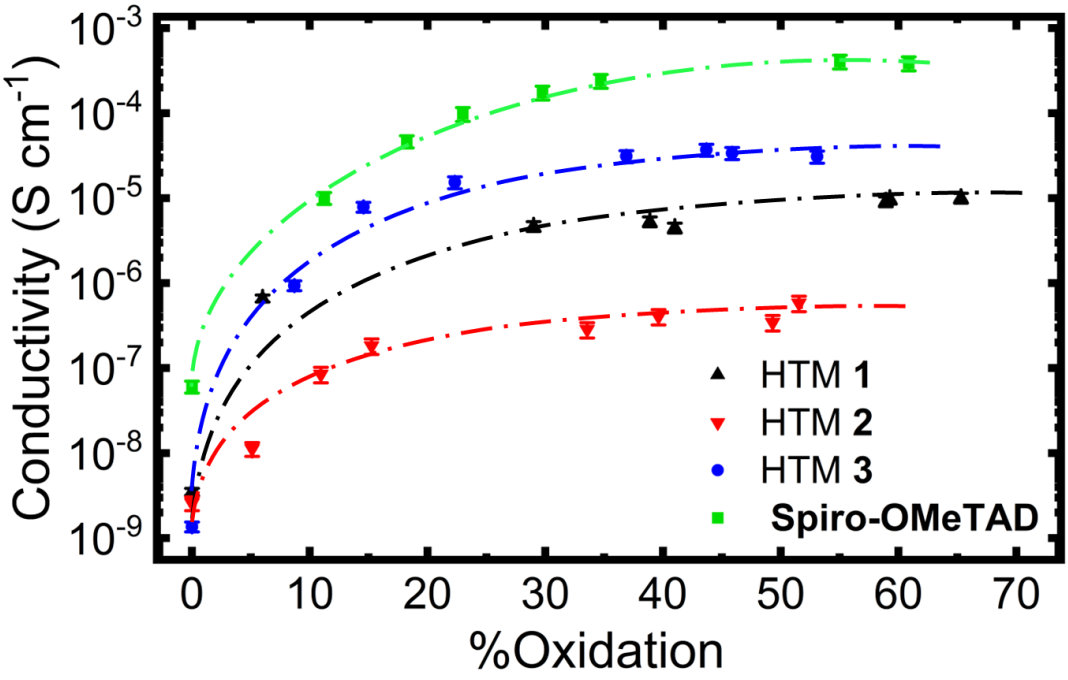

Figure 2-19: Estimated film conductivities of our HTMs with increasing extent of oxidation. Dashed lines added only to guide the eye. %Oxidation on the x-axis was calculated based off of the UV-Visible absorption spectra of films on glass slides at each additive loading, through Equation 2-6 derived in Section 2.4.5. Error bars are the propagated error from all parameters in the calculation, through the propagation equation derived in Section 5.3.5. Doping levels and thickness measurements involved in these experiments are given in Tables 2-9 – 2-11.

Another important charge transport parameter to consider when developing new HTMs is the hole mobility. A high hole mobility is paramount to ensure the feasibility of OSs for energy applications. Here, in devices such as PSCs, a high mobility ensures efficient charge extraction from the active layer and efficient transport to the electrode, on which the PCE hinges. For molecular materials, mobility is influenced by the packing of molecules within the film. Our computational results indicate that the presence of dipoles can negatively impact mobility if the relative orientation of the dipoles is disordered. However, we predict that the formation of zero-Debye molecular pairs will improve the hole mobility of the HTM by reducing the energetic disorder within the film.

In order to verify this effect, hole mobilities of pristine amide HTMs were measured through the SCLC technique. Single-carrier devices were prepared using the following architecture: FTO/HTM/Ag. The silver top electrodes were deposited onto the thin film devices by Fraser J. Angus of the Docampo group, by thermal evaporation. The current-voltage curves of the devices were then recorded, and the mobilities were calculated from the space-charge limited region at higher voltages. The resulting hole mobilities of the three amide HTMs follow a trend identical to that seen in the conductivity measurements. The JV-curves are shown in Figure 2-20 below. HTM **3** is found to have the highest hole mobility at 3.2×10^{-6} cm^2 V^{-1} s^{-1}, and HTM **2** has the lowest mobility at 1.6×10^{-6} cm^2 V^{-1} s^{-1}. HTM **1** has an intermediate mobility of 2.4×10^{-6} cm^2 V^{-1} s^{-1}.

This trend correlates with the increase in dipole ordering in going from compounds 2 < 1 < 3. **Spiro-OMeTAD** has a measured hole mobility of 1.8×10^{-6} cm^2 V^{-1} s^{-1}, comparable to the highly disordered compound **2**. This further illustrates the importance of ordered dipoles within the film as a means towards efficient hole conduction.

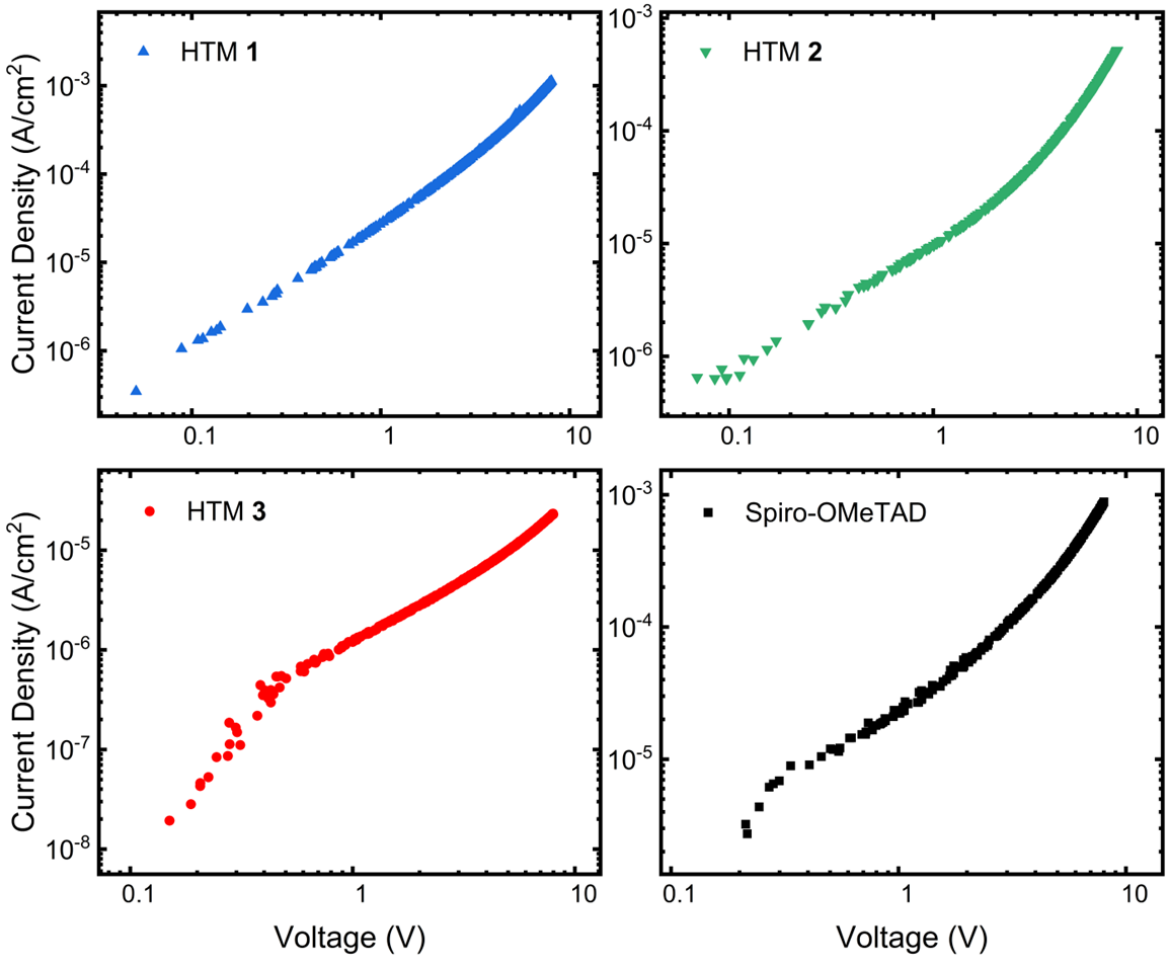

Figure 2-20: Current-density measurements of amide HTMs **1** – **3** and **Spiro-OMeTAD**, recorded for thin film samples and plotted on a log-log scale.

2.2.8 PSC Devices

All solar cells in this section were fabricated and measured by Marcin Giza of the Docampo group.

The amide HTMs were implemented into PSCs in order to test their photovoltaic performance as part of a full device. A triple-cation perovskite composition (FAMACs) was used as the active layer, as such compositions have been reported to outperform single-cation alternatives such as $MAPbI_3$.[110] The device architecture employed was as follows: FTO/TiO_2/C_{60}-SAM/Al_2O_3 nanoparticles/FAMACs/HTM/Au. Here, the FTO acts as the bottom electrode and TiO_2 functions as electron-transporting layer (**ETL**). C_{60} is used to form a self-assembled monolayer on top of the ETL to improve charge injection.

As C_{60} is a hydrophobic substance, Al_2O_3 nanoparticles were added on top as a wetting agent, to allow smooth deposition of the perovskite active layer on top.[54,111] HTLs were treated with **FK209** and **LiTFSI** as oxidants, and tert-butylpyridine (tBP) was also included as a non-doping additive, to aid the dissolution of the ionic additives and also to improve HTL film formation on top of the perovskite layer.[112] The experimental results for the champion devices are summarised in Figures 2-21, 2-22, and Table 2-6.

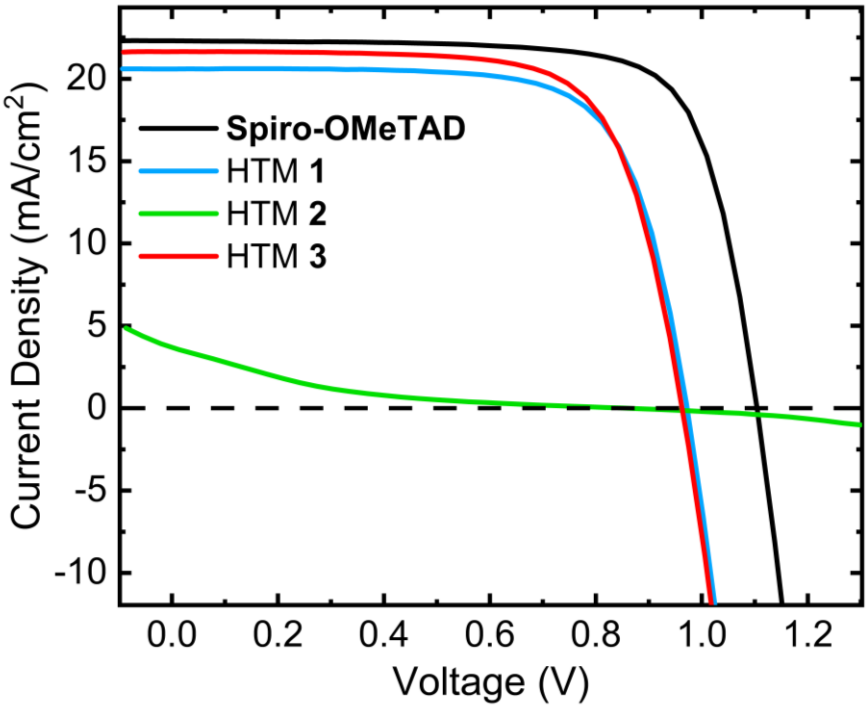

Figure 2-21: Current-voltage characteristics of the champion devices employing the amide materials **1** - **3** or **Spiro-OMeTAD** as HTMs, collected under one sun illumination (AM 1.5 simulated sunlight).

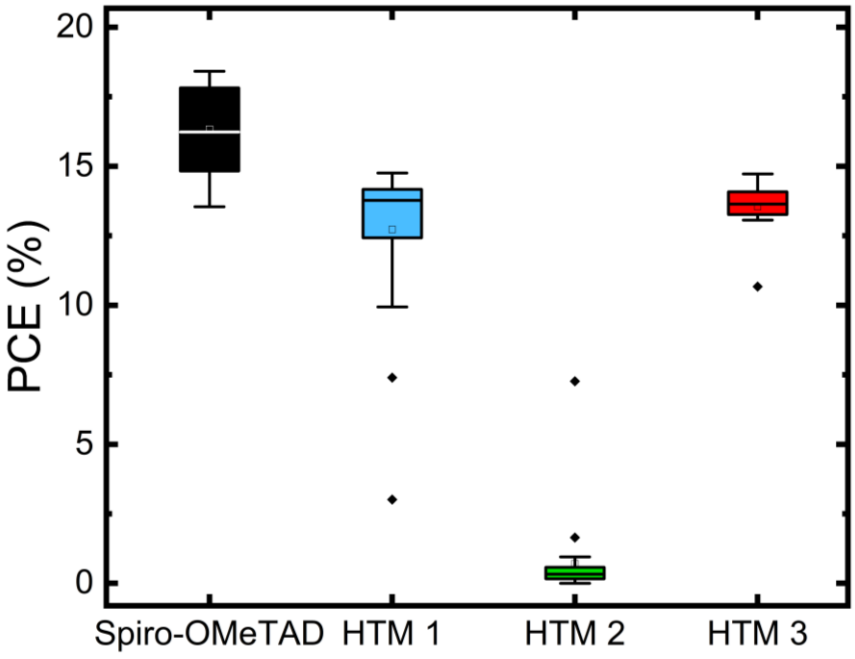

Figure 2-22: Box plots showing the measured PCE distribution for all solar cells fabricated for this study. Distribution shows results from 10 – 24 devices per HTM. Line within the box gives the median PCE, while the top and bottom of each box represents the lower and upper quartile PCE. Black dots represent outlier PCE measurements.

Table 2-6: Solar cell performance parameters measured for champion devices, containing **Spiro-OMeTAD** or amide materials **1** – **3** , extracted from the JV-curves in Figure 2-21.

HTL	J_{SC} (mA/cm^2)	V_{OC} (V)	FF	PCE (%)
Spiro	22.31	1.1	0.75	18.42
1	20.59	0.97	0.71	14.29
2	3.00	0.95	0.58	1.65
3	21.65	0.96	0.71	14.73

HTMs **1** and **3**, as well as the **Spiro-OMeTAD** references are found to drastically outperform HTM **2** with respect to all solar cell parameters. As a result of the reduced conductivity and mobility of HTM **2**, devices employing this HTM suffer from high series resistance leading to insufficient short-circuit current. We can reasonably conclude that this drop arises from the reduced charge transport efficiency within the HTL, which allows more time for recombination processes to take place thus reducing the overall PCE.[113,114] The increase in dipole ordering through hydrogen bonding previously observed in HTM **3** results in an increase in J_{SC} compared to HTM **1**, thus leading to HTM **3** achieving the highest PCE across the amide series.

2.3 Conclusions

The solid-state and solution hydrogen bonding, as well as charge transport properties of three amide-based HTMs were investigated. Through a combination of SCXRD, NMR/FTIR spectroscopy, and DFT modelling, an increased dipole ordering in HTM **3** is seen compared to HTM **1**, with both materials having much more ordered dipoles than HTM **2**. This increased ordering reflects the behaviour of ordered domains in an amorphous film. Previous research has shown the detrimental effect of dipole disorder on the hole conductivity of HTMs. The results in this chapter suggest that the observed improvement in charge transport is a result of increased dipole ordering within the film, likely achieved through hydrogen bond assisted pairing. Such pair formation would lead to increased dipole ordering and a reduced net dipole within the film, thus reducing the overall energetic noise and improving the film conductivity compared to a species that cannot form these aggregates. While HTM **1** also shows pairing, the similar binding energies of parallel and antiparallel-oriented dipoles leads to no overall change in the net dipole ordering, as both orientations are equally likely to be present in the matrix.

Films of HTM **3** show improved conductivity over HTM **1**, with an order of magnitude conductivity increase over HTM **2** which has no hydrogen bonding capacity. While many other parameters also influence the conductivity, the likelihood of HTM **3** to form energetically favoured, zero Debye pairs through hydrogen bonding, in contrast with HTMs **1** and **2**, may explain its order of magnitude higher measured conductivity. The same goes for the measured hole mobilities, where HTM **3** again shows the highest hole mobility across the amide series. The improved charge transport properties of HTM **3** lead to an increase in J_{SC} in fabricated solar cells leading to increased PCE, thus demonstrating the applicability of the work presented in this chapter.

2.4 Methodology

2.4.1 NMR Studies

To prepare samples for the concentration NMR study in Section 2.2.3, stock solutions of the amide HTMs were prepared in $CDCl_3$ and divided into separate vials for dilution. Each vial was diluted with additional $CDCl_3$ to obtain the requisite concentration. Spectra were then recorded at 25 °C.

For VT-NMR studies, ^{1}H-NMR spectra were recorded as before at three temperatures by first cooling the samples to 0°C, then heating back up to 25 °C, then 50°C. Samples were left to equilibrate at the desired temperature for 5 minutes prior to acquisition. Solutions of our HTMs were prepared by dissolving 10 mg of HTM in 0.6 mL $CDCl_3$, thus yielding solutions at a concentration of 20 mM for HTM **1**, 19.3 mM for HTM **2**, and 21.5 mM for HTM **3**. For the DMSO-d6 titrations, solutions with similar concentrations as above were prepared, as well as a stock solution of DMSO-d6 in $CDCl_3$ to allow for the gradual addition of DMSO-d6 into the NMR solution.

The HTM solutions above are of sufficient concentration to not be significantly diluted by the addition equivalents of DMSO-d6 from the stock solution, thus minimising dilution effects in the NMR spectrum.

2.4.2 XRD

PXRD measurements discussed in Section 2.2.4 were performed on a Rigaku Miniflex bench-top diffractometer using Cu K_α radiation. Neat powder samples or thin films of HTMs **1** – **3** on FTO-coated glass were used for the measurements as specified in the text. The film XRD measurements were referenced to the prominent FTO peaks.

For SCXRD in Section 2.2.4, single crystals of HTMs **2** and **3** were grown via slow evaporation of solutions in chlorobenzene, while crystals of **1** were grown via slow evaporation from a 1:1 dichloromethane:methanol solution. Crystal structures of **1** were resolved by the UK National Crystallography Service, while **2** and **3** were resolved by Dr. Claire Wilson at the School of Chemistry.

Computational details for the resolved structures of HTMs **2** and **3** are as follows:

Data collection: *APEX3* Ver. 2016.9-0 (Bruker-AXS, 2016); cell refinement: *SAINT* V8.40B (Bruker, 2016); data reduction: *SAINT* V8.40B (Bruker, 2016); program(s) used to solve structure: SHELXT 2018/2 (Sheldrick, 2018); program(s) used to refine structure: *SHELXL* 2018/3 (Sheldrick, 2015); molecular graphics: Olex2 1.5 (Dolomanov *et al.*, 2009); software used to prepare material for publication: Olex2 1.5 (Dolomanov *et al.*, 2009).

Resolved structures were analysed in VESTA 3 software. In order to estimate the different packing behaviour of different amide-based HTMs, the nearest HOMO distance between molecules in the crystal was estimated as the shortest N-N distance between the TPA groups, where the HOMO is mainly situated.

CCDC Deposition numbers are:

EDOT-Amide-TPA (Compound **1**): Deposition Number **2301541**

Unit Cell Parameters: a 55.7783(6) b 55.7783(6) c 10.4905(2) I41/a

DEDOT-Amide-TPA (Compound **2**): Deposition Number **2301539**

Unit Cell Parameters: a 16.6681(5) b 18.0603(6) c 16.6318(5) P21/c

TPABT (Compound **3**): Deposition Number **2301540**

Unit Cell Parameters: a 12.1294(3) b 14.8596(3) c 27.9555(8) P21/c

2.4.3 DFT calcualtions

DFT calculations in Section 2.2.5 were performed by Miriam Fsadni at Newcastle University. Calculations were run at the DFT (PBE0)/def2-sv(p) level of theory as implemented within the Orca (v. 5.1) quantum chemistry package.[100] From these calculations all molecular properties, including the Debye dipole moments, were obtained. Consistent with previous work,[13] calculations were performed both in vacuum and in dichloromethane to approximate the effect of the film environment, using the conductor-like polarisable continuum model (**C-PCM**). Based on a procedure by Chi, *et al*. adapted to calculations performed at the PBE0/def2-sv(p) level,[115] a linear correction factor of -0.206 eV was applied to the HOMO energies for molecules optimised in dichloromethane.

2.4.4 kMC simulations

kMC simulations in Section 2.2.6 were also run by Miriam Fsadni at Newcastle University. The HTM film is represented as a cubic lattice with 8 million hopping sites, with a lattice spacing of 10 Å. Site dipoles were initially set to 10 Debye and oriented randomly as described in previously published work.[13] In systems with a non-zero pair population, paired site dipoles were reset to 0 Debye and aligned with the reference frame. Marcus hopping rates for a range of pair populations at different field strengths were found. All other parameters were kept constant including uncorrelated noise, hole density and reorganisation energy, so that the effect of pair density on mobility could be definitively probed. Holes are distributed over the sites randomly to achieve a given hole density, $\boldsymbol{\rho_0}$, and the energies recalculated. For each step in the simulation, holes are able to hop to vacant neighbouring sites within a radius of $\sqrt{3}\mathrm{L}$, where $\mathbf{L}$ is the lattice spacing.

For each possible hop, the energy change, $\Delta\mathrm{E}$, as well as the associated Marcus hopping rate are found. For a hop between sites $\mathbf{i}$ and $\mathbf{j}$, this is given by Equations 2-1 and 2-2 respectively,

$$\Delta \mathrm{E}_{\mathrm{ij}} = \Delta \mathrm{E}_{\mathrm{ij}}^{\mathrm{corr}} + \Delta \mathrm{E}_{\mathrm{ij}}^{\mathrm{coulomb}} + \Delta \mathrm{E}_{\mathrm{ij}}^{\mathrm{field}} \tag{2-1}$$

$$\mathrm{k}_{\mathrm{ij}} = \omega_0 \mathrm{e}^{-2\gamma|\mathrm{R}_{\mathrm{ij}}|} \times \mathrm{e}^{-(\lambda+\Delta\mathrm{E})^2/4\lambda\mathrm{k}_\mathrm{B}\mathrm{T}} \tag{2-2}$$

Here, $\boldsymbol{\omega_0}$ is the hopping attempt frequency, $\mathbf{R_{ij}}$ is the spatial vector between the sites and $\boldsymbol{\lambda}$ is the reorganisation energy. The free parameters for the simulation are outlined in Table 2-7 below.

Table 2-7: List of parameter settings for the kMC calculation.

Parameter	Description	Value	Units
$\mathbf{E_{HOMO}}$	HOMO energy	0.0	eV
$\mathbf{E_F}$	Fermi energy	0.0	eV
$\boldsymbol{\rho_0}$	Initial charge density	10^{-5}	nm^{-1}
L	Lattice spacing	1	nm
ϒ	Inverse charge localisation	2.0	nm^{-1}
$\boldsymbol{\omega_0}$	Hopping attempt frequency	10^{12}	s^{-1}
$\boldsymbol{\epsilon_R}$	Relative permittivity	3.0	ϵ_0
$\mathbf{d_M}$	Monomer Dipole	5.0	D
$\mathbf{d_P}$	Pair Dipole	0.0	D
N	System Dimensions	200	grid points

In calculating the change in site energies, $\mathbf{E_{HOMO}}$ is kept constant over each site, and any variance, $\mathbf{E_i^{unc}}$, was neglected so that the effect of correlated noise on hole mobility could be selectively probed. This simplifies the energy differences between sites, which then only depend on the change in electric field, the Coulomb repulsion and correlated noise term. The change in Coulomb energy results from the change in the electrostatic interaction of the hole and all other holes in the system on changing site and is given by Equation 2-3:

$$\Delta E_{ij}^{coulomb} = \frac{1}{\epsilon_r}\left(\sum_{\substack{k\neq j \\ k=occupied}} \frac{1}{|R_{jk}|} - \sum_{\substack{k\neq i \\ k=occupied}} \frac{1}{|R_{ik}|}\right) \quad (2\text{-}3)$$

where $\boldsymbol{\epsilon_r}$ is the relative permittivity of the medium.

The correlated disorder term, $\Delta\mathbf{E_{ij}^{corr}}$, reflects the energy change due to the interaction of electronic dipole moments on neighbouring sites, and is given by Equation 2-4.

$$\Delta E_{ij}^{corr} = \frac{1}{\epsilon_r}\left(\sum_{k\neq j} \frac{d_k \cdot R_{jk}}{|R_{jk}|^3} - \sum_{k\neq i} \frac{d_k \cdot R_{ik}}{|R_{ik}|^3}\right) \quad (2\text{-}4)$$

The dipole magnitude is kept constant for all sites and the direction is generated semi-randomly by defining the azimuthal and polar angles, as previously detailed by Pope, *et al*..[13] For systems with a non-zero pair density, grid point pairs are distributed randomly, and the pair magnitude is set to zero and aligned with the reference frame.

For each hopping event, all possible hopping rates are probabilistically weighted, and an event is chosen at random. The event is executed, the time is added to the total simulation run time and the site energy grid is updated. The simulation is allowed to proceed over 1,000,000 steps, to ensure convergence. For each system, the outputs from 88 simulations are taken to obtain an average mobility.

2.4.5 Oxidative Titrations

To determine the molar extinction coefficients of the oxidised HTMs in Section 2.2.7, a titrimetric procedure published by Nguyen, *et al*. was followed.[48] In a nitrogen-filled glove box, a standard solution of **AgTFSI** in CB was prepared by adding 297.5 mg **AgTFSI** to 100 mL CB in a volumetric flask, thus forming a 7.67 mM solution of **AgTFSI**. Standard solutions of compounds **1**, **2**, **3**, and **Spiro-OMeTAD** were similarly prepared in 50 mL CB. One mole equivalent of **AgTFSI** oxidant was then titrated into the HTM solutions using a micropipette, causing an immediate colour change. HTMs **1** – **3** turned different shades of dark green, while **Spiro-OMeTAD** formed a dark red solution. The measurements for these titrations are summarised in Table 2-8.

Table 2-8: Table of numbers for the preparation of oxidised HTM solutions used for spin coating, to produce the thin films for the titrimetric UV absorption experiment in Section 2.2.7.

HTM	Mass of HTM (mg)	Volume of Solvent (mL)	[HTM] (mM)	**AgTFSI** added (mg)	**AgTFSI** eq.	[HTM^+] (mM)
1	26.5	50	0.635	4406.5	0.96	0.564
2	11.7	50	0.271	1705.0	0.87	0.229
3	10.4	50	0.268	1903.2	0.98	0.254
Spiro	11.6	50	0.189	1710.2	1.25	0.184

Thin films were deposited onto glass slides through by spin coating 70 µL of HTM solution through a static method. Spin coating was performed at 1000 rpm for 10 seconds, followed by 5000 rpm for 5 seconds to remove traces of solvent from the edge of the spinning slides. The resulting films were visually inspected to ensure even film formation. Films were left in the glove box overnight for 16 hours, to allow for the evaporation of residual solvent. The UV-Visible absorption spectra of the thin films were then recorded and these are given in Figure 2-18.

The molar extinction coefficients were then calculated according to the Beer-Lambert law (Equation 2-5) which equates absorbance to the concentration of the absorbing species:

$$A = \varepsilon\, b\, c \qquad (2\text{-}5)$$

Where A = absorbance, b = path length, and c = concentration.

All estimated molar extinction coefficients are summarised in Table 2-5 above.

From the known molar extinction coefficients of all of our HTMs, Equation 2-6 is derived for the ratio of oxidised species in oxidised HTM films, expressed as a percentage:

$$c = \frac{A}{\varepsilon b}$$

$$c_{unox} = \frac{A_{unox}}{\varepsilon_{unox} b} \qquad c_{ox} = \frac{A_{ox}}{\varepsilon_{ox} b}$$

$$\%\text{oxidation} = \frac{c_{ox}}{c_{unox}} \times 100$$

$$= \frac{A_{ox}/\varepsilon_{ox} b}{A_{unox}/\varepsilon_{unox} b} \times 100$$

The path length in this is equal for both oxidised and unoxidised species and so is cancelled out.

$$\%\ \text{oxidation} = \frac{A_{ox}\varepsilon_{unox}}{A_{unox}\varepsilon_{ox}} \times 100 \qquad (2\text{-}6)$$

Equation 2-6 was then used to estimate the extents of oxidation of HTM films across the **FK209** concentration range as measured through film UV absorption spectroscopy. The calculated values were then used to compare the conductivity measurements of different HTMs on the same axes.

2.4.6 Conductivity Measurements

To prepare the HTM solutions for spin coating, one stock solution each was prepared for HTMs **1**, **2**, **3**, and **Spiro-OMeTAD**. The choice of appropriate solvent is very important when preparing a spin coating solution, as good solubility in an inert solvent is paramount for film formation. For all conductivity measurements in this thesis, pure CB or CB/CF mixtures were used as they fully dissolve all HTMs used. HTM **1** has markedly lowered solubility compared to the other HTMs used, so a CB/CF mixture at elevated temperatures was used to keep the HTM in solution during the experiment.

Stock solutions were thus prepared by weighing out dry powders of compounds **1** – **3** in separate vials within a nitrogen-filled glove box. Weighed amounts of anhydrous CB was then added to each vial according to the measurements in Table 2-9 below. The solvent weight was noted in order to calculate the corresponding volume from the density. CF was then added to the mixtures until complete dissolution of the solute was observed. Vials of HTM **1** and **3** were kept sealed on a hot plate at 70 °C between spin coating steps in order to keep the HTMs dissolved. All vials were kept sealed throughout the experiment to minimise evaporation of volatile CF and the resulting precipitation of the HTMs. The **FK209** stock solution was prepared in a similar manner, with acetonitrile (ACN) as the solvent. All solutions were then passed through a hydrophobic syringe filter, into a new vial before use to remove any other particulate matter.

Table 2-9: Measurements for preparation of spin coating solutions used for preparation of thin films for conductivity measurements.

Species	Amount added	Solvents	Concentration
1	18.4 mg	1037.0 mg CB + 1293.2 mg CF	12.2 mM
2	17.2 mg	1016.0 mg CB + 1428.1 mg CF	10.6 mM
3	52.6 mg	602.5 mg CB + 3269.5 mg CF	24.7 mM
Spiro-OMeTAD	39.2 mg	2213.4 mg CB	16.0 mM
FK209 Stock	187.2 mg	804.8 mg ACN	121.6 mM

Each HTM stock vial was then roughly split into 7 individual vials for further processing. The mass of stock solution transferred into each vial was noted. Each of these portions was individually treated with increasing amounts of **FK209** dopant.

By using the known transferred solution mass, the number of moles of HTM in each vial could be estimated, thus allowing calculation of required **FK209** additive stock to achieve a particular doping level. Doping was performed by directly adding known volumes of **FK209** solution into the HTM vials using a micropipette, which caused an immediate and strong colour change to blue or dark blue solutions in all cases, as a result of the chemical reaction forming the oxidised HTM. The additive volumes used for each condition are given in Table 2-10.

Table 2-10: Measurements and doping equivalents for the conductivity experiment. The mol% values were calculated based off of the concentrations of the HTM and dopant solutions, the moles of HTM in the transferred portion, and the moles of dopant in the added volume.

Spiro-OMeTAD Vial	**S1**	**S2**	**S3**	**S4**	**S5**	**S6**	**S7**
Stock solution mass (mg)	214.6	220.6	220.1	221.7	219.7	221.1	222.1
Added **FK209** (µL)	1	3	5	7	9	12	15
mol%	3.9	11.4	19.1	26.6	34.5	45.7	56.8
%oxidised	**11.2**	**18.2**	**23.0**	**29.8**	**34.7**	**55.0**	**60.9**
HTM 1 Vial	**E1**	**E2**	**E3**	**E4**	**E5**	**E6**	**E7**
Stock solution mass (mg)	178.9	142.7	197.1	200.1	196.1	195.7	194.3
Added **FK209** (µL)	1	2	4	5	6	7	8
mol%	7.2	18.0	26.1	32.1	39.3	46.0	53.0
%oxidised	**6.0**	**29.0**	**38.9**	**41.0**	**58.9**	**59.3**	**65.3**
HTM 2 Vial	**D1**	**D2**	**D3**	**D4**	**D5**	**D6**	**D7**
Stock solution mass (mg)	218.3	232.3	207.4	222.2	228.1	232.2	223.4
Added **FK209** (µL)	1	2	3	5	6	8	9
mol%	6.8	12.8	21.6	33.6	39.2	51.4	60.1
%oxidised	**5.1**	**10.9**	**15.3**	**33.5**	**39.6**	**49.3**	**51.5**
HTM 3 Vial	**T1**	**T2**	**T3**	**T4**	**T5**	**T6**	**T7**
Stock solution mass (mg)	246.0	240.4	283.9	251.5	246.6	250.7	244.0
Added **FK209** (µL)	1	4	8	12	15	18	20
mol%	2.8	11.6	19.6	33.2	42.3	49.9	57
%oxidised	**8.7**	**14.6**	**22.3**	**36.9**	**45.9**	**53.1**	**43.7**

Thin films were spin coated onto patterned ITO slides for conductivity measurements, and onto glass slides for UV-Visible absorption spectroscopy as well as film thickness measurements. 50 µL of solution from each condition was dropped onto a glass or ITO slide using a micropipette. Spin coating was then performed through a static method, at a speed of 1000 rpm for 10 seconds, followed by 5000 rpm for 5 seconds to remove traces of solvent from the edge of the spinning slides. The resulting films were visually inspected to ensure even film formation. Films were left in the glove box overnight for 16 hours, to allow for the evaporation of residual solvent. The UV-Visible absorption spectra of the thin films were then recorded and these are given in Figure 2-17.

Film thicknesses were measured across each HTM doping series by etching a valley into the glass slide using a razor, and measuring the depth of the valley using contact profilometry. Individual measurements are thus given as negative thicknesses since a depth is being measured. The resulting measurements are given in Table 2-11. Averages based off of six measurements per HTM were then calculated, and the standard deviation across these six measurements was used as the error from the thickness measurements.

Table 2-11: Measured film thicknesses for the thin films deposited for conductivity measurements, including the calculated average thicknesses and the standard deviation used in the conductivity calculation.

	Film thickness (nm)			
	1	**2**	**3**	**Spiro**
	-71.7139	-65.1971	-195.162	-111.40582
	-64.558	-55.9587	-218.848	-143.53449
	-83.3414	-34.984	-177.286	-86.71381
	-76.0184	-55.6843	-147.753	-104.09324
	-74.6759	-60.4043	-176.869	-115.10376
	-78.2829	-52.0813	-201.474	-108.57964
Average (nm)	**74.8**	**54.1**	**186.2**	**111.6**
Standard Deviation (nm)	**5.79**	**9.47**	**22.5**	**16.9**

The calculated conductivities for each condition are plotted in Figure 2-19. Due to the volume of the dataset, only one conductivity measurement per condition was performed. The error bars in the graph are the propagated error which was calculated according to Equation 5-20 derived in Section 5.3.5.

2.4.7 SCLC measurements

Hole-only devices were prepared for SCLC measurements through a combination of solution spin coating and thermal evaporation. In order to prepare sufficiently thick films for SCLC, concentrated solutions were prepared for spin coating as detailed in Table 2-12.

Table 2-12: Table of measurements for the preparation of the spin coating solutions for SCLC measurement. Film thicknesses are averages of three readings per film, and error shown is the standard deviation.

Species	Amount added	Solvents	Concentration
1	15.3 mg	325.0 mg CB + 857.6 mg CF	21.1 mM
2	76.0 mg	441.7 mg CB	221.3 mM
3	52.3 mg	238.4 mg CB + 294.4 mg CF	163.2 mM
Spiro	120.0 mg	571.5 mg CB	190.2 mM

Stock solutions were prepared by weighing out dry powders of compounds **1** – **3** and **Spiro-OMeTAD** in separate vials within a nitrogen-filled glove box. Weighed amounts of anhydrous CB was then added to each vial according to the measurements in Table 2-12. The solvent weight was noted in order to calculate the corresponding volume from the density. CF was then added to the mixtures until complete dissolution of the solute was observed. Vials of HTM **1** and **3** were kept sealed on a hot plate at 70 °C between spin coating steps in order to keep the HTMs dissolved. All vials were kept sealed throughout the experiment to minimise evaporation of volatile CF and the resulting precipitation of the HTMs. All solutions were then passed through a hydrophobic syringe filter, into a new vial before use to remove any other particulate matter. Extra care was taken to prevent the precipitation of solid HTM from these highly concentrated solutions after filtration. Solutions of HTMs **1** – **3** were kept sealed on a hot plate at 70°C to prevent precipitation of the HTM, ensuring good film formation. Films were deposited through static spin coating using slower spinning speeds to further increase film thickness. 70 µL of HTM solution was transferred onto a UV/Ozone cleaned ITO or glass slide, and was then spread across the surface by a back-and-forth motion of the side of the pipette tip. The spin coater was then closed and the program was started (1000 rpm for 5 seconds, followed by 5000 rpm for 10 seconds). This procedure produced films of sufficient thickness to ensure that a space charge-limited regime is formed within the film. Samples were left in a dessicator for one week to allow for the evaporation of residual solvent. Finally, silver (Ag) electrodes were deposited on top of the HTM films to complete the device architecture. Silver electrodes were deposited by Fraser J. Angus of the Docampo group.

Film thicknesses were measured across a thin channel etched into the HTM film on glass using a razor. The low solubility of compound **1** in organic solvents leads to a much lower saturation concentration for this HTM compared to **2** and **3**. This resulted in the thinnest films across all tested samples. However, a space charge-limited regime was still seen in the resulting JV curves so the thickness was deemed to be adequate for experimental purposes. The resulting measurements are given in Table 2-13. Averages based off of three measurements per HTM were then calculated, and the standard deviation across these measurements was used as the error from the thickness measurements.

Table 2-13: Measured film thicknesses for the thin films deposited for SCLC measurements, including the calculated average thicknesses and the standard deviation used in calculating mobility.

	Film thickness (nm)			
	1	**2**	**3**	**Spiro**
	-395.96265	-430.19566	-1385.67302	-410.57628
	-401.37685	-436.70922	-1366.28568	-405.09747
	-390.16946	-437.56781	-1367.29587	-396.27684
Average (nm)	**395.84**	**434.82**	**1373.08**	**403.98**
Standard Deviation (nm)	**4.58**	**3.29**	**8.91**	**5.89**

2.4.8 Solar cell measurements

All solar cells were prepared and analysed by Marcin Giza of the Docampo group. Detailed procedures for substrate preparation, as well as the preparation of the ETL and perovskite absorbing layer are given in Section 5.3.7 in the Methodology. Spin coating solutions of the amide HTMs and **Spiro-OMeTAD** were then prepared as follows:

Spiro-OMeTAD: A 80 mg/mL solution was prepared in CB. 19 µL of **LiTFSI** solution (519 mg / mL in ACN), 14 µL of **FK209** solution (374 mg/mL in ACN) and 34 µL of 4-tert-butylpyridine (tBP), then spin coated on top of the perovskite at 3000 rpm for 30 seconds.[116]

HTM **1**: A 10 mg/mL solution in 4:1 v/v CB : CF was dissolved at 100°C and mixed with 30 µL of **LiTFSI** solution (170 mg / mL in ACN), and 10 µL of tBP, then spin coated on top of the perovskite at 1000 rpm for 30 seconds and 2000 rpm for 5 seconds. The solution was kept at 70°C at all times during the preparation and spin coating process.[54]

HTM **2**: A 10 mg/mL solution in 4:1 v/v CB : CF was mixed with 20 µL of **LiTFSI** solution (170 mg / mL in ACN), and 10 µL of tBP, then spin coated on top of the perovskite at 1000 rpm for 30 seconds and 2000 rpm for 5 seconds.

HTM **3**: A 10 mg/mL solution in 2:1 v/v CB : CF was mixed with 25 µL of **LiTFSI** solution (170 mg / mL in ACN), and 10 µL of tBP, then spin coated on top of the perovskite at 1250 rpm for 40 seconds and 2000 rpm for 5 seconds.[80]

Finally, 50 nm thick gold (Au) electrodes were deposited on all films via thermal evaporation. JV-curves were then measured under AM 1.5G simulated sunlight.

3 The role of lithium coordination in the **LiTFSI** doping mechanism of amide small molecule HTMs

3.1 Introduction

In order to improve the conductivity of many OSs, researchers commonly resort to additives such as **LiTFSI** and **FK209**, either by themselves or as a mixture.[40,117,118] While many different doping recipes are employed in as many different laboratories around the globe, it is still unclear what makes up the perfect additive 'cocktail'. This is an inherently unsolvable problem given the extensive array of HTM families currently in development, and their diverse reactivity. The indiscriminate addition of the same additive mixture to different HTM systems can lead to sub-optimal doping which can result in an excess of reactive or hygroscopic substances within the film that can catalyse degradation mechanisms.[29,112] An incorrect choice of additives may even lead to the misguided disqualification of potential HTMs if the reactivity of the building blocks hinder the doping pathway, when the HTM of interest may perhaps be better suited to an alternative doping recipe. Therefore, a fundamental understanding of the doping mechanism of each particular HTM is essential in order to ensure that doping occurs effectively for the system of interest.

In the case of **Spiro-OMeTAD**, the typical HTM of choice for PSCs, the **LiTFSI** oxidation mechanism is well understood, taking place via redox reactions which generate **Spiro-OMeTAD$^{+\cdot}$** radical cations (**spiro^{+}**).[35,37] In this mechanism, the lithium ions do not bond directly with the **Spiro-OMeTAD**, but only transfer charge through redox reactions. Lithium is consumed in the reaction, generating a series of lithium oxides which, under continued operation of the device cause degradation from water ingress, due to their hygroscopic nature.[35] Furthermore, certain device preparations may necessitate additional additives within the HTL for improved interfaces with adjacent components. In PSC fabrication for instance, the additive *tert*-butylpyridine (**tBP**) is introduced which itself partakes in non-negligible side-reactions with the oxidised HTM. Indeed, tBP is found to cause dedoping of oxidised **Spiro-OMeTAD** by directly reacting with, and thus quenching, the spiro^{+} cation as it forms in a **LiTFSI**-treated **Spiro-OMeTAD** film.[85,119] This forms tBP$^{+\cdot}$ radical species which can react with another spiro^{+} thus forming a final adduct between **Spiro-OMeTAD** and tBP. These competing oxidation and dedoping mechanisms are summarised in Scheme 3-1.

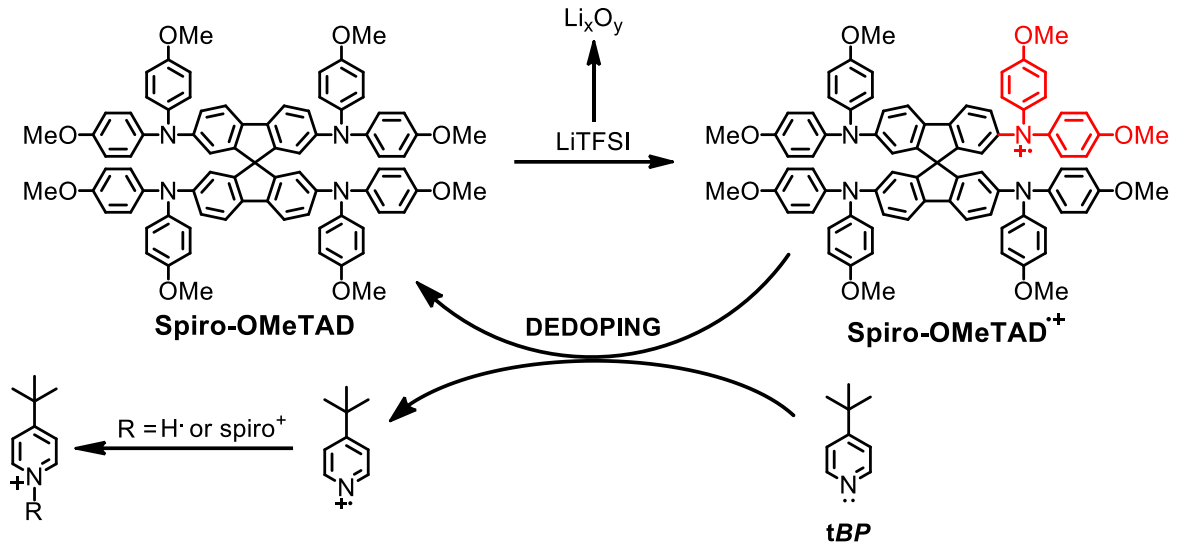

Scheme 3-1: The redox doping mechanism of **Spiro-OMeTAD**, as well as the dedoping mechanism involving tBP.[6-9]

Amide-based HTMs have recently been introduced as low-cost alternatives to **Spiro-OMeTAD**. HTMs such as **1** and **3** (introduced in Chapter 2) are shining examples of the great potential that exists in condensation chemistry as a route towards low-cost HTMs, but there has not yet been a significant research effort focusing on their doping mechanisms.[54,80] It is evident that the building blocks of a hole transporter are intimately tied to the chemical reactivity of the species, and standard chemical additives such as **LiTFSI**/**FK209** are likely to react in a completely different manner with new HTMs, which may or may not lead to successful doping. It follows that each newly developed HTM necessitates a time-consuming optimisation of the additive mixture to achieve optimal conductivities. Despite this, a large portion of recently reported new HTMs are still commonly doped with some combination of **LiTFSI** and **FK209**, even when their chemical properties are unclear. Furthermore, little to no information is provided as to whether this recipe has been optimised, as the main focus of published literature is likely to only present the most appealing results (i.e. highest PCE, highest conductivity).[29,120–123]

An excellent illustration of the relationship between HTM structure and reactivity is the case of compound **1**. It has been demonstrated that the amide linkers in HTM **1** can coordinate with lithium ions from the **LiTFSI** additive through the carbonyl group, which acts as a Lewis base.[54] This phenomenon is not unique to this compound; it has been observed in other amide and imide-based HTMs where this coordination has been used to immobilise the lithium ions, preventing their migration under bias during the operation of perovskite solar cells, thus improving long-term device stability.[124,125]

While the positive impact of lithium coordination on device stability has been demonstrated, a fundamental investigation on how this coordination impacts the doping process has not been carried out. The coordination of lithium ions to the carbonyl group could either positively or negatively affect the doping efficiency. As studies have previously demonstrated strong trapping of lithium ions through coordination,[124] the interaction may be strong enough to sequester lithium ions away from the HOMO, hindering charge transfer required for doping. Alternatively, participation of lithium ions in a reversible coordination to the carbonyl groups could increase the effective concentration of lithium ions around the HOMO on the TPA moieties (Chapter 2, Figure 2-14) and increase the likelihood of successful ionisation. Therefore, a thorough investigation into the role of lithium coordination is vital in order to develop robust structure-function relationships to inform the development of future HTMs and doping recipes.

In this chapter, the effect of lithium coordination through the amide carbonyl group on the oxidation mechanism is investigated through a combination of UV-Visible absorption and infrared spectroscopy, DFT modelling, and film conductivity measurements. Through various doping studies using HTM **1**, it is revealed that lithium coordination by the HTM is vital for the doping mechanism, and that blocking this coordination also curtails the doping efficiency. This leads to a proposed **LiTFSI** doping mechanism for HTM **1**, in which the formation of a coordinated intermediate catalyses the ionisation of the HOMO. The importance of stabilising the iminium cation formed through coordination is also highlighted by using the dimethylated analogue HTM **2**, which is found to resist coordination despite enhanced electron density around the carbonyl group. The results presented within this chapter illustrate how minor structural changes to the chemical structure of a HTM can lead to large ramifications on the reactivity with the applied dopant, which can hinder the utility of said dopant for improving conductivity.

3.2 Results and Discussion

Synthesis, as well as spectroelectrochemical and thermal characterisation of the three amide HTMs **1 - 3** is described in Chapter 2, Sections 2.2.1 and 2.2.2.

3.2.1 Spectroscopic analysis of **LiTFSI** oxidation

As discussed earlier, routine absorption spectroscopy techniques are indispensable in the study of HTM doping mechanisms, as the reactions involved lead to new spectral features that allow close monitoring of the oxidation of the HTM. UV-Visible absorption spectroscopy is a useful tool that can reveal the formation of radical cations, which often absorb light in the visible region of the electromagnetic spectrum.[109,126]

Thin films of HTMs **1** – **3** and **Spiro-OMeTAD** were prepared by solution spin coating in order to study the absorption behaviour upon addition of **LiTFSI**. Portions of **LiTFSI** solution were added into the spin coating solution between depositions in order to obtain a range of oxidation levels across the dataset. Detailed procedures for preparation and spin coating are given in Section 3.2.1. The resulting changes in the UV-Visible absorption spectra of HTM **1** and **Spiro-OMeTAD** are shown in Figure 3-1. **Spiro-OMeTAD** films show an absorbance maximum at λ_{max} = 386 nm, and after ageing for one week in a dessicator display the growth of a new peak at λ = 525 nm assigned to the oxidised species, in this case **Spiro^{+}TFSI^{-}**.[35] HTM **1** shows similar growth of a new absorption peak with increasing **LiTFSI** at 760 nm. Additionally, a gradual bathochromic shift of up to 30 nm is observed in its main absorption peak originally at 400 nm. This red shift is not observed when **FK209** is used as the oxidising additive (Chapter 2, Figure 2-17) although the peak from the oxidised species is seen growing at the same wavelength.

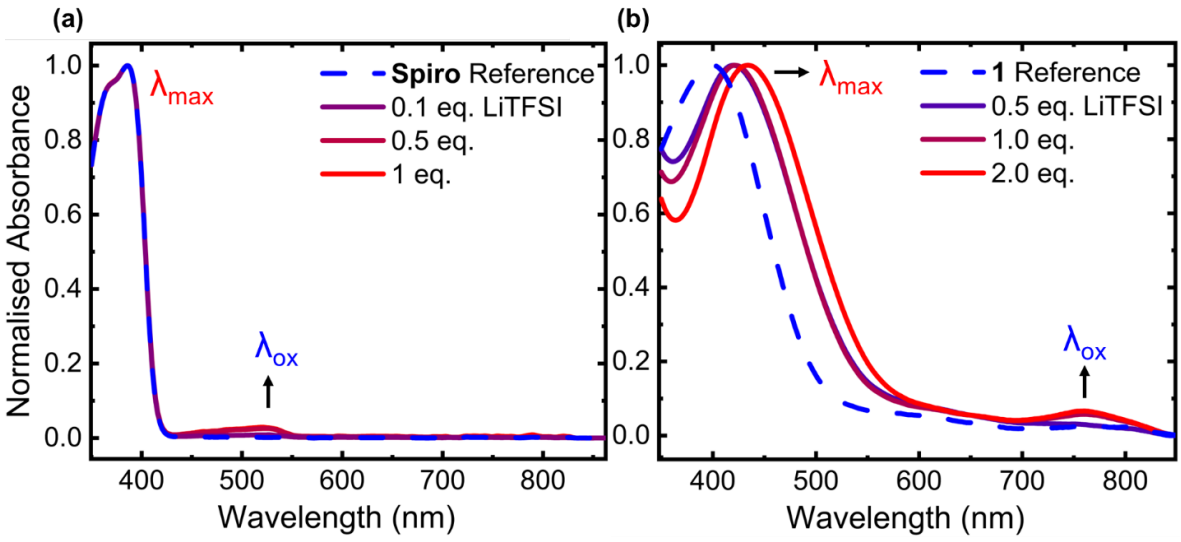

Figure 3-1: Film UV-Visible absorption spectra of (a) **Spiro-OMeTAD** and (b) HTM **1** films with increasing concentration of **LiTFSI**, after curing in a dessicator for 1 week. All spectra normalised to λ_{max}.

This combination of features points towards two phenomena happening simultaneously as the lithium content increases. The bathochromic shift arises from coordination of lithium by the carbonyl group, shifting electron density away from the carbonyl bond resulting in a shift to longer absorption wavelengths for the n-π* transition.[54] The new peak growing at 760 nm is assigned to the oxidised $HTM^{+}TFSI^{-}$ species, and as with **Spiro-OMeTAD**, the strength of this absorption is directly related to the degree of oxidation.

The coordination of C=O bonds to lithium can also be directly observed through FTIR spectroscopy, since the interaction causes a reduction in double-bond character for the carbonyl group, resulting in a shift to shorter wavenumbers. Dry powders were prepared for FTIR spectroscopy by removing the solvent from the solutions of HTM **1** + **LiTFSI** using a rotary evaporator. The resulting FTIR spectra are shown in Figure 3-2. The characteristic carbonyl C=O stretching vibration observed at 1662 cm^{-1} splits into two vibrations (Figure 3-2). A new vibration at 1652 cm^{-1} is ascribed to the coordinated C=O---Li stretch. As each molecule of HTM **1** has two carbonyl groups, the majority remain uncoordinated at 0.5 equivalents of **LiTFSI** and thus, the original $\nu_{C=O}$ peak dominates. At 1 equivalent of lithium, around half the carbonyl groups are now coordinated to lithium ions explaining the near 1:1 peak ratio between the coordinated and uncoordinated carbonyl signals. Increasing the lithium content to 2 equivalents leaves very few uncoordinated carbonyl groups and so the original $\nu_{C=O}$ signal is significantly reduced. A broad signal at 1635 cm^{-1} appears from **LiTFSI** itself.

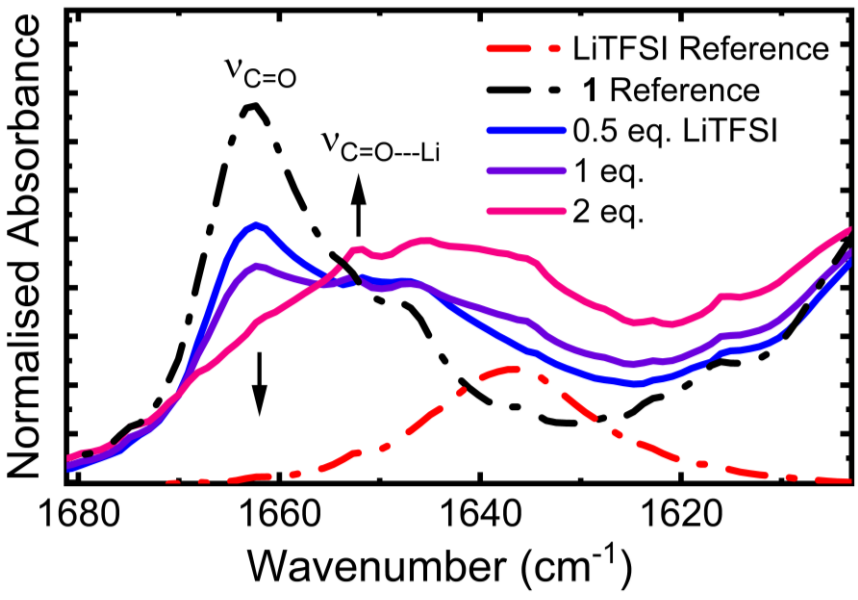

Figure 3-2: Stacked powder FTIR spectra of HTM **1** doped with increasing amounts of **LiTFSI**, showing the diminishing of the original carbonyl peak and the growth of the coordinated carbonyl peak.

The interactions between the carbonyl groups of HTM **1** with lithium ions has been observed in the literature, but no information was given about its role in the doping mechanism.[54] Here, it is further demonstrated that coordination is a separate mechanism to oxidation, as the addition of **LiTFSI** to compound **1** causes an immediate colour change in the spin coating solution while the solutions are still in a N_2-filled glove box. This shows that the mechanism behind the colour change is oxygen-independent. Indeed, UV-Visible absorption spectra of the same films measured directly after spin coating (without allowing to oxidise in a dessicator) show the characteristic bathochromic shift due to coordination, with no growth of the oxidised peak (Figure 3-3).

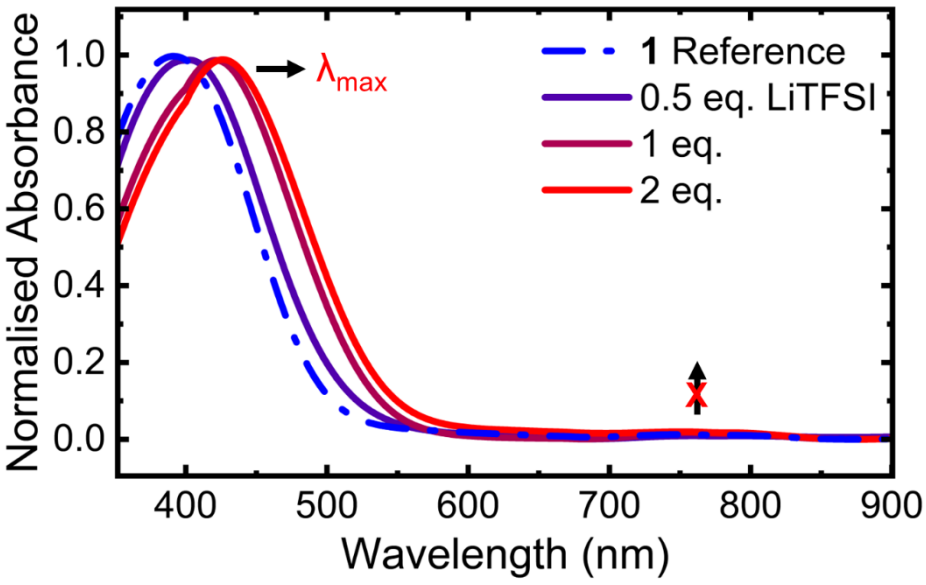

Figure 3-3: Film UV-Visible absorption spectra of HTM **1** with increasing **LiTFSI**, measured immediately after spin coating with no oxidation step. Spectra normalised to λ_{max}.

It is clear from the above results that the interaction of lithium ions with the carbonyl groups can proceed spontaneously, and independent of oxidation. However, a key question remains unanswered: what role, if any, does this coordination play in the oxidation mechanism? The interaction of lithium ions with the carbonyl groups could either positively or negatively affect doping: if the interaction is strong enough to sequester lithium ions away from the HOMO, then the reaction is hindered, and the equilibrium is not shifted towards more HTM^+. Alternatively, participation of lithium ions in a reversible coordination to the carbonyl groups could increase the effective concentration of lithium ions around the HOMO on the TPA moieties and enhance the likelihood of successful ionisation. This is investigated in the forthcoming sections in order to paint a full picture of the oxidation mechanism.

3.2.2 Modulating lithium coordination through complexation

As lithium ions have one 2s and three 2p orbitals available for accepting electrons,[112] their capacity for further coordination may be hindered by introducing a crown ether into the additive solution. 12-crown-4 ether (**12-C-4**) in the **LiTFSI** solution readily acts as a Li^+ ionophore, forming four coordinative bonds with the ions. Crowning lithium ions in this way was recently introduced by Shen, *et al*. to reduce the hygroscopicity of lithium-doped HTLs. The researchers demonstrated that the crowned lithium complex still effectively transfers charge to **Spiro-OMeTAD**, retaining all of the oxidative properties of pure **LiTFSI**.[51] Doping and increased conductivity were still achieved, but the formation of the hygroscopic salts was hindered due to Li^+ ions being trapped within the crowned complex.

The methodology from this study provides the framework for testing the lithium coordination hypothesis. In this regard, the oxidative reactions leading to HTM^+ can proceed while the interactions between Li^+ and the carbonyl groups have been selectively blocked. Three solutions of HTM **1** were thus prepared: a 'Reference' solution of pristine HTM **1**; a 'Control' solution containing HTM **1** with 2 equivalents of **LiTFSI**; and a 'Target' solution containing a similar amount of **LiTFSI** with 1.2 Li-equivalents of 12-C-4. This stoichiometry ensures that all Li^+ ions in the additive solution are fully entrapped in crown ether complexes.

Through UV-visible spectroscopy of the thin films, a complete blocking of C=O---Li coordination is seen, resulting in a lack of red shift in the main absorption peak (Figure 3-4a). This coincides with no growth of the oxidised species characteristics as previously observed at 760 nm even after leaving the samples for a week in a dessicator. This disruption of the oxidation reaction scales inversely with the fraction of crown ether in the **LiTFSI** solution (Figure 3-4b). No $\nu_{C=O}$ peak splitting is observed in the FTIR spectrum (Figure 3-4c).

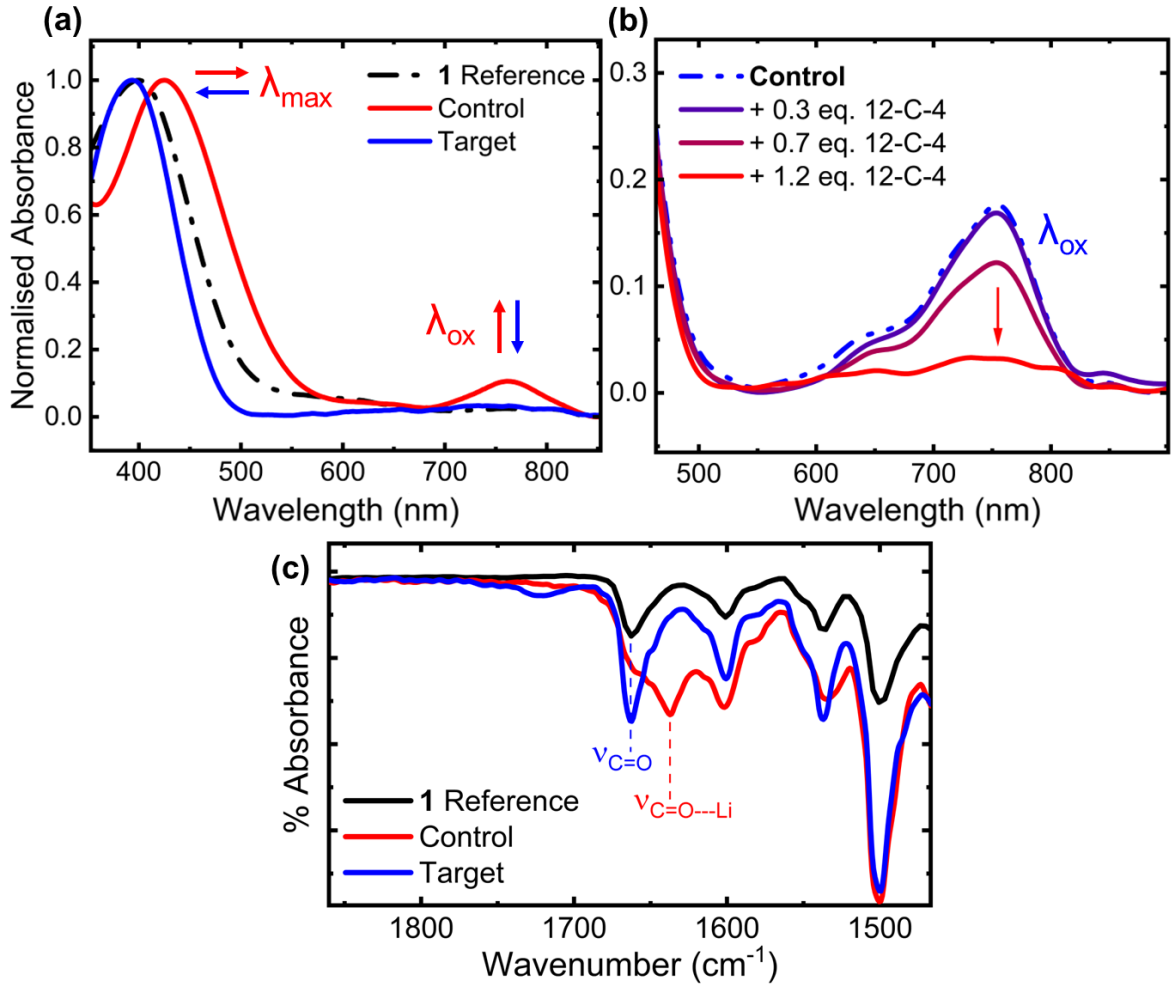

Figure 3-4: (a) Film UV-Visible absorption study of the three solutions of compound **1**. (b) Partial film UV-Visible absorption spectrum of HTM **1** + 2 eq. of **LiTFSI**, with increasing 12-C-4 content in the **LiTFSI** solution. Spectra in (a) and (b) were normalised by setting λ_{max} to 1. (c) Powder FTIR spectra recorded from the Reference, Control, and Target residues left after evaporation of the solvent. See Methodology Section 3.5.2 for experimental details.

A progressive decrease in conductivity is seen upon increasing the 12-C-4 content in the **LiTFSI** solution, as a result of hindered doping (Figure 3-5). These results provide conclusive evidence that the coordination of lithium by the carbonyl groups on the HTM molecules catalyses the doping reaction. While coordination is not itself an oxidative process (Figure 3-3), it appears to positively benefit the doping characteristics of HTM **1**. The spectroscopic and conductivity evidence shown above validate the hypothesis that coordination brings Li^+ close to the HOMO, where a positive charge can be then transferred to the HTM molecule. Preventing this coordination decreases the effective concentration of oxidising species around the HOMO, completely hindering the doping.

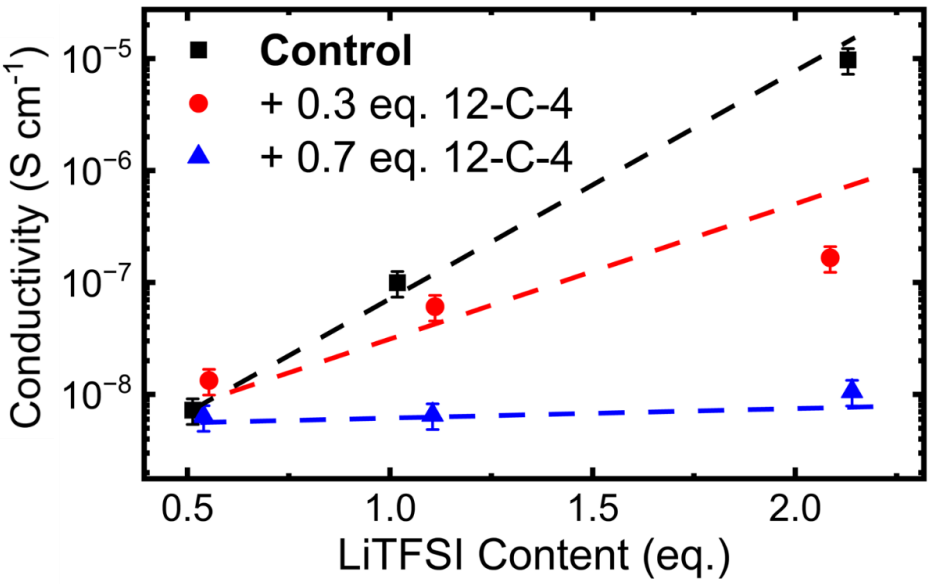

Figure 3-5: HTM **1** film conductivity measured at various **LiTFSI** loadings, varying the amount of crown ether in the additive solution, showing a downward trend in conductivity for similar Li^+ concentrations with increasing 12-C-4. See Tables 3-4 – 3-6 for experimental details. Error bars represent the propagated error calculated from the derived equation in Section 5.3.5. Dotted lines serve only as a guide to the eye.

A mechanism for **LiTFSI** oxidation of HTM **1**, which summarises these observations, is presented in Scheme 3-2.

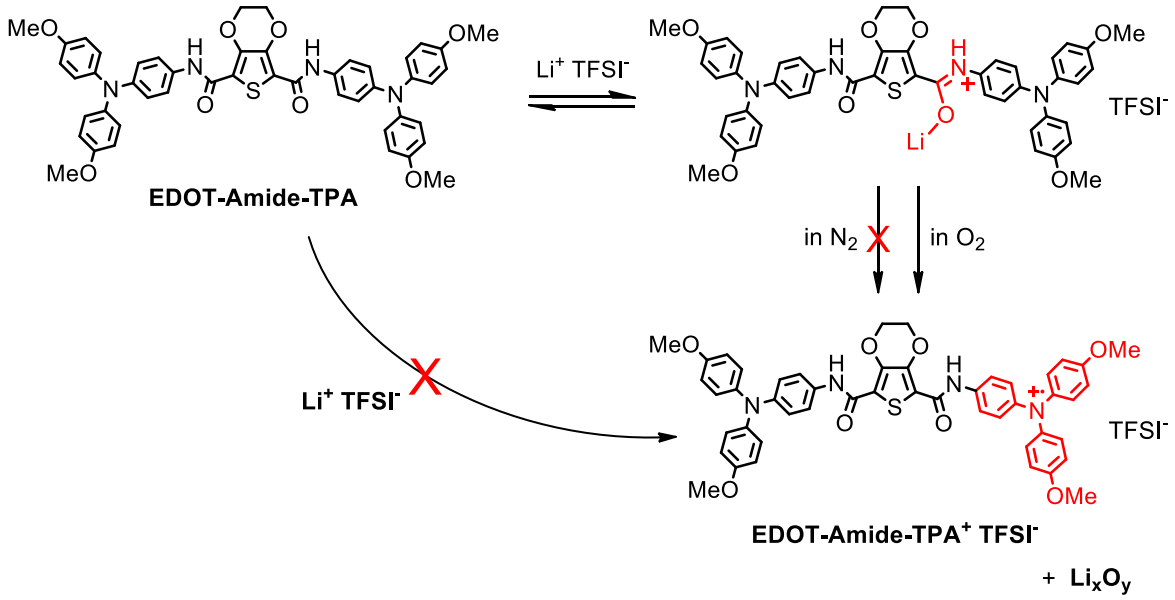

Scheme 3-2: Proposed **LiTFSI** doping mechanism for HTM **1** which summarises the spectroscopy and conductivity results.

The proposed mechanism is similar to that for **Spiro-OMeTAD**, but requires the formation of the coordinated intermediate before progressing to the oxidised HTM^+TFSI^- state. The fate of the lithium ions is likely to be identical, forming the hygroscopic lithium oxides at the end of the reaction.[35] This does not rule out the possibility that the oxidised HTM may also still have lithium ions coordinated to it.

Indeed, the red shift in the main absorption peak arising from Li^+ coordination is stable over long periods of time, even after suitable conductivity is achieved in the doped film. As each HTM molecule possesses two amide bonds and two TPA moieties, a film of HTM **1** treated with **LiTFSI** is likely to contain the HTM in myriad states such as: neutral + uncoordinated; neutral + coordinated; oxidised + uncoordinated; and oxidised + coordinated. The absorption spectrum of a particular film will therefore contain features from a mixture of these possible states.

3.2.3 Rationalising dissimilar amide reactivity

Having illustrated the deleterious effects of hindering coordination on the doping from the additive end, it follows that the oxidation of TPA-based HTMs possessing nearby carbonyl groups could benefit from stronger interactions between C=O and Li^+. A greater propensity towards coordination increases the likelihood of a successful reaction between the additive and the HTM. This can be achieved through chemical modification of the amide bond, which can be used to modulate the nucleophilicity of the carbonyl group.

In Chapter 2, two analogues of HTM **1** were introduced in HTMs **2** and **3**, which have different bonding environments around the amide linkers. HTM **2** possesses tertiary amide groups, which should render the carbonyl group more nucleophilic than that of HTM **1** due to the electron-donating methyl groups. HTM **3** has secondary amides linkers akin to those in HTM **1**, but with different hydrogen bonding environments that also affect the electron density of the carbonyl groups. As it has been determined that lithium coordination at the amide carbonyl groups is an essential step towards doping, electrostatic potential (**ESP**) maps were calculated from the DFT-optimised structures of the amide HTMs to probe the electron density around the carbonyl groups. In the interest of computational efficiency and accuracy, the B3LYP functional was chosen to optimise the structures. By using this functional with the 6-311G** basis set, convergence was rapidly obtained for the three structures. From these optimised structures the electrostatic potential maps could then be easily calculated. The predicted structures from these calculations closely match those obtained by the PBE0/def2-sv(p) method, thus the B3LYP functional was deemed to be suitable for the rest of the analysis detailed herein.

As expected, the carbonyl group of compound **2** shows the most concentrated electron density around the C=O groups across the series (Figure 3-6c). HTM **3** shows reduced electron density on the carbonyl group involved in an intramolecular hydrogen bond, due to sharing of electron density with the opposite N-H group. The free carbonyl group on HTM **3** is thus expected to be the main coordinating moiety on this molecule.

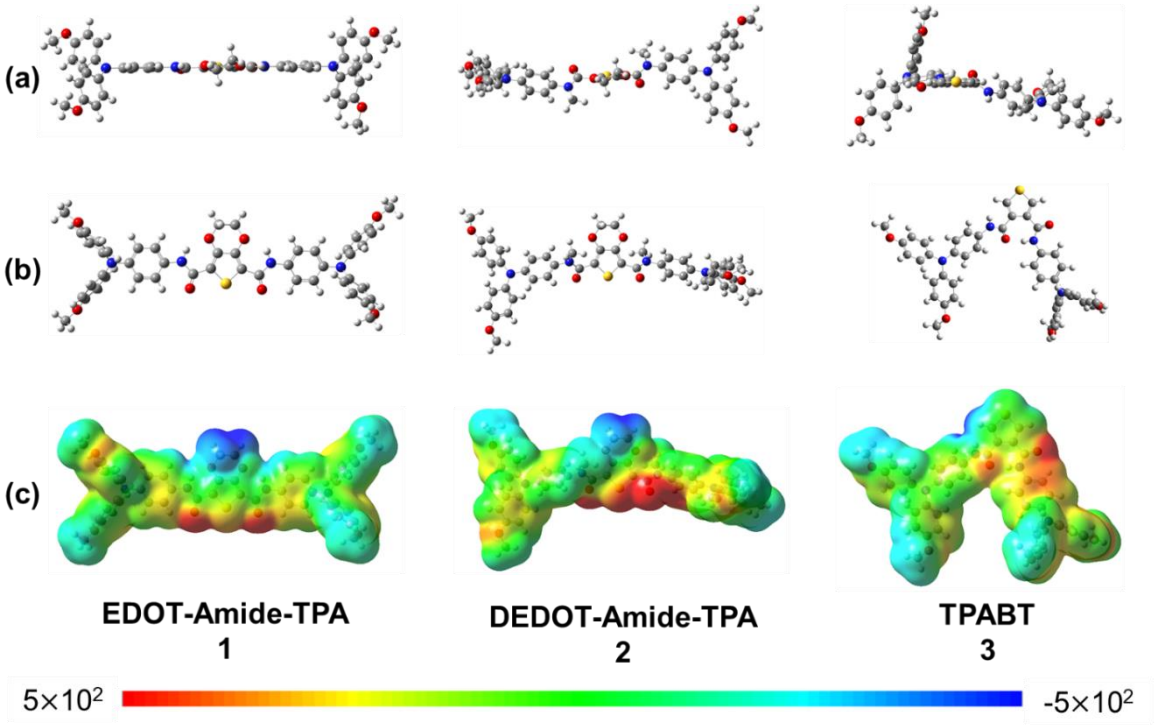

Figure 3-6: (a) top view, (b) side-view structures of B3LYP 6-311G** optimised amide HTMs. (c) electrostatic potential maps generated from the optimised structures.

The suitability of an oxidising additive towards a particular HTM system is tied to their reactivities towards each other. As Figure 3-7 shows, the film UV-visible absorption profile of HTM **2** remains nearly unchanged upon adding **LiTFSI**, in stark contrast to the behaviour of HTM **1** (Figure 3-1b). The very slight growth of a peak from the oxidation product was only seen once the films were redissolved into a dichloromethane solution after two weeks in an oxygen-rich environment (Figure 3-7b).

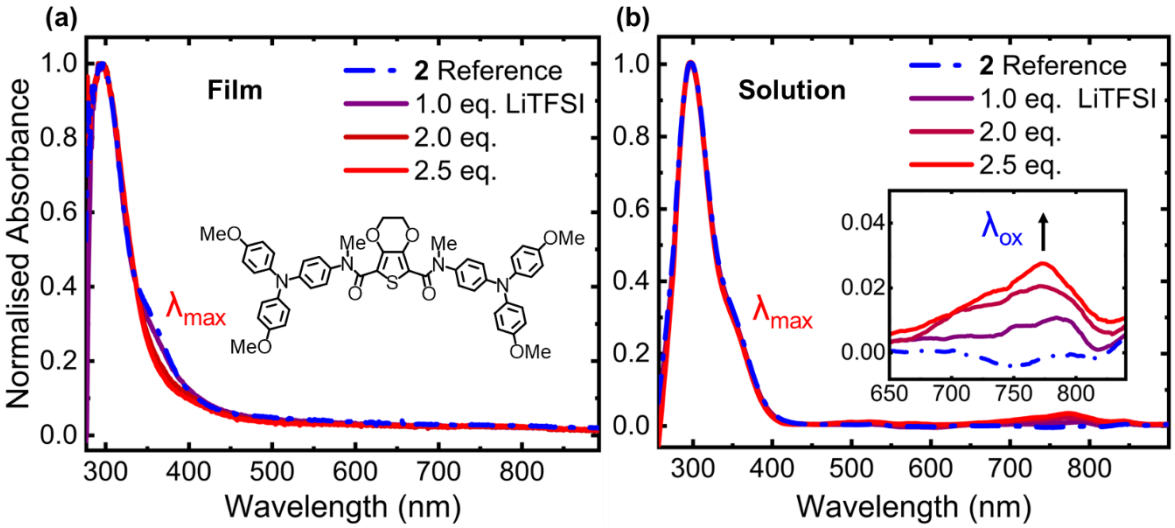

Figure 3-7: UV-Visible absorption spectra of HTM **2** with increasing concentrations of **LiTFSI** (a) in thin films; (b) redissolved in dichloromethane solution. All spectra normalised to the most intense peak at 300 nm, which was set to 1. See Table 3-2 for experimental details.

The spectra above point towards greatly reduced oxidation efficiency for HTM **2** compared to HTM **1**. The peak arising from the oxidation product of HTM **2** has insufficient signal-to-noise ratio to be visible in the film UV-Visible spectrum, requiring the increased path length of the solution measurement to be observed. The unchanged absorption maximum also indicates that carbonyl coordination does not occur in HTM **2** as with its parent HTM **1**. In the case of HTM **3**, the oxidised HTM peak grows in the film UV as before, and a bathochromic shift is observed in the main absorption profile indicating lithium coordination, although this is less intense than in the case of HTM **1**. (Figure 3-8).

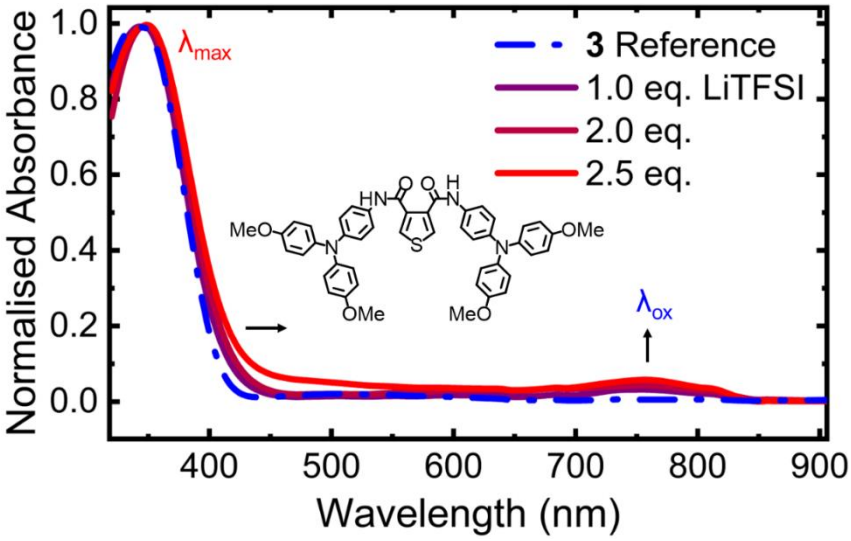

Figure 3-8: Film UV-Visible absorption spectra of HTM **3** doped with increasing amounts of HTM **3**. All spectra were normalised by setting λ_{max} to 1. See Table 3-2 for experimental details.

These spectroscopic results are reflected in the thin-film conductivities of the three amide materials, displayed in Figure 3-9 below. Identical conductivities are observed across the **LiTFSI** concentration range for HTMs **1** and **3**, and significantly reduced conductivity for HTM **2** by up to three orders of magnitude. This surprising result challenges the “one-size-fits-all” approach towards chemical doping that is routinely employed in the literature. Common additives such as **LiTFSI** clearly have widely varying reactivity, even between species of similar molecular structure. This can lead to discrepancies in the actual degree of oxidation with the same amount of oxidant added to different HTM solutions, which introduces errors when comparing the oxidation behaviour of different HTMs.

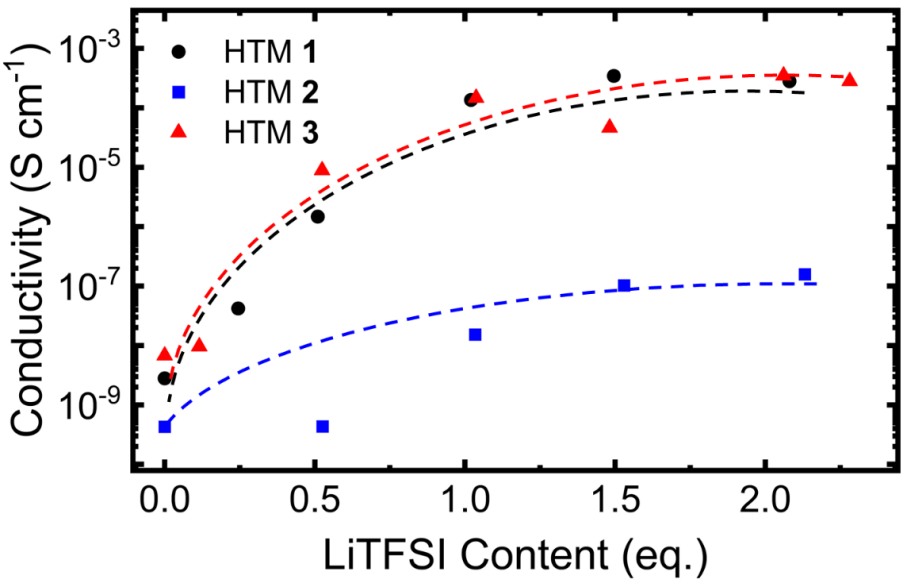

Figure 3-9: Film conductivities of HTMs **1 – 3** with increasing **LiTFSI**, showing the drastic drop in conductivity across the range for HTM **2** compared to HTMs **1** and **3**. See Table 3-2 for experimental details. Error bars were calculated through propagating the error as described in Section 5.3.5, but were removed from this graph for clarity, as they are completely hidden behind the point markers. Dotted lines added only as a guide to the eye – there are no significant differences in conductivity between HTMs **1** and **3**.

Similar conductivity data for HTMs **1 - 3** were presented in Chapter 2, where **FK209** was used as the oxidant. In the case of **FK209** oxidation, only one order of magnitude drop in conductivity was observed HTM **2** compared to HTM **1**, which was determined to arise from dipole disorder in the film (Chapter 2, Figure 2-19). The **LiTFSI** system presented in this chapter (Figure 3-9) therefore leaves two orders of magnitude in conductivity drop unaccounted for between HTMs **1** and **2**, which is likely to arise from these differing interactions with lithium ions.

The counterintuitive results obtained from HTM **2** + **LiTFSI** suggest that the coordination itself is not the deciding factor in the doping mechanism. Rather, the difference lies within the stability of the reaction product. The coordination of lithium through the carbonyl group causes a shift in the electron density around the whole amide bond, decreasing the double bond character for the C=O bond and increasing double bond character for the C-N bond. These changes are reflected in the infrared and UV-visible spectral properties of the amide bond as seen in Figures 3-1, 3-2, 3-3, and in various publications in the literature.[54,127] The positive charge from the lithium cation is transferred onto the amide nitrogen, forming an iminium cation. It follows that the stability of the coordinated amide is dependent on the stabilisation of the positive charge. The N-H proton is rendered more acidic by this coordination, which in the case of HTMs **1** and **3** strengthens the pre-existing intramolecular hydrogen bonds, thus contributing to the delocalisation of positive charge.

This stabilises the coordinated species, allowing it to act as an intermediate for successful oxidation of the HOMO in contrast to HTM **2**, where there are no internal hydrogen bonds available to delocalise charge (Figure 3-10).[128]

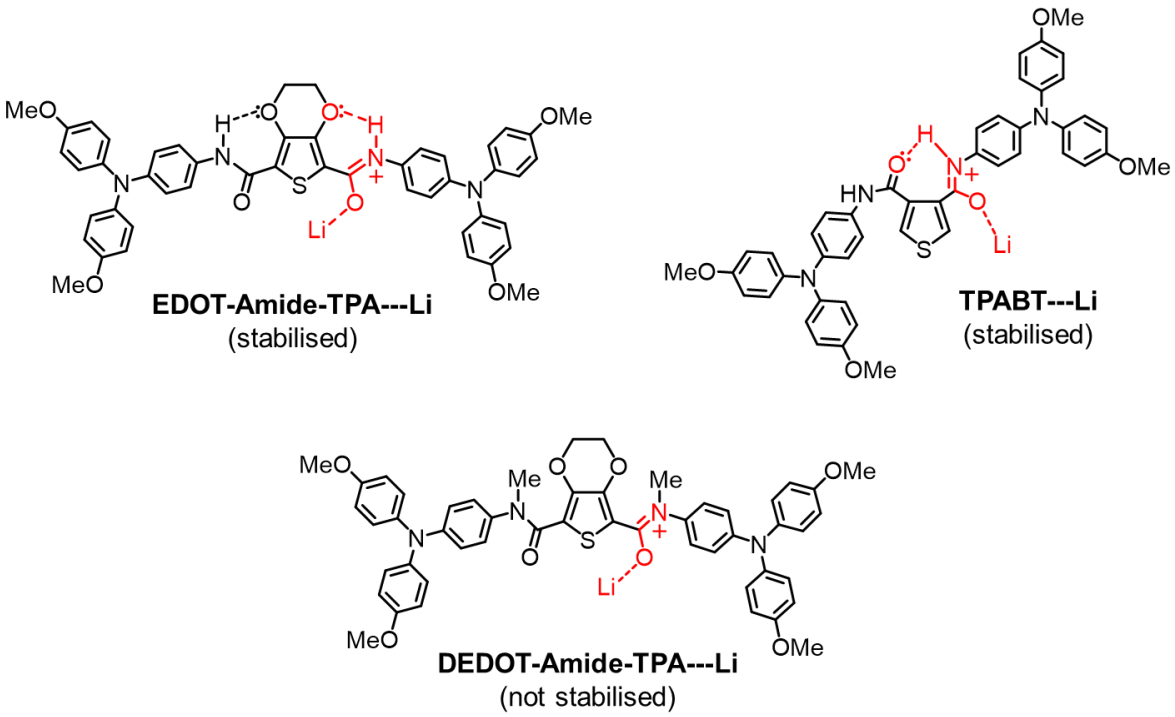

Figure 3-10: Schematic of coordinated amide species, showing the formed iminium cation and presence or absence of stabilising hydrogen bonds.

Resonance stabilisation may also contribute to the stability of the coordinated species through delocalisation of the positive charge across an extended π-system. The planarity of the amide bonds in HTMs **1** and **3** provide favourable orbital overlap with the adjacent aromatic rings for resonance stabilisation. Further DFT investigation on the optimised coordinated structures depicted in Figure 3-10 above reveals that the planar core of HTM **1**, afforded by strong intramolecular hydrogen bonds, persists upon lithium coordination (Figure 3-11). Performing the same analysis on HTM **3** reveals that in this case, the coordination twists the adjacent TPA phenyl ring out of plane. Resonance stabilisation may still be possible through delocalisation onto the thiophene core. In HTM **2**, both amide bonds are already twisted out of plane from the adjacent aromatic systems, leading to minimal contribution from resonance.

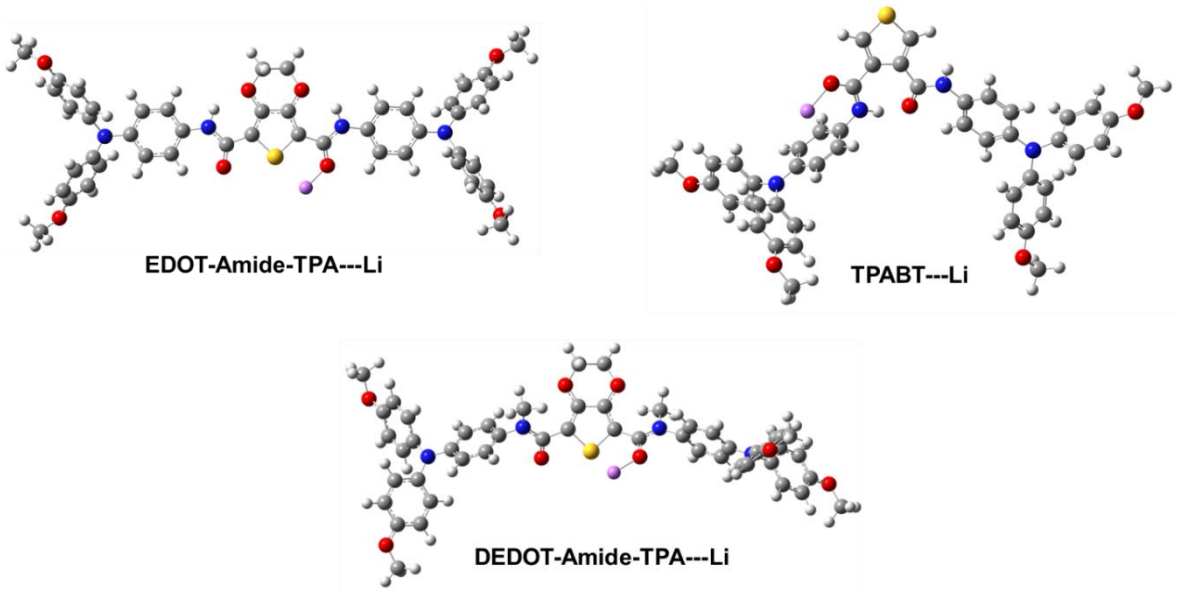

Figure 3-11: DFT-optimised structures (B3LYP 6-311G** level) of the three amide HTMs coordinated to a lithium cation.

The discussion above may explain the observed trend in the bathochromic shifts of the absorption maxima in Figures 3-1, 3-7, and 3-8, wherein the strongest shift is seen with HTM **1** due to the possibility of forming stable iminium cations. HTM **3** shows more subtle bathochromic shifts as a result of reduced resonance stabilisation, while HTM **2** shows no red shift due to no resonance or hydrogen bond-assisted stabilisation of the iminium ion. We observe from our conductivity results that the differences between HTMs **1** and **3** have minimal effect on the **LiTFSI** doping efficiency, but the differences in stabilisation are much more pronounced when comparing these two amides to HTM **2**.

3.3 Conclusions

In this chapter, the critical role of reversible lithium coordination to carbonyl groups in the lithium doping mechanism for amide-based HTMs is elucidated. Through the 12-crown-4 study, the ability of a HTM to coordinate with lithium ions in solution was found to significantly impact its doping efficiency. Specifically, it was shown that in systems where coordination did not occur (HTM **2**), doping was hindered at equal dopant loading compared to systems that did coordinate (HTMs **1** and **3**). This highlights the importance of considering the coordination capabilities of HTMs when designing doping strategies for improved conductivity. It was also discovered that the degree of coordination does not directly correlate with conductivity enhancement, as despite HTM **1** exhibiting a higher degree of coordination compared to HTM **3**, identical conductivity levels were achieved by both HTMs.

Interestingly, a counterintuitive observation was revealed by the study, wherein despite HTM **2** having increased electron density around the carbonyl group, the HTM resists coordination with lithium ions, hindering the doping thus resulting in lower conductivity. This phenomenon was attributed to the instability of the resulting iminium cation, which lacks stabilisation through hydrogen bonding or resonance. As there is no thermodynamic driving force for the formation of the coordinated species, lithium ions are more likely to remain uncoordinated in solution, and oxidation of the HOMO is less efficient.

These findings underscore the intricate relationship between the chemical structures and reactivity of dopants and HTMs. The insights detailed in this chapter contribute to a deeper understanding of the factors governing HTM-dopant interactions, providing a sound basis for more rational design of effective dopant-HTM pairs.

3.4 Methodology

3.4.1 **LiTFSI** oxidation of amide HTM films

To prepare films of HTMs **1** – **3** at different loadings of **LiTFSI** for the discussion in Section 3.2.1, a series of solutions at the same concentration were prepared through HTM stock solutions of known HTM and solvent masses, similarly to previous procedures reported above. For HTMs **1** and **3**, solutions were prepared in mixtures of chloroform CF and CB, while HTM **2** was prepared in pure CB due to its increased solubility. Due to the low solubility of HTM **1**, the solution was kept in a sealed vial, heated on a hot plate at 70°C for the duration of the experiments to prevent precipitation prior to and during spin coating. All **LiTFSI** solutions were prepared in acetonitrile (**ACN**). **LiTFSI** stock was prepared at sufficiently high concentration to ensure that the concentration of the HTM stock is not significantly affected after the addition of the dopant solution. Relevant measurements are summarised in Table 3-1:

Table 3-1: Measurements for the stock solutions prepared for **LiTFSI** oxidation of the three amide HTMs.

Stock solution:	**Species Mass**	**Solvents**	**Concentration**
LiTFSI	66 mg	666.3 mg ACN	271 mM
HTM 1	16.2 mg	503.8 mg CB 1601.7 mg CF	12.7 mM
HTM 2	9.9 mg	1019.3 mg CB	12.5 mM
HTM 3	18.6 mg	1114.3 mg CB 960.7 mg CF	14.5 mM

The combined volume of solvent was estimated using the solvent densities, and was then used to estimate the concentration of the HTM solutions. Portions of known mass were then dispensed from the stock solutions into separate vials. Different quantities of **LiTFSI** were then added to each vial to initiate the doping reactions. All relevant measurements are summarised in Table 3-2:

Table 3-2: Additive loading calculations for thin-film conductivity and UV-Visible absorption measurements of amide HTMs **1** - **3**.

HTM 1					
Condition Label:	**E1**	**E2**	**E3**	**E4**	**E5**
Mass of Stock (mg)	122.3	141.5	162.6	131	148.9
LiTFSI added (µL)	1	2.5	5.7	8.2	9.3
…in equivalents:	**0.2**	**0.5**	**1**	**1.5**	**2.1**
HTM 2					
Condition Label:	**D1**	**D2**	**D3**	**D4**	
Mass of Stock (mg)	161.2	140.9	140.6	141.2	
LiTFSI added (µL)	3.6	6.1	9	12.5	
…in equivalents:	**0.5**	**1**	**1.5**	**2.1**	
HTM 3					
Condition Label:	**T1**	**T2**	**T3**	**T4**	**T5**
Mass of Stock (mg)	137.5	153.8	145.6	122.9	150.4
LiTFSI added (µL)	0.7	3.4	6.5	9.2	10.8
…in equivalents:	**0.1**	**0.5**	**1**	**1.5**	**2.1**

Thin films were spin coated onto patterned ITO slides for conductivity measurements, and onto glass slides for UV-Visible absorption spectroscopy as well as film thickness measurements. 50 µL of solution from each condition was dropped onto a glass or ITO slide using a micropipette. Spin coating was then performed through a static method, at a speed of 1000 rpm for 10 seconds, followed by 5000 rpm for 5 seconds to remove traces of solvent from the edge of the spinning slides. The resulting films were visually inspected to ensure even film formation. UV-Visible absorption spectra were measured immediately after spin coating to obtain the absorption profiles prior to **LiTFSI** oxidation. These spectra are given for HTM **1** in Figure 3-3. After this, the films were left in a dessicator for one week, to allow for the oxygen-mediated oxidation of the HTMs. The UV-Visible absorption spectra of the thin films were again recorded and these are given for **Spiro-OMeTAD** and HTMs **1** – **3** in Figures 3-1, 3-7, and 3-8. The JV-characteristics of each condition were measured, and the conductivities were obtained. The error bars in the graph are the propagated error which was calculated according to Equation 5-20 derived in Section 5.3.5.

Film thicknesses were measured across each HTM doping series by etching a valley into the film on a glass slide using a razor, and measuring the depth of the valley using contact profilometry. The resulting measurements are given in Table 3-3. Averages based off of six measurements per HTM were then calculated, and the standard deviation across these six measurements was used as the error from the thickness measurements.

Table 3-3: Measured film thicknesses for the thin films deposited for UV absorption and conductivity measurements, including the calculated average thicknesses and the standard deviation used in the calculations.

	Film thickness (nm)		
	1	**2**	**3**
	-71.71388	-58.76619	-64.3725
	-83.34136	-70.8554	-79.30499
	-76.01843	-69.00322	-80.11068
	-74.67593	-64.78846	-76.02513
	-78.28288	-79.97846	-83.94522
	-64.55795	-83.22385	-65.05112
Average (nm)	**75.38**	**71.10**	**74.80**
Standard Deviation (nm)	**6.16**	**8.39**	**7.50**

In order to obtain dry powders of doped HTM **1** for FTIR spectroscopy, the doped solutions prepared above were placed into a vacuum tube and attached to a rotary evaporator to remove the solvent. Once solvent was removed, further drying was achieved by placing the vials in a vacuum oven at 50 °C for 4 hours. The dried powder could then be retrieved from the vials using a spatula. FTIR was performed on these powders without any further processing, and the FTIR spectra are given in Figure 3-2.

3.4.2 Li-12-crown-4 complex studies

In order to prepare the 12-C-4 ether complex of **LiTFSI** for Section 3.2.2, solutions of **LiTFSI** were prepared in acetonitrile, with different fractions of 12-C-4 ether added to the solution prior to adding to vials of HTM **1**. Stock solutions were prepared and split as described in Tables 3-3 and 3-5. This created a matrix of three **LiTFSI** loading concentrations with four loadings each of 12-C-4 in the additive solution.

Table 3-4: Measurements for the HTM and **LiTFSI** stock solutions prepared for the crown ether experiment.

Stock solution:	**Species Mass**	**Solvents**	**Concentration**
LiTFSI (L0)	105.9 mg	1537.6 mg ACN	189 mM
HTM **1**	29.8 mg	1018.1 mg CB 2829.9 mg CF	12.7 mM

Table 3-5: Preparation of crowned **LiTFSI** solutions.

Solution Label:	**L1**	**L2**	**L3**
Mass of L0 Stock (mg)	339.3	342.8	339.6
12-C-4 added (mg)	4.1	10.2	17.2
12-C-4 fraction (eq.)	**0.3**	**0.7**	**1.2**

Table 3-6: Table of numbers for preparation of solutions of HTM **1** using the four **LiTFSI**-12-C-4 vials.

Label:	**E1**	**E2**	**E3**	
Mass of HTM Stock (mg)	219.8	332.0	335.0	0 eq.
L0 added (µL)	5.5	16.5	35	12-C-4
…in equivalents of Li	**0.5**	**1.0**	**2.1**	
Label:	**E4**	**E5**	**E6**	
Mass of HTM Stock (mg)	339.4	338.0	342.1	0.3 eq.
L1 added (µL)	8.5	17	35	12-C-4
…in equivalents of Li	**0.5**	**1.0**	**2.1**	
Label:	**E7**	**E8**	**E9**	
Mass of HTM Stock (mg)	347.8	340.0	333.5	0.7 eq.
L2 added (µL)	9	17	33	12-C-4
…in equivalents of Li	**0.5**	**1.0**	**2.0**	
Label:	**E10**	**E11**	**E12**	
Mass of HTM Stock (mg)	334.0	339.8	342.1	1.2 eq.
L3 added (µL)	8.5	17	35	12-C-4
…in equivalents of Li	**0.5**	**1.0**	**2.1**	

The JV-characteristics of each condition were measured, and the conductivities were obtained. The error bars in the graph are the propagated error which was calculated according to Equation 5-20 derived in Section 5.3.5. Film thicknesses were measured across the 12-C-4 loading series by etching a valley into the glass slide using a razor, and measuring the depth of the valley using contact profilometry. The resulting measurements are given in Table 3-7. The calculated average and standard deviation were then used in the conductivity calculation.

Table 3-7: Measured film thicknesses for the thin films deposited for UV absorption and conductivity measurements, including the calculated average thicknesses and the standard deviation used in the calculations.

	Film thicknesses (nm)	
	-55.24794	-119.79579
	-65.23819	-126.50604
	-79.18128	-73.07059
	-83.52474	-53.91268
	-82.62107	-84.48886
	-100.23528	-104.98275
	-139.90218	-81.82728
	-108.37639	-105.55782
	-113.26798	-88.12734
Average (nm)	**92.55**	
Standard Deviation (nm)	**23.30**	

4 Investigation into the oxidation characteristics of isomeric imine HTMs

The contents of this chapter are in the process of being prepared for publication as an article provisionally titled: “The role of structural isomerism in the properties of imine-based organic hole-transporting materials”

4.1 Introduction

In Chapters 2 and 3, the importance of smart molecular design for new HTMs was demonstrated, emphasising the importance of low energetic disorder in a HTM film as well as an understanding of the materials’ reactivity with selected dopants. The utility of condensation chemistry as a route towards low-cost HTMs was also highlighted through the three amide HTMs. The analogous Schiff base condensation is an equally good candidate for creating a new generation of economical HTMs, with **EDOT-OMeTPA** being an exemplar of this approach.[58]

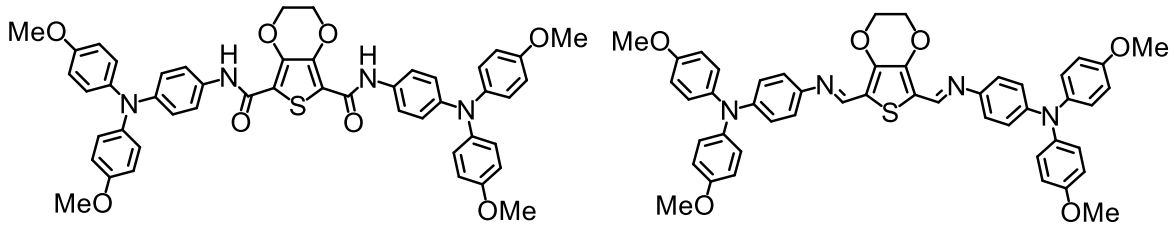

EDOT-Amide-TPA **EDOT-OMeTPA**

Figure 4-1: Structures of the amide-based HTM **1** (left) and the imine-based **EDOT-OMeTPA** (right).

EDOT-OMeTPA is the imine analogue of HTM **1**, with one key difference: the imine bond allows for extended conjugation through the core of the molecule (Figure 4-1). An extended π-network was initially expected to aid in intermolecular charge transfer, but the improved packing afforded by HTM **1** through hydrogen bonding compensated for a lack of extended conjugation.[54] Nevertheless, condensation chemistry again provides a very simple pathway towards low-cost and greener HTMs, allowing reactions at ambient conditions and very simple purification since water is the only side product. The imine bond created in the final HTM is isoelectronic to the alkene bond, but differs in that it contains an electronegative nitrogen atom which affects the electron distribution over the molecule.

As with many other newly developed HTMs, the conductivity of **EDOT-OMeTPA** and other imine materials can be greatly improved by doping through the action of chemical oxidants.[16,58] In this regard, the complexity and unclear reaction pathways in HTM doping mechanisms have been thoroughly discussed in previous chapters.

With imine-based systems, another degree of complexity is introduced when considering the two possible orientations of the imine bond, as well as its inherent chemical reversibility. **EDOT-OMeTPA** above has imine bond nitrogen bonded to the TPA donor arms ('**N-to-TPA'**), but an alternative system could be developed wherein the imine bond is inverted, with the nitrogen bonded to the **EDOT** core ('**N-to-Core**').

On the surface, this may seem like a trivial change between two isomeric structures. However, Petrus, *et al*. have highlighted the significance of imine bond orientation in a range of HTMs and its impact on the power conversion efficiency (**PCE**) in PSCs (Figure 4-2).[16]

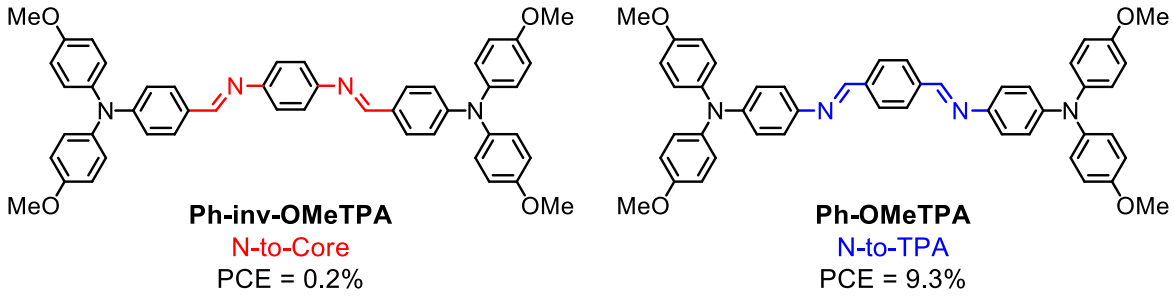

Figure 4-2: Two isomeric imine structures studied in Petrus, *et al*. (2017). The two symmetrical imine bond orientations are illustrated, along with the drastically reduced PCE for the N-to-Core orientation compared to N-to-TPA.[16]

A sharp drop in PCE was seen in devices employing isomeric imine HTMs for N-to-Core orientations compared to N-to-TPA, which was assigned to a significantly lowered HOMO energy for the N-to-Core orientation. This was thought to introduce a hole injection barrier at the perovskite interface, thus high series resistance which limited the short circuit current ($\mathbf{J_{sc}}$) of the device. However, the largest reported changes in HOMO energies calculated from DFT or estimated as IPs from CV between the two HTMs in Figure 4-2 were only around 0.1 eV.[16] A more telling discrepancy was observed in the conductivity of the two HTMs after doping, where an order of magnitude drop in conductivity for the N-to-Core orientation was observed compared to N-to-TPA for the same additive concentration. This points towards differences in the oxidation and doping mechanisms of the two HTMs as the likely factor for the discrepancy seen in PCE. Despite this, a fundamental investigation into how the imine bond orientation affects the reaction between the HTM and the chemical additives is still lacking.

The PCE itself gives no information regarding the 'correct' imine bond orientation, as it is a metric that depends on countless factors other than molecular structure of the HTM. These

include the doping level of the HTM, film and interface quality, energy level alignment, as well as the age of the cell.[21] Furthermore, an unforeseen 'butterfly effect' of small chemical changes to a HTM on its doping efficiency (discussed in Chapter 3) could cause large differences in conductivity between isomeric imine HTMs, potentially contributing to the PCE drop seen in Figure 4-2.

In this chapter, the mechanisms by which the orientation of the imine bond impacts the oxidation mechanisms and conductivity of imine-based HTMs is investigated. By means of two newly synthesised HTMs **Biph-OMeTPA** (HTM **4**, N-to-Core) and **inv-Biph-OMeTPA** (HTM **5**, N-to-TPA), the significant impact of the position of the nitrogen atom in the imine bond is revealed. DFT, UV-Visible absorption spectroscopy and CV reveal significant differences in electron density distribution and oxidation behaviour between the two orientations. Molecular structures of HTMs **4** and **5** are given in Figure 4-3.

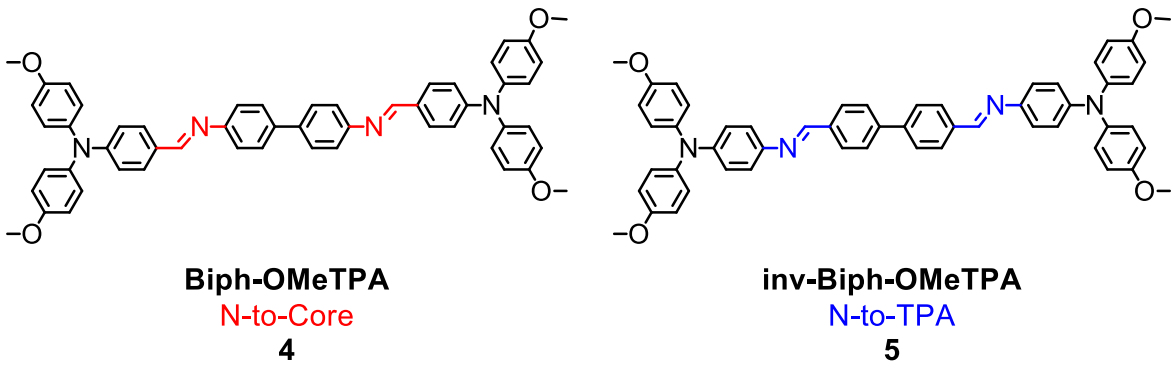

Figure 4-3: Structures of the two imine-based HTMs studied in this chapter.

DFT modelling reveals the enhanced electron density around the biphenyl core of HTM **4**, which may lead to competing oxidation of the biphenyl core when the compound is exposed to chemical oxidants. In order to decouple the effects of the imine bond orientation on the biphenyl core and the TPA arms, four additional model imines were also synthesised (Compounds **6** – **9**, Figure 4-4). Through further CV experiments on the four model compounds, it is revealed that the biphenyl core can undergo irreversible oxidation, independent of the orientation of the imine bond. The oxidation behaviour of the TPA arms is reversible in both cases, with a variation in oxidation potential as a result of the position of the electronegative nitrogen atom.

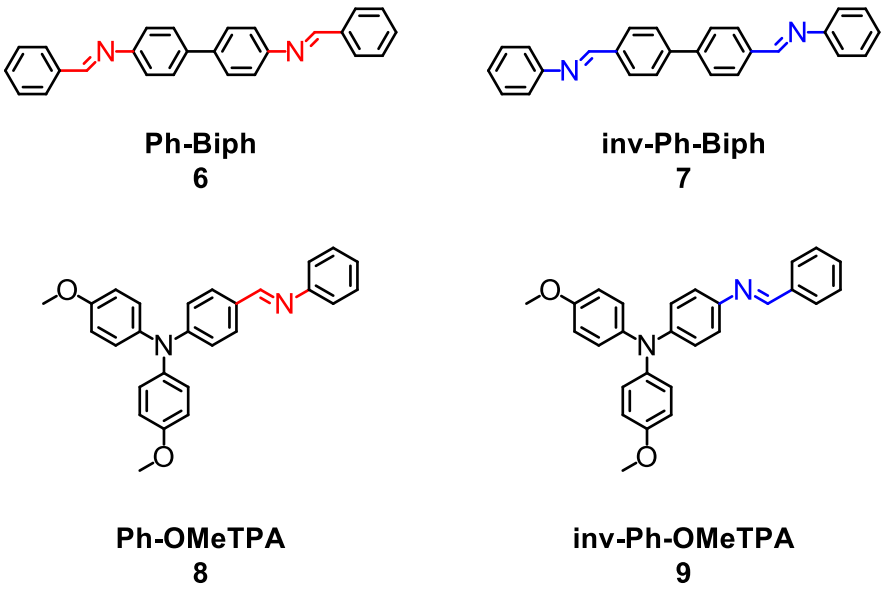

Figure 4-4: Structures of the four model compounds **6 – 9** developed for further electrochemical characterisation.

As one-electron oxidations of organic molecules lead to the creation of unpaired electrons, the resulting ionised species has paramagnetic character. Successful doping reactions can therefore be monitored by spectroscopic techniques such as NMR or electron paramagnetic resonance (**EPR**) techniques. In ^{1}H-NMR spectroscopy, the presence of paramagnetic species causes significant broadening of proton signals due to a hyperfine interaction between the unpaired electrons and the proton nuclei. This broadening can give important information about the system such as the spatial arrangement of protons with respect to the paramagnetic centres, or information regarding delocalisation of unpaired electrons between ligands and metal centres.[129] However, it often complicates the interpretation of NMR data due to the large degree of broadening which can completely hide certain proton signals, thus NMR is only used as a preliminary indication of the presence of paramagnetic species in this thesis. Unpaired electrons in radical species are more definitively probed by techniques such as EPR, wherein the spins of unpaired electrons in a magnetic field are excited through absorption of microwave radiation. For molecular organic radicals, in addition to the external magnetic field, the unpaired electrons interact with the nuclei of the surrounding atoms possessing non-zero spin. This leads to additional hyperfine splitting of the EPR signal that can reveal information about the location of the unpaired electron.[130] Furthermore, the stability of the radical can be qualitatively determined by monitoring the time taken for the EPR signal to decay to zero.

NMR and EPR measurements on samples of HTMs **4** and **5** oxidised with **AgTFSI** further demonstrate that the chemical oxidation of HTM **4** does not generate appreciable hole concentration for improved conductivity. HTM **5**, on the other hand, is able to form stable and mobile holes which can contribute to orders of magnitude improvements in conductivity within a film.

This research therefore further stresses the importance of structure-function relationships in HTM design. Much like the amide HTMs discussed in previous chapters, even miniscule changes on the HTM structure can lead to large ramifications on the charge transport properties of OSs, that can render them unusable as HTMs.

4.2 Results and Discussion

4.2.1 Synthesis

The two imine HTMs **4** and **5**, were prepared through simple condensation reactions using cheap building blocks that were either easy to prepare according to published literature, or otherwise commercially available (Scheme 4-1). Here, HTM **4** was prepared by Dr. Dylan Wilkinson of the Cooke group.

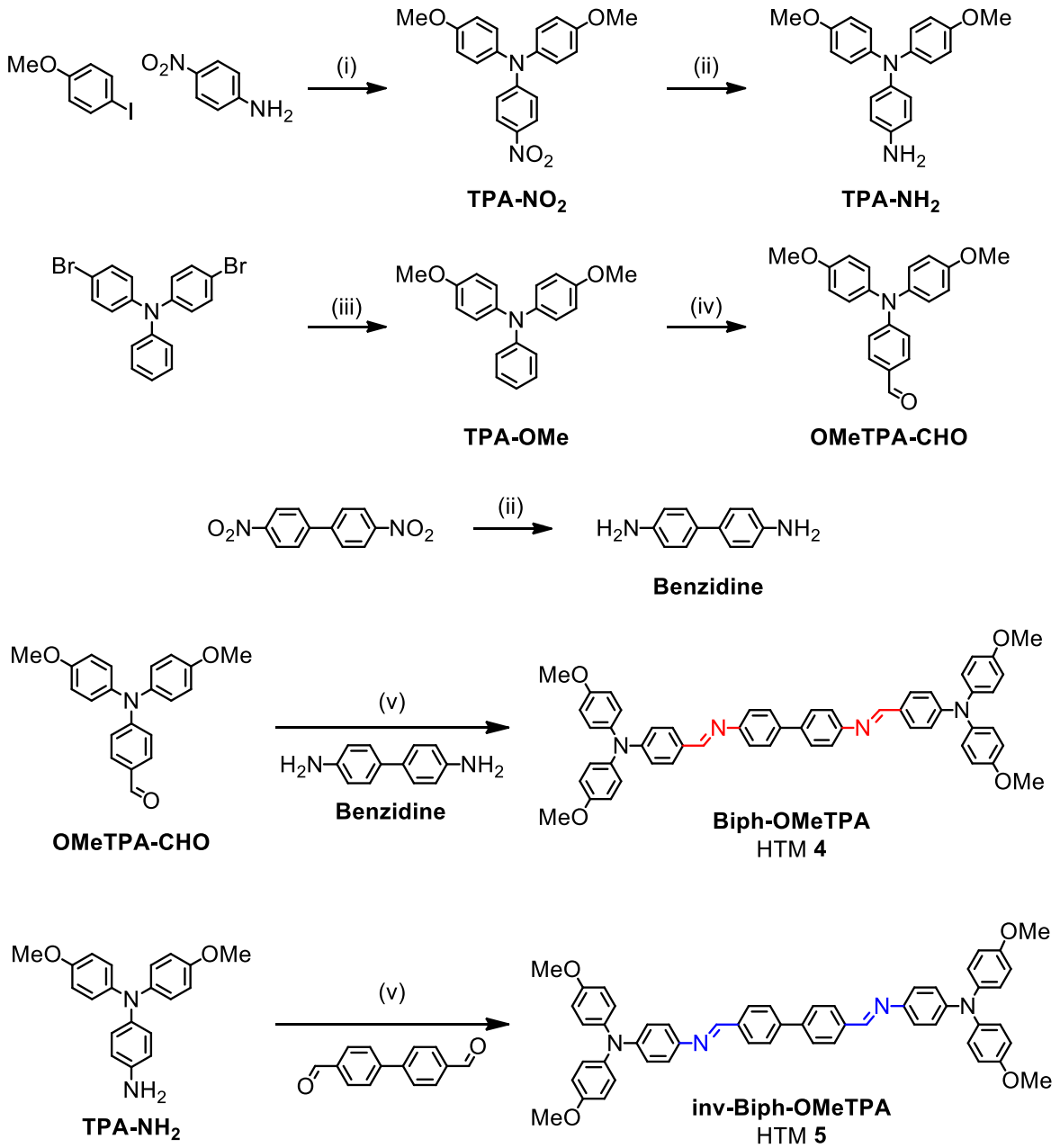

Scheme 4-1: Synthesis of imine HTMs. Conditions: (i) K_2CO_3, copper powder, 18-crown-6, DMF, reflux (150 °C, 16 hours), yield 67%; (ii): 10% palladium on carbon, hydrazine hydrate, dry THF, reflux (66 °C, 16 hours); (iii) Sodium metal, methanol, 0°C then copper (I) iodide, DMF, 90°C, 48 hours; (iv) $POCl_3$, DMF, 90°C, 16 hours; (v) $MgSO_4$, p-TsOH, EtOH, 3 hours. Detailed syntheses in the Methodology, Section 5.1.3.

The oxidation behaviour of the two HTMs is paramount in determining their oxidation behaviour and resulting charge transport properties. As the effect of the electronegative nitrogen atom greatly affects the electron density around the whole molecule, it is helpful to decouple the electronic properties of the biphenyl core and the TPA arms in order to study the redox properties of both components separately. An additional four model compounds **6** – **9** were therefore synthesised as detailed in Scheme 4-2. Compound **9** was synthesised by Dr. Dylan Wilkinson of the Cooke group.

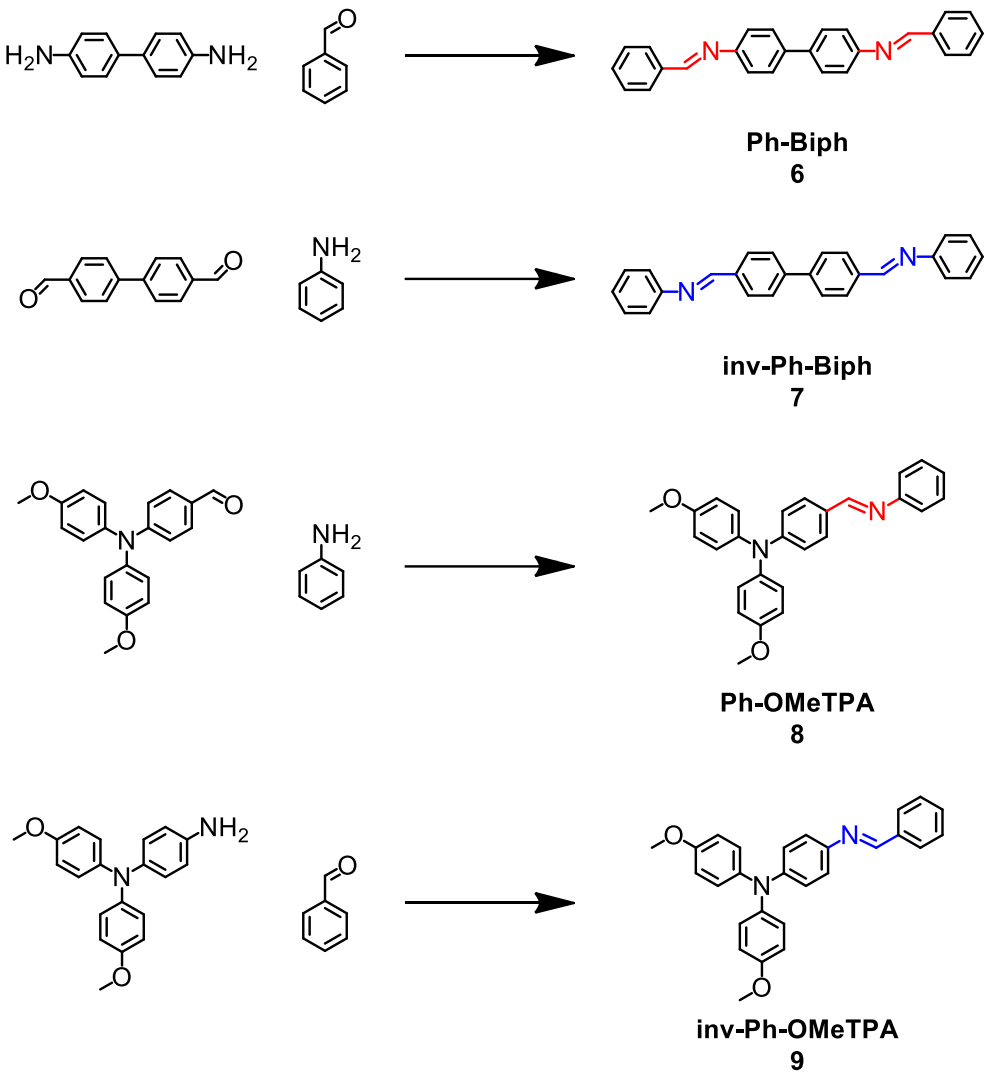

Scheme 4-2: Synthesis of model compounds **6** - **9**. Reaction conditions are identical for all: $MgSO_4$, p-TsOH, EtOH, stirred at 25 °C for 3 hours. Detailed syntheses in the Methodology, Section 5.1.3.

All materials **4** – **9** were placed in a vacuum oven at 50 °C for at least 4 hours prior to further analysis, in order to remove any volatile solvents from the samples. The purity of the synthesised materials was assessed through ^{1}H and ^{13}C NMR spectroscopy as well as mass spectrometry. For imine materials, extra care must be taken during handling and storage to ensure that the hydrolytically unstable imine bond remains intact. Therefore, compounds **4** – **9** were all stored in a nitrogen-filled glove box between experiments, in order to ensure a water-free atmosphere.

Figures 9-6 – 9-8 in the Appendix, Section 9.1 show the ^{1}H NMR spectra of the intermediate **TPA-OMe** and **OMeTPA-CHO** functionalised triphenylamines, as well as the **benzidine** intermediate. Only a minor component of residual solvent remained after purification and drying, with no other side products observed. To characterise the final compounds, ^{1}H and ^{13}C NMR spectroscopy was performed on the samples after purification. The spectra are shown in Figures 9-9 – 9-14. The spectra show that the final compounds **4** – **9** have been appropriately purified by column chromatography, with only traces of solvent left behind in the samples. Mass spectra were also recorded for compounds **4** – **9** courtesy of Dr. Giovanni Enrico Rossi and Eirinn-Rose McWilliams at the School of Chemistry. These are given in the Appendix, Section 9.2, in Figures 9-18 – 9-23. The molecular ion peaks seen in the mass spectra confirm the identities of the final products.

4.2.2 Characterisation

The thermal stability of newly developed HTMs is an important characteristic to investigate for systems which operate at elevated temperatures, such as organic photovoltaics. Here, the stability of the amorphous state is important to ensure good interfacial contact. Good thermal stability has previously been noted in conjugated imines which would make them suitable for these purposes.[58,131] Thermochemical measurements were again performed by Andy Monaghan at the School of Chemistry.

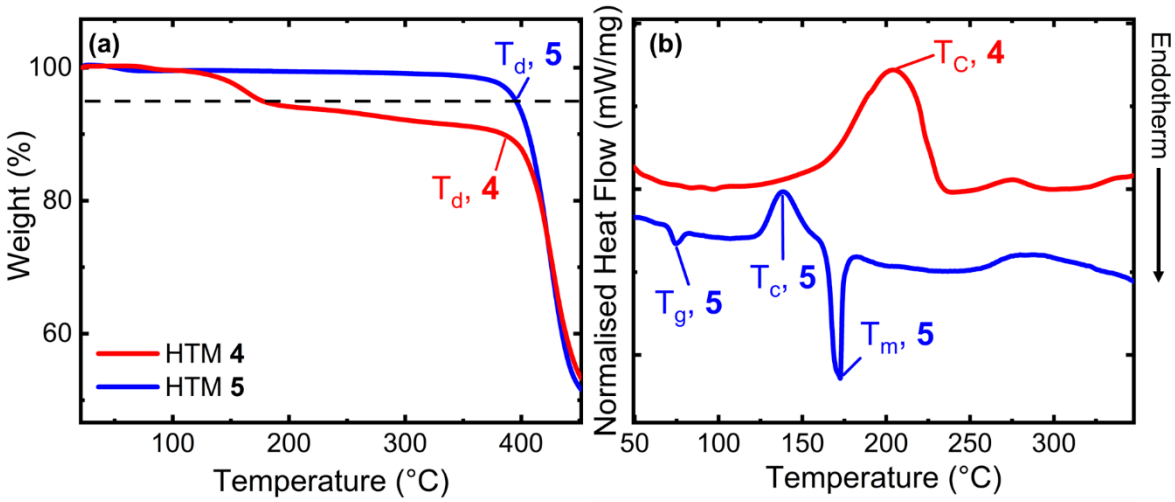

Figure 4-5: (a) Stacked TGA; and (b) Stacked DSC thermograms of the two imine HTMs. Heating rate was 10 °C min^{-1}. Dotted line in TGA represents 95% weight. Scale omitted from DSC graph as the lines were offset for clarity.

Significant differences in the thermal properties of the materials are observed, despite their isomeric nature. In Figure 4-5a, HTM **4** is seen to undergo an initial mass loss of 5% between 100 – 180 °C, after which the thermogram exhibits a plateau until decomposition at ~400 °C.

This is in contrast to HTM **5** which does not undergo significant mass loss until decomposition at ~400 °C. The most significant loss in mass is decomposition which occurs at similar temperatures for both isomers. The initial mass loss seen for HTM **4** is not reflected in the DSC (Figure 4-5b). While such mass loss is normally suspected to be due to loss of solvent, this possibility was ruled out as all samples were thoroughly dried in a vacuum oven as described in Section 4.2.1 before further analysis, in order to ensure that no volatile solvents remain in the sample. No high-boiling point solvents were used in the synthesis or purification of HTM **4**. The mass loss which occurs must therefore come from the material itself, as confirmed by a repeat measurement (Figure 4-6).

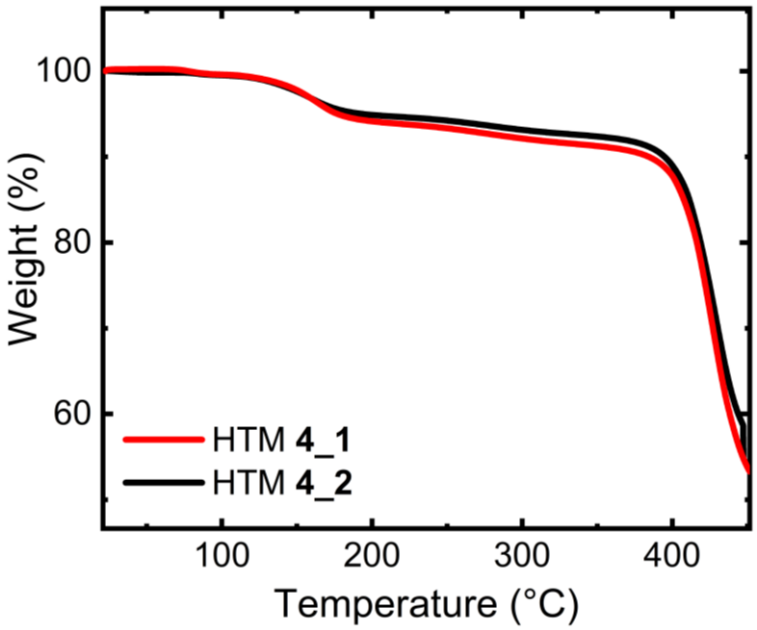

Figure 4-6: Two stacked thermograms for different powder samples of HTM **4**, labelled **4_1** and **4_2**. Heating rate was 10 °C min^{-1}.

The phase change behaviour is also markedly different for the two imines. HTM **4** only undergoes a single exothermic phase transition, likely to be a crystallisation or aggregation as a result of increased mobility at higher temperatures. As this transition happens around 205 °C, it occurs directly following the mass loss that was seen up to 180 °C in the TGA. It is likely that the two processes are related, but there is insufficient information available to fully deconvolute these processes. HTM **5,** on the other hand, exhibits more straightforward phase change behaviour, with a glass transition at 75 °C which is close to the highest operational temperatures reached by solar cells. The glass transition is followed by a crystallisation exotherm at 138 °C, and a sharp melting endotherm at 173 °C. In this regard, the long-term operational stability of potential solar cell devices made with HTM **5** may be limited by glass transitions at the highest operational temperatures. HTM **4** would be more thermally stable under these conditions.

The optical and electrochemical properties of an OS are pivotal when aiming to use them as HTMs, as the materials' energy levels must be well-aligned to the energetics of the rest of the device to efficiently shuttle charges to their respective electrodes. In this regard, the orientation of the imine bond is found to strongly influence the absorption and emission characteristics of the imine materials, as seen in Figure 4-7a. Comparing HTMs **4** and **5**, a noticeable shift in the absorption maximum is observed from 402 nm to 422 nm when switching between the N-to-Core and N-to-TPA orientations. This absorption is assigned to the C=N π→π* transition, and the bathochromic shift of 20 nm indicates a reduced optical bandgap for HTM **5**, suggesting potential variations in planarity and, consequently, conjugation across the entire molecule. Using Tauc plots (Figure 4-6b,c), a decrease in optical bandgap from 2.79 to 2.63 eV is estimated for the N-to-TPA (HTM **5**) orientation compared to the N-to-Core system (HTM **4**). These observations mirror previous reports.[16,132]

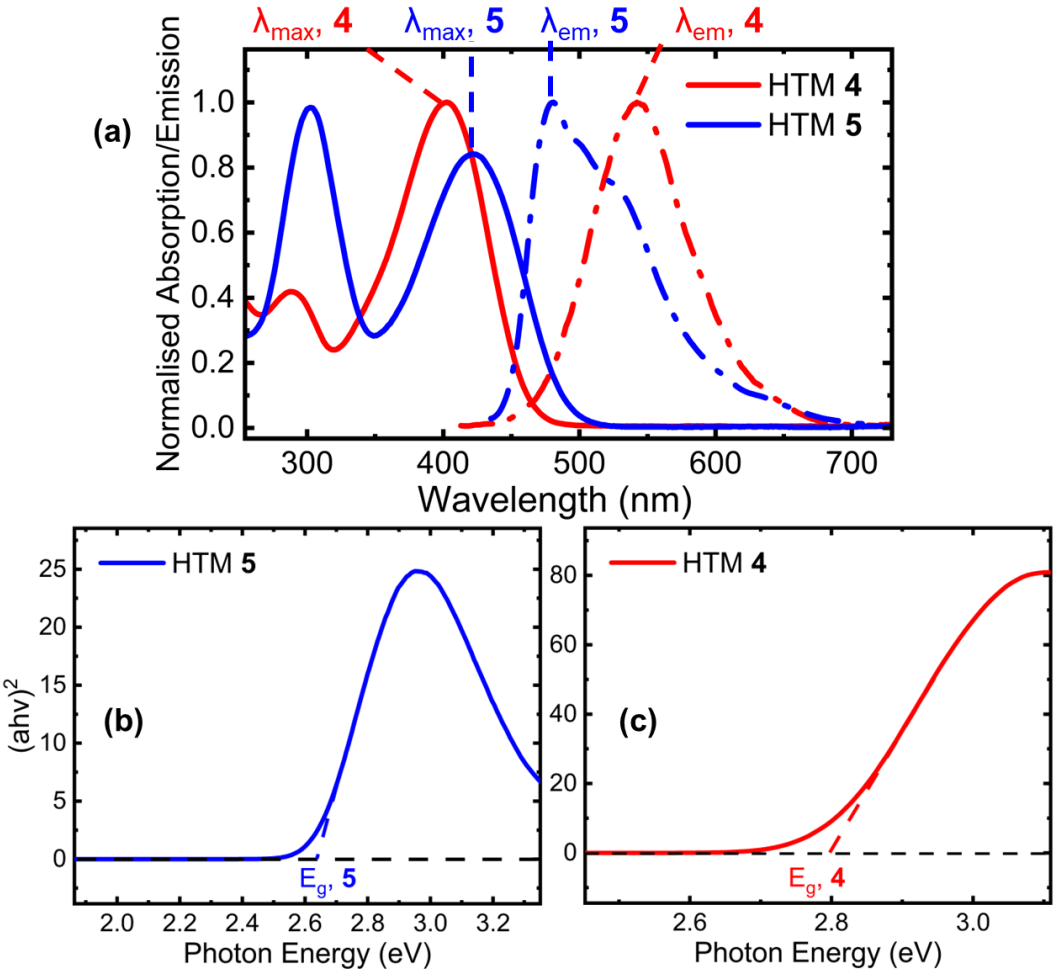

Figure 4-7: (a) Solution UV-Visible absorption and emission spectra of HTMs **4** and **5**, measured in dichloromethane at a concentration of 10^{-5} M. Fluorescence spectra were acquired after excitation at the labelled λ_{max} of the corresponding absorption spectrum. All absorption and emission spectra were normalised by setting the most intense peak to 1. (b) and (c): Tauc plots prepared from their UV-Visible absorption spectrum.

A drastically increased Stokes shift for HTM **4** (142 nm, 6493 cm^{-1}) compared to HTM **5** (58 nm, 2863 cm^{-1}) is also observed, indicating a much larger degree of flexibility in the molecule and greater structural deformations upon light excitation.[53,62]

It is equally important to gain knowledge about the electronic energy levels and oxidation behaviour of a material when seeking to implement is as a HTM in device structures. The HOMO energy level is an important parameter for charge hopping, as these orbitals are the site through which holes must hop to reach the electrodes. CV is a powerful tool used to obtain the IP of materials in solution, which is routinely used as a rough estimate of the HOMO in the literature.[16,54,58] CV measurements were performed against the Fc/Fc^+ redox couple in DMF, which was chosen as solvent because it fully dissolves both imine HTMs as well as the four model imines. Compounds **6** and **7** showed particularly low solubility in other organic solvents. The IPs were extracted from the square-wave voltammograms.

The oxidation curves of HTMs **4** and **5** are shown in seen in Figure 4-8a. HTM **5** is found to have a lower IP (5.04 eV) compared to HTM **4** (5.27 eV). HTM **4** also undergoes another irreversible oxidation centred around 0.05 V, which does not appear in the subsequent square-wave voltammogram (Figure 4-8b). Irreversible features arising from the oxidation of the solvent are also observed at – 0.75 V.

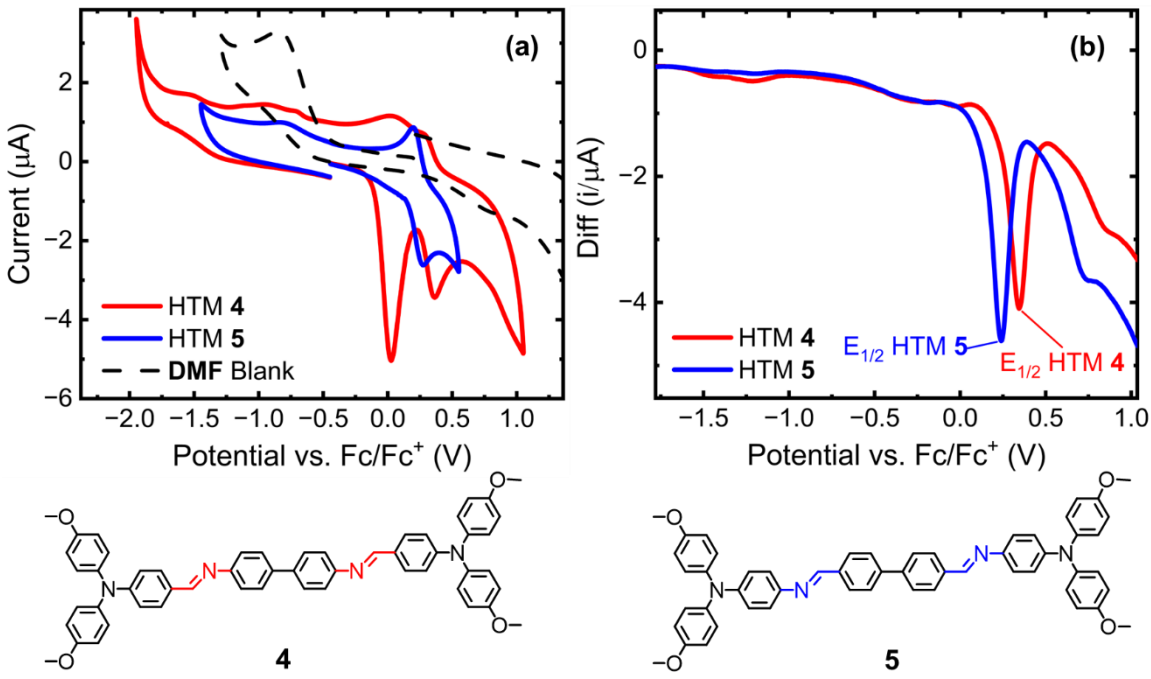

Figure 4-8: Stacked (a) cyclic voltammograms and (b) square-wave voltammograms of HTMs **4** and **5**, recorded from 10^{-4} M solutions in anhydrous DMF. Voltammograms recorded using a platinum disc working electrode, platinum wire counter electrode, and silver wire pseudo-reference electrode, 0.1 M $TBAPF_6$ electrolyte. Fc^+/Fc was used as external reference. Scan rate 0.1 V s^{-1}.

The different oxidation profile seen in the N-to-Core orientation for HTM **4** in Figure 4-8a compared to the N-to-TPA orientation has significant implications for its use as an HTM. The irreversible oxidation seen in the cyclic voltammogram suggests that a side reaction is taking place upon oxidation that is chemically irreversible. Another possibility is the precipitation of the oxidised product, which can be responsible for the irreversible wave. As conductivity relies on redox reactions between radical cations and neutral molecules to shuttle charge across the layer, the oxidation must be reversible in order for the HTM to perform correctly. The N-to-Core orientation in HTM **4** may draw sufficient electron density into the biphenyl core so as to increase the likelihood of an electron being removed from this region of the molecule as opposed to the TPA sidearm. If this oxidation is irreversible, then a permanent chemical change has occurred within the molecule, which does not generate a mobile hole.

To investigate this hypothesis, DFT modelling was performed on HTMs **4** and **5** which was used to produce electrostatic potential maps of the two molecules. The electronegative nitrogen atom in the imine bond, as well as its orientation relative to the rest of the structure, has ramifications on the distribution of electron density across the molecule. The calculated ESP maps (Figure 4-9) demonstrate that the electron density is significantly shifted as a result of imine bond orientation. In HTM **4**, the biphenyl core is rendered significantly more electron-rich than that in HTM **5**, due to being directly bonded to the nitrogen atom in the imine bond. The nitrogen atoms in the imine bond serve to shift the electron density towards the moiety they are attached to, thus drawing electron density towards the core in HTM **4** and towards the TPA arms in HTM **5**.

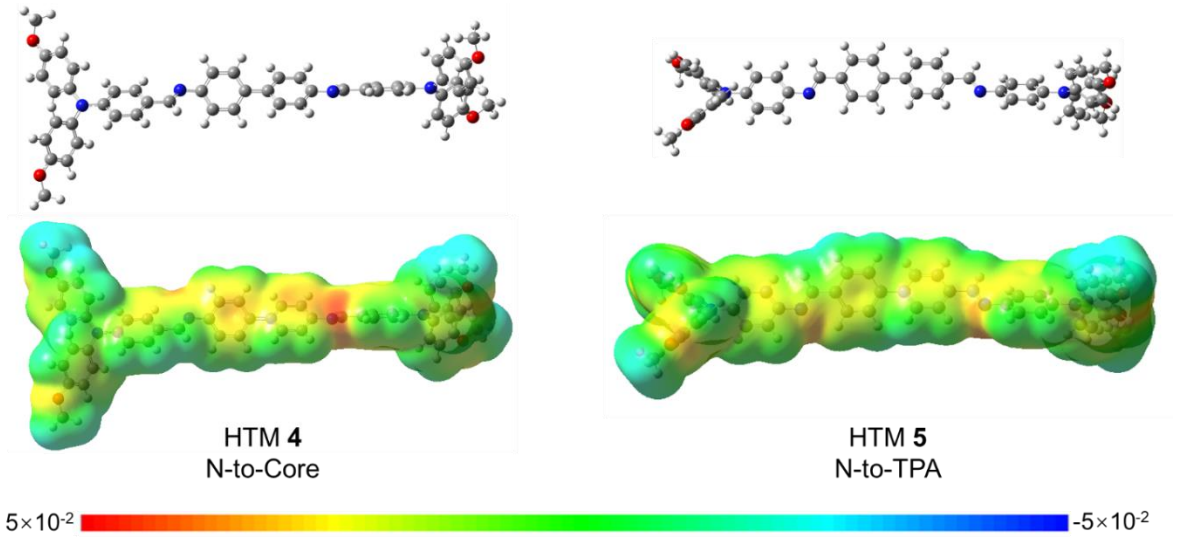

Figure 4-9: Top: Optimised geometries of HTMs **4** and **5** at the B3LYP 6-311G** level. Bottom: ESP maps generated from the optimised structures.

DFT can also provide useful predictions of the electronic structure of a material, giving information about the HOMO and LUMO distribution across the molecule. The position of the HOMO is of particular interest when investigating HTM doping mechanisms, as this is the orbital into which a hole should be injected during the oxidation reaction. The HOMO energy levels were estimated from the optimised DFT structures using the empirically obtained procedure published by Chi, *et al.*[115] The molecular orbital diagrams and their corresponding energy levels are summarised in Figure 4-10. The calculated HOMO and LUMO energies, as well as the HOMO-LUMO gap nicely corroborate the results from the spectroscopic and electrochemical studies. The shallower HOMO level from CV and narrowed optical bandgap from the absorption spectrum of HTM **5** compared to HTM **4** is mirrored in the DFT calculations. Significantly different HOMO and LUMO distributions are observed in the two isomeric structures. When the imine bond is oriented nitrogen-to-TPA in HTM **5**, the frontier orbitals are isolated on discrete parts of the molecules, with the HOMO located on the triphenylamine moieties and the LUMO centred around the core. In the nitrogen-to-core orientation, there is significant overlap between the HOMO and LUMO.

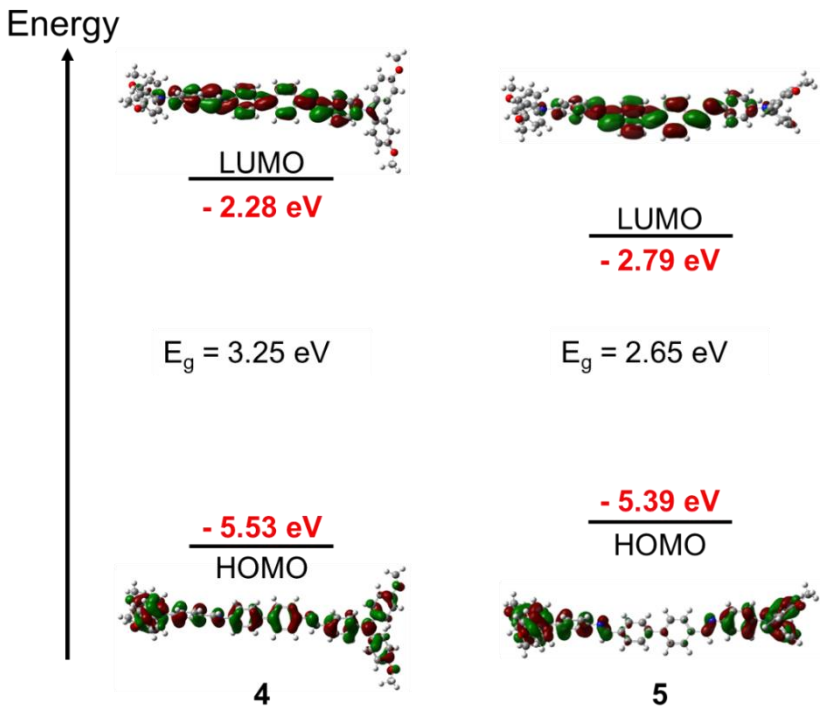

Figure 4-10: DFT-calculated molecular orbital diagrams of HTMs **4** and **5** at the B3LYP 6-311G** level, as well as the corresponding HOMO and LUMO energies estimated from the procedure by Chi, et al. [115]

In order to further investigate the molecular region responsible for the irreversible oxidation of HTM **4**, spectroscopic and electrochemical characterisation was performed for model compounds **6 – 9**. Their UV-visible absorption and fluorescence spectra, as well as the cyclic and square-wave voltammograms are depicted in Figures 4-11 and 4-12. Stokes shift and estimated IPs are then summarised in Tables 4-1 and 4-2.

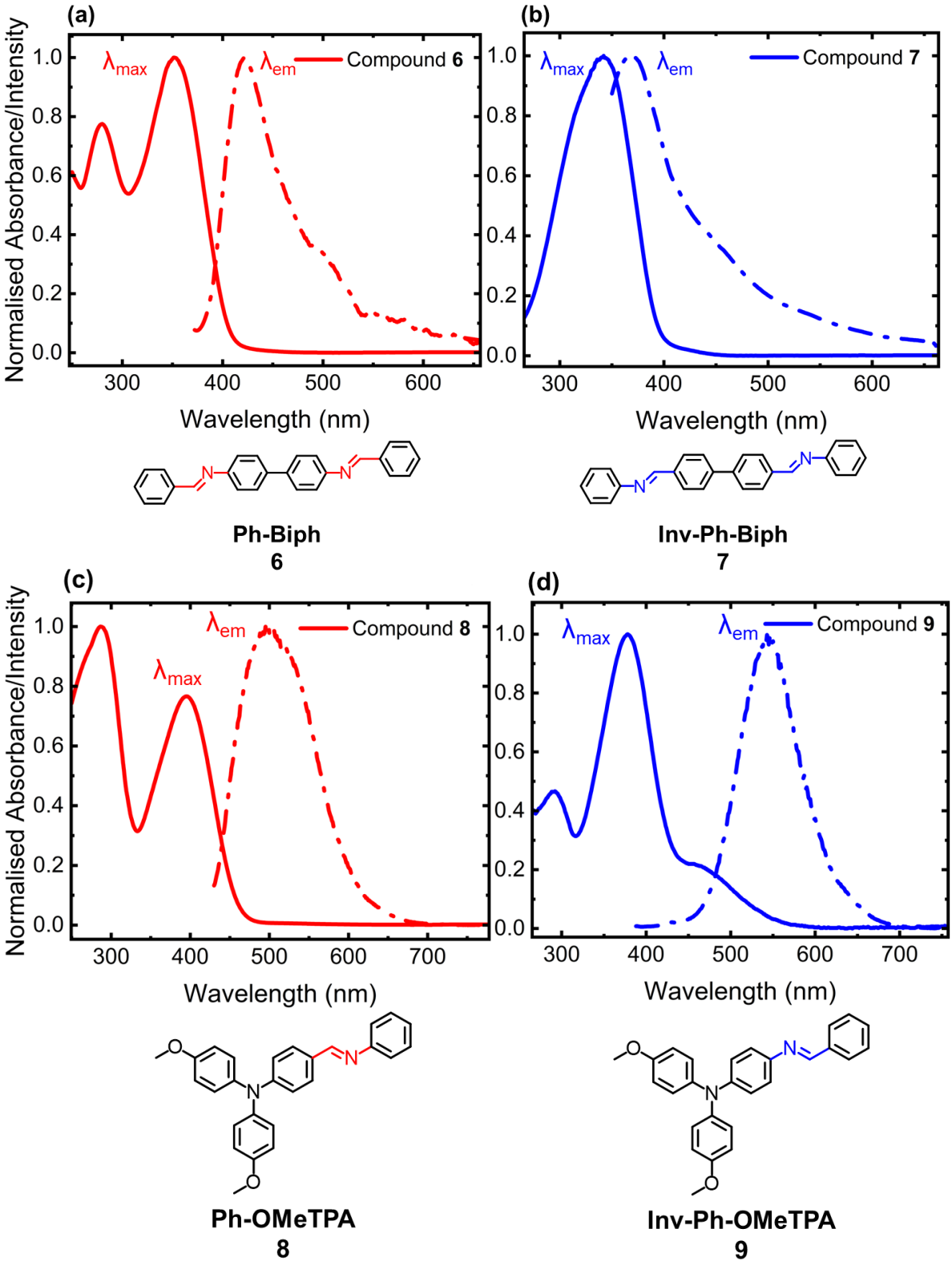

Figure 4-11: Solution UV-Visible absorption and fluorescence spectra of model compounds (a) **6;** (b) **7;** (c) **8;** and (d) **9**, recorded in dichloromethane at a concentration of 10^{-5} M. Emission spectra obtained by using λ_{max} as the excitation wavelength. Spectra normalised by setting λ_{max} or λ_{em} to 1.

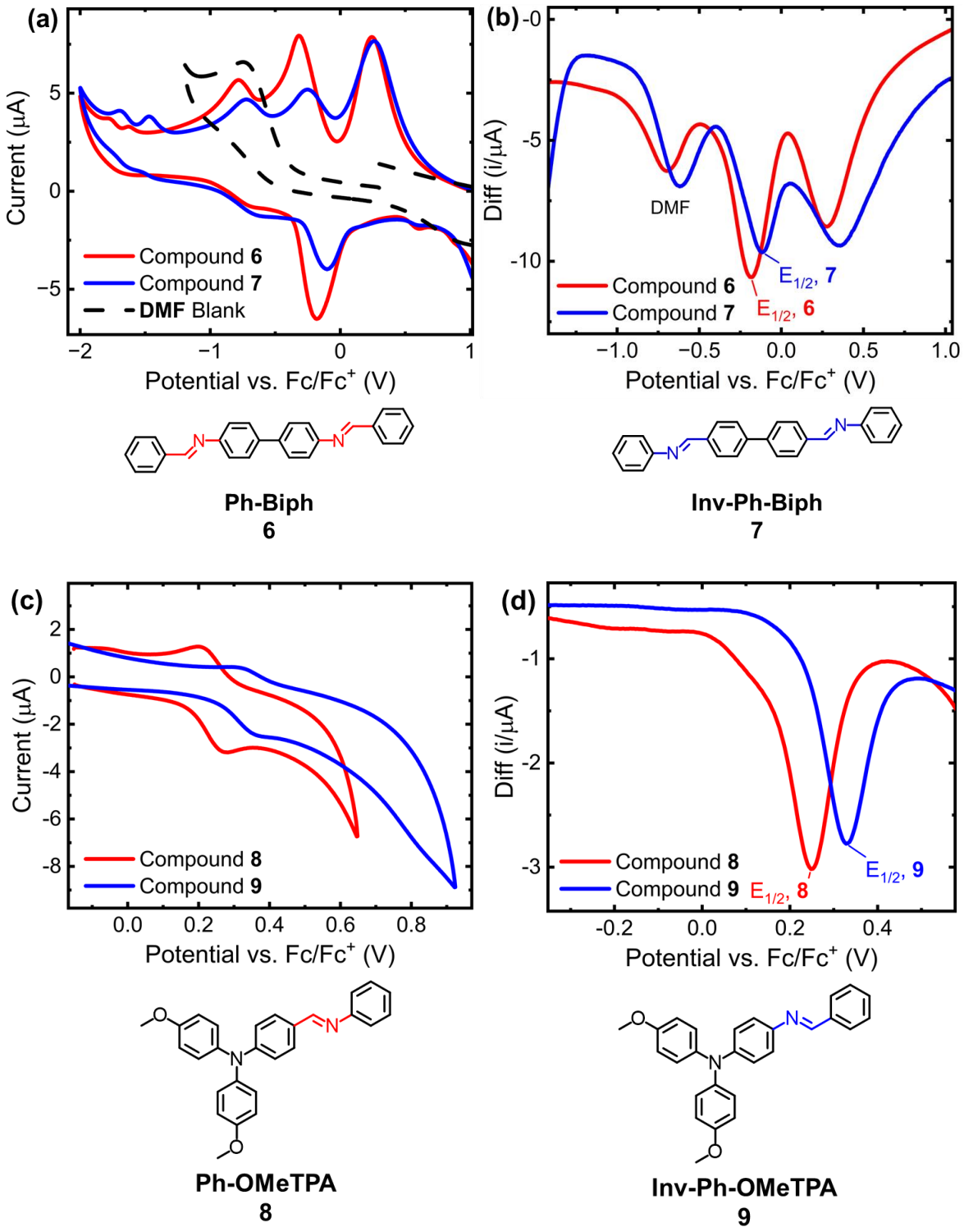

Figure 4-12: (a) stacked CVs and (b) stacked SWVs of biphenyl model imines **6** and **7**. (c) stacked CVs and (d) stacked SWVs of TPA-based model imines **8** and **9**. Voltammograms recorded in anhydrous DMF solvent at a concentration of 10^{-4} M, using a platinum disc working electrode, platinum wire counter electrode, and silver wire pseudo-reference electrode. 0.1 M $TBAPF_6$ added as electrolyte, and Fc^+/Fc was used as external reference. Scan rate 0.1 V s^{-1}.

Table 4-1: Summary of spectroscopic data collected for HTMs **4** and **5**, as well as the model compounds **6** – **9**.

	λ_{max} (nm)	λ_{em} (nm)	Stokes shift (nm)	Stokes shift (cm^{-1})	E_g (eV)
4	402	544	142	6493	2.79
5	422	480	58	2863	2.63
6	353	422	69	4632	3.10
7	341	369	28	2225	3.19
8	396	499	103	5212	2.81
9	380	545	165	7967	2.76

Table 4-2: Summary of estimated IPs from the square-wave voltammetry experiments. $HOMO_{calc}$ represents the calculated HOMO energy from DFT calculations.

Compound	$E_{1/2}$ vs. Fc^+/Fc (V)	IP (eV)	$HOMO_{calc}$ (eV)
4	0.47	5.27	-5.53
5	0.24	5.04	-5.39
6	-0.12	4.69	-5.62
7	-0.18	4.62	-5.72
8	0.33	5.13	-4.86
9	0.25	5.05	-4.70

It is evident that the orientation of the imine bond does not significantly affect the oxidation of the isolated biphenyl core in compounds **4** and **5**, as the IPs estimated for the two models are nearly identical. Conversely, a ~0.1 eV difference in IP for TPA-based models **8** and **9** reflects similar differences seen in HTMs **4** and **5**. Interestingly, biphenyl-based models **6** and **7** show similar irreversible features at 0.25 V in the CV as HTM **4**, suggesting that the irreversible feature arises from the biphenyl core of the HTM and not the TPA arms, and indicates that inverting the imine bond in HTM **5** improves the electrochemical reversibility of the system. In HTM **5**, the reversible oxidation of the TPA sidearm dominates, but in HTM **4** an irreversible oxidation of the biphenyl core occurs first. It is likely that, as seen from the DFT experiments, the delocalisation of the HOMO across both donor and acceptor units in HTM **4** can result in the unwanted oxidation of the biphenyl core when this HTM is treated with a chemical oxidant.

4.2.3 **FK209** Oxidation of Imine HTMs

The different oxidation behaviour for HTMs **4** and **5** seen from the CV analysis should manifest in vastly different oxidation behaviour when the imines are treated with chemical oxidants. A very wide range of dopants have been successfully applied for this purpose, chief among them being the **TFSI**$^-$ based dopants such as **LiTFSI** and **FK209**. These oxidise the material through different mechanisms, but the end result is the same: numerous HTM molecules within the bulk matrix are oxidised by the additives to create a radical cation, which functions as the 'dopant' containing an additional hole. In a doped HTM, this hole is free to move under the influence of an electric field, thus increasing the conductivity within the bulk. To test the chemical oxidation properties as well as the conductivities of HTMs **4** and **5**, while ensuring minimal variation across the samples, **FK209** was once again employed as the oxidant. As discussed in the Introduction and in Chapter 2, **FK209** oxidises the HTM through a redox reaction, generating a radical cation with the concomitant reduction of its Co(III) centre to Co(II). Crucially, the reaction does not require oxygen as in the case of **LiTFSI**, thus removing the need for ambiguous curing steps in a dessicator, helping to standardise the experiments. The degree of oxidation can be controlled by varying only the amount of **FK209** dopant added to the HTM solutions. The use of **FK209** by itself does not lead to hygroscopic byproducts remaining in the film, as is the case with **LiTFSI**.[35,44] This is especially important when dealing with imine-based systems, as the imine bond is unstable to aqueous hydrolysis.[133] The degradation of the HTM would result in irreversible loss in conductivity that is difficult to decouple from any fundamental changes in the doping mechanism between the two isomers.

The oxidation reaction can be monitored by a number of spectroscopic techniques which have already been presented in this thesis, such as UV-Visible absorption spectroscopy. Thin films of HTMs **4** and **5** were prepared with increasing amounts of **FK209** in the spin coating solution. Films were spin coated onto glass slides for UV-Visible absorption spectroscopy, as well as onto patterned ITO slides for conductivity measurements, according to the procedures detailed in Section 4.4.1. Figure 4-13 shows the film UV-Visible absorption spectra of HTMs **4** and **5** with increasing **FK209** content. **FK209** oxidation results in the growth of new peaks in the visible absorption profile of our materials, and an immediate colour change in the HTM solution.

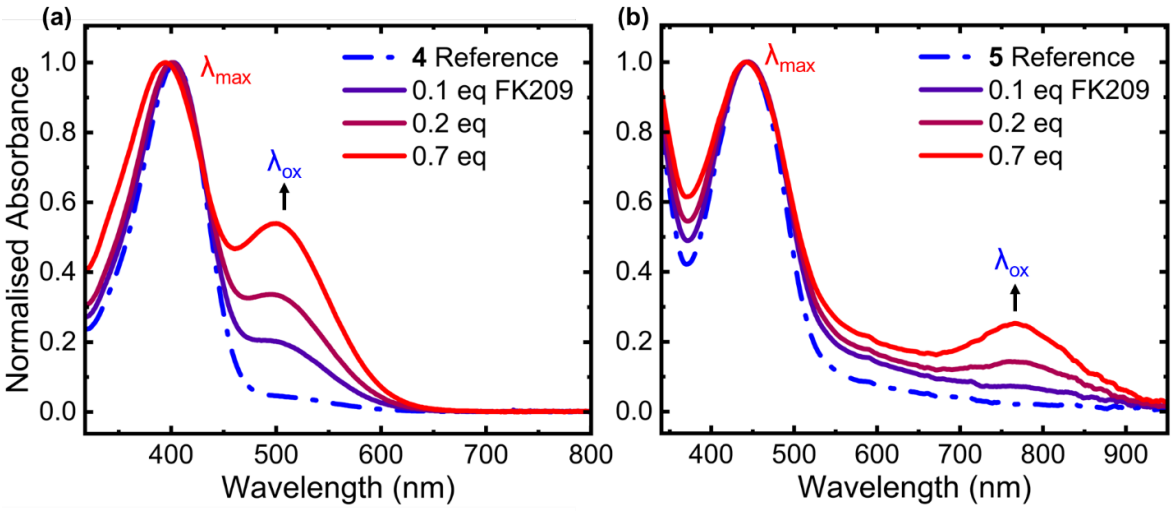

Figure 4-13: Film UV-Visible absorption spectra of doped films of (a) HTM **4** and (b) HTM **5** recorded immediately after spin coating, with increasing concentration of **FK209**. Relevant experimental parameters are summarised in Tables 4-3 and 4-4. All spectra normalised by setting λ_{max} to 1.

A large difference of ~255 nm is seen in the position of the oxidised species absorption between HTMs **4** and **5**. The absorption of oxidised HTM **5** has a maximum at much longer wavelengths than HTM **4**. While the starting materials are isomeric, the reaction products have vastly different optical bandgaps and are likely to be very different chemical species. From this surprising result, it is evident that the **FK209** reactions proceeded through very different pathways, despite both HTM solutions immediately taking on a dark red colour.

As the oxidation reaction only leads to successful doping if mobile holes are generated, the film conductivity of the imine materials was also tested. Thin films of pristine HTMs **4** and **5**, as well as films treated with increasing amounts of **FK209** were prepared by solution spin coating as described in Section 4.4.1. Interestingly, very different conductivity behaviour for the two HTMs was observed across the **FK209** concentration range. (Figure 4-14). With HTM **4**, conductivity only increased by around an order of magnitude while the conductivity of HTM **5** increases by several orders of magnitude as the **FK209** content is increased, reaching a maximum of 10^{-5} S cm^{-1} at 0.6 equivalents of additive. This further points towards significant differences in reaction pathways between HTMs **4** and **5**. The conductivity results indicate significantly reduced doping efficiency for the N-to-core orientation compared to the N-to-TPA orientation, which is doped successfully by **FK209** thus exhibiting a significant conductivity increase. As the hole conductivity is dependent on both the hole concentration and their mobility through the film, the observed lack of conductivity for HTM **4** could either mean insufficient hole mobility, or insignificant generation of additional holes. The simplest method to decouple these two possibilities is the use of spectroscopic techniques to probe for the presence of radical species, as discussed in the next section.

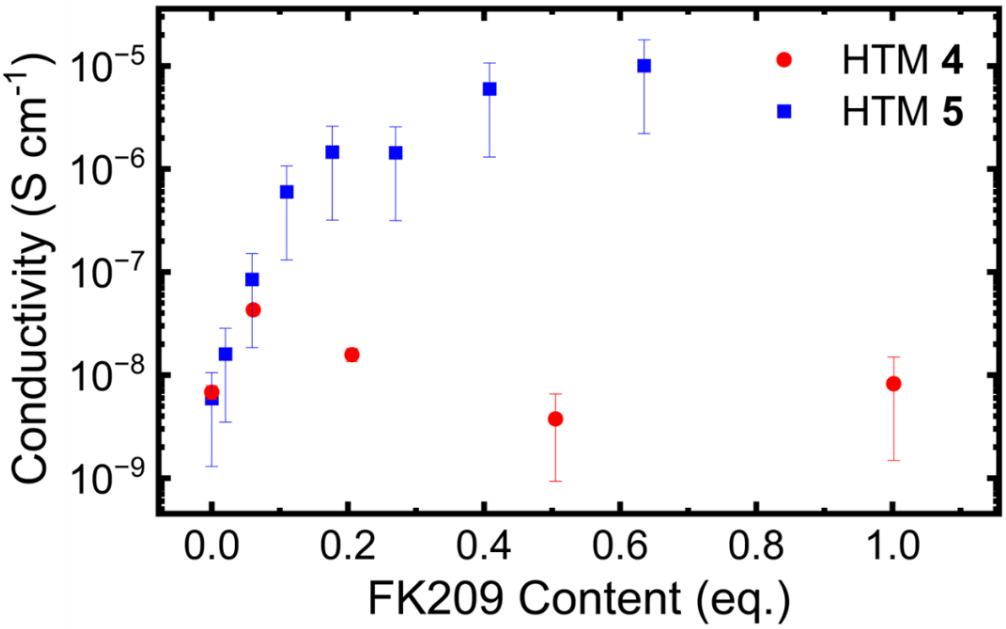

Figure 4-14: Film conductivities of HTMs **4** and **5**, with increasing **FK209** concentration. See Tables 4-4 and 4-5 for experimental parameters. Error bars calculated by propagating the error from the measurements as described in Section 5.3.5.

4.2.4 NMR and EPR analysis of imine oxidation pathways

The formation of radical cations within the HTM is an essential first step towards doping. To this end, the qualitative detection of stable radical species can be easily achieved through routine ^{1}H-NMR studies, as the interaction between unpaired electrons and NMR-active nuclei results in paramagnetic broadening of the NMR peaks of the molecular regions involved. This has been employed in various studies in the literature investigating the oxidation of **Spiro-OMeTAD**.[107,134] Solutions of both of HTMs were prepared for NMR, with and without the addition of one equivalent of **AgTFSI** as described in Section 4.4.2. Here, **AgTFSI** is used as a strong chemical oxidant that can produce the HTM radical while leaving no side products in the reaction mixture, as only metallic silver is produced which precipitates out of solution and is easily removed by filtration. This avoids the use of **FK209**, which would complicate analysis since **FK209** is itself reduced to a Co(II) species at the end of the reaction, contributing its own paramagnetic broadening.[40] The addition of **AgTFSI** to solutions of both imine HTMs **4** and **5** in toluene caused an immediate colour change from orange to red solutions. This observation, coupled with the observed precipitation of metallic silver at the bottom of the reaction vial confirmed a successful reaction between the imines and **AgTFSI**, resulting the reduction of Ag(I) to $Ag_{(s)}$.

Following the isolation of the reaction products through filtration and evaporation of solvent, the ^{1}H-NMR spectra of the isolated reaction product(s) were recorded in toluene-d8. Figure 4-15 shows the aromatic region of the ^{1}H-NMR spectrum of HTMs **4** and **5** as well as the corresponding **AgTFSI**-oxidised spectra.

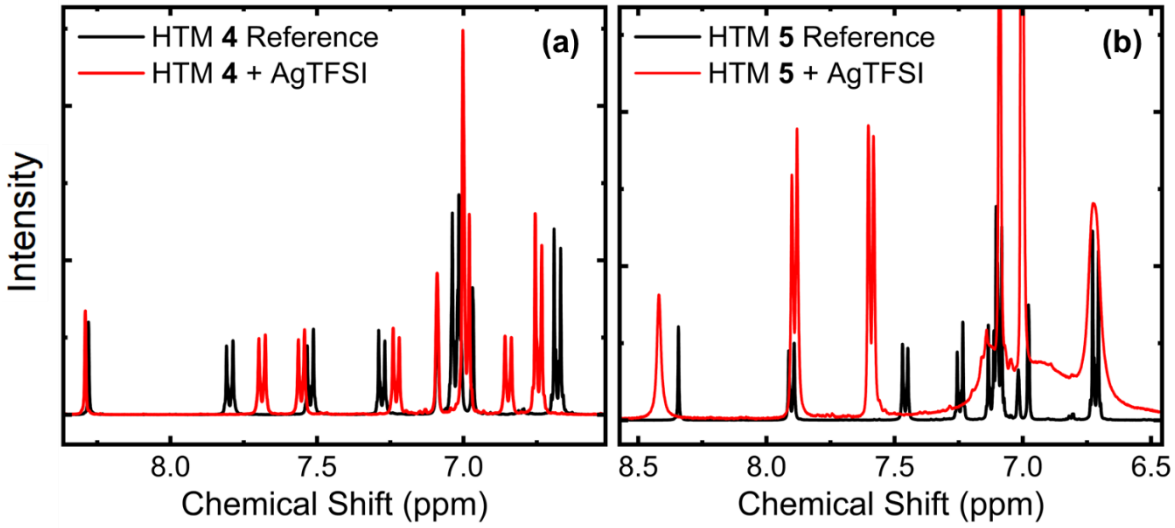

Figure 4-15: The aromatic region of (a) HTM **4** and (b) HTM **5** ^{1}H-NMR spectra, recorded at 25 °C in toluene-d8 before (black lines) and after (red lines) the addition of 1 equivalent of **AgTFSI**. See Section 4.4.2 for experimental details.

As Figure 4-15 shows, the aromatic proton signals for both HTMs shift upon addition of **AgTFSI**. In the case of HTM **5**, there is significant broadening in the aromatic peaks assigned to protons on the TPA moiety, as well as broadening of the imine proton peak. This broadening is a result of the paramagnetism of the unpaired electron generated through **AgTFSI** oxidation. The peaks arising from protons on the biphenyl core are not broadened, suggesting that the radical is entirely located on the TPA arms.[107] No such broadening is observed in the case of HTM **4**. This further suggests that the reaction of HTM **4** with **AgTFSI** leads to side reactions which do not generate an appreciable concentration of radical species, corroborating the lack of conductivity increase through the addition of **FK209** shown in Figure 4-14.

The conductivity of a HTM cannot increase if the hole transporter is not able to stabilise the cationic radical state. In the absence of these radicals, the system is not doped and no additional charge carriers are created to increase the conductivity. To further confirm this hypothesis, the formation of radical species was probed directly through EPR spectroscopy. EPR is a very powerful technique used to detect radical species and can be used to identify the formation of radicals through the reactions between HTMs **4** and **5** with **AgTFSI**. We observe little to no EPR signal for the control HTM solutions containing no additive as expected (Figure 4-16a). Adding one equivalent of **AgTFSI** generates a strong signal for HTM **5** indicating the generation of a radical species with the concomitant reduction of Ag(I) to $Ag_{(s)}$. Some hyperfine splitting is seen in the signal, although this is not sharp enough to resolve any individual multiplets. However, ^{14}N interactions from the TPA nitrogen atoms contribute strong hyperfine coupling and may be the source of the slight splitting seen in Figure 4-16b.

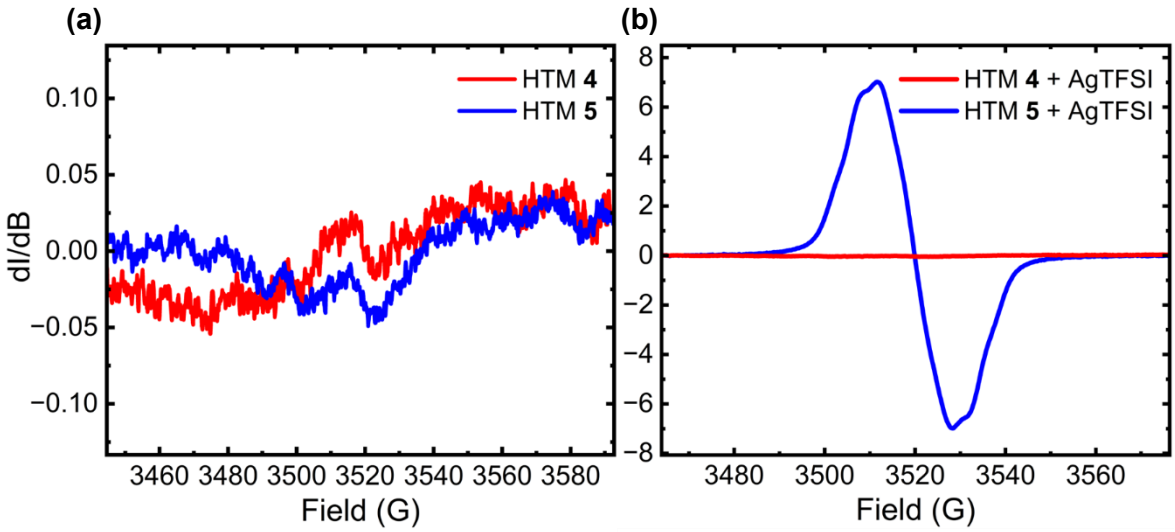

Figure 4-16: (a) Reference EPR spectra for the undoped solutions of HTMs **4** and **5** in dry toluene. (b) Solution EPR spectra of HTMs **4** and **5** in dry toluene treated with **AgTFSI**. Samples measured at 298 K with 1 G modulation amplitude. See Section 4.4.2 for experimental details.

The strong signal for HTM **5** + **AgTFSI** contrasts with the observations for HTM **4**, wherein no significant differences to the reference sample were observed upon the addition of **AgTFSI**. As the solution of HTM **4** in toluene also exhibited a colour change from orange to red, it is reasonable to conclude that while a chemical reaction has taken place, it does not lead to the formation of stable holes. This does not exclude the possibility that the side products are formed through an unstable radical intermediate.

The spectroscopic results presented above corroborate the electrochemical observations: the oxidation of HTM **4** leads to a non-conductive side product that is not a stable radical cation. Due to enhanced electron density around the biphenyl core in the N-to-Core orientation, it is possible that the undesirable oxidation of the core rather than the TPA arm in HTM **4** leads to an immediate quenching of the radical through a more energetically favourable mechanism. As a result, the HTM is not successfully doped through conventional additives such as **FK209**, and is unsuitable for photovoltaic applications.

4.3 Conclusions

The significant effect of imine bond orientation on the suitability of an imine material for HTM applications has been demonstrated above. The imine bond and the oxidation mechanisms and conductivity of imine-based HTMs are intimately linked. The differences in electron density distribution and resulting oxidation behaviour between the two orientations indicated competing oxidation pathways which can hamper the utility of one orientation over the other. HTM **5** exhibits the formation of stable and mobile holes upon chemical oxidation with **FK209**, leading to orders of magnitude improvement in conductivity within a film. Conversely, HTM **4** failed to generate appreciable hole concentration, limiting its utility as an effective HTM.

This study builds upon our findings in earlier chapters, further stressing the significance of structure-function relationships in HTM design. The results provided herein emphasise how subtle modifications, such as imine bond orientation, can exert profound effects on charge transport properties, and pave the way for the rational design and optimisation of future HTMs.

Careful consideration of imine bond orientation can therefore streamline the development of high-performance materials with enhanced charge transport capabilities, while maintaining the benefits of reduced synthetic cost afforded by the Schiff base condensation. As HTM **5** is the isomer with superior charge transport properties, it is a far more attractive candidate for photovoltaics compared to HTM **4**. Due to time constraints, SCLC and solar cell measurements could not be performed for these materials. However, it can be reasonably predicted that HTM **4** would yield minimal PCE when employed in solar cells due to severe series resistance. HTM **5** is the far more promising candidate to use as HTL.

4.4 Methodology

Detailed synthesis of all HTMs and model compounds is detailed in the Materials and Methods Chapter, Section 5.1.3.

4.4.1 Spectroscopy and Conductivity Measurements

The procedure for measuring the film conductivity of imine thin films is as described in the Materials and Methods chapter, Section 5.3.2. Stock solutions were prepared by weighing out dry powders of compounds **4** and **5** in separate vials within a nitrogen-filled glove box. Weighed amounts of anhydrous CB was then added to each vial according to the measurements in Table 4-3 below. The solvent weight was noted in order to calculate the corresponding volume from the density. All imine compounds were fully soluble in pure CB and therefore, no CF was added to the vials. The **FK209** stock solution was prepared in a similar manner, with acetonitrile (ACN) as the solvent. All solutions were then passed through a hydrophobic syringe filter, into a new vial before use to remove any other particulate matter.

Table 4-3: Table of numbers for the stock solutions used for UV-Visible absorption spectroscopy and conductivity measurements.

Species	Amount added	Solvents	Concentration
Biph-OMeTPA	13.6 mg	1148.9 mg CB	16.1 mM
Inv-Biph-OMeTPA	15.9 mg	1281.4 mg CB	16.9 mM
FK209 Stock	147.3 mg	797.1 mg ACN	96.6 mM

In order to spin coat films of the two HTMs at increasing concentrations of **FK209**, an incremental doping method was employed. Portions of **FK209** stock solution were added to the stock HTM vials, while keeping track of the volumes removed for spin coating and the volumes of **FK209** solution added. In this case, two 50 µL portions were taken for spin coating at each condition, in order to spin coat one patterned ITO slide for conductivity measurements and one glass slide for film UV-Visible absorption measurement. The concentrations of HTM and additive within the vial was estimated for each condition, thus allowing estimation of the additive equivalents. All relevant measurements are summarised in Table 4-4 below.

Table 4-4: Table of numbers summarising the relevant measurements for preparation of HTM **4** and **5** thin films, for both conductivity and UV-Visible absorption measurements.

HTM 4 Increment	**0**	**1**	**2**	**3**	**4**			
Initial Solution Volume (µL)	1035.0	945.0	865.0	802.0	755.0			
Added **FK209** (µL)	0	10	20	37	53			
HTM Concentration (mM)	16.1	16.0	15.6	14.9	13.8			
Additive Concentration (mM)	0.00	1.02	3.23	7.54	13.79			
Additive equivalents	**0**	**0.06**	**0.21**	**0.51**	**1.00**			
HTM 5 Increment	**0**	**1**	**2**	**3**	**4**	**5**	**6**	**7**
Initial Solution Volume (µL)	1154.4	1058.4	964.4	872.4	781.4	691.9	605.4	524.4
Added **FK209** (µL)	0	4	6	8	9	10.5	13.5	19
HTM Concentration (mM)	16.9	16.8	16.7	16.6	16.4	16.1	15.7	15.2
Additive Concentration (mM)	0.00	0.37	0.96	1.84	2.93	4.35	6.41	9.68
Additive equivalents	**0**	**0.02**	**0.06**	**0.11**	**0.18**	**0.27**	**0.41**	**0.64**

The JV-characteristics of each condition were measured, and the conductivities were obtained. The error bars in the graph are the propagated error which was calculated according to Equation 5-20 derived in Section 5.3.5. Film thicknesses were measured across each HTM doping series by etching a valley into the glass slide using a razor, and measuring the depth of the valley using contact profilometry. The resulting measurements are given in Table 4-5. Averages based off of six measurements per HTM were then calculated, and the standard deviation across these six measurements was used as the error from the thickness measurements.

Table 4-5: Measured film thicknesses for the thin films deposited for UV absorption and conductivity measurements, including the calculated average thicknesses and the standard deviation used in the calculations.

	Film thickness (nm)	
	4	**5**
	-41.91307	-51.28393
	-60.63973	-39.27814
	-76.78038	-45.00383
	-40.82794	-51.03438
	-27.21395	-35.32536
	-70.41448	-79.01325
Average (nm)	**52.96**	**43.97**
Standard Deviation (nm)	**14.07**	**5.85**

4.4.2 NMR and EPR Sample preparation

In order to prepare solutions of imine compounds **4** and **5** for paramagnetic NMR and EPR measurements, solutions of the two imines were prepared at known concentration in chloroform. **AgTFSI** stock was prepared in acetonitrile and added to the HTM solutions as described in Section 5.3.3. Relevant measurements are detailed in Table 4-6.

Table 4-6: Summary of the measurements taken for solution preparation for the NMR and EPR measurements.

Species	Amount added	Solvents	Concentration
4	82.5 mg	4430.9 mg CF	34.0 mM
5	78.3 mg	4400.3 mg CF	32.5 mM
AgTFSI Stock	175.2 mg	749.0 mg ACN	473.8 mM

Both HTM stock solutions were then split into two portions, to which just over 1 equivalent of **AgTFSI** was added through the additive stock, for the oxidation reaction. This oxidant concentration was chosen to ensure adequate hole generation (if any) to allow detection through spectroscopic techniques. An immediate colour change to a red solution was seen for all HTM solutions, confirming a successful reaction. Relevant measurements are summarised in Table 4-7 below.

Table 4-7: Measurements for the HTM stock solutions prepared for NMR and EPR measurements. For each HTM, sample **1** was used for NMR and sample **2** was used for EPR.

HTM **4** sample	**1**	**2**
Stock solution mass (mg)	2050	2142
Added **AgTFSI** (µL)	110	110
…in equivalents	**1.1**	**1.1**
HTM **5** sample	**1**	**2**
Stock solution mass (mg)	2201	2004
Added **AgTFSI** (µL)	110	110
…in equivalents	**1.1**	**1.2**

The reaction mixtures were filtered using syringe filters to remove any suspended metallic silver. Solvents were then removed from all solutions through rotary evaporation to isolate the reaction products. For NMR analysis, the contents of each HTM vial **1** were redissolved in 0.6 mL toluene-d_8 and the NMR spectrum was then recorded. For EPR, the contents of each HTM vial **2** were redissolved in 1 mL of toluene for measurement.

X band EPR measurements were then carried out using a Bruker ELEXSYS E500 spectrometer. Samples in toluene solution were transferred into soda glass capillary tubes of 2 mm diameter, sealed at one end, and filled to a height of 20 mm for measurement. Samples measured under non-saturating conditions at 298K with typical parameters of: Microwave Frequency 9.8 GHz, Microwave Power 2 mW, Modulation Amplitude 1 G, and receiver gain 30 dB. Field correction was carried out by comparison to the Bruker Strong Pitch standard with g = 2.0028.

5 Materials and Methods

5.1 Synthesis

5.1.1 General Experimental

All reagents were purchased from commercial sources and used as received. Dry solvents were obtained from a Pure Solv 500 MD™ solvent purification system or purchased from Merck. All reactions were performed under nitrogen atmosphere. Brine, in this context, refers to a saturated solution of sodium chloride. Column chromatography was carried out using 60 Å silica gel purchased from Fluorochem/Doug Discovery®. Merck silica gel (60 Å) covered aluminium plates (F254) were used for thin layer chromatography. ^{1}H and ^{13}C NMR spectra were acquired using a Bruker AVIII 400 MHz spectrometer at 25 °C. All chemical shift values are reported in ppm relative to tetramethylsilane (TMS), and are referenced to the residual solvent peaks. All mass spectra were obtained using a Bruker Microtof-q for electrospray ionisation (ESI) measurements. Mass spectrometry measurements were carried out by Dr. Giovanni Enrico Rossi at the School of Chemistry. Infrared spectra were obtained using the neat solids on a Jasco FTIR-4100 spectrometer. Melting points were determined on a Reichert platform melting point apparatus.

Biph-OMeTPA and **inv-Ph-OMeTPA** were synthesised by Dr. Dylan Wilkinson of the Cooke group due to time constraints, as specified in the text.

5.1.2 Synthesis of Amide-Based Materials

4,4'-Dimethoxy-4''-nitrotriphenylamine (TPA-NO_2)[54]

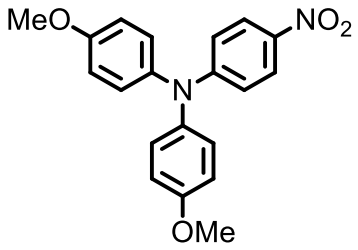

4-Nitroaniline (410 mg, 2.97 mmol), 1-methoxy-4-iodobezene (1458 mg, 6.23 mmol), copper powder (184.9 mg, 2.91 mmol), potassium carbonate (862.4 mg, 6.24 mmol), and 18-crown-6 (31.7 mg, 0.12 mmol) were added to a round-bottomed flask. The reagents were dissolved in DMF (5 mL). The mixture was stirred vigorously at reflux temperature (150 °C) for 16 hours. The product appeared on the TLC plate as an orange spot. The mixture was allowed to cool to 25 °C and was then diluted with ethyl acetate and extracted with H_2O and brine. The organic layer was dried over $MgSO_4$, filtered, and the solvent was then removed under vacuum.

The product was further purified by column chromatography (30% diethyl ether/petroleum ether), and then recrystallised from isopropanol to yield red crystals of the pure product (690 mg, 67%). Melting point: 132 – 134 °C (lit.[58,135] 125 – 129 °C). R_f = 0.37 (30% diethyl ether/petroleum ether). ^{1}H-NMR ($CDCl_3$, 400MHz) δ = 7.93 (dt, *J* = 9.36, 3.28 Hz, 2H), 7.07 (dt, *J* = 8.96, 2.24 Hz, 4H), 6.84 (dt, *J* = 9.00, 2.28 Hz, 4H), 6.69 (dt, *J* = 9.36, 2.16 Hz, 2H), 3.75 (s, 6H) ppm.

4-Amino-4',4''-dimethoxytriphenylamine (TPA-NH_2)[58]

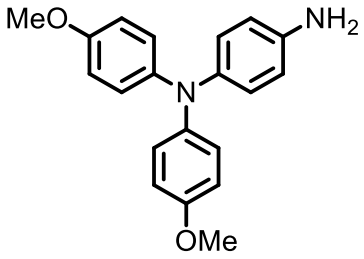

4,4'-Dimethoxy-4''-nitrotriphenylamine (404 mg, 1.15 mmol), 10% palladium on carbon (41.3 mg) were added to a round-bottomed flask. The reaction mixture was suspended in dry THF (10 mL). The mixture was vigorously stirred while degassing with nitrogen, during which time hydrazine hydrate (0.39 ml, 8.07 mmol) was added dropwise. The mixture was then heated at reflux temperature (66 °C) for 24 hours, causing the solution to lose its dark red colour. The product was observed on the TLC plate as a UV-visible spot that turned grey over time. After reaction completion, the mixture was cooled to 25 °C after which it was filtered through a short pad of celite to remove the palladium catalyst. Ethyl acetate was used to collect washings from the flask. The product was then ether/petroleum ether recrystallised from H_2O and collected as grey crystals (350 mg, 95% crude yield). The entire yield was used immediately for the final condensation step, due to its instability in air which was observed during NMR sample preparation. The colourless solution gradually turned dark grey when exposed to the air for a short period of time. R_f = 0.1 (30% diethyl ether/petroleum ether). ^{1}H-NMR ($CDCl_3$, 400MHz) δ = 6.95 (dt, *J* = 9.04, 2.24 Hz, 4H), 6.87 (dt, *J* = 8.68, 2.12 Hz, 2H), 6.76 (dt, *J* = 9.04, 2.32 Hz, 4H), 6.60 (dt, *J* = 8.68, 2.12 Hz, 2H), 3.77 (s, 6H) ppm. No amine protons are visible in the ^{1}H NMR spectrum, which is consistent with literature observations.[58]

3,4-Ethylenedioxythiophene-2,5-dicarbonyl chloride[54]

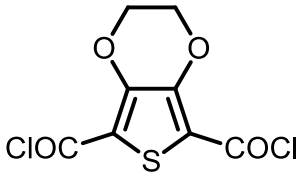

3,4-Ethylenedioxythiophene-2,5-dicarboxylic acid (300 mg; 1.30 mmol) was dissolved in THF (25 mL). DMF (0.01 mL; 0.14 mmol) was added. Thionyl chloride (0.23 mL, 3.12 mmol) was then added dropwise, causing the evolution of fumes and a colour change from a white suspension to a clear yellow solution. After heating the solution at 80 °C for 2 hours with vigorous stirring, the solution was left to cool down to 25 °C. The remaining thionyl chloride and THF were removed under vacuum, yielding the product acid chloride as a pale, yellow solid. The product was used immediately in the next step without purification, due to its sensitivity to moisture, causing hydrolysis back to the dicarboxylic acid starting material.

N^5,N^7-Bis(4-(bis(4-methoxyphenyl)amino)phenyl)-2,3-dihydrothieno [3,4-][1,4]dioxine-5,7-dicarboxamide (EDOT-Amide-TPA, HTM 1)[54]

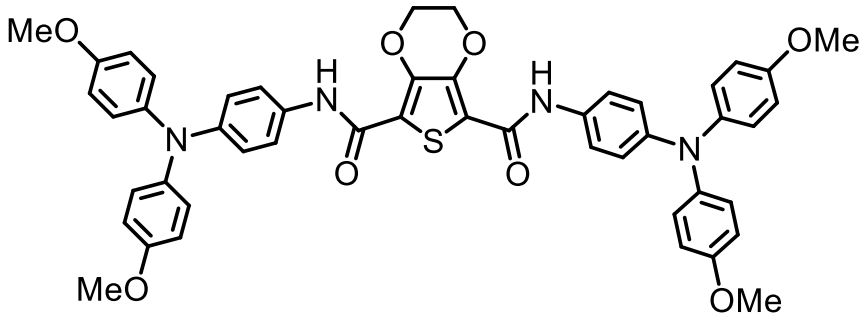

4-Amino-4',4''-dimethoxytriphenylamine (914.4 mg, 2.85 mmol) was dissolved in THF (10 mL) and transferred to a flask containing 3,4-ethylenedioxythiophene-2,5-dicarbonyl chloride (363.2 mg, 1.36 mmol). Triethylamine (0.44 mL, 3.13 mmol) was added, causing the evolution of fumes and the formation of an orange precipitate. The reaction mixture was heated to reflux (66 °C) while stirring vigorously for 1 hour. Heating was removed and the reaction mixture was allowed to cooled to 25 °C over 16 hours. The reaction mixture was filtered under vacuum to collect the orange precipitate, which was washed with 1:1 MeOH/H_2O and cold THF. A final wash with petroleum ether was done to remove residual THF. The product was then dried and collected as a yellow powder (790 mg, 70%). Melting point: 290 – 293°C. R_f = 0.27 (30% EtOAc/petroleum ether). ^{1}H-NMR ($CDCl_3$, 400MHz) δ = 8.36 (s, 2H), 7.39 (dt, *J* = 8.96, 1.96 Hz, 4H), 6.99 (dt, *J* = 8.96, 2.16 Hz, 8H), 6.91 (dt, J = 8.92, 1.96 Hz, 4H), 6.60 (dt, *J* = 9.00, 2.24 Hz, 8H), 4.54 (s, 4H), 3.79 (s, 12H) ppm.

^{13}C-NMR ($CDCl_3$, 101 MHz) δ = 158.19, 155.76, 145.71, 141.28, 138.92, 130.91, 126.18, 121.94, 121.44, 119.22, 114.81, 65.47, 55.65 ppm; FTIR: v(cm^{-1}): 3369 (weak), 2832 (very weak), 1662 (medium), 1600 (medium), 1537 (medium), 1498 (strong), 1372 (weak), 1233 (strong), 1094 (medium), 1032 (medium), 822 (broad, medium); HRMS (ESI$^+$): m/z calculated for $C_{48}H_{42}N_4O_8S^+$ $[M+Na]^+$: 857.2616; found: 857.2595.

N^5,N^7-Bis(4-(bis(4-methoxyphenyl)amino)phenyl)-N^5,N^7-dimethyl-2,3-dihydrothieno[3,4-b][1,4]dioxine-5,7-dicarboxamide (DEDOT-Amide-TPA, HTM 2)

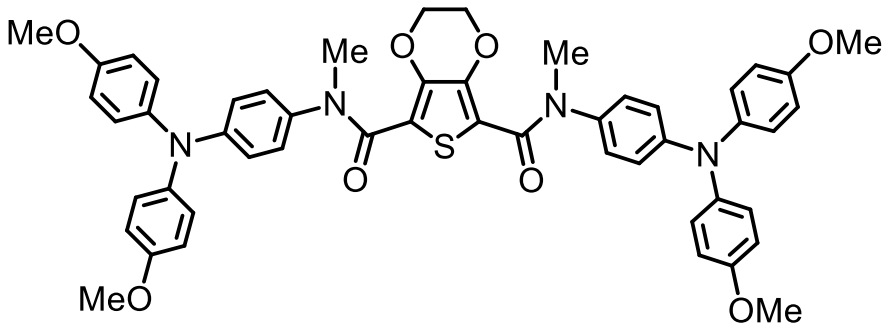

EDOT-Amide-TPA (1016 mg, 1.22 mmol) and sodium hydride (60% in mineral oil, 278 mg, 6.95 mmol) were dissolved in DMF (30 mL). The reaction mixture was heated at 130 °C for 2 hours, causing the reactants to dissolve, forming a red solution. The mixture was then allowed to cool down to around 40 °C after which iodomethane (0.23 mL, 3.60 mmol) was added dropwise. This caused the formation of a yellow precipitate in the flask. The reaction was left to stir at 40 °C over 16 hours. After reaction completion, product was fully precipitated by the addition of petroleum ether. The crude product was collected by vacuum filtration as a pale green powder and was purified by column chromatography (10% acetone/DCM) to yield the pure product as a yellow solid (507 mg, 48%). Melting point: 198 – 200 °C. ^{1}H NMR (400 MHz, $CDCl_3$) δ = 7.06 – 6.98 (8H, m), 6.87 – 6.79 (12H, m), 6.77 – 6.72 (4H, m), 3.96 (4H, s), 3.78 (12H, s), 3.34 (6H, s) ppm. ^{13}C NMR (101 MHz, $CDCl_3$) δ = 162.43, 156.17, 148.14, 140.80, 140.59, 135.71, 128.00, 126.79, 120.25, 114.90, 114.55, 64.49, 64.14, 55.57, 53.54, 38.44, 25.47 ppm. FTIR: v(cm^{-1}): 3041 (very weak), 2946 (weak), 2899 (weak), 2829 (weak), 1634 (strong), 1604 (medium), 1500 (strong), 1235 (strong), 1092 (strong), 1031 (strong), 815 (strong). HRMS (ESI$^+$): m/z calculated for $C_{50}H_{46}N_4O_8S^+$ $[M+H]^+$: 863.9872; found: 863.3121.

Thiophene-3,4-dicarbonyl dichloride[80]

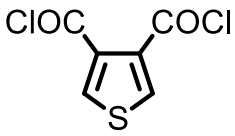

Thiophene-3,4-dicarboxylic acid (2.48 g, 14.43 mmol) was dissolved in dry THF (20 mL) and DMF (0.022 mL, 0.28 mmol) was added. Thionyl chloride (2.42 mL, 33.19 mmol) was added dropwise, causing the starting material to dissolve into a yellow solution. The solution was degassed with nitrogen and heated at reflux temperature (80 °C) for 2 hours.

The solution was then allowed to cool down to 25 °C, and the remaining thionyl chloride and solvent were removed under vacuum, yielding the resulting acid chloride in a quantitative yield as a brown solid (3.02 g crude yield). The product was used without further purification due to sensitivity to moisture, which causes hydrolysis of the acid chloride to yield the dicarboxylic acid starting material.

***N*$_3$,*N*$_4$-Bis(4-(bis(4-methoxyphenyl)amino)phenyl)thiophene-3,4-dicarboxamide (TPABT, HTM 3)** [80]

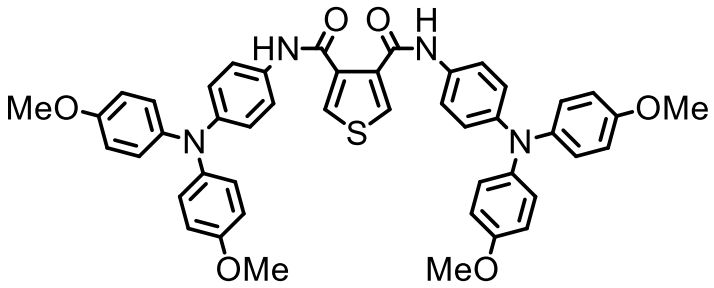

The total yield of thiophene-3,4-dicarbonyl dichloride was dissolved in dry THF (20 mL). 4-Amino-4',4''-dimethoxytriphenylamine (9.706 g, 30.29 mmol) was added, followed by triethylamine (4.62 mL, 33.18 mmol) which was slowly added to the solution causing the formation of a dark red solution. The reaction mixture was then heated to reflux for 2 hours. The mixture was allowed to cool to 25 °C over 16 hours. The mixture was concentrated under vacuum and diethyl ether (50 mL) was added to precipitate a pale yellow solid. After cooling for 16 hours in the freezer, the precipitate was filtered to give the crude product. The product was purified by column chromatography (10% acetone/DCM) to obtain an amorphous solid, that was then recrystallised from ethanol yielding pale yellow crystals of pure product (2.47 g, 22%). Melting point 226 – 229 °C. ^{1}H-NMR ($CDCl_3$, 400MHz) δ = 10.20 (2H, s), 7.94 (2H, s), 7.56 (4H, dt), 7.06 (8H, dt), 6.98 (4H, dt), 6.85 (8H, dt), 3.82 (12H, s) ppm.

^{13}C NMR (101 MHz, $CDCl_3$) δ = 162.48, 155.67, 145.70, 141.12, 135.64, 132.45, 131.23, 129.71, 129.05, 128.62, 128.23, 126.43, 126.09, 121.44, 114.69, 55.52 ppm. FTIR: ν(cm^{-1}): 3258 (very weak), 3100 (very weak), 3037 (weak), 2941 (weak), 2829 (weak), 1605 (strong), 1557 (medium), 1536 (weak), 1500 (strong), 1464 (medium), 1441 (weak), 1313 (weak), 1235 (strong), 1175 (medium), 1104 (medium), 1031 (strong), 892 (weak), 824 (strong), 779 (medium), 716 (medium), 632 (weak), 617 (weak), 572 (medium). HRMS (ESI^+): m/z calculated for $C_{46}H_{40}N_4O_6S^+$ ($M+H^+$) = 777.2669; found = 777.2747.

5.1.3 Synthesis of Imine-Based Materials

4-Methoxy-N-(4-methoxyphenyl)-N-phenylaniline (TPA-OMe) [136]

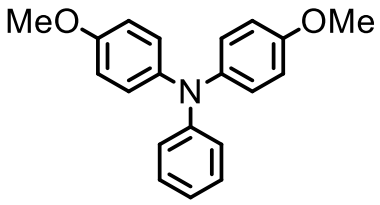

Methanol (50 mL) was added to a dry round-bottomed flask and cooled down to 0 °C in an ice bath. Sodium (3420 mg, 148.8 mmol) was added in small portions to the solvent, causing effervescence as the metal dissolved in the solvent. The mixture was left to stir at 0 °C until no traces of sodium metal were left in the reaction flask. After complete dissolution of the sodium was observed, 4-bromo-N-(4-bromophenyl)-N-phenylaniline (3000 mg, 7.48 mmol), copper (I) iodide (5810 mg, 30.5 mmol) and DMF (20 mL) were added, causing a colour change to an opaque green in the reaction flask. The mixture was degassed with nitrogen, heated to 100 °C, and stirred vigorously for 12 hours, during which time a colour change to a red-brown mixture was observed. The product appeared as a UV-visible spot on a TLC plate. The reaction mixture was then allowed to cool to 25 °C and washed three times with brine and once with distilled water. The organic layer was then collected and dried over anhydrous $MgSO_4$. The dried mixture was then filtered, and the solvent was removed under vacuum. The solid obtained was further purified by column chromatography (10% ethyl acetate/petroleum ether) to yield the pure product as an off-white solid. Recrystallisation from 2-propanol yielded white crystals of the product (1746 mg, 77%). Melting point 109 – 111°C. R_f = 0.67 (10% ethyl acetate/petroleum ether). ^{1}H-NMR ($CDCl_3$, 400MHz) δ = 7.20 – 7.13 (2H, m), 7.02 – 6.95 (4H, m), 6.94 – 6.85 (4H, m), 6.85 – 6.80 (1H, m), 6.80 – 6.69 (2H, m), 3.73 (6H, s) ppm.

4-(Bis(4-methoxyphenyl)amino)benzaldehyde (TPA-CHO) [137]

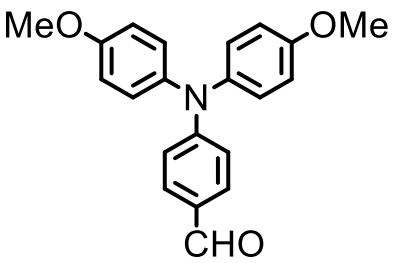

4-Methoxy-N-(4-methoxyphenyl)-N-phenylaniline (629 mg, 2.05 mmol) was dissolved in DMF (10 mL) and the mixture was cooled to 0 °C by stirring over an ice bath. Phosphorus (V) oxychloride (0.38 mL, 4.10 mmol) was added dropwise to the solution under a nitrogen atmosphere, causing the reaction mixture to turn from pale yellow to bright yellow. The mixture was heated to 90 °C with vigorous stirring for 12 hours, during which time the solution took on a dark red colour. The product appeared as a yellow spot on a TLC plate. The reaction was quenched when no more starting material was observed by TLC, by cooling to 25 °C and washing with a saturated solution of sodium acetate to neutralise the acid mixture. Further washing with distilled water was performed to remove traces of the sodium salt and other polar impurities, and the organic layer was then collected and dried over anhydrous $MgSO_4$. After filtering off the drying agent, the solvent was removed under vacuum, and the crude product was further purified by column chromatography (50% ethyl acetate/petroleum ether) and collected as a bright yellow solid (380 mg, 55%). Melting point 124 – 126°C. R_f = 0.72 (50% ethyl acetate/petroleum ether). ^{1}H-NMR ($CDCl_3$, 400MHz) δ = 9.75 (1H, s), 7.65 – 7.59 (2H, dt), 7.17 – 7.06 (4H, dt), 6.92 – 6.87 (4H, dt), 6.86 – 6.82 (2H, dt), 3.82 (6H, s).

4,4’-Diaminobiphenyl (Benzidine)[138]

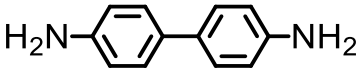

4,4'-Dinitro-1,1'-biphenyl (776 mg, 3.18 mmol) and 10% palladium on carbon (111.5 mg) were added to a clean and dry round-bottomed flask. Dry THF (20 mL) was added to suspend the reaction mixture, which was then degassed thoroughly with N_2 with vigorous stirring. Hydrazine hydrate (1.0 mL, 21.5 mmol) was added dropwise, after which the reaction mixture was heated at reflux temperature (66°C) for 16 hours. The product appeared as a UV-visible spot on the TLC plate. After reaction completion, the mixture was cooled to 25 °C after which it was filtered through a short pad of celite to remove the palladium catalyst. Ethyl acetate was used to collect washings from the flask. The product was then recrystallised from isopropanol and collected as off-white crystals (380 mg, 67%).

These were confirmed to be of excellent purity by NMR, and so were used directly in the final condensation step without further purification. R_f = 0.11 (50% ethyl acetate/petroleum ether). Melting point 124 – 126°C. ^{1}H-NMR ($CDCl_3$, 400MHz) δ = 7.42 – 7.28 (4H, dt), 6.77 – 6.68 (4H, dt), 3.65 (4H, s).

(N^4E,$N^{4'}$E)-N^4,$N^{4'}$-Bis(4-(bis(4-methoxyphenyl)amino)benzylidene)-[1,1'-biphenyl]-4,4'-diamine (Biph-OMeTPA, HTM 4 – synthesis by Dr. Dylan Wilkinson)[16]

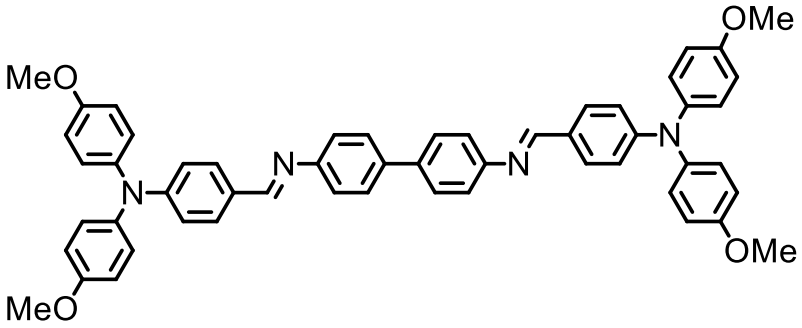

4-[bis(4-Methoxyphenyl)amino]benzaldehyde (350 mg, 1.05 mmol) and 4,4'-diaminobiphenyl (100 g, 0.52 mmol) were added to ethanol (30 mL) along with a spatula of anhydrous magnesium sulfate (~100 mg). The reaction was heated to reflux and a catalytic amount of *para*-toluenesulfonic acid (~1 mg) was added. The reaction mixture immediately turned red followed by the gradual precipitation of the yellow product. After 16 hours, The reaction was cooled to 25 °C. Distilled water was then added to quench the reaction and fully precipitate any dissolved product (500 mL). The product was separated from the reaction mixture by vacuum filtration, and was washed with a 10% NaOH solution (100 mL) followed by distilled water (100 mL). The crude product was allowed to dry under vacuum and then further purified by column chromatography using base-treated silica (20% ethyl acetate/petroleum ether with ~1% Et_3N). The product was then precipitated from dichloromethane/petroleum ether to yield a yellow solid (370 mg, 43%). Product decomposes around 85°C. ^{1}H NMR (400 MHz, $CDCl_3$) δ = 8.39 (s, 2H), 7.76 – 7.67 (m, 4H), 7.63 (d, J = 8.5 Hz, 4H), 7.30 – 7.23 (m, 4H), 7.18 – 7.07 (m, 8H), 6.93 (d, J = 8.8 Hz, 4H), 6.91 – 6.80 (m, 8H), 3.82 (s, 12H). ^{13}C NMR (100 MHz, $CDCl_3$) δ = 159.46, 156.67, 151.62, 139.85, 137.82, 129.97, 127.83, 127.49, 127.47, 121.41, 118.58, 114.90, 77.22, 55.51. FTIR: v(cm^{-1}): 2950 (weak), 2825 (weak), 1580 (strong), 1554 (medium), 1500 (strong), 1427 (medium), 1321 (medium), 1277 (medium), 1237 (strong), 1156 (strong), 1032 (strong), 824 (strong), 722 (medium), 673 (medium). HRMS (ESI+): m/z calculated for $[C_{54}H_{46}N_4O_4]H^+$ = 815.3592; found = 815.3588

(N^1,$N^{1'}$E,N^1,$N^{1'}$E)-N^1,$N^{1'}$-([1,1'-Biphenyl]-4,4'-diylbis(methanylylidene))bis(N^4,N^4-bis(4-methoxyphenyl)benzene-1,4-diamine) (inv-Biph-OMeTPA, HTM 5) [16]

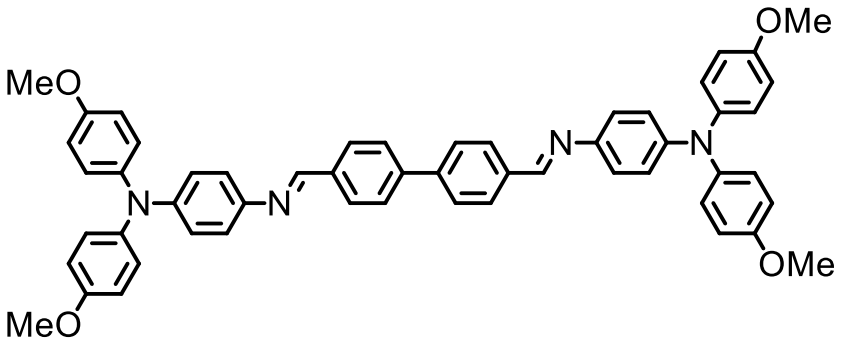

[1,1'-Biphenyl]-4,4'-dicarbaldehyde (201.9 mg, 0.96 mmol) and 4-amino-4',4''-dimethoxytriphenylamine (685.6 mg, 2.14 mmol) were dissolved in ethanol (20 mL) in a round-bottomed flask. A spatula of anhydrous magnesium sulfate (~100 mg) was added. The mixture was degassed with N_2, after which a catalytic amount of *para*-toluenesulfonic acid (~1 mg) was added. The reaction mixture immediately turned red, and the gradual precipitation of an orange product was observed. The reaction mixture was heated at reflux temperature (80°C) for 16 hours to ensure completion. The reaction was then allowed to cool down to 25 °C, after which distilled water (500 mL) was added to ensure complete precipitation of the product. The crude product was collected by filtration as an orange solid. The solid product was collected and dissolved in dichloromethane (30 mL) and washed with brine (2×100 mL) and distilled water (100 mL). The organic layer was collected and dried over anhydrous magnesium sulfate, which was then removed by filtration. The crude product was further purified by column chromatography using base-treated silica (40% ethyl acetate/petroleum ether and ~1% Et_3N). The pure product was collected as an orange solid (408 mg, 49%). R_f = 0.89 (40% ethyl acetate/petroleum ether and ~1% Et_3N). Melting point 166 – 169 °C. ^{1}H NMR (400 MHz, $CDCl_3$) δ = 8.55 (2H, s), 8.00 – 7.94 (4H, d), 7.78 – 7.71 (4H, d), 7.20 – 7.13 (4H, dt), 7.10 – 7.04 (8H, dt), 7.01 – 6.94 (4H, dt), 6.87 – 6.80 (8H, dt), 3.80 (12H, s). ^{13}C NMR (100 MHz, toluene-d_8) δ = 156.46, 148.02, 145.37, 142.78, 141.61, 137.46, 136.85, 129.47, 127.49, 126.70, 122.65, 122.07, 54.90. FTIR: ν(cm^{-1}): 3030 (weak), 2990 (weak), 2929 (weak), 2833 (weak), 1622 (medium), 1603 (medium) 1580 (weak), 1500 (strong), 1316 (medium), 1235 (strong), 1170 (medium), 1103 (medium), 1031 (strong), 880 (weak), 822 (strong), 719 (weak), 574 (medium). HRMS (ESI+): m/z calculated for $[C_{54}H_{46}N_4O_4]H^+$ = 815.3599, found = 815.3519.

($N^4E,N^{4'}E$)-$N^4,N^{4'}$-Dibenzylidene-[1,1'-biphenyl]-4,4'-diamine (Ph-Biph, Compound 6)

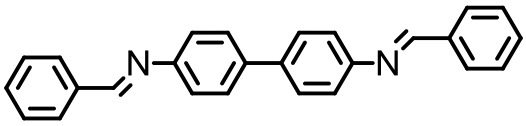

Benzidine (217.4 mg, 1.18 mmol) and benzaldehyde (0.23 mL, 2.28 mmol) were dissolved in ethanol (20 mL) in a round-bottomed flask, forming a yellow solution. A spatula of anhydrous magnesium sulfate (~100 mg) was added. The mixture was degassed with N_2, after which a catalytic amount of para-toluenesulfonic acid (~1 mg) was added. The solution immediately turned cloudy as the product precipitated out of solution as a yellow solid. The reaction mixture was allowed to continue stirring at 25 °C over 16 hours to ensure reaction completion. The reaction mixture was then diluted with petroleum ether (50 mL) in order to fully precipitate the product, which was then collected by filtration and recrystallised from toluene to form yellow crystals (256.3 mg, 65%). Melting point: 268 – 271 °C ^{1}H NMR (400 MHz, toluene-d_8) δ = 8.22 (s, 2H), 7.84 – 7.81 (d, 4H), 7.53 – 7.49 (d, 4H), 7.27 – 7.21 (d, 4H), 7.17 – 7.12 (m, 6H). Only solvent peaks are visible in the ^{13}C NMR, due to insufficient solubility in deuterated solvents combined with the low natural abundance of the ^{13}C nuclei. HRMS (ESI+): m/z calculated for $[C_{26}H_{20}N_2]H^+$ = 361.1706, found = 361.1697.

(N,N'E,N,N'E)-N,N'-([1,1'-Biphenyl]-4,4'-diylbis(methanylylidene))dianiline (Inv-Ph-Biph, Compound 7)

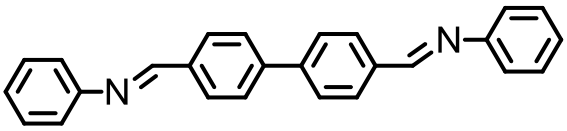

[1,1'-biphenyl]-4,4'-dicarbaldehyde (508 mg, 2.42 mmol) and aniline (0.45 mL, 5.0 mmol) were dissolved in ethanol (20 mL) in a round-bottomed flask, forming a brown solution. A spatula of anhydrous magnesium sulfate (~100 mg) was added. The mixture was degassed with N_2, after which a catalytic amount of para-toluenesulfonic acid (~1 mg) was added causing an immediate precipitation of a white solid. The reaction mixture was allowed to continue stirring at 25 °C for 16 hours to ensure reaction completion. The reaction mixture was then diluted with petroleum ether (50 mL) in order to fully precipitate the product, which was then collected by filtration and recrystallised from toluene to form pale yellow crystals (688.7 mg, 80%). Melting point 290 – 292°C. ^{1}H NMR (400 MHz, toluene-d_8) δ = 8.18 (2H, s), 7.87 – 7.84 (4H, d), 7.45 – 7.41 (4H, d), 7.25 – 7.15 (8H, m), 7.07 – 7.03 (2H, m). Only solvent peaks are visible in the ^{13}C NMR, due to insufficient solubility in deuterated solvents combined with the low natural abundance of the ^{13}C nuclei. HRMS (ESI+): m/z calculated for $[C_{26}H_{20}N_2]H^+$ = 361.1706, found = 361.1704.

(E)-4-Methoxy-N-(4-methoxyphenyl)-N-(4-((phenylimino)methyl)phenyl)aniline (Ph-OMeTPA, Compound 8)

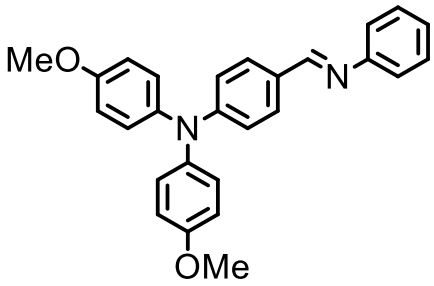

4-(Bis(4-methoxyphenyl)amino)benzaldehyde (500 mg, 1.50 mmol) and aniline (0.15 mL, 1.65 mmol) were dissolved in ethanol (20 mL) in a round-bottomed flask, forming a brown solution. A spatula of anhydrous magnesium sulfate (~100 mg) was added. The mixture was degassed with N_2, after which a catalytic amount of para-toluenesulfonic acid (~1 mg) was added causing an immediate colour change to a red solution. The reaction mixture was allowed to stir at 25 °C over 16 hours. Reaction was monitored by TLC until no limiting reagent (aldehyde) remained. The reaction was then diluted with petroleum ether (100 mL) in order to precipitate the product as pale brown crystals (235.7 mg, 38.5%). R_f = 0.77 (30% ethyl acetate/petroleum ether). Melting point 121 – 123°C. ^{1}H NMR (400 MHz, acetone-d_6) δ = 8.44 (s, 1H), 7.79 – 7.74 (d, 2H), 7.44 – 7.35 (m, 2H), 7.25 – 7.13 (m, 7H), 7.04 – 6.94 (m, 4H), 6.91 – 6.84 (m, 2H), 3.85 (s, 6H). ^{13}C NMR (100 MHz, acetone-d_6) δ = 160.3, 158.2, 153.8, 152.8, 140.7, 130.9, 130.1, 128.8, 126.1, 121.8, 118.7, 116.0, 55.95. HRMS (ESI+): m/z calculated for $[C_{27}H_{24}N_2O_2]H^+$ = 409.1918, found = 409.1925.

(E)-N^1-Benzylidene-N^4,N^4-bis(4-methoxyphenyl)benzene-1,4-diamine (Inv-Ph-OMeTPA, Compound 9 – synthesis by Dr. Dylan Wilkinson)

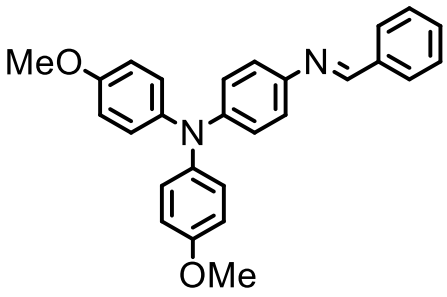

4-Amino-4',4''-dimethoxytriphenylamine (685.6 mg, 2.14 mmol) and benzaldehyde (0.24 mL, 2.35 mmol) were dissolved in ethanol (20 mL) to form a dark yellow solution. A spatula of anhydrous magnesium sulfate (~100 mg) was added. The mixture was degassed with N_2, after which a catalytic amount of para-toluenesulfonic acid (~1 mg) was added causing an immediate colour change to a dark red solution. The reaction mixture was allowed to stir at 25 °C over 16 hours.

Reaction was monitored by TLC until no limiting reagent (amine) remained. The crude product was concentrated under vacuum, and then further purified by column chromatography (1% triethylamine in petroleum ether) to collect the pure product as a waxy, brown solid (235.7 mg, 38.5%). R_f = 0.77 (30% ethyl acetate/petroleum ether). As the product was a very sticky substance, a melting point could not be recorded. ^{1}H NMR (400 MHz, acetone-d_6) δ = 8.64 (s, 1H), 7.98 – 7.91 (m, 2H), 7.54 – 7.47 (m, 3H), 7.23 (dt, 2H), 7.07 (dt, 4H), 6.92 (dt, 6H), 3.81 (s, 6H). ^{13}C NMR (100 MHz, acetone-d_6) δ = 158.22, 157.26, 148.59, 145.49, 141.95, 138.10, 131.80, 129.69, 129.42, 127.49, 123.06, 121.97, 115.80, 55.89. HRMS (ESI+): m/z calculated for $[C_{27}H_{24}N_2O_2]H^+$ = 409.1918, found = 409.1902

5.2 Characterisation

5.2.1 UV-Visible Absorption and Fluorescence Spectroscopy

All solution UV-vis spectra were recorded on a Shimadzu UV-3600 UV-Vis-NIR spectrophotometer. Solutions were prepared using purified powder samples at concentrations of 10^{-5} M. The choice of solvent therefore reflected the solubility of the target species at this concentration. Fluorescence measurements were carried out using a RF-5301PC spectrofluorimeter at a concentration of 10^{-5} M. For solutions with insufficient fluorescence at this concentration, 10^{-4} M solutions were used to obtain better signal. Stokes shifts in nanometres were estimated by subtracting the wavelengths of the maximum absorbance ($\boldsymbol{\lambda_{max}}$) from the wavelengths of the maximum emission ($\boldsymbol{\lambda_{em}}$). To estimate the Stokes shifts in wavenumbers, the same wavelengths were converted to centimetre units and the wavenumber then estimated as the inverse of these values. The Stokes shift is then described by Equation 5-1:[139]

$$\text{Stokes Shift } (\text{cm}^{-1}) = \Delta\nu = \frac{1}{\lambda_{\text{max}}}\ (\text{cm}^{-1}) - \frac{1}{\lambda_{\text{em}}}\ (\text{cm}^{-1}) \qquad (5\text{-}1)$$

All optical bandgaps (E_g) were estimated using Tauc plots, which were prepared by first converting the absorption wavelengths to photon energies using Equation 5-2:[131]

$$h\nu\ (\text{eV}) = \frac{1240}{\lambda\ (\text{nm})} \qquad (5\text{-}2)$$

Here, 1240 is the product of two constants, the Planck constant (6.626×10^{-34} J s) and the speed of light (3×10^{8} m s^{-1}).

The absorbances are then converted to the quantity $(\alpha h\nu)^2$ where 'α' is the absorption coefficient, estimated to be 2.303A, where A is the absorption at a particular wavelength. This value is derived as follows:

$$A = \log\left(\frac{I_0}{I}\right) \tag{5-3}$$

'I_0' is the incident light intensity and 'I' is the transmitted light intensity. 'I' is also given by Equation 5-4 through the Beer-Lambert relation:

$$I = I_0 e^{-\alpha b} \tag{5-4}$$

Here, 'b' is the path length of the cell. All solution absorption and fluorescence spectra presented in this thesis were measured in cuvettes with a path length of 1 cm, thus the path length can be disregarded from the exponent.

$$\frac{I}{I_0} = e^{-\alpha}$$

Taking reciprocals:

$$\frac{I_0}{I} = e^{\alpha}$$

Taking the natural logarithm and converting to $\log_{10}$:

$$\ln\left(\frac{I_0}{I}\right) = 2.303 \times \log\left(\frac{I_0}{I}\right) = \alpha$$

Using the relation in Equation 5-3, $\log\left(\frac{I_0}{I}\right)$ is substituted by the absorbance. Thus:

$$\alpha = 2.303A \tag{5-5}$$

The quantity $(\alpha h\nu)^2$ is then calculated by multiplying the absorption at each wavelength by 2.303 and the calculated photon energy. The exponent '2' is selected as it is appropriate for these systems which involve allowed transitions on direct bandgap semiconductors.[140]

All film UV-Visible absorption spectra were recorded on thin films deposited onto glass slides by solution spin coating. Films were affixed to the slits through which the laser beam passed by means of adhesive putty. Care was taken when handling films to avoid contamination through contact with nitrile gloves, thus the films were held only by their edges using plastic tweezers.

5.2.2 Cyclic Voltammetry

Cyclic and square wave voltammetry measurements were carried out using a CH Instruments 440A electrochemical analyser. All voltammograms of amide-based materials were measured using 10^{-4} M solutions in dry dichloromethane. Imine-based materials gave better resolution using dry DMF as the solvent. 6 mL of each solution was used for the measurement, to which tetrabutylammonium hexafluorophosphate was added at a concentration of 0.1 M as a supporting electrolyte. All solutions were thoroughly purged with nitrogen and kept in this inert atmosphere throughout all measurements.

Electrodes used were: platinum disc working electrode, platinum wire counter electrode, and a silver wire pseudo-reference electrode. Ferrocene was also added as an internal calibrant, and thus the reported spectra were referenced to the Fc^+/Fc redox couple. All electrodes were cleaned before use and between each measurement. The ionisation potentials (IPs) of all materials were estimated from the square wave voltammograms using Equation 5-6:[141]

$$IP = (E_{1/2} \text{ vs. } Fc^+/Fc) + 4.8 \text{ (eV)} \qquad (5\text{-}6)$$

5.2.3 Melting point determination

A Stuart Scientific SMP10 melting point apparatus was used for determining the melting points of all synthesised materials in this thesis. Small amounts of powder samples were introduced into capillary tubes, which were then inserted into the apparatus and heated at a rate of 10°C per minute for a rough determination of a melting point. Two further repetitions with slower heating were performed on fresh material for each sample in order to determine an average melting range for each material. The apparatus was allowed to cool down at least 25 °C below the melting point of each material before the next sample was introduced.

5.2.4 TGA and DSC

All thermochemical measurements were undertaken by Andy Monaghan at the School of Chemistry. TGA was performed using powder samples on a TA Instruments SDT Q600 V8.3 thermogravimetric analyser. Decomposition of the samples was taken to begin when > 5% of the mass of the sample is lost.

DSC was performed on a TA Instruments DSC2A-01781, ensuring that the heating did not exceed 10°C below their decomposition temperature determined from TGA. All the thermal analyses were carried out under N_2, at a rate of 10°C per minute.

5.2.5 DFT Calculations

DFT calculations on HTMs **1** – **3** were performed by Miriam Fsadni at Newcastle University at the PBE0/def2-sv(p) level of theory in Orca (v. 5.1) quantum chemistry package.[100] From these calculations, all molecular properties including the Debye dipole moments were obtained. Calculations were performed both in vacuum and in dichloromethane to approximate the effect of the film environment, using the CPCM model. Based on a procedure by Chi, *et al*. adapted to calculations performed at the PBE0/def2-sv(p) level,[115] a linear correction factor of -0.206 eV was applied to the HOMO energies for molecules optimised in dichloromethane. All other DFT calculations were performed using Gaussian09 software package, at the B3LYP/6-311G** level of theory. The geometries of all structures were optimised in vacuum at this level, ensuring convergence the end of all calculations. HOMO and LUMO energies as well as ESP maps were then extracted from the optimised structures.

5.3 Device fabrication and characterisation

5.3.1 Substrate Preparation

All glass substrates were cleaned by scrubbing both sides with a 2% solution of HELLMANEX III detergent in deionised water. More deionised water was then used to wash off the detergent, after which successive washings with acetone, ethanol, and deionised water were applied to remove traces of organic contaminants on the substrates. A nitrogen gun was used to push remaining water towards and off the corners of the substrate, so as to minimise evaporation which leaves undesirable residues on the substrate. Substrates used were: ITO-coated glass for conductivity and SCLC measurements, microscope slides (glass) for film UV-Visible absorption measurements, and FTO-coated glass for solar cells.

Patterned ITO substrates were transferred to a nitrogen-filled glove box for deposition after UV/Ozone cleaning for 15 minutes. This last step of cleaning ensures atomically clean surfaces by destroying any remaining organic contaminants through reaction with UV light, which generates free radicals and ions.

These react with ozone and atomic oxygen, which is also generated by the reaction of dioxygen with light. As a result, organic contaminants are converted into volatile molecules such as CO_2, H_2O, and N_2 which can leave the surface as gases.[142] The UV/Ozone cleaning procedure renders the substrate surface more hydrophilic, thus improving the surface wetting and further aiding the formation of even thin films. Deposition was started quickly after the UV/Ozone treatment as the hydrophilic effect is temporary.[143]

All cleaned substrates were patterned using a Rofin EasyMark IV F20 laser etcher. ITO was used for conductivity and SCLC measurements. For conductivity, an interdigitated pattern was etched onto ITO slides (Figure 5-1), creating a channel ~60 μm wide and 37.2 cm long across which the conductivity of a thin film could be measured. The resistance across the channel was measured for all the blank slides, and any short circuits arising from instrumental error were discarded.

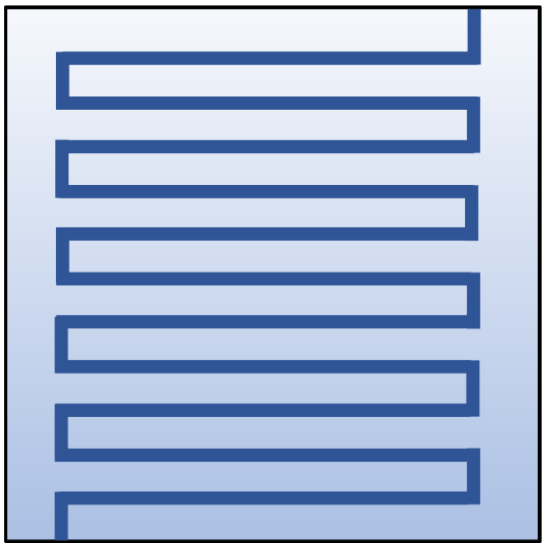

Figure 5-1: Schematic of the pattern etched into conductive ITO slides for conductivity measurements.

The cleaning procedure described above was repeated on all patterned substrates to remove conductive residues from the channel. Each substrate was then cut into individual slides by scribing with a diamond-tipped glass cutter and breaking off the individual slides, thus preparing them for subsequent film deposition procedures. Before depositing the first layer onto the slides, they were each treated in a UV/Ozone cleaner for 15 minutes to improve the surface wettability, immediately before depositing the films.

For SCLC measurements, a different pattern was etched into ITO that consisted of 8 pads in a symmetrical pattern, as shown in Figure 5-2. All patterned substrates were cleaned once again to remove conductive residues, and treated with UV/Ozone for 15 minutes prior to spin coating the HTM films.

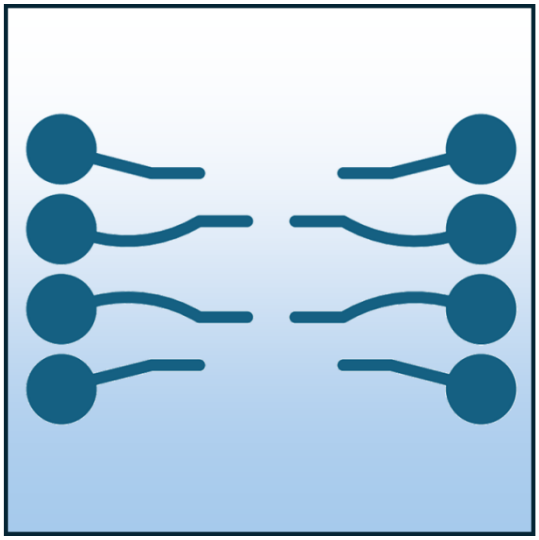

Figure 5-2: Schematic of the pattern etched into conductive ITO slides for SCLC measurements.

5.3.2 Preparation of spin coating solutions

All HTM solutions were prepared in CB solvent, using some proportion of CF to help dissolve HTMs with limited solubility such as HTMs **1** and **3**. If undissolved solute remains suspended in solution, it can result in significant defects in the resulting film morphology and a rough surface which complicates spectroscopy and film thickness measurements. CB, or mixtures of CB and CF were thus chosen as spin coating solvents for all HTMs in this thesis. In these mixtures, CF provides most of the solubilising power, except for **Spiro-OMeTAD** which is fully soluble in pure CB.[102] Compounds **1** – **3** have limited solubility in pure CB due to the polarity of the amide groups. However, attempts to deposit films from HTM solutions in pure CF resulted in incomplete and irregular HTM deposition on the substrate. This is likely due to a combination of high volatility and insufficient wetting of the CF solvent, which did not give the solvent time to adhere to and spread over the substrate surface before being propelled off the substrate. Therefore, a component of CB solvent was always present in the solvent mixtures, which provided adequate wetting and lead to far better quality films. Indeed, the CB/CF mixture is now widespread in numerous spin coating preparations for preparing high-quality, reproducible films.[16,54,80] The CB/CF mixture is also advantageous in that the individual components are both orthogonal to a potential perovskite underlayer, allowing their use in fabricating thin-film solar cells.[144]

The concentration of the HTM solution was chosen to reflect the needs of the experiments. As the final film thickness is related to the concentration of the solution, more concentrated solutions were used for measurements where a thicker film is required such as SCLC. An electronic balance was used to weigh all HTM powders and solvents, and solvent volumes were then calculated from the corresponding densities.

This was done to account for transfer errors arising from using the micropipettes, which are only calibrated for water. Using the weight of transferred solvent is a more accurate approach as it also accounts for solvent lost during transfer if droplets fall out of the micropipette before it is taken to the vial.

Volume of solvent is given by: $$V_{solv} = {}^{m_{solv}}/_{\rho_{solv}} \quad (5\text{-}7)$$

m_{solv} is the mass of solvent transferred and ρ_{solv} is its density. The concentration of stock solutions is then given by Equation 5-8

$$[S] = \frac{m_S}{RMM_S} \times \sum \frac{m_{solv}}{\rho_{solv}} \quad (5\text{-}8)$$

[S] is the concentration of the species in M. The RMM is the formula mass of the species in g mol^{-1}. $\sum \frac{m_{solv}}{\rho_{solv}}$ is the sum of volumes of each solvent in the component mixture. It is assumed that there is no significant change in volume upon mixing. For example, in the case of an HTM dissolved in a CB/CF mix, the concentration is given by:

$$[HTM] = \frac{m_{HTM}}{RMM_{HTM}} \times \left(\frac{m_{CB}}{\rho_{CB}} + \frac{m_{CF}}{\rho_{CF}}\right)$$

All masses are in units of g, and all densities are in g cm^{-3}.

5.3.3 Chemical doping

HTM doping was initiated by direct addition of known quantities of the chosen additive solution into HTM solutions prior to spin coating. From the known concentrations of the additive and HTM solutions, the number of moles of additive in a chosen volume could be calculated. The doping level is roughly quantified as the equivalents of additive relative to the HTM, unless specified otherwise such as in Chapter 2. The volume of additive stock added to the HTM solution is termed the doping volume, $\mathbf{V_d}$. The number of moles of additive in the doping volume ($\mathbf{mol_d}$) is given by:

$$mol_d = V_d \times [S] \quad (5\text{-}9)$$

where V_d is in L and [S] is in M.

The doping equivalents for each sample were then calculated using Equation 5-10.

$$\text{doping eq.} = \frac{mol_d}{mol_{HTM}} = \frac{mol_d}{{}^{m_{HTM}}/_{RMM_{HTM}}} \quad (5\text{-}10)$$

All solutions (HTMs and additives) were prepared and stored in a nitrogen-filled glove box, and were passed through syringe filters immediately before use.

5.3.4 Film deposition

HTM films were spin coated on the substrates using a static deposition method, wherein the volume of solution was deposited onto the substrate before spinning was initiated. The droplet was spread over the substrate using the edge of the pipette tip, and the substrate was then accelerated to 3000 rpm and spun at this speed for 5 seconds. This allowed the rapid formation of an even HTM film on the substrate. Films were visually inspected immediately after deposition. Any films that appeared cloudy were discarded – cloudiness in the film is indicative of a rough surface formed through uneven precipitation of the mixture on the substrate.

For each HTM film deposited for charge transport measurements on ITO, an identical film was also spin coated on a glass substrate for film thickness measurements. After deposition, all films were kept in a dessicator for one week to allow for oxidation reactions to take place (if **LiTFSI** was used) as well as the evaporation of residual solvent from the films.

5.3.5 Conductivity Measurements

The current-voltage characteristics of all HTMs were measured using a pulsed voltage setup whereby a range of voltages were randomly pulsed through our HTM films by means of a source meter, measuring the resulting current. The rapid pulsing of voltages, as opposed to a voltage sweep, has the effect of eliminating any effect of ionic conductivity, allowing selective measurement of electron/hole conductivity.

To complete the conductivity calculation, film thicknesses were measured using a DekTak XT contact profiler equipped with a 2 μm stylus tip. Three separate valleys were etched into a thin film of each HTM on glass using a metal ruler and a cotton bud wetted with dichloromethane. The film thickness was then measured as the height difference across the etched valley. Three separate measurements across each valley allowed calculation of the film thickness as an average of 9 measurements across each film, as well as the standard deviation.

The conductivity of the samples was calculated by taking the inverse of the resistivity equation:

$$\sigma = \frac{l}{RA} \tag{5-11}$$

Here, **σ** is the conductivity, **R** = resistance, **A** = cross-sectional area of the medium through which charges are flowing, and **l** is the conduction length. From the current-voltage curves, the resistance is extracted through calculating the gradient as 1/R, through Ohm's law (V = IR). Defining slope as **S**:

$$S = \frac{d(I)}{d(V)} = \frac{1}{R} \tag{5-12}$$

On the patterned slides (Figure 5-1), the conducting length is given by the channel width **W**. The cross-sectional area is thus given by the product of the total length of the channel (**L**) and the film thickness (**T**). Substituting these terms, Equation 5-13 is derived:

$$\sigma = \frac{d(I)}{d(V)} \times \frac{W}{T \cdot L} = \frac{W}{T \cdot L \cdot R} \tag{5-13}$$

$$\sigma = \frac{W \cdot S}{T \cdot L}$$

Error bars were calculated for all data points by propagating the uncertainty from the individual variables using a first-order Taylor approximation.[145] For a function **f(x)**, the first order Taylor expansion is:

$$f(x) \approx f(x_0) + \frac{\partial f}{\partial x}(x - x_0) \tag{5-14}$$

Here, **x** is some arbirtary value, $\mathbf{x_0}$ is a measured value some distance away from **x**, which forms the basis of the approximated function. The term $\mathbf{x - x_0}$ thus represents how far off the measured value is from the fixed value. $\frac{\partial \mathbf{f}}{\partial \mathbf{x}}$ is the partial derivative of the function with respect to **x**. When the difference between **x** and $\mathbf{x_0}$ is small, $\mathbf{x - x_0}$ represents the error in the measured value, **Δx**. The error **Δx** in **x** introduces uncertainty into **f(x)**, represented by **Δf**. Rewriting the Taylor expansion:

$$f(x_0 + \Delta x) \approx f(x_0) + \frac{\partial f}{\partial x}(\Delta x) \tag{5-15}$$

The error in the function **Δf** then becomes the difference in function values between the actual value and the approximation:

$$\Delta f = f(x_0 + \Delta x) - f(x_0) = \frac{\partial f}{\partial x}(\Delta x) \tag{5-16}$$

The error **Δf** may be quantified as a standard deviation since **Δx** represents the uncertainty in **x**. :

$$\Delta f = \sqrt{\sum (\Delta f)^2} \tag{5-17}$$

Substituting into Equation 5-16,

$$\Delta f = \sqrt{\sum \left(\frac{\partial f}{\partial x} \times \Delta x\right)^2} \tag{5-18}$$

To generalise for a function with more than one variable, $\mathbf{\Delta f(x_i)}$ is defined as the error of a function comprised of a series of independent variables $\mathbf{x_i}$. $\frac{\partial \mathbf{f}}{\partial \mathbf{x_i}}$ is the first partial derivative of the function with respect to each variable, which is multiplied by $\mathbf{\Delta x_i}$, the error in each variable. The error contribution from each variable is used to estimate the error in the function through Equation 5-19.

$$\Delta f(x_i) = \sqrt{\sum_{x_i} \left(\frac{\partial f}{\partial x_i} \times \Delta x_i\right)^2} \tag{5-19}$$

From the conductivity equation (Equation 5-13), there are three variables with associated error, these being:

1.) Channel width **W**: carries error **ΔW** which is the standard deviation of measured channel widths as measured using an optical microscope.
2.) Film thickness **T**: carries error **ΔT** which is the standard deviation of measured film thicknesses from the profilometer.
3.) Resistance **R**: carries error **ΔR** from the error of the fit of the IV characteristic graphs.

The channel length **L** is dictated by the pattern design (Figure 5-1) and is taken to have negligible error, so it was not included in the derivation. Thus the expanded propagated error equation becomes:

$$\Delta\sigma = \sqrt{\left(\frac{\partial\sigma}{\partial W} \times \Delta W\right)^2 + \left(\frac{\partial\sigma}{\partial T} \times \Delta T\right)^2 + \left(\frac{\partial\sigma}{\partial R} \times \Delta R\right)^2}$$

Solving partial derivatives, and substituting Equation 5-13:

$$\frac{\partial}{\partial W}\left(\frac{W \cdot S}{T \cdot L}\right) = \frac{S}{T \cdot L} = \mathbf{\frac{\sigma}{W}}$$

$$\frac{\partial}{\partial T}\left(\frac{W \cdot S}{T \cdot L}\right) = -\frac{W \cdot S}{T^2 \cdot L} = -\mathbf{\frac{\sigma}{T}}$$

$$\frac{\partial}{\partial R}\left(\frac{W \cdot S}{T \cdot L}\right) = -\frac{W \cdot S}{T \cdot L \cdot R} = -\mathbf{\frac{\sigma}{R}}$$

Substituting:

$$\Delta\sigma = \sqrt{\left(\frac{\sigma}{W}\right)^2 \Delta W^2 + \left(-\frac{\sigma}{T}\right)^2 \Delta T^2 + \left(-\frac{\sigma}{R}\right)^2 \Delta R^2}$$

Simplifying,

$$\Delta\sigma = \sigma\sqrt{\left(\frac{\Delta W}{W}\right)^2 + \left(\frac{\Delta T}{T}\right)^2 + \left(\frac{\Delta R}{R}\right)^2}$$

$$\Delta\sigma = \sigma\sqrt{\left(\frac{\Delta W}{W}\right)^2 + \left(\frac{\Delta T}{T}\right)^2 + (S\Delta R)^2} \quad (5\text{-}20)$$

Equation 5-16 was then used to calculate the propagated error in the conductivity values obtained from each measurement, taking into account the error introduced through the thickness, resistance, and measured channel widths.

5.3.6 SCLC Measurements

HTM films for mobility measurements through the SCLC technique were prepared through solution spin coating, using concentrated solutions of the HTMs and slower spin coating speeds to ensure maximum thickness of the HTM film. “Hole-only” devices were then prepared with the following architecture: FTO/ HTM/Ag.[146] Silver electrodes were deposited on all devices by Fraser J. Angus of the Docampo group. The mask used for electrode deposition is identical to the etching pattern used on the ITO slide, but rotated 90° so as to be perpendicular to the etched pattern. The result is a device wherein the conductivity could be measured through the HTM film (i.e. vertical conductivity) through 8 pads as shown in Figure 5-3.

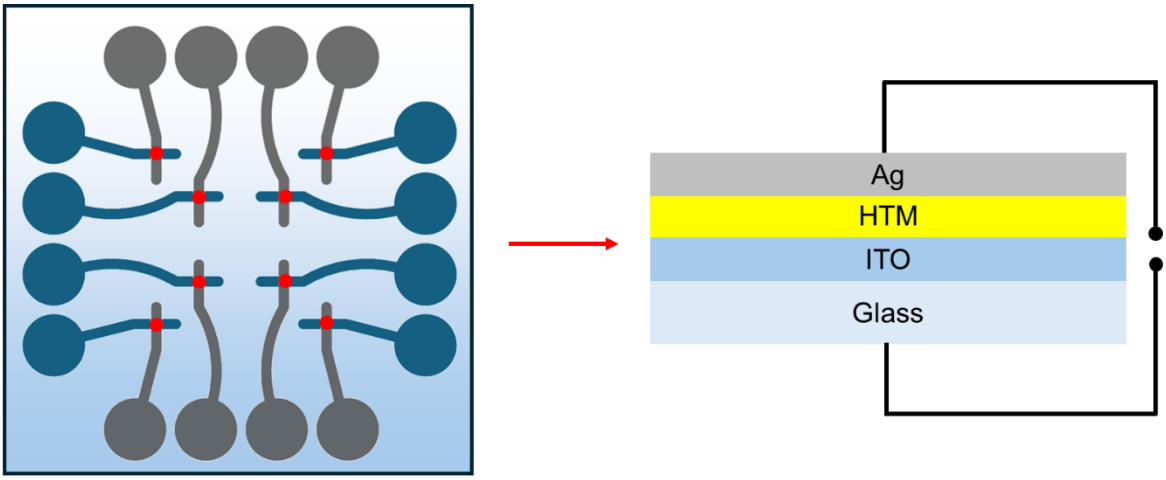

Figure 5-3: Schematic of the finished hole-only devices prepared for SCLC measurement. The 8 pads marked in red are the points at which the current flow through the HTM film were measured by a pulsed JV method.

Current-voltage characteristics were then measured through similar pulsed JV methodology as used for conductivity measurements. Assuming Ohmic contacts, the current at higher voltages is taken to be space-charge limited. Carrier mobility was thus estimated by fitting to the Mott-Gurney law (Equation 5-21):[9]

$$J = \frac{9}{8}\varepsilon_0\varepsilon_r\mu\frac{V^2}{L^3} \quad (5\text{-}21)$$

Here, **J** is the current density, $\boldsymbol{\varepsilon_0}$ is the permittivity of free space, $\boldsymbol{\varepsilon_r}$ is the relative permittivity of the HTM, **μ** is the hole mobility, **V** is the applied voltage and **L** is the HTM film thickness. Current density was estimated for a channel of area 0.26 mm^2. Relative permittivity is taken to be 3, which is common for most OSs.[147]

5.3.7 PSC Devices

All solar cell devices in this thesis were prepared and analysed by Marcin Giza of the Docampo group.

Synthesis of perovskite precursors

To prepare the methylammonium (**MAI**) crystals, methylamine (40% wt. in H_2O, 79.1 mL, 913.7 mmol) and hydriodic acid (without stabilisers, 55% wt. in H_2O, 50 mL, 365.5 mmol) were added to a round bottomed flask containing ethanol (300 mL) and stirred for 16 hours at 25 °C, resulting in a colourless solution. Residual ethanol and water were removed through rotary evaporation, yielding a white, crystalline solid. The crude product was washed with diethyl ether, then recrystallised three times from dry ethanol, and washing with diethyl ether after each procedure to yield white crystals of the pure product (19.152 g, 33%). The triple-cation (FAMACs) perovskite solution was prepared by mixing 0.07M cesium iodide (**CsI**), 0.08 M MAI, 1.32 M formamidinium iodide (**FAI**), 1.54M lead (II) iodide ($\mathbf{PbI_2}$) and 0.5M methylammonium chloride (**MACl**) and dissolving them in a 4:1 v/v DMF:DMSO mixed solvent system.[116]

Solar Cell Fabrication

Solar cells were fabricated and analysed by Marcin Giza of the Docampo group.

Substrates (FTO Glass) were washed with Hellmanex III 2 vol% in deionised (DI) water, rinsed with DI-water, acetone, ethanol and DI-water again, and finally dried with nitrogen. Substrates were treated with UV/ozone for 20 minutes. A compact titanium oxide ($\mathbf{TiO_2}$) electron transport layer was deposited via a sol-gel method. 370 μL of titanium (IV) isopropoxide was added to 2.5 mL of IPA under constant stirring. This solution was then mixed with 35 μL of 2M HCl in 2.5 mL of IPA under stirring. 300 μL of the TiO_2 solution was spincoated dynamically onto the substrates at 2000 rpm for 45s. The films were annealed at 150°C for 30 minutes, followed by 500°C for 45 minutes.

Substrates were then transferred into a nitrogen-filled glovebox, where a layer of 4-(1',5'-Dihydro-1'-methyl-2'H-[5,6]fullereno-C_{60}-I_h-[1,9-c]pyrrol-2'-yl)benzoic acid ($\mathbf{C_{60}}$**-SAM**, 0.5 mg/mL in chlorobenzene) was deposited via spin coating 50 μL at 2000 rpm for 30 seconds, and annealed at 100°C for 10 minutes.

A layer of Al_2O_3 nanoparticles (0.16 wt% in IPA) was then deposited via spin coating 50 µL at 2000 rpm for 30 seconds, and annealed at 100°C for 10 minutes.[111]

The perovskite solution was deposited via a two-step spin coating process. 50 µL of solution was dynamically deposited onto the substrates during a 10 s, 1000 rpm step, followed by a 40s/4000 rpm step. At the last 5 seconds of the second step, 300 µL of ethyl acetate antisolvent was deposited onto the substrate. The substrates were then annealed at 100°C for 45 minutes, and at 150°C for 10 minutes. HTM films were then deposited onto the perovskite layer as described in Section 2.4.8.

6 Final Conclusions

The work presented in this thesis seeks to advance the understanding of molecular OSs as HTMs, by exploring the fundamental characteristics that influence charge transport. Using accessible amide and imine condensation chemistry, families of related HTM structures were synthesised, allowing in-depth analysis of how the molecular structure influences charge transport. Key findings reveal that enhancing dipole ordering within HTM films minimises energetic noise. Introducing zero-dipole pairs through hydrogen bonding significantly improves conductivity and hole mobility, showcasing the critical role of ordered dipole arrangements (Chapter 2). Chapter 3 then focused on the importance of tailored chemical doping for HTMs, highlighting that lithium coordination efficiency varies with molecular structure and directly impacts the doping efficiency and resulting conductivity. This stresses the need for designing doping strategies specific to each HTM to optimise charge transport properties. Even with increased electron density around the carbonyl group, HTM **2** resists lithium coordination resulting in lower conductivity, challenging assumptions about coordination as a universal solution towards increased conductivity. Chapter 4 further examines the impact of molecular orientation in imine-based HTMs. It shows that bond orientation directly affects electron density distribution and oxidation behaviour, with certain orientations leading to improved charge transport and others proving ineffective as HTMs. This chapter highlights that even minor structural changes, such as imine bond orientation, can drastically alter conductivity. When two isomeric imine bond orientations are possible, the preferred orientation is thus the one that directs electron density away from the molecular core and towards the TPA donor groups.

Overall, the work in this thesis can be used to set up design rules for understanding the structural factors that lead to good charge transport in organic HTMs. In general, tight packing of the HTL is desired to ensure short hole hopping distances. A robust intermolecular hydrogen bonding network between HTM molecules may help achieve tight packing by allowing molecules to adhere close together in the spin coating solution and eventually in the thin film. This close packing is further aided by strong dipoles in the HTM molecules which self-neutralise through a preferred antiparallel arrangement, thus reducing the energetic noise within the film providing optimal conditions for hole hopping. These findings pave the way for new, cost-effective materials with improved performance in organic electronics. Section 7 below details additional experimental work that would further strengthen the conclusions in this thesis.

7 Future Work

To further verify the effects that differing intermolecular interactions may have on film morphology, it would be helpful to conclusively show the presence of molecular pairs in thin films or the amorphous powder. Since it has been demonstrated that even a low molecular pair concentration could be responsible for greatly improved charge transport, the proportion of antiparallel pairs formed during spin coating may be below the limit of detection of many analytical techniques that could be used to identify them. In solution, these would include two-dimensional NMR techniques like nuclear Overhauser effect spectroscopy (**NOESY**) or diffusion-ordered spectroscopy (**DOSY**) techniques. Solid-state nuclear magnetic resonance (**SS-NMR**) may prove useful for this purpose, as it is routinely used to detect and characterise dimers in the solid state.[148,149]

The degree of molecular pairing may also be improved through a slower and more controlled film forming process. Many parameters may be adjusted during the spin coating procedure that affect the properties of the final film, such as solution and substrate temperature, solution concentration and viscosity, spin speed, deposition volume, and acceleration of the substrate in the case of static spin coating. Molecular pairing may be improved if spin coating is performed using a slower acceleration and spin speed. This yields thicker films that are formed more slowly thus allowing more time for pair formation. Using a procedure such as dip coating, where the HTM film is allowed to form much more slowly, may help to further reduce the dipole disorder by allowing further opportunities for pair formation as the HTL is formed.[150]

Finally, future HTMs may be designed with tailored structures that promote long-range pairing beyond simple pairs. Crystalline OSs are the logical extreme of this design, which benefit from extended intermolecular interactions to achieve closer packing and enhanced mobilities. Oligacenes and oligothiophenes are prime examples of such materials, where extended π-π stacking facilitates hole transport through the crystal. From the results presented above, one possible next step would be to design a HTM that possesses both a strong central dipole as well as intermolecular hydrogen bonding moieties. This HTM should be able to form supramolecular structures where each repeating unit aligned antiparallel to the adjacent unit such that the whole assembly has net zero dipole. Establishing long-range order via hydrogen bonding may sufficiently approximate the charge transport landscape of organic crystals, imparting improved mobility.

Having illustrated the importance of lithium coordination in Chapter 3, the next logical step is to design a HTM that utilises these design rules. For optimal reactivity, a HTM with carbonyl groups situated close to the HOMO is beneficial for increasing the likelihood for a successful ionisation. In the case of amide materials, the resulting iminium cation should be suitably stabilised. As resonance and hydrogen bonding appear to have beneficial effects on the stability of the coordinated species, tertiary amides such as HTM **2** are not suitable for iminium cation stability due to decreased planarity around the amide bond as well as no hydrogen bonding capacity.

While all our results point towards the proposed amide doping mechanism in Scheme 3-1, some further analysis would be required to confirm the fate of the lithium cations. ^{7}Li-NMR would be an appropriate tool for this purpose, as lithium in different bonding environments would display different signals as they form in the film. The technique has previously been used in **LiTFSI**-oxidised systems to reveal the redox properties of this dopant, and in the case of the **Spiro-OMeTAD** doping mechanism, lithium was found to form the oxides Li_2O and Li_2O_2 at the end of the doping reaction.[35] For amide HTMs, resolved signals may even be obtained for coordinated vs. uncoordinated lithium which would strengthen the mechanism even further. SCXRD would also provide unambiguous evidence for the presence of lithium coordination through the carbonyl groups. SCXRD also gives information about bond lengths within the crystal, which would also help confirm our DFT observations that the intramolecular H-bonding in our amide HTMs is preserved upon Li^+ coordination. Producing appropriate single crystals for SCXRD may prove challenging due to the large number of different species in a doped HTM solution which are likely to co-crystallise together.

The studies in Chapter 4 described the dissimilar reactivity towards chemical oxidants for two isomeric imine HTMs. The identification of the reaction products would help solidify the claims laid out therein. While it is abundantly clear through NMR and EPR experiments that HTM **5** has a far greater propensity towards forming stable radicals through oxidation, the fate of HTM **4** upon reaction with **AgTFSI** remains unclear. As successful doping was not achieved with this isomer, it would be useful to conduct further NMR analysis to determine the fate of the HTM.

The conclusions above can help inform the design of novel HTM materials. Inspired from the crystal structure of HTM **3**, novel analogues can be proposed wherein dipoles are paired within the same molecule, by using two covalently bonded units of thiophene or **EDOT** as the core. This ensures that each dipole is paired up and cancelled out within the same molecule. Thiophene cores may be fused to further enforce the antiparallel arrangement, although covalent bonds may suffice, as conjugation across the ring systems may serve to planarise the cores thus orienting the dipoles antiparallel.

Non-conjugated (amide bonds) and conjugated (imine bonds) variants may be proposed (Figure 7-1), with the imine alternatives employing the N-to-TPA orientation as deemed to be suitable in Chapter 4.

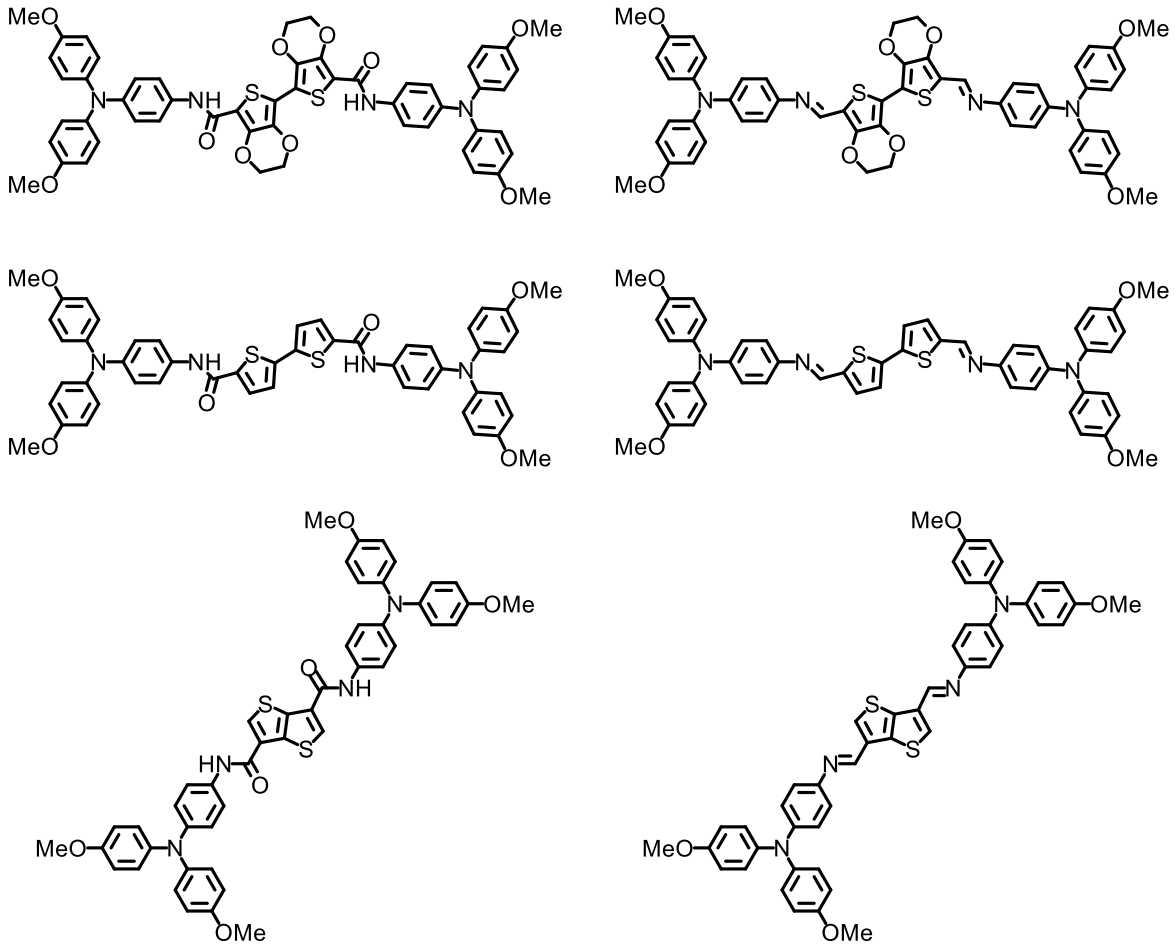

Figure 7-1: Proposed novel HTM structures, informed from the conclusions in this thesis.

The HTM structures above may prove to have the ideal structural conditions for hole hopping through a thin film. However, it is difficult to predict this with absolute certainty prior to synthesising the materials and fabricating the thin films. For these purposes, the methodologies in this thesis present useful guidelines for the characterisation of future HTMs.

8 References

1 G. W. Kim, H. Choi, M. Kim, J. Lee, S. Y. Son and T. Park, *Adv. Energy Mater.*, 2020, **10**, 1–30.

2 C. Enriquez, D. Hodges, A. De La Rosa, L. Valerio Frias, Y. Ramirez, V. Rodriguez, D. Rivera and A. Telles, *Perovskite Solar Cells*, 2019.

3 UNFCCC, What is the Paris Agreement?, https://unfccc.int/process-and-meetings/the-paris-agreement/what-is-the-paris-agreement, (accessed 8 December 2020).

4 COP26: Negotiations Explained, https://ukcop26.org/wp-content/uploads/2021/11/COP26-Negotiations-Explained.pdf, (accessed 2 April 2022).

5 H. J. Snaith, *J. Phys. Chem. Lett.*, 2013, **4**, 3623–3630.

6 S. R. Forrest, *Organic electronics: Foundations to applications*, 2020.

7 M. Schwarze, W. Tress, B. Beyer, F. Gao, R. Scholz, C. Poelking, K. Ortstein, A. A. Günther, D. Kasemann, D. Andrienko and K. Leo, *Science*, 2016, **352**, 1446–1449.

8 S. Poncé, W. Li, S. Reichardt and F. Giustino, *Rep. Prog. Phys.*, 2020, **83**, 036501.

9 J. Nelson, *The Physics of Solar Cells*, Imperial College Press, 2003.

10 S. Morab, M. M. Sundaram and A. Pivrikas, *Coatings*, 2023, **13**, 1657.

11 D. Poplavskyy, *Hole Injection and Transport in Organic Semiconductors*, University of London, 2003.

12 S. V. Novikov, *Phys. Stat. Sol. B*, 2003, **236**, 119–128.

13 T. J. Pope, T.; Giret, Y.; Fsadni, M.; Docampo, P.; Groves, C.; Penfold, *Org. Electron.*, 2023, **115**, 106760 (1–6).

14 J. L. Bredas, *Mater. Horizons*, 2014, **1**, 17–19.

15 R. Li, C. Li, M. Liu, P. Vivo, M. Zheng, Z. Dai, J. Zhan, B. He, H. Li, W. Yang, Z. Zhou and H. Zhang, *CCS Chem.*, 2022, **41**, 3084–3094.

16 M. L. Petrus, A. Music, A. C. Closs, J. C. Bijleveld, M. T. Sirtl, Y. Hu, T. J. Dingemans, T. Bein and P. Docampo, *J. Mater. Chem. A*, 2017, **5**, 25200–25210.

17 J. Roncali, *Chem. Rev.*, 1997, **97**, 173–205.

18 N. N. Greenwood and A. Earnshaw, *Chemistry of the Elements*, Butterworth Heinemann, 2005.

19 X. Sun, Z. Zhu and Z. Li, *Front. Optoelectron.*, 2022, **15**, 1–14.

20 S. Wang, H. Zhang, B. Zhang, Z. Xie and W. Y. Wong, *Mater. Sci. Eng. R Reports*, 2020, **140**, 100547.

21 W. Yin, L. Pan, T. Yang and Y. Liang, *Molecules*, 2016, **21**, 837.

22 L. Grandell and M. Höök, *Sustain.*, 2015, **7**, 11818–11837.

23 C. Ballif, F.-J. Haug, M. Boccard, P. J. Verlinden and G. Hahn, *Nat. Rev. Mater.*, 2022, **7**, 597–616.

24 M. A. Green, *Prog. Photovoltaics Res. Appl.*, 2009, **17**, 183–189.

25 C. C. Farrell, A. I. Osman, R. Doherty, M. Saad, X. Zhang, A. Murphy, J. Harrison,

A. S. M. Vennard, V. Kumaravel, A. H. Al-Muhtaseb and D. W. Rooney, *Renew. Sustain. Energy Rev.*, 2020, **128**, 109911.

26 R. G. Charles, M. L. Davies and P. Douglas, *Electronics Goes Green 2016+,* 2017, 1–8.

27 V. Coropceanu, J. Cornil, D. A. da S. Filho, Y. Olivier, R. Silbey and Jean-Luc Brédas, *Chem. Rev.*, 2007, **107**, 926–952.

28 P. Uprety, I. Subedi, M. M. Junda, R. W. Collins and N. J. Podraza, *Sci. Rep.*, 2019, **9**, 1–12.

29 T. H. Schloemer, J. A. Christians, J. M. Luther and A. Sellinger, *Chem. Sci.*, 2019, **10**, 1904–1935.

30 S. Daskeviciute-Geguziene, Y. Zhang, K. Rakstys, C. Xiao, J. Xia, Z. Qiu, M. Daskeviciene, T. Paskevicius, V. Jankauskas, A. M. Asiri, V. Getautis and M. K. Nazeeruddin, *Adv. Funct. Mater.*, 2023, **33**, 2208317 (1–8).

31 J. Urieta-Mora, I. García-Benito, A. Molina-Ontoria and N. Martín, *Chem. Soc. Rev.*, 2018, **47**, 8541–8571.

32 X. Yin, Z. Song, Z. Li and W. Tang, *Energy Environ. Sci.*, 2020, **13**, 4057–4086.

33 T. Leijtens, I. K. Ding, T. Giovenzana, J. T. Bloking, M. D. McGehee and A. Sellinger, *ACS Nano*, 2012, **6**, 1455–1462.

34 N. A. N. Ouedraogo, G. O. Odunmbaku, B. Guo, S. Chen, X. Lin, T. Shumilova and K. Sun, *ACS Appl. Mater. Interfaces*, 2022, **14**, 34303–34327.

35 A. Abate, T. Leijtens, S. Pathak, J. Teuscher, R. Avolio, M. E. Errico, J. Kirkpatrik, J. M. Ball, P. Docampo, I. McPherson and H. J. Snaith, *Phys. Chem. Chem. Phys.*, 2013, **15**, 2572–2579.

36 M. U. Munshi, G. Berden, J. Martens and J. Oomens, *Phys. Chem. Chem. Phys.*, 2017, **19**, 19881–19889.

37 S. Wang, W. Yuan and Y. S. Meng, *ACS Appl. Mater. Interfaces*, 2015, **7**, 24791–24798.

38 J. Y. Seo, H. S. Kim, S. Akin, M. Stojanovic, E. Simon, M. Fleischer, A. Hagfeldt, S. M. Zakeeruddin and M. Grätzel, *Energy Environ. Sci.*, 2018, **11**, 2985–2992.

39 M. Armand, F. Endres, D. R. MacFarlane, H. Ohno and B. Scrosati, *Nat. Mater.*, 2009, **8**, 621–629.

40 J. Burschka, F. Kessler, M. K. Nazeeruddin and M. Grätzel, *Chem. Mater.*, 2013, 25, 2986–2990.

41 J. H. Noh, N. J. Jeon, Y. C. Choi, M. K. Nazeeruddin, M. Grätzel and S. Il Seok, *J. Mater. Chem. A*, 2013, **1**, 11842–11847.

42 W. Zhang, F. Zhang, B. Xu, Y. Li, L. Wang, B. Zhang, Y. Guo, J. M. Gardner, L. Sun and L. Kloo, *ACS Appl. Mater. Interfaces*, 2020, **12**, 33751–33758.

43 J. Luo, C. Jia, Z. Wan, F. Han, B. Zhao and R. Wang, *J. Power Sources*, 2017, **342**, 886–895.

44 M. Liu, S. Dahlström, C. Ahläng, S. Wilken, A. Degterev, A. Matuhina, M. Hadadian, M. Markkanen, K. Aitola, A. Kamppinen, J. Deska, O. Mangs, M. Nyman, P. D. Lund, J. H. Smått, R. Österbacka and P. Vivo, *J. Mater. Chem. A*, 2022, **10**, 11721–11731.

45 J. Wang, X. Wu, Y. Liu, T. Qin, K. Zhang, N. Li, J. Zhao, R. Ye, Z. Fan, Z. Chi and Z. Zhu, *Adv. Energy Mater.*, 2021, **11**, 2100967 (1–9).

46 D. Fan, R. Zhang, Y. Li, C. Shan, W. Li and Y. Wang, *Front. Chem.*, 2021, **9**, 1–11.

47 W. Wang, J. Zhou and W. Tang, *J. Mater. Chem. A*, 2022, **10**, 1150–1178.

48 W. H. Nguyen, C. D. Bailie, E. L. Unger and M. D. McGehee, *J. Am. Chem. Soc.*, 2014, **136**, 10996–11001.

49 S. Ma, G. Yuan, Y. Zhang, N. Yang, Y. Li and Q. Chen, *Energy Environ. Sci.*, 2022, **15**, 13–55.

50 Z. Hawash, L. K. Ono, S. R. Raga, M. V. Lee and Y. Qi, *Chem. Mater.*, 2015, **27**, 562–569.

51 Y. Shen, K. Deng, Q. Chen, G. Gao and L. Li, *Adv. Mater.*, 2022, **34**, 2200978 (1–9).

52 P. Xia, D. Guo, S. Lin, S. Liu, H. Huang, D. Kong, Y. Gao, W. Zhang, Y. Hu and C. Zhou, *Sol. RRL*, 2021, **5**, 2100408 (1–9).

53 H. Li, K. Fu, A. Hagfeldt, M. Grätzel, S. G. Mhaisalkar and A. C. Grimsdale, *Angew. Chemie - Int. Ed.*, 2014, **53**, 4085–4088.

54 M. L. Petrus, K. Schutt, M. T. Sirtl, E. M. Hutter, A. C. Closs, J. M. Ball, J. C. Bijleveld, A. Petrozza, T. Bein, T. J. Dingemans, T. J. Savenije, H. Snaith and P. Docampo, *Adv. Energy Mater.*, 2018, **8**, 1–11.

55 S. Chen, X. Dai, S. Xu, H. Jiao, L. Zhao and J. Huang, *Science*, 2021, **373**, 902–907.

56 F. M. Rombach, S. A. Haque and T. J. Macdonald, *Energy Environ. Sci.*, 2021, **14**, 5161–5190.

57 S. Tsarev, I. K. Yakushchenko, S. Y. Luchkin, P. M. Kuznetsov, R. S. Timerbulatov, N. N. Dremova, L. A. Frolova, K. J. Stevenson and P. A. Troshin, *Sustain. Energy Fuels*, 2019, **3**, 2627–2632.

58 M. L. Petrus, T. Bein, T. J. Dingemans and P. Docampo, *J. Mater. Chem. A*, 2015, **3**, 12159–12162.

59 P. K. Samanta and R. Misra, *J. Appl. Phys.*, 2023, **133**, 020901 (1–17).

60 R. Qin, W. Yang, S. Li, T. K. Lau, Z. Yu, Z. Liu, M. Shi, X. Lu, C. Z. Li and H. Chen, *Mater. Chem. Front.*, 2019, **3**, 513–519.

61 S. Khodabakhsh, D. Poplavskyy, S. Heutz, J. Nelson, D. D. C. Bradley, H. Murata and T. S. Jones, *Adv. Funct. Mater.*, 2004, **14**, 1205–1210.

62 D. Alberga, G. F. Mangiatordi, F. Labat, I. Ciofini, O. Nicolotti, G. Lattanzi and C. Adamo, *J. Phys. Chem. C*, 2015, **119**, 23890–23898.

63 X. Liu, T. Li, C. Zhang and X. Li, *Angew. Chemie - Int. Ed.*, 2023, **62**, 1–7.

64 M. Yano, Y. Ishida, K. Aoyama, M. Tatsumi, K. Sato, D. Shiomi, A. Ichimura and T. Takui, *Synth. Met.*, 2003, **137**, 1275–1276.

65 N. Elgrishi, K. J. Rountree, B. D. McCarthy, E. S. Rountree, T. T. Eisenhart and J. L. Dempsey, *J. Chem. Educ.*, 2018, **95**, 197–206.

66 U. P. Ojha, C. Ramesh and A. Kumar, *J. Polym. Sci. Part A Polym. Chem.*, 2005, **43**, 5823–5830.

67 L. Han, K. Zhang, H. Ishida and P. Froimowicz, *Macromol. Chem. Phys.*, 2017, **218**, 1–10.

68 N. S. Myshakina, Z. Ahmed and S. A. Asher, *J. Phys. Chem. B*, 2008, **112**, 11873–11877.

69 A. M. Martin, R. S. Butler, I. Ghiviriga, R. E. Giessert, K. A. Abboud and R. K. Castellano, *Chem. Commun.*, 2006, 4413–4415.

70 J. Kroon, L. M. J. Kroon-Batenburg, B. R. Leeflang and J. F. G. Vliegenthart, *J. Mol. Struct.*, 1994, **322**, 27–31.

71 K. P. Goetz and O. D. Jurchescu, *Conductivity measurements of organic materials using field-effect transistors (FETs) and space-charge-limited current (SCLC) techniques*, Elsevier Ltd., 2nd edn., 2018.

72 Y. Ma, S. Zhang, Y. Yi, L. Zhang, R. Hu, W. Liu, M. Du, L. Chu, J. Zhang, R. Xia, X. Li and W. Huang, *J. Mater. Chem. C*, , DOI:10.1039/d2tc00283c.

73 B. Domercq, J. Yu, B. R. Kaafarani, T. Kondo, S. Yoo, J. N. Haddock, S. Barlow, S. R. Marder and B. Kippelen, *Mol. Cryst. Liq. Cryst.*, 2008, **481**, 80–93.

74 C. Dong, Z. K. Wang and L. S. Liao, *Energy Technol.*, 2020, **8**, 1–14.

75 M. Saliba, T. Matsui, J. Y. Seo, K. Domanski, J. P. Correa-Baena, M. K. Nazeeruddin, S. M. Zakeeruddin, W. Tress, A. Abate, A. Hagfeldt and M. Grätzel, *Energy Environ. Sci.*, 2016, **9**, 1989–1997.

76 R. H. Young and J. J. Fitzgerald, *J. Phys. Chem.*, 1995, **99**, 4230–4240.

77 S. K. Mishra and N. Suryaprakash, *Molecules*, 2017, **22**, 1–41.

78 S. Tiwari, N. Arya, S. K. Mishra and N. Suryaprakash, *RSC Adv.*, 2021, **11**, 15195–15202.

79 F. Jensen, *Introduction to Computational Chemistry*, Wiley, 2nd edn., 2007.

80 E. A. A. Alkhudhayr, D. Sirbu, M. Fsadni, B. Vella, B. T. Muhammad, P. G. Waddell, M. R. Probert, T. J. Penfold, T. Hallam, E. A. Gibson and P. Docampo, *ACS Appl. Energy Mater.*, 2023, 11573–11582.

81 T. P. Osedach, T. L. Andrew and V. Bulović, *Energy Environ. Sci.*, 2013, **6**, 711–718.

82 Merck, https://www.sigmaaldrich.com/GB/en (accessed 29 May 2024).

83 Y. Liang, J. Chen, X. Zhang, M. Han, R. Ghadari, N. Wu, Y. Wang, Y. Zhou, X. Liu and S. Dai, *J. Mater. Chem. A*, 2022, **10**, 10988–10994.

84 B. Lyu, L. Yang, Y. Luo, X. Zhang and J. Zhang, *J. Mater. Chem. C*, 2022, **10**, 10775–10798.

85 F. Lamberti, F. Schmitz, W. Chen, Z. He and T. Gatti, *Sol. RRL*, 2021, **5**, 1–21.

86 S. Gangala and R. Misra, *J. Mater. Chem. A*, 2018, **6**, 18750–18765.

87 U. Bach, D. Lupo, P. Comte, J. E. Moser, F. Weissörtel, J. Salbeck, H. Spreitzer and M. Grätzel, *Lett. to Nat.*, 1998, **395**, 583–585.

88 R. M. Edkins, E. Hayden, J. W. Steed and K. Fucke, *Chem. Commun.*, 2015, **51**, 5314–5317.

89 A. Kalra, P. Tishmack, J. W. Lubach, E. J. Munson, L. S. Taylor, S. R. Byrn and T. Li, *Mol. Pharm.*, 2017, **14**, 2126–2137.

90 Z. Xiao, K. Sun, J. Subbiah, S. Ji, D. J. Jones and W. W. H. Wong, *Sci. Rep.*, 2014, **4**, 2–8.

91 A. K. Patel, S. K. Mishra, K. Krishnamurthy and N. Suryaprakash, *RSC Adv.*, 2019, **9**, 32759–32770.

92 J. Wu, A. Fechtenkötter, J. Gauss, M. D. Watson, M. Kastler, C. Fechtenkötter, M. Wagner and K. Müllen, *J. Am. Chem. Soc.*, 2004, **126**, 11311–11321.

93 C. Shao, M. Grüne, M. Stolte and F. Würthner, *Chem. - A Eur. J.*, 2012, **18**, 13665–13677.

94 P. Froimowicz, K. Zhang and H. Ishida, *Chem. Eur. J.*, 2016, **22**, 2691–2707.

95 V. R. Mundlapati, S. Gautam, D. K. Sahoo, A. Ghosh and H. S. Biswal, *J. Phys. Chem. Lett.*, 2017, **8**, 4573–4579.

96 S. H. Gellman, G. P. Dado, G. B. Liang and B. R. Adams, *J. Am. Chem. Soc.*, 1991, **113**, 1164–1173.

97 A. G. Nurioglu, H. Akpinar, F. E. Kanik, D. Toffoli and L. Toppare, *J. Electroanal. Chem.*, 2013, **693**, 23–27.

98 J. Matern, Z. Fernández, N. Bäumer and G. Fernández, *Angew. Chem.*, 2022, **61**, e202203783 (1-9).

99 Z. Hawash, L. K. Ono, S. R. Raga, M. V. Lee and Y. Qi, *Chem. Mater.*, 2015, **27**, 562–569.

100 F. Neese, *WIREs Comput. Mol. Sci.*, 2012, **2**, 73–78.

101 F. Weigend and R. Ahlrichs, *Phys. Chem. Chem. Phys.*, 2005, **7**, 3297–3305.

102 M. Cariello, N. Pant, A. H. Harkiss, F. M. Tracey, J. Cameron, P. J. Skabara, P. J. Holliman, P. Docampo and G. Cooke, *Mol. Syst. Des. Eng.*, 2022, **7**, 899–905.

103 B. Acemioglu, M. Arik, H. Efeoglu and Y. Onganer, *J. Mol. Struct.*, 2001, **548**, 165–171.

104 S. K. Patil, M. N. Wari, C. Y. Panicker and S. R. Inamdar, *Spectrochim. Acta - Part A Mol. Biomol. Spectrosc.*, 2014, **123**, 117–126.

105 M. Bouhassoune, S. L. M. va. Mensfoort, P. A. Bobbert and R. Coehoorn, *Org. Electron.*, 2009, **10**, 437–445.

106 Y. Li, H. Li, C. Zhong, G. Sini and J. L. Brédas, *npj Flex. Electron.*, 2017, **1**, 1–7.

107 T. Zhang, F. Wang, H.-B. Kim, I.-W. Choi, C. Wang, E. Cho, R. Konefal, Y. Puttisong, K. Terado, L. Kobera, M. Chen, M. Yang, S. Bai, B. Yang, J. Suo, S.-C. Yang, X. Liu, F. Fu, H. Yoshida, W. Chen, J. Brus, V. Coropceanu, A. Hagfelt, J.-L. Brédas, M. Fahlman, D. S. Kim, Z. Hu and F. Gao, *Science*, 2021, **377**, 495–501.

108 A. Magomedov, E. Kasparavičius, K. Rakstys, S. Paek, N. Gasilova, K. Genevičius, G. Juška, T. Malinauskas, M. K. Nazeeruddin and V. Getautis, *J. Mater. Chem. C*, 2018, **6**, 8874–8878.

109 B. Xu, J. Huang, H. Ågren, L. Kloo, A. Hagfeldt and L. Sun, *ChemSusChem*, 2014, **7**, 3252–3256.

110 K. Pydzińska-Białek, V. Drushliak, E. Coy, K. Załęski, J. Flach, J. Idígoras, L. Contreras-Bernal, A. Hagfeldt, J. A. Anta and M. Ziółek, *ACS Appl. Mater. Interfaces*, 2020, **12**, 30399–30410.

111 M. Schultes, N. Giesbrecht, J. Küffner, E. Ahlswede, P. Docampo, T. Bein and M. Powalla, *ACS Appl. Mater. Interfaces*, 2019, **11**, 12948–12957.

112 S. Wang, Z. Huang, X. Wang, Y. Li, M. Günther, S. Valenzuela, P. Parikh, A. Cabreros, W. Xiong and Y. S. Meng, *J. Am. Chem. Soc.*, 2018, **140**, 16720–16730.

113 J. Lu, A. D. Scully, J. Sun, B. Tan, A. S. R. Chesman, S. Ruiz Raga, L. Jiang, X. Lin, N. Pai, W. Huang, Y. B. Cheng, U. Bach and A. N. Simonov, *J. Phys. Chem. Lett.*, 2019, **10**, 4675–4682.

114 T. S. Sherkar, C. Momblona, L. Gil-Escrig, J. Ávila, M. Sessolo, H. J. Bolink and L. J. A. Koster, *ACS Energy Lett.*, 2017, **2**, 1214–1222.

115 W. J. Chi, Q. S. Li and Z. S. Li, *Nanoscale*, 2016, **8**, 6146–6154.

116 J. Petrulevicius, Y. Yang, C. Liu, M. Steponaitis, E. Kamarauskas, M. Daskeviciene, A. S. R. Bati, T. Malinauskas, V. Jankauskas, K. Rakstys, M. G. Kanatzidis, E. H. Sargent and V. Getautis, *ACS Appl. Mater. Interfaces*, 2024, **16**, 7310–7316.

117 Y. Saygili, H. S. Kim, B. Yang, J. Suo, A. B. Muñoz-Garcia, M. Pavone and A. Hagfeldt, *ACS Energy Lett.*, 2020, **5**, 1271–1277.

118 J. Burschka, A. Dualeh, F. Kessler, E. Baranoff, N. L. Cevey-Ha, C. Yi, M. K. Nazeeruddin and M. Grätzel, *J. Am. Chem. Soc.*, 2011, **133**, 18042–18045.

119 F. Lamberti, T. Gatti, E. Cescon, R. Sorrentino, A. Rizzo, E. Menna, G. Meneghesso, M. Meneghetti, A. Petrozza and L. Franco, *Chem*, 2019, **5**, 1806–1817.

120 H. Chen, D. Bryant, J. Troughton, M. Kirkus, M. Neophytou, X. Miao, J. R. Durrant and I. McCulloch, *Chem. Mater.*, 2016, **28**, 2515–2518.

121 P. Agarwala and D. Kabra, *J. Mater. Chem. A*, 2017, **5**, 1348–1373.

122 Z. Yu and L. Sun, *Adv. Energy Mater.*, 2015, **5**, 1500213 (1–17).

123 Y. Kim, G. Kim, N. J. Jeon, C. Lim, J. Seo and B. J. Kim, *ACS Energy Lett.*, 2020, **5**, 3304–3313.

124 H. Bao, H. Liu, S. Wang, J. Ma and X. Li, *Chem. Eng. J.*, 2022, **433**, 133534 (1–9).

125 S. G. Kim, T. H. Le, T. de Monfreid, F. Goubard, T. T. Bui and N. G. Park, *Adv. Mater.*, 2021, **33**, 1–10.

126 S. Fantacci, F. De Angelis, M. K. Nazeeruddin and M. Grätzel, *J. Phys. Chem. C*, 2011, **115**, 23126–23133.

127 D. Balasubramanian and R. Shaikh, *Biopolymers*, 1973, **12**, 1639–1650.

128 R. L. Jones, L. J. Morris, C. G. Collins Rice, Z. R. Turner and D. O'Hare, *Phys. Chem. Chem. Phys.*, 2023, 15463–15468.

129 A. J. Pell, G. Pintacuda and C. P. Grey, *Prog. Nucl. Magn. Reson. Spectrosc.*, 2019, **111**, 1–271.

130 S. Pluczyk, M. Vasylieva and P. Data, *J. Vis. Exp.*, 2018, 1–13.

131 M. L. Petrus, R. K. M. Bouwer, U. Lafont, S. Athanasopoulos, N. C. Greenham and T. J. Dingemans, *J. Mater. Chem. A*, 2014, **2**, 9474–9477.

132 D. Sek, A. Iwan, B. Jarzabek, B. Kaczmarczyk, J. Kasperczyk, Z. Mazurak, M. Domanski, K. Karon and M. Lapkowski, *Macromolecules*, 2008, **41**, 6653–6663.

133 P. Nitschke, B. Jarząbek, M. Vasylieva, D. Honisz, J. G. Małecki, M. Musioł, H. Janeczek and P. Chaber, *Synth. Met.*, 2021, **273**, 116689 (1–14).

134 C. Geffroy, E. Grana, T. Bessho, S. Almosni, Z. Tang, A. Sharma, T. Kinoshita, F. Awai, E. Cloutet, T. Toupance, H. Segawa and G. Hadziioannou, *ACS Appl. Energy Mater.*, 2020, **3**, 1393–1401.

135 G. S. Liou and C. W. Chang, *Macromolecules*, 2008, **41**, 1667–1674.

136 R. Matsubara, T. Shimada, Y. Kobori, T. Yabuta, T. Osakai and M. Hayashi, *Chem. Asian. J.*, 2016, **11**, 2006–2010.

137 X. R. Jia, H. J. Yu, J. Chen, W. J. Gao, J. K. Fang, Y. S. Qin, X. K. Hu and G. Shao, *Chem. Eur. J.*, 2018, **24**, 19053–19059.

138 J. P. Jeon, Y. J. Kim, S. H. Joo, H. J. Noh, S. K. Kwak and J. B. Baek, *Angew. Chem. Int.*, 2023, **62**, e202217416 (1-7).

139 B. Valeur and M. N. Berberan-Santos, *Molecular Fluorescence: Principles and*

Applications, Wiley Publishing, 2012.

140 Ł. Haryński, A. Olejnik, K. Grochowska and K. Siuzdak, *Opt. Mater.*, 2022, **127**, 11205 (1–9).

141 E. Speckmeier, T. G. Fischer and K. Zeitler, *J. Am. Chem. Soc.*, 2018, **140**, 15353–15365.

142 J. R. Vig, *J. Vac. Sci. Technol. A*, 1985, **3**, 105–113.

143 H. C. Wei and G. D. J. Su, *IEEE Photonics Technol. Lett.*, 2012, **24**, 300–302.

144 L. Calió, S. Kazim, M. Grätzel and S. Ahmad, *Angew. Chemie*, 2016, **55**, 14522–14545.

145 H. W. Coleman and W. G. Steele, *AIAA Journal*, 1995, **33**, 1888–1896.

146 P. Huang, A. Hernández, S. Kazim, J. Ortiz, Á. Sastre-Santos and S. Ahmad, *Sustain. Energy Fuels*, 2020, **4**, 6188–6195.

147 H. J. Snaith and M. Grätzel, *Appl. Phys. Lett.*, 89, 26, 2006, 262114 (1-3)

148 B. H. Meier, F. Graf and R. R. Ernst, *J. Chem. Phys.*, 1982, **76**, 767–774.

149 A. B. Elliott, G. Versfeld, M. D. Halling, J. S. Miller and J. K. Harper, *Chem. - A Eur. J.*, 2020, **26**, 230–236.

150 P. Yimsiri and M. R. MacKley, *Chem. Eng. Sci.*, 2006, **61**, 3496–3505.

9 Appendix

9.1 NMR Spectra

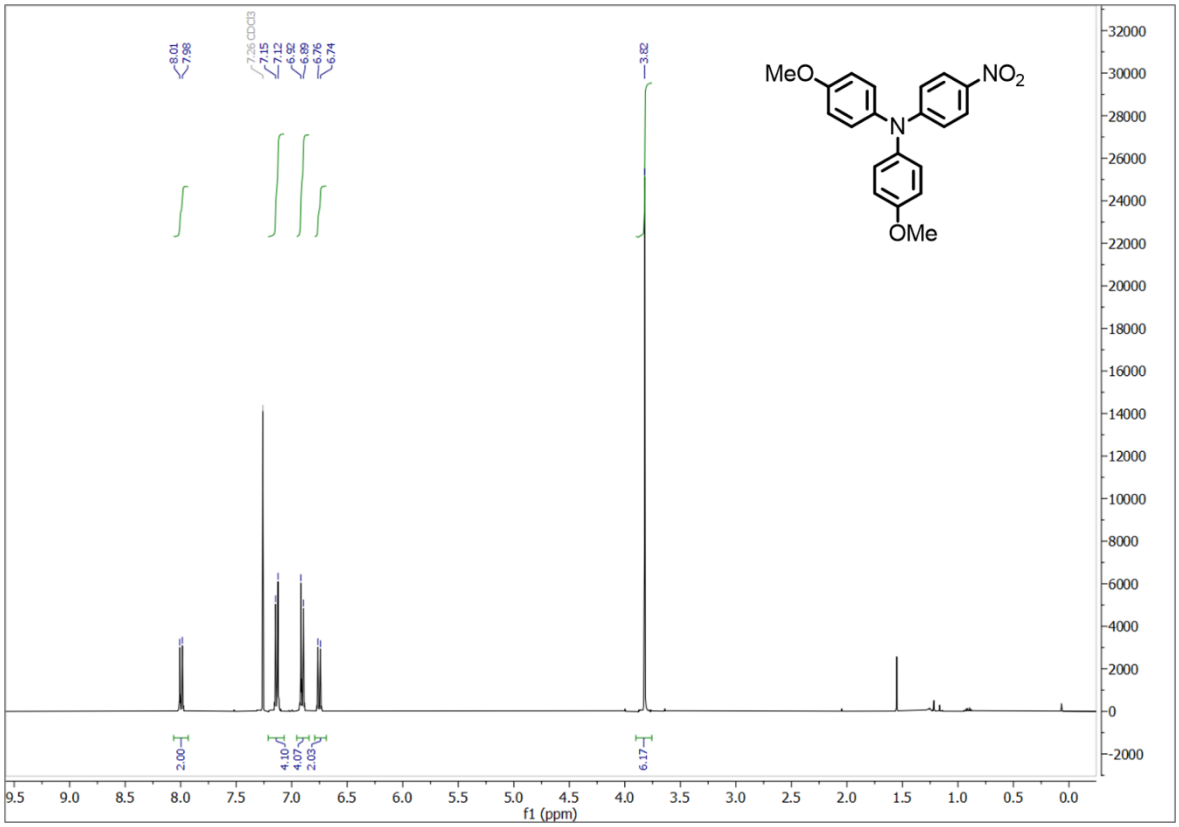

Figure 9-1: ^{1}H-NMR spectrum of TPA-NO_2, recorded in $CDCl_3$ at 25 °C, referenced to the $CDCl_3$ peak.

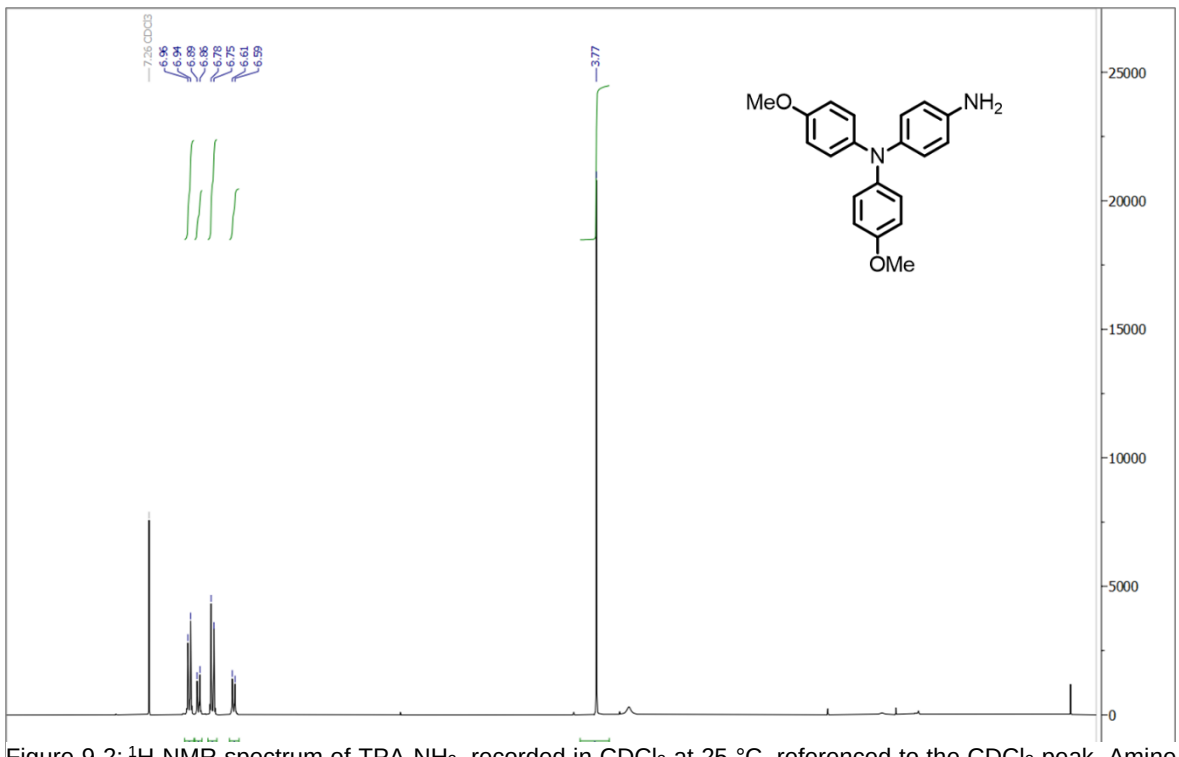

Figure 9-2: ^{1}H-NMR spectrum of TPA-NH_2, recorded in $CDCl_3$ at 25 °C, referenced to the $CDCl_3$ peak. Amine peaks are not visible which is consistent with observations from the literature.[58]

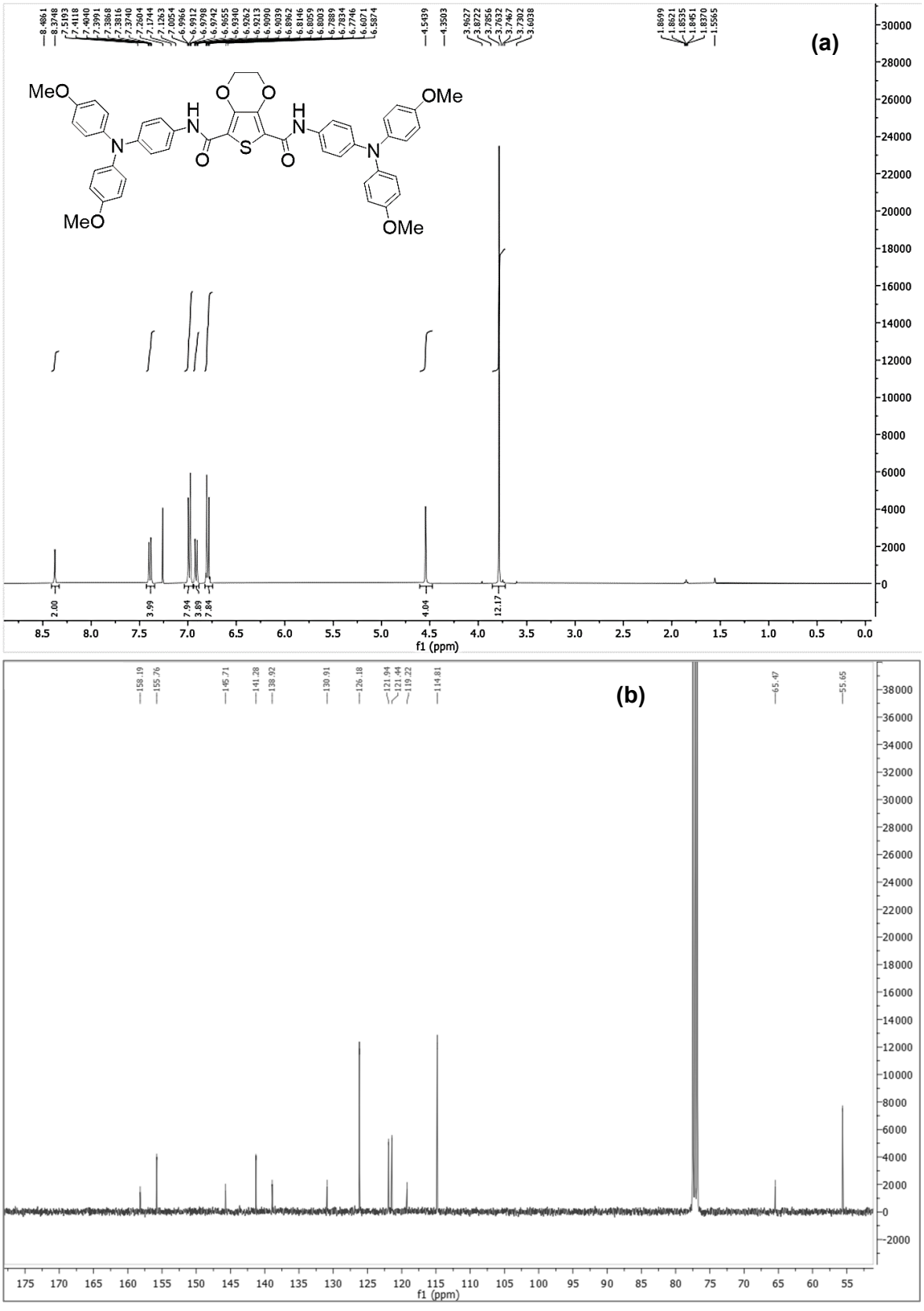

Figure 9-3: (a) ^{1}H-NMR and (b) ^{13}C-NMR spectra of compound **1**, recorded in $CDCl_3$ at 25 °C.

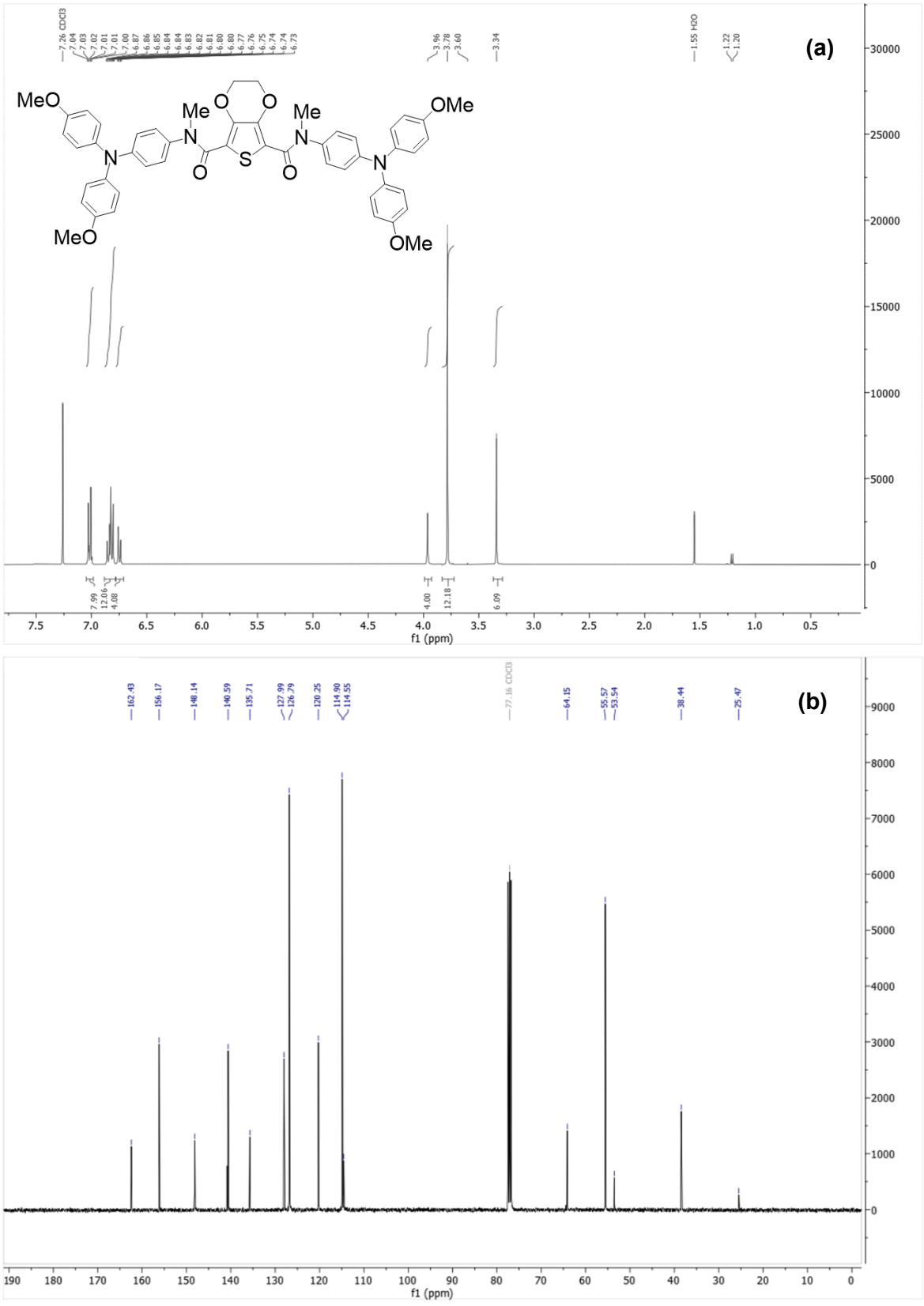

Figure 9-4: (a) ^{1}H-NMR and (b) ^{13}C-NMR spectra of compound **2**, recorded in $CDCl_3$ at 25 °C.

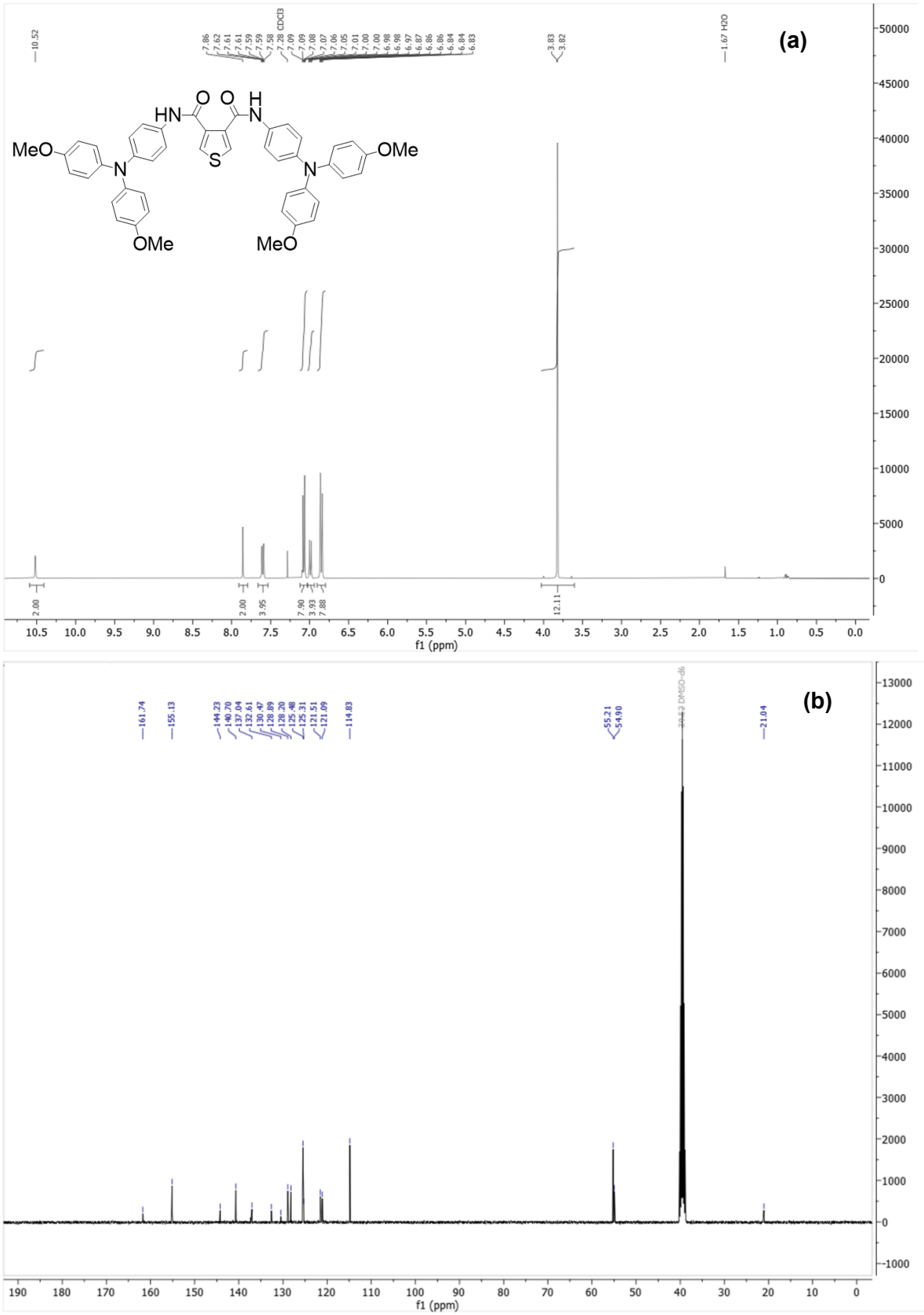

Figure 9-5: (a) ^{1}H-NMR and (b) ^{13}C-NMR spectra of compound **3**, recorded (a) in $CDCl_3$ and (b) in DMSO-d6 at 25 °C.

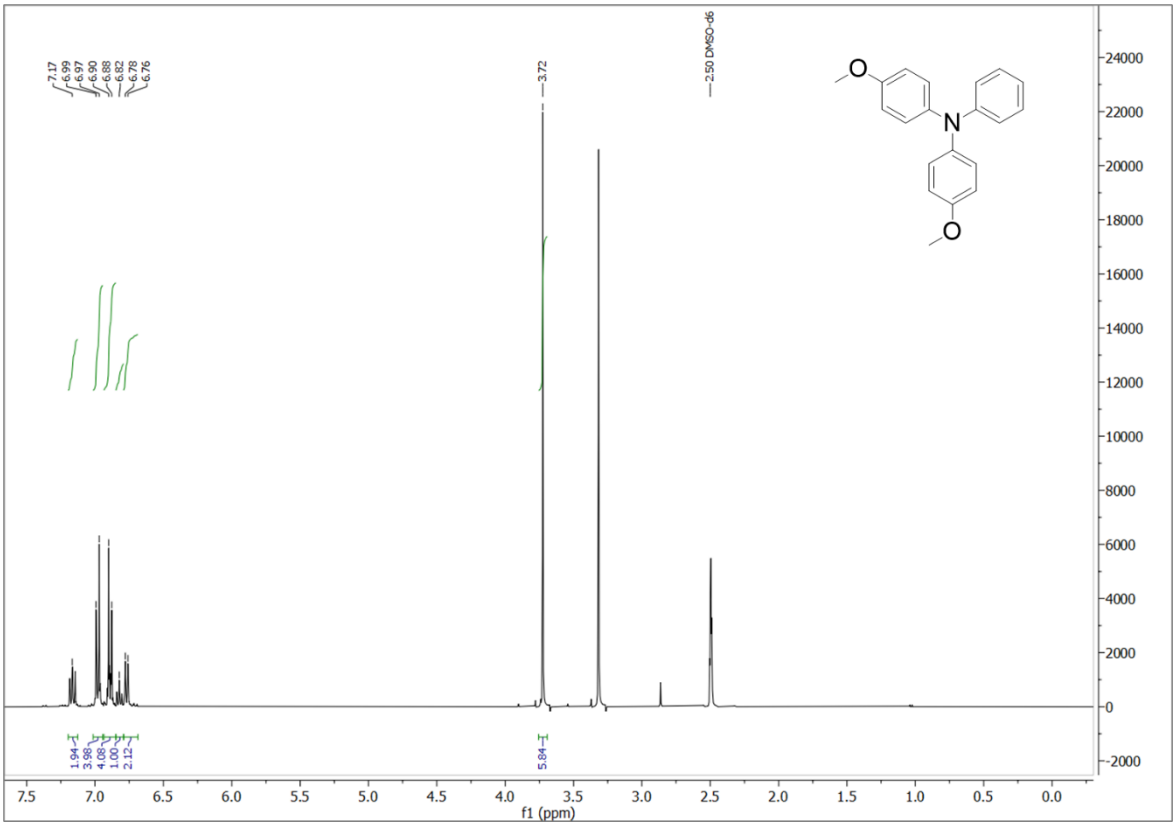

Figure 9-6: ^{1}H-NMR spectrum of **TPA-OMe**, recorded in DMSO-d6 at 25 °C.

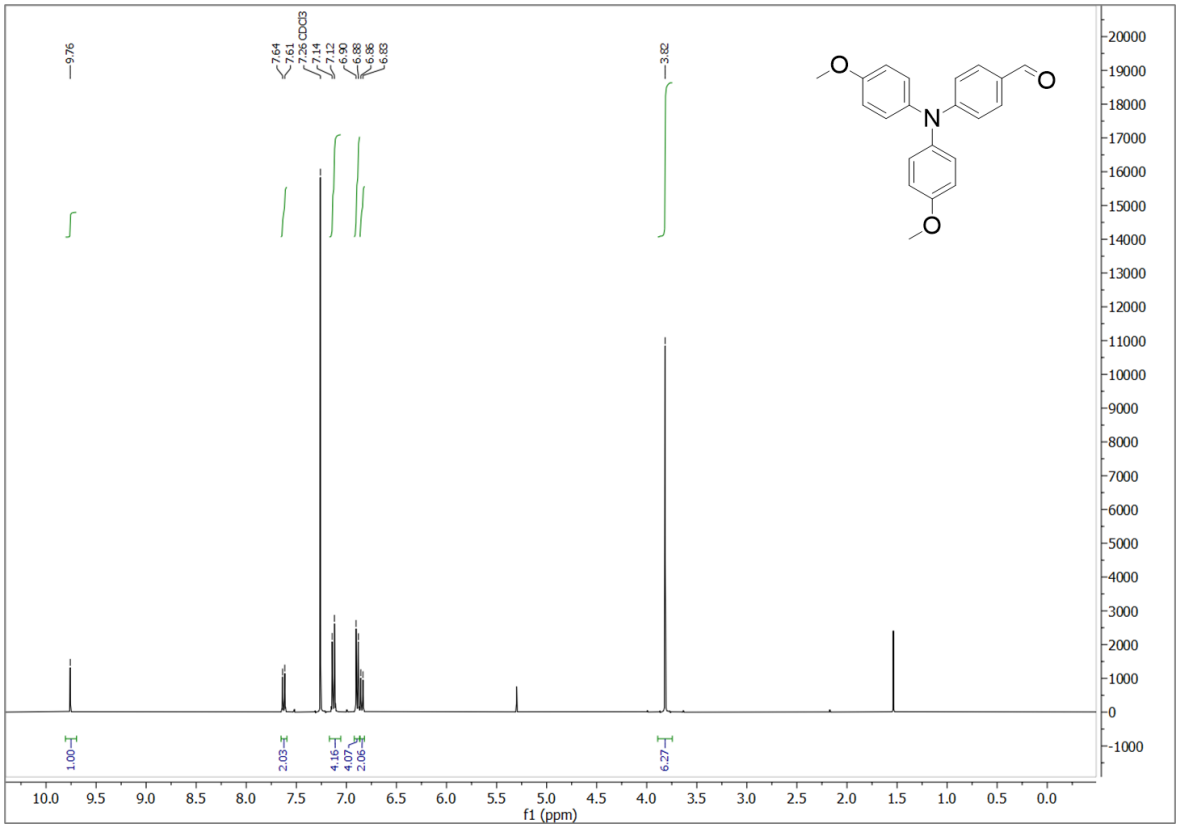

Figure 9-7: ^{1}H-NMR spectrum of **OMeTPA-CHO**, recorded in $CDCl_3$ at 25 °C.

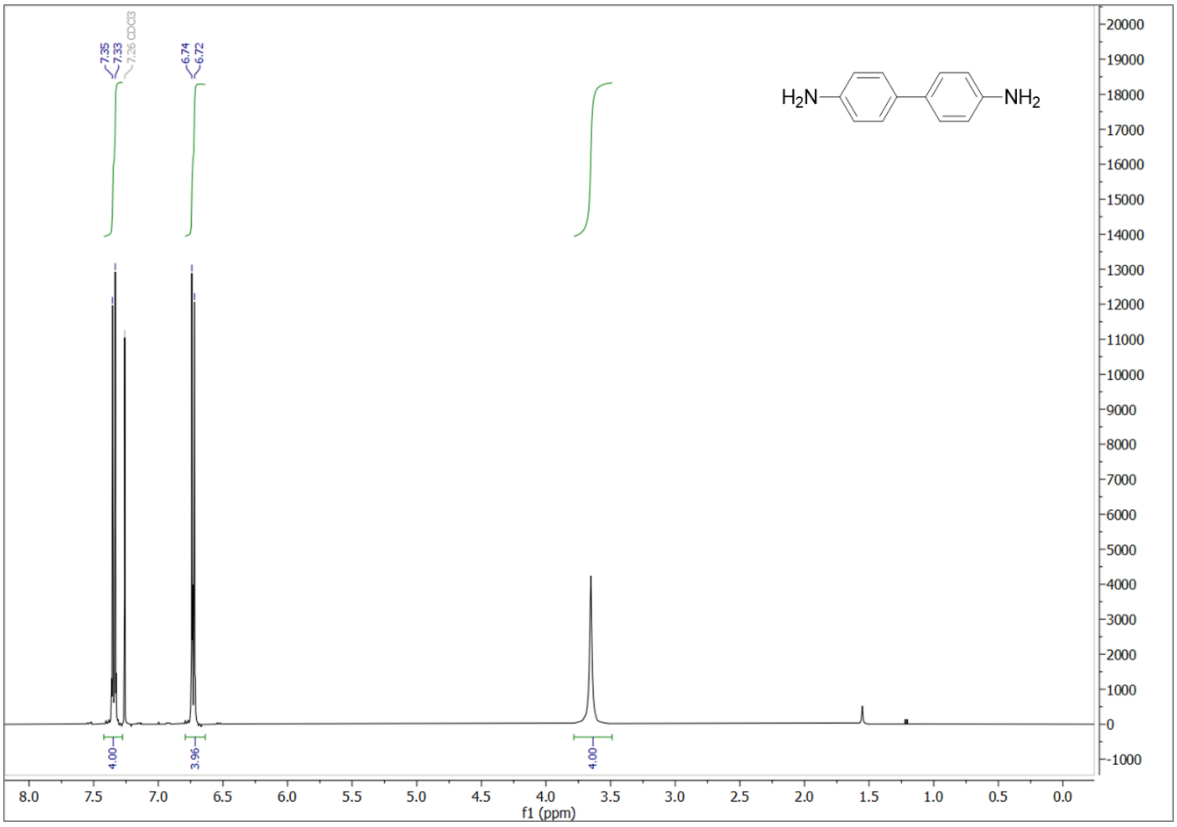

Figure 9-8: ^{1}H-NMR spectrum of synthesised **Benzidine**, recorded in $CDCl_3$ at 25 °C.

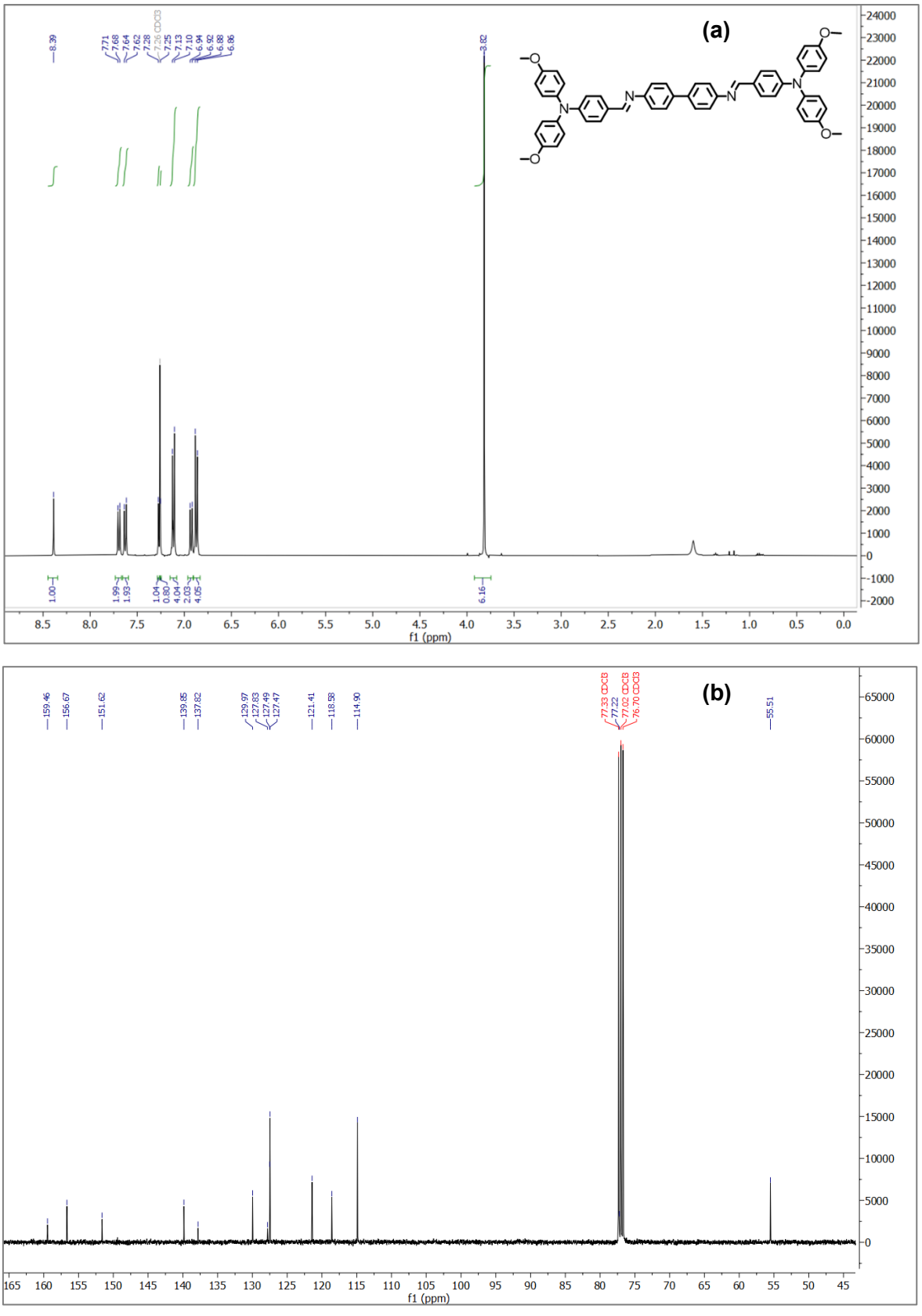

Figure 9-9: (a) ^{1}H-NMR and (b) ^{13}C-NMR spectra of HTM **4**, recorded in $CDCl_3$ at 25 °C.

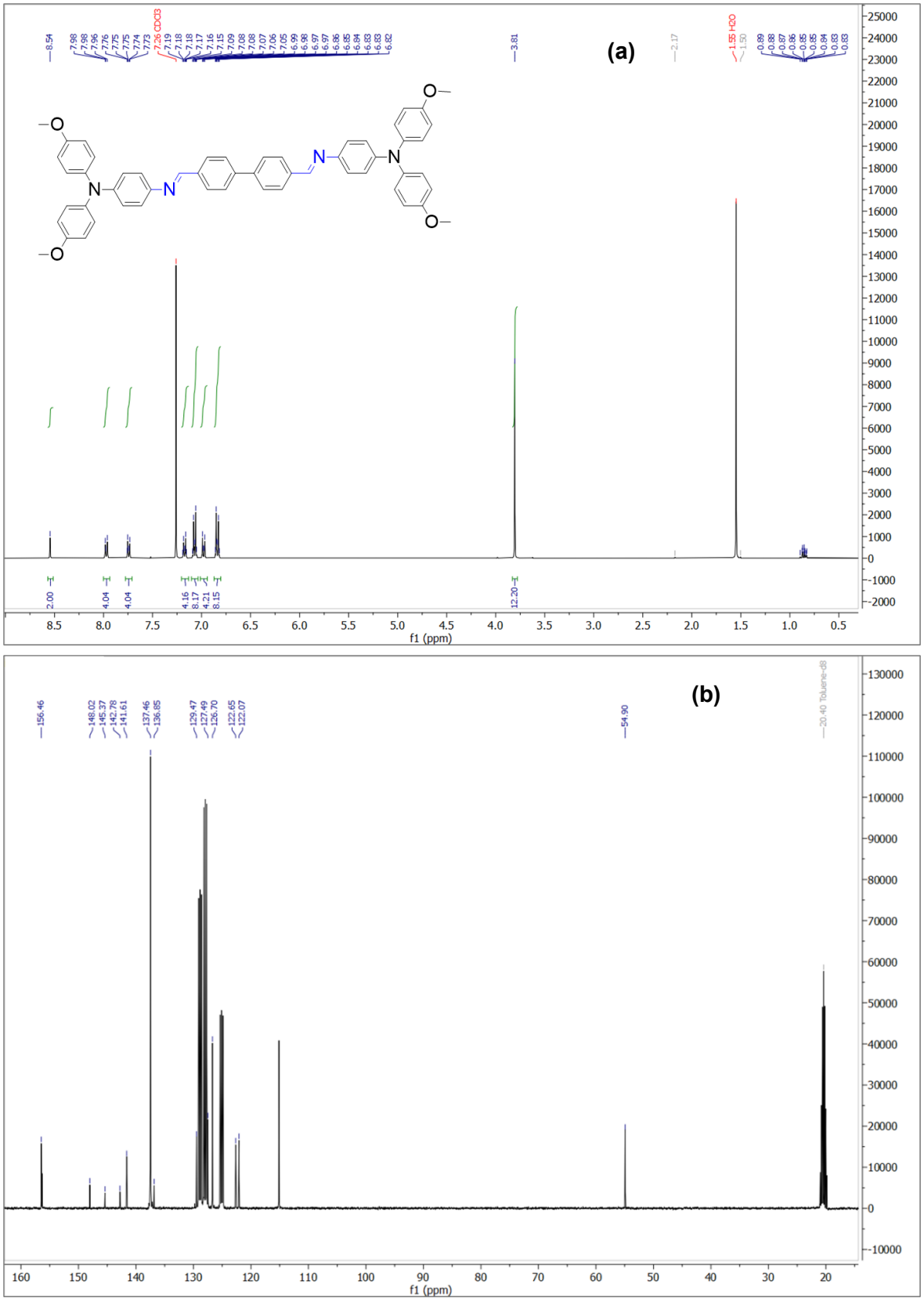

Figure 9-10: (a) ^{1}H-NMR and (b) ^{13}C-NMR spectra of HTM **5**, recorded in (a) $CDCl_3$ and (b) toluene-d8 at 25 °C.

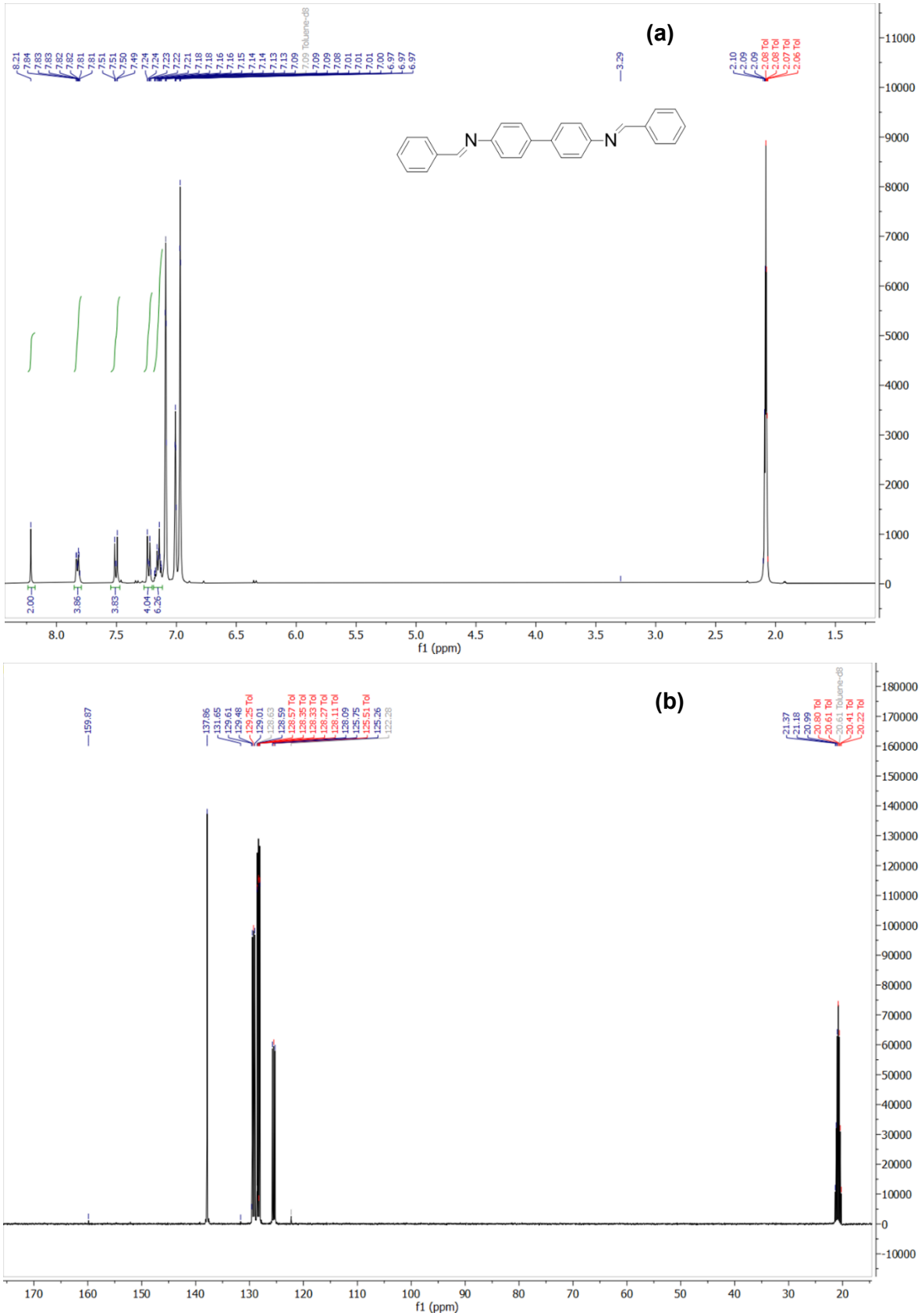

Figure 9-11: (a) ^{1}H-NMR and (b) ^{13}C-NMR spectra of compound **6**, recorded in toluene-d8 at 25 °C.

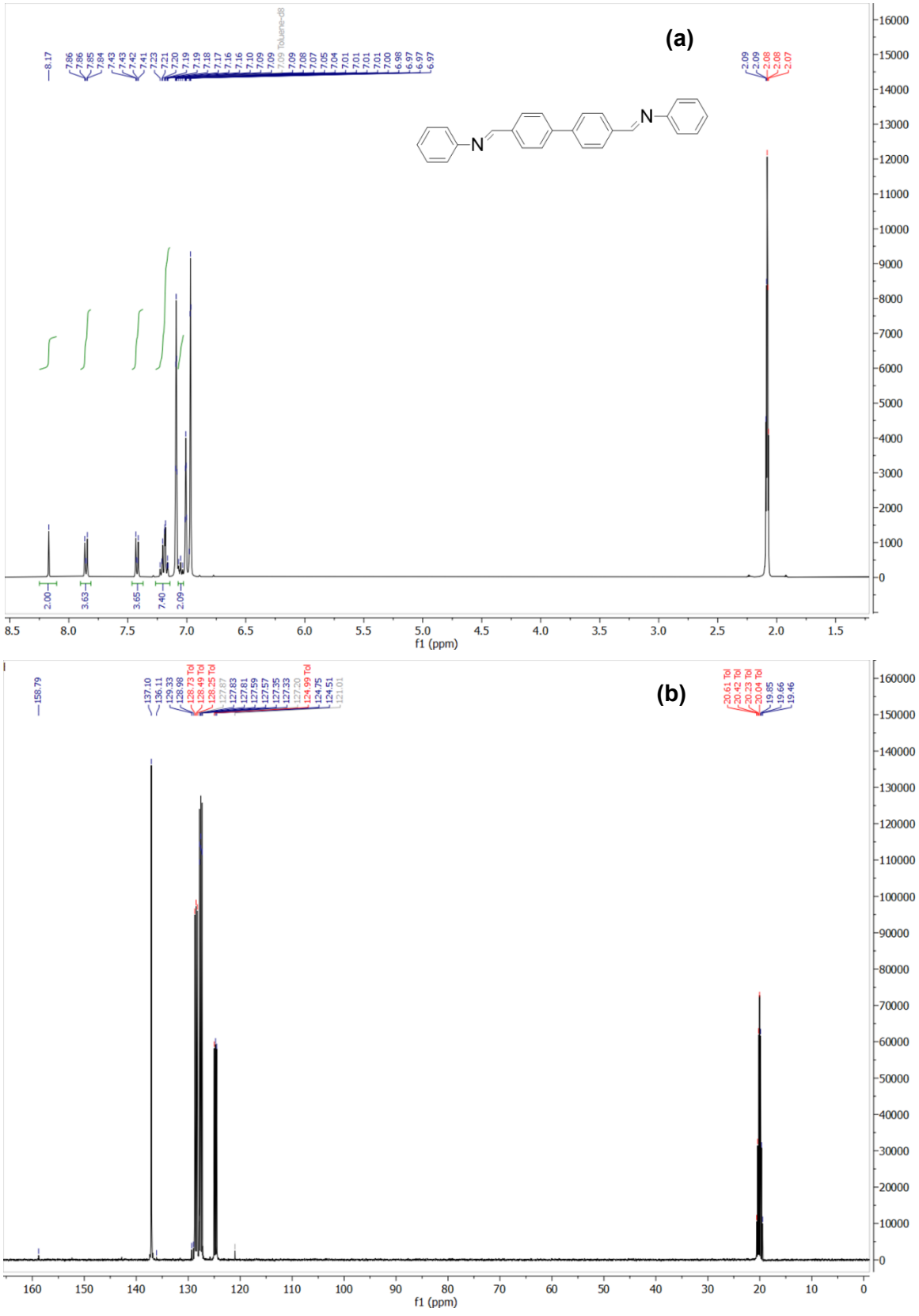

Figure 9-12: (a) ^{1}H-NMR and (b) ^{13}C-NMR spectra of compound **7**, recorded in toluene-d8 at 25 °C.

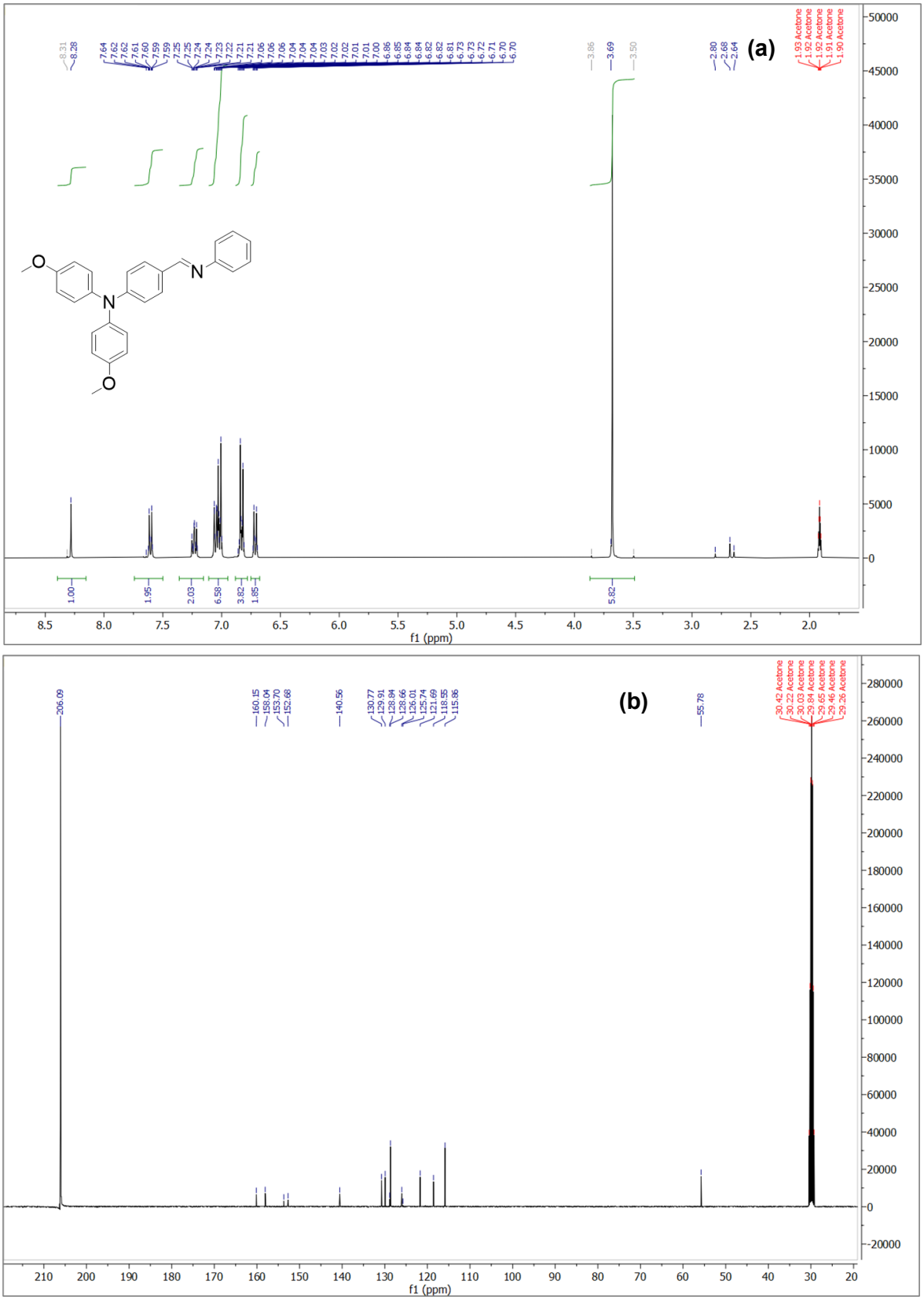

Figure 9-13: (a) ^{1}H-NMR and (b) ^{13}C-NMR spectra of compound **8**, recorded in acetone-d6 at 25 °C.

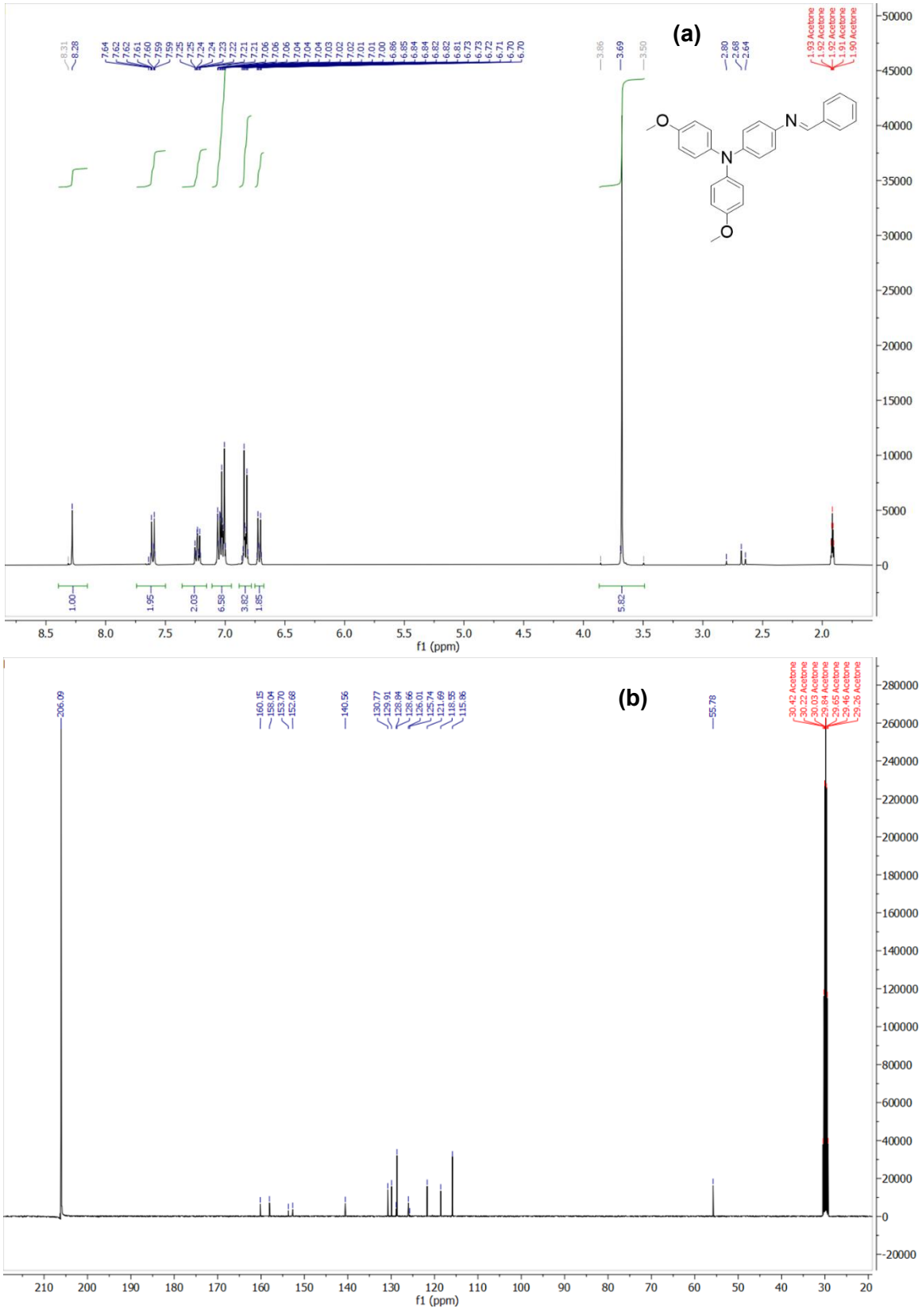

Figure 9-14: (a) ^{1}H-NMR and (b) ^{13}C-NMR spectra of compound **9**, recorded in acetone-d6 at 25 °C.

9.2 Mass Spectra

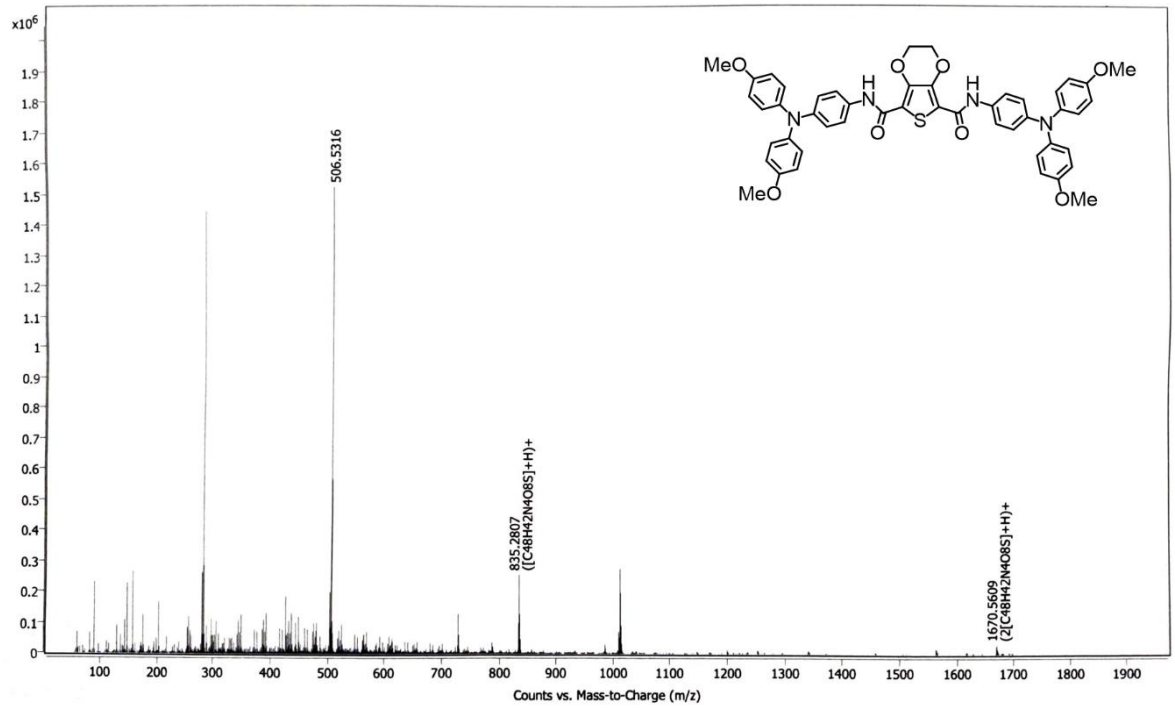

Figure 9-15: Mass spectrum of HTM **1**.

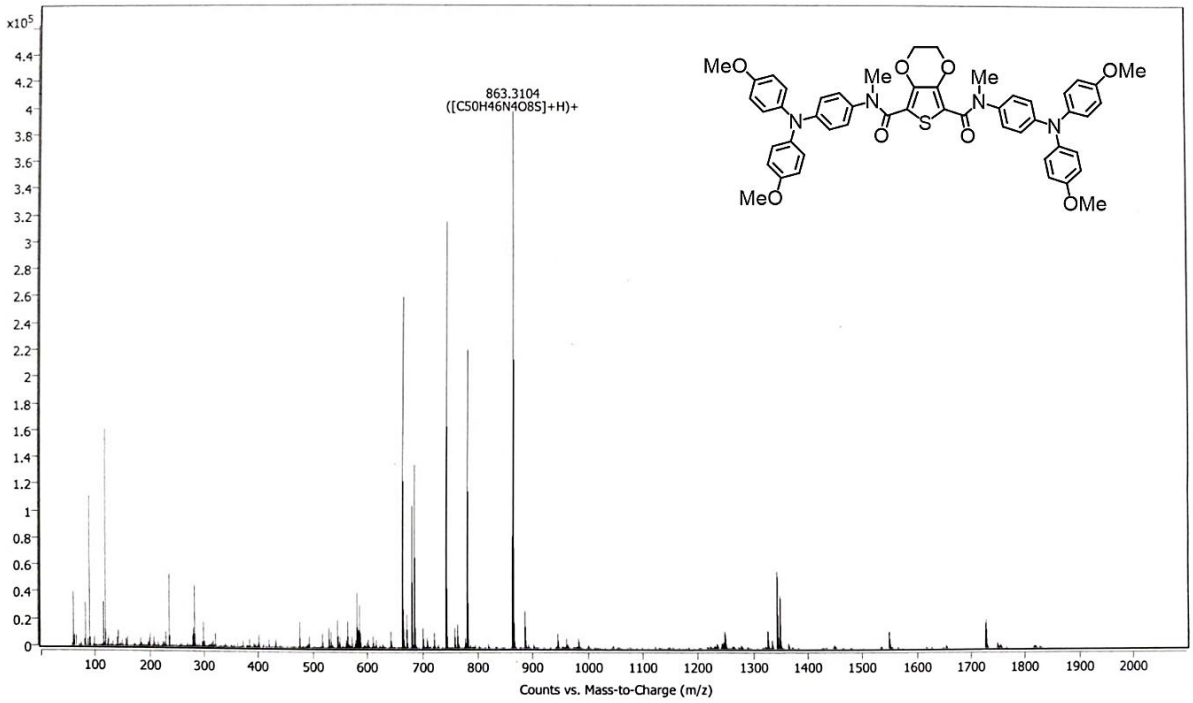

Figure 9-16: Mass spectrum of HTM **2**.

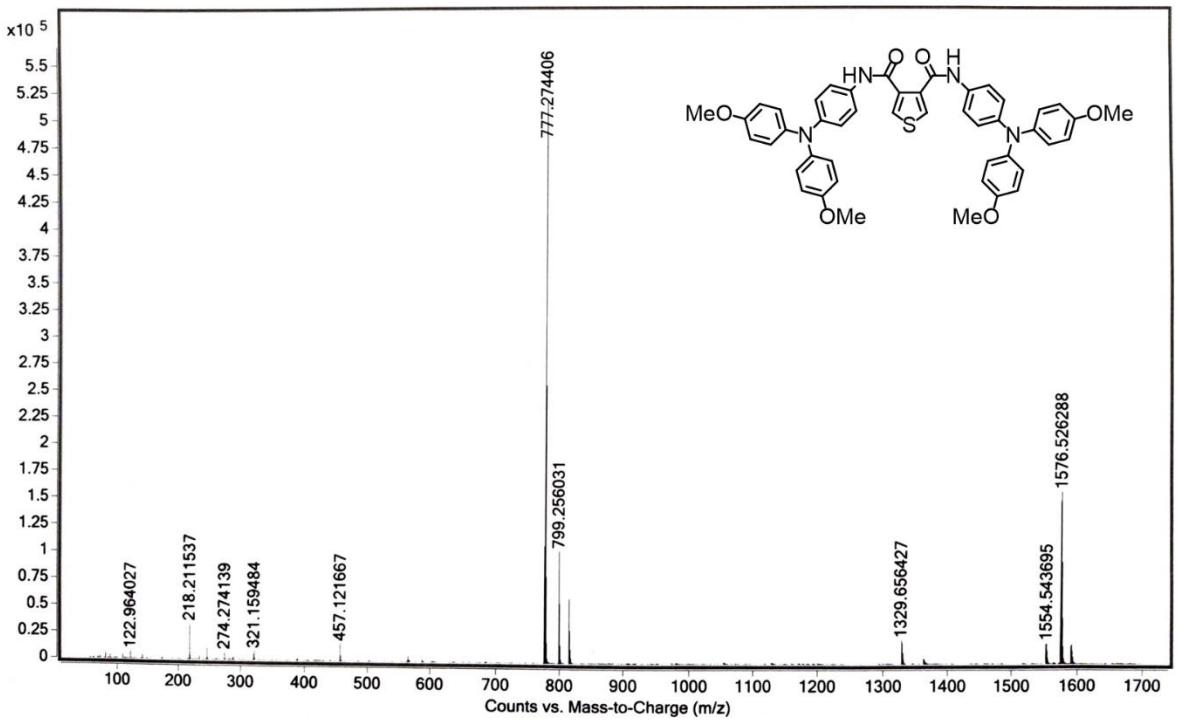

Figure 9-17: Mass spectrum of compound **3**.

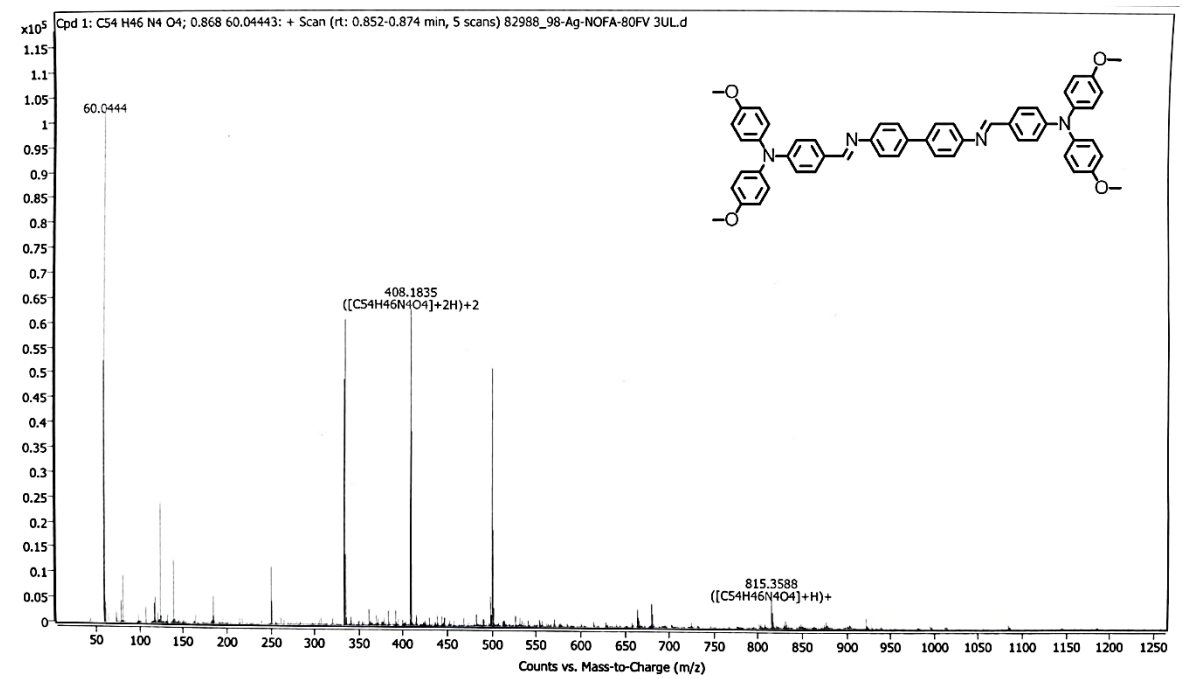

Figure 9-18: Mass spectrum of compound **4**.

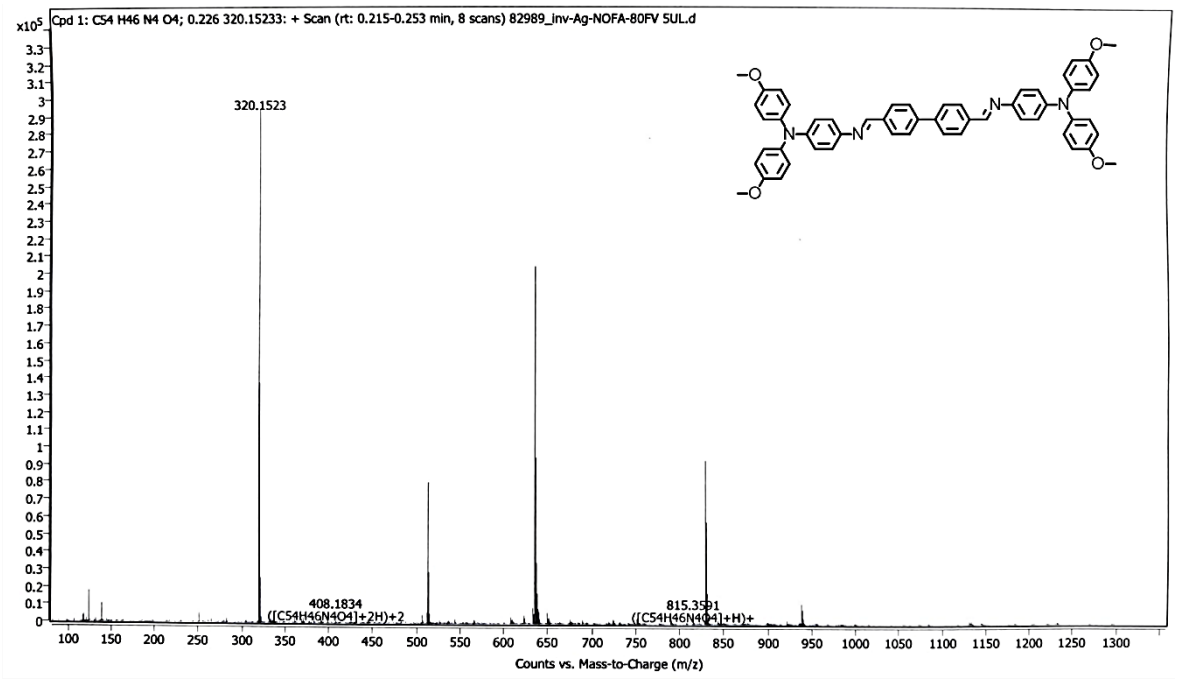

Figure 9-19: Mass spectrum of compound **5**.

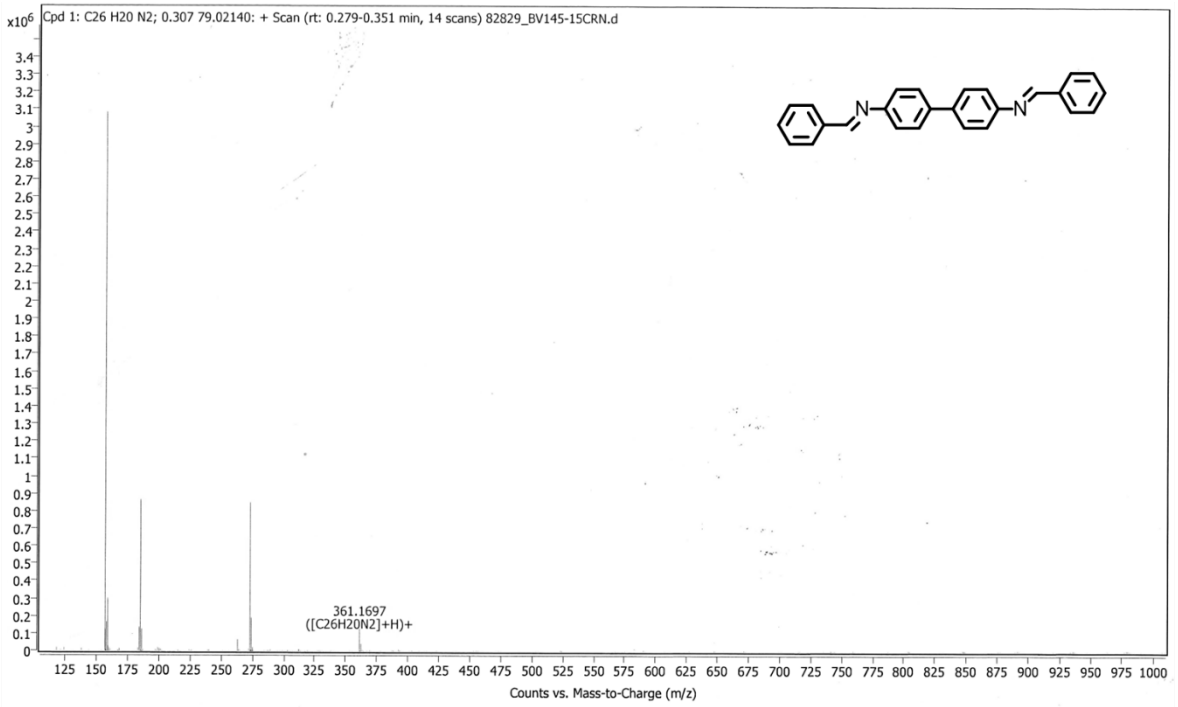

Figure 9-20: Mass spectrum of compound **6**.

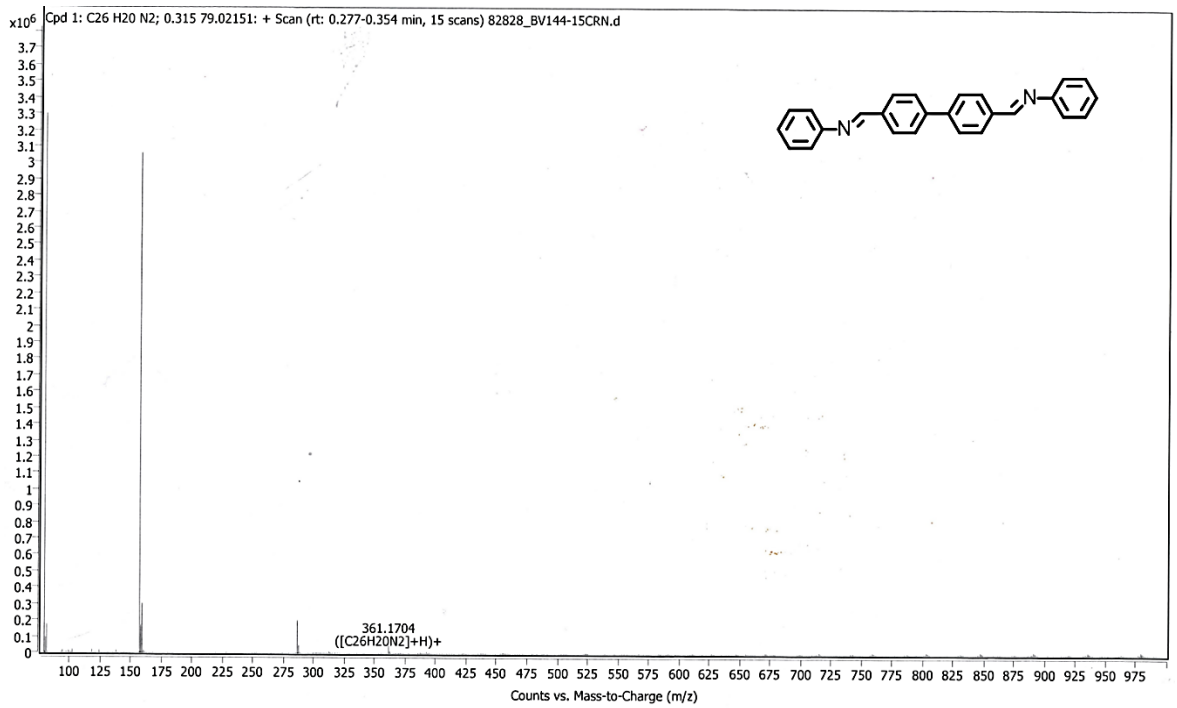

Figure 9-21: Mass spectrum of compound **7**.

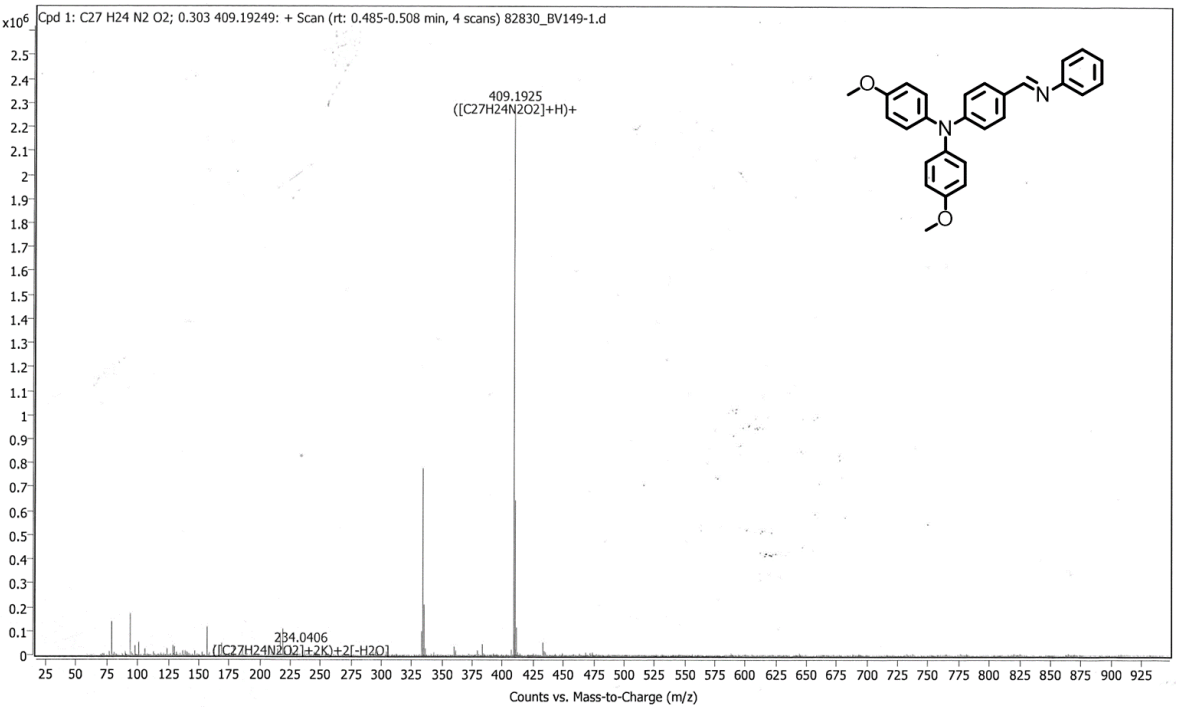

Figure 9-22: Mass spectrum of compound **8**.

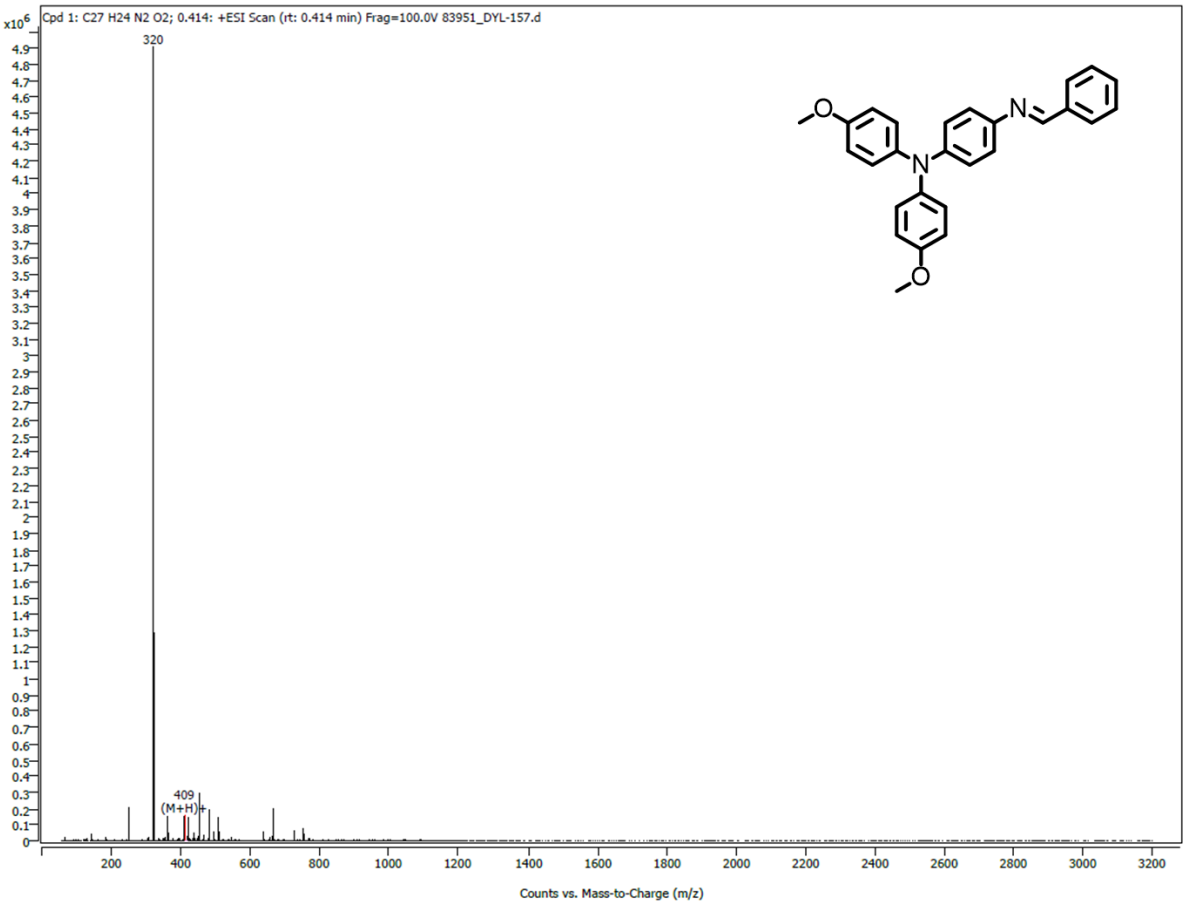

Figure 9-23: Mass spectrum of compound **9**.

9.3 Amide HTM Cost Analysis

Full cost analysis tables used in the working of synthetic cost for amide HTMs **1** – **3**, discussed in Section 2.2.1.

Table 9-1: Cost analysis for HTM **1**

Compound	Mass used (kg)	Cost per kg ($)	Material cost ($)
EDOT-COOH	0.000300	5455.36	1.64
DMF	0.00000950	5.09	0.000048
$SOCl_2$	0.000377	27.67	0.01
THF	0.0178	9.24	0.16
TPA-NH_2 [58]	0.000914	2280.00	2.08
Triethylamine	0.000316	21.54	0.01
THF (solvent)	0.00888	9.24	0.08
MeOH (wash)	0.00396	2.21	0.01
THF (wash)	0.00888	9.24	0.08
Petroleum ether (wash)	0.00320	142.40	0.46
		Total	$4.53
		Yield	0.79 g
		Total Material Cost	**$5.74 / g**

Table 9-2: Cost analysis for HTM **2**

Compound	Mass used (kg)	Cost per kg ($)	Material cost ($)
EDOT-Amide-TPA	0.00102	5455.36	5.54
NaH 60%	0.000278	231.68	0.064
DMF	0.0143	5.09	0.073
CH_3I	0.000524	154.94	0.081
Petroleum ether (precipitation)	0.0192	142.40	2.73
Acetone (Purification)	0.0791	83.98	6.64
Dichloromethane (Purification)	1.325	11.16	14.79
		Total	$8.49
		Yield	0.507 g
		Total Material Cost	**$16.76 / g**

Table 9-3: Cost analysis for HTM **3**

Compound	Mass used (kg)	Cost per kg ($)	Material cost ($)
Th-COOH	0.00248	3120.00	7.74
$SOCl_2$	0.000278	231.68	0.064
DMF	0.0000209	5.09	0.00011
THF	0.0178	154.94	2.75
TPA-NH_2 [58]	0.00971	83.98	0.82
Triethylamine	0.00337	11.16	0.038
THF (solvent)	0.0178	9.24	0.16
Diethyl ether (precipitation)	0.0353	142.40	5.03
Ethanol (Recrystallisation)	0.0789	2.78	0.22
Acetone (Purification)	0.0791	83.98	6.64
Dichloromethane (Purification)	1.325	11.16	14.79
		Total	$38.25
		Yield	2.47 g
		Total Material Cost	**$15.48 / g**

9.4 Single-crystal structure data

Data obtained courtesy of Dr. Claire Wilson at the School of Chemistry.

Table 9-4: Crystal data for HTM **1**

$C_{48}H_{42}N_4O_8S$	D_x = 1.359 Mg m^{-3}
M_r = 834.91	Cu $K\alpha$ radiation, λ = 1.54178 Å
Tetragonal, $I4_1/a$	Cell parameters from 14810 reflections
a = 55.7783 (6) Å	θ = 4.5–70.6°
c = 10.4905 (2) Å	μ = 1.22 mm^{-1}
V = 32638.2 (9) Å^3	T = 100 K
Z = 32	Needle, yellow
F(000) = 14016	0.5 × 0.02 × 0.01 mm

Table 9-5: Crystal data for HTM **2**.

$C_{50}H_{46}N_4O_8S$	F(000) = 1816
M_r = 862.97	D_x = 1.299 Mg m^{-3}
Monoclinic, $P2_1/c$	Mo $K\alpha$ radiation, λ = 0.71073 Å
a = 16.6681 (5) Å	Cell parameters from 9989 reflections
b = 18.0603 (6) Å	θ = 2.6–26.3°
c = 16.6318 (5) Å	μ = 0.13 mm^{-1}
β = 118.212 (1)°	T = 150 K
V = 4411.9 (2) Å^3	Block, yellow
Z = 4	0.23 × 0.11 × 0.08 mm

Table 9-6: Crystal data for HTM **3** CB solvate.

$C_{46}H_{40}N_4O_6S{\cdot}2(C_6H_5Cl)$	F(000) = 2096
M_r = 1001.98	D_x = 1.328 Mg m^{-3}
Monoclinic, $P2_1/c$	Mo $K\alpha$ radiation, λ = 0.71073 Å
a = 12.1294 (3) Å	Cell parameters from 9902 reflections
b = 14.8596 (3) Å	θ = 2.7–28.1°
c = 27.9555 (8) Å	μ = 0.23 mm^{-1}
β = 96.092 (1)°	T = 150 K
V = 5010.2 (2) Å^3	Block, colourless
Z = 4	0.41 × 0.13 × 0.1 mm